Semiconductor nanodevices as a probe of strong electron correlations

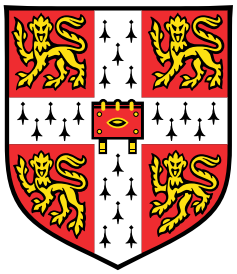

Pedro Manuel Trocado Vianez

Department of Physics
University of Cambridge

This thesis is submitted for the degree of
Doctor of Philosophy

Clare College December 2021

Declaration

This thesis is the result of my own work and includes nothing which is the outcome of work done in collaboration except as declared in the Preface and specified in the text. I further state that no substantial part of my thesis has already been submitted, or, is being concurrently submitted for any such degree, diploma or other qualification at the University of Cambridge or any other University or similar institution except as declared in the Preface and specified in the text. It does not exceed the prescribed word limit for the relevant Degree Committee.

Pedro Manuel Trocado Vianez
December 2021

Semiconductor nanodevices as a probe of strong electron correlations

Pedro Manuel Trocado Vianez

An electron is usually considered to have only one type of kinetic energy, but could it have more, for both its spin and charge, or by exciting other electrons? In one dimension (1D), the physics of interacting electrons is captured well at low energies by the linear Tomonaga-Luttinger Liquid (TLL) model, with hallmark predictions, such as spin-charge separation, having already been observed. Recent theoretical work has focused on extending the theory to deal with more realistic curved dispersions. However, experimental realisations have remained elusive until recently. Here, we report on measurements of many-body modes using a momentum-resolved tunnelling spectroscopy technique in gated 1D wires connected via air-bridges. We map the 1D dispersion in a variety of devices, both in and out of equilibrium, and observe the formation of two separate Fermi seas, associated with spin and charge excitations, at energies up to five times that of the Fermi energy, which cannot be accounted for by the noninteracting model. By reducing the length of the system, we also observe the emergence of higher-order 'replica' parabolic dispersions with higher momenta or negative effective mass, which is consistent with one of the leading nonlinear Luttinger theories. Determining the bare electron mass m_0 in crystals is also another problem often hindered by many-body effects. Here, Fermi-liquid physics renormalises the band mass, making the observed values density-dependent. In 1D geometries, however, the effect of interactions is strongly amplified, and they naturally decouple from the mass. By changing the level of confinement in the wires, we are able to tune the electron density down to about 18 electrons per micron or, equivalently, an interaction parameter of $r_s \sim 4$. This allows us to extract a constant bare mass value of $m_0 = 0.0545 m_e$, about 20% lighter than observed in GaAs in geometries of higher dimensionality. Finally, by progressively occupying more 1D subbands, our system also allows us to change the amount of inter-subband screening by over 50%, consequently varying the effective interaction strength, in situ, all the way from the weakly to the strongly interacting regime. This ability is the first of its kind for 1D solid-state system. Our spectroscopy technique therefore offers itself as an important and powerful tool for probing strongly correlated systems where new emerging phenomena are occurring. This knowledge is now being used to develop systems for improved energy efficiency and could prove useful in designing the next generation of sustainable materials.

Acknowledgements

This thesis would not have been possible were not for a group of people whom, in one way or another, allowed me to pursue a PhD in Physics at Cambridge. To them I owe a great deal of support and encouragement over the past few years.

First, I would like to acknowledge my supervisor, Prof. Chris Ford, for allowing me to embark on the journey that has been the past four years. This project would not have succeeded without his guidance and (what seems limitless) patience. Chris always supported me in all my endeavours and, for that, I am truly thankful. I look forward to continue working together over the next few years and I am sure that no matter where my career may lead me I will always carry his teachings with me.

The second person who I would like to acknowledge is Dr. Oleksandr Tsyplyatyev at the Institut für Theoretische Physik, Goethe-Universität Frankfurt. A *de facto* second supervisor, I estimate that over the past two years Alex and I probably met at least once a week. To him I owe the patience and willingness to always guide me through the latest theoretical developments and what implications might they have for our data. In a time when experiment and theory sometimes seem to become ever more widely separated, I am thankful for Alex's support in allowing me to bring these two fields together as much as I possibly could.

Towards the end of my second year I had the opportunity to visit Prof. Leonid Glazman at the Yale Quantum Institute thanks to the support of a Clare-Yale Fellowship. Though short, the opportunity of being away from Cambridge for a few months made this indeed a very productive and positive experience. In fact, it was while at Yale that the two-Fermi-sea idea, probably the most important contribution of the present thesis, first started coming into shape. For that, I thank Leonid and everyone else I met at Yale for so kindly accepting to host me. I would also like to acknowledge the Engineering and Physical Sciences Research Council and Clare College which, financially and otherwise, have supported me during my doctoral studies.

One of the most enjoyable parts of my PhD work was the fact that it gave me the opportunity to be involved in almost every stage of research, from conception to design, fabrication and measurement, and finally analysis. This would not have been possible were not for the incredible equipment and facilities I had available to me at the Cavendish

Laboratory, as well as the people who helped me along the way. For that, I would like to thank Shak Fernandes, Gulzat Jaliel, Nikita Almond, Wooi Kiat Tan, and Yiqing Jin, who made my time at SP a little bit more special, as well as Melanie and Abbie in the cleanroom, Harvey and Chong who were always available to answer all my MBE-related questions, and Jon in the e-beam. I would also like to show my gratitude towards the Integrated Quantum Materials group, Dr. Stephen Rowley, Dan Scott, and Shuyu Liu, who adopted me in my final year of PhD and where now I am excited to continue my postdoctoral research.

My time at Cambridge, with all its ups and downs, also led me to meet a number of people, many of which I know I will carry for life. To my friends Kian, Oak, Jonny, Ana, and Blanca, thank you for putting up with me. To my Summer of '67 Chesterton Road housemates, Laura, Lotte, Lucy and Ross, thank you for all the fun nights at the MCR. To the 1-16 Clare Court 'lockdown(s)' crew, Anneli, Dan, Marina, Thomas, Sam, Jas, Will, Lena, and Anis, if I ever find myself in another pandemic I know who to call.

I would also like to acknowledge a number of individuals who, though far geographically, have nevertheless always been present. To my UCL friends Aishwarya Paliwal and Pavlina Tsiapi, the three of us haven't been together for over 6 years but thank you for always being there for me. To Sofia Ferreira Teixeira, you know what they say, lab partners once, lab partners for life. Finally, to Ana Castro and Sandra Silva, two of my oldest friends, I am finally free to join you on Discord!

Going from my undergraduate days in Porto, almost a decade ago, to where I am now, was only possible thanks to the early words of encouragement and support from two particular academics. To Prof. Carlos Martins, you paved my way to Cambridge, and Prof. Fátima Mota, who first showed me the ropes of quantum mechanics, thank you.

The unsung hero of this thesis, to whom I owe a lot over the past few years and, even more, the past few months, is my partner and teammate Aaron Fleming. Cambridge brought me many academic experiences but it also led me to meet you. Thank you for always having my back.

Finally, I dedicate this work to my family and, in particular, my mother and grandmother, who have been there since the start. They are the two strongest women I know, and to them I owe more than I could ever repay. I hope to have made you proud.

To my mother and grandmother,
who have been there since the start.

Table of contents

List of figures

List of tables

Chapter 1

Introduction

1.1 Motivation

The many-body problem could be an inconspicuous title for an Agatha Christie novel, yet in this thesis it will mean a vast category of physical problems where one attempts to infer the properties of the whole based on knowledge of its constituent parts. The challenge of modelling systems made out of multiple interacting elements is probably as old as physics itself, yet to date it remains largely an open field. Indeed, by *many* we mean anywhere from three up to infinity, the two-body problem being so far the only one where a full analytical solution has been found.

A particularly interesting facet of this problem concerns the study of electrons inside solid crystals. While electron-electron interactions are known to be quite strong, a surprisingly large number of models can make a number of accurate predictions despite simply disregarding them. Landau solved this apparent disparity by developing what came to be known by the name of Fermi liquid theory, therefore explaining why the properties of so many fermionic systems seemingly resemble those of an ideal Fermi gas. While the Fermi liquid model successfully captured the behaviour of many metals at low temperatures, soon an equally if not larger number of systems were discovered where Landau's quasiparticle formalism apparently broke down. Such non-Fermi liquids, also commonly referred to as strange metals, range nowadays from heavy-fermion compounds, Mott insulators, unconventional superconductors, to topological insulators, to name but a few. Here, in general, interactions take over the ability of electrons to freely move around, leading to the emergence of some form of correlated response.

Possibly the simplest example of non-Fermi liquid behaviour concerns electrons in one dimension. Here, geometry alone imposes strong correlations even in the absence of strong interactions. The beauty of 1D, however, lies in the fact that unlike its higher dimension

counterparts, a full analytical solution can now be achieved, albeit only at low energies, in what has come to be known as Tomonaga-Luttinger liquids. These are qualitatively different from Fermi liquids in many ways, the separation of the spin from the charge modes being a well-known example. Other approximations made by this model include the assumption of infinite system length and subband spacing.

The work now being reported started from the desire to investigate the emerging spectrum of an experimental 1D system where the assumptions of the Tomonaga-Luttinger liquid model were deliberately being broken. This included not only high energy, nonlinear regimes, far from the Fermi surface, but also finite-length systems where multiple 1D subbands could be occupied. The greater simplicity of modelling 1D geometries (at least when compared to higher dimensions) makes these the perfect platform for testing theoretical tools and approximations in a controlled way. That is the topic of the present thesis, as will be discussed over the next few chapters.

1.2 Publications and pre-prints

The work presented in this thesis has resulted in the following pre-prints and publications:

- P. M. T. Vianez, Y. Jin, W. K. Tan, J. P. Griffiths, I. Farrer, D. A. Ritchie, O. Tsyplyatyev, C. J. B. Ford, *Decoupling of many-body effects from the electron mass in GaAs by means of reduced dimensionality* [arXiv: 2110.14539]

- P. M. T. Vianez, Y. Jin, M. Moreno, A. Anirban, A. Anthore, W. K. Tan, J. P. Griffiths, I. Farrer, D. A. Ritchie, A. J. Schofield, O. Tsyplyatyev, C. J. B. Ford, *Observing spin and charge separated Fermi seas in a strongly-correlated one-dimensional conductor* [arXiv: 2102.05584]

- Y. Jin, M. Moreno*, P. M. T. Vianez*, J. P. Griffiths, I. Farrer, D. A. Ritchie, C. J. B. Ford, *Microscopic metallic air-bridge arrays for connecting quantum devices*, Appl. Phys. Lett. **118**, 162108 (2021) [* equal contribution]

In addition, most of chapter 2 has been reorganised and published as a book chapter:

- P. Vianez, O. Tsyplyatyev, C. Ford, *Semiconductor nanodevices as a probe for strong electron correlations. In: Semiconductors Nanodevices: Physics, Technology and Applications*, David Ritchie (Ed.), Elsevier (2021)

1.3 Contributions to the original material

Below is an account of my own contributions to all the work mentioned above.

Regarding Vianez *et al.* arXiv 2110.14539 and 2102.05584, where I am the first and lead author, my contributions include fabrication of the experimental devices, performance of the transport measurements shown, analysis of the data, discussion of the results, and writing of the manuscript. For both manuscripts I am also one of the corresponding authors.

Regarding the work Jin, Moreno*, Vianez*, *et al.*, APL **118**, 162108 (2021) [* equal contribution], where I am joint-second author, my main contribution to this work was improving the original air-bridge technique to fabricate longer bridges, pushing the maximum length value by about an order of magnitude. This enabled improved results as well as greater flexibility of use when compared to the shorter bridges. Specifically, I fabricated some of the devices used, as well as optimised the resist profile and development time, and conducted the transport measurements shown at the end of the paper. I also contributed significantly to the writing of the manuscript.

Finally, regarding the work Vianez *et al.*, Semiconductor nanodevices as a probe of strong electron correlations, in: Semiconductor Nanodevices: Physics, Technology and Applications, David Ritchie (Ed.), Elsevier (2021), where I am first-author, I wrote most of the chapter, including all experimental sections and most of the theory sections (apart from section 3.2).

1.4 Outline

This thesis is structured as follows. Chapter 2 introduces the many-body problem, starting with a brief overview of Fermi-liquid theory and its general applicability to higher-dimensional fermionic systems, before introducing the Tomonaga-Luttinger liquid (TLL) model, valid only in one dimension (1D). Here, we review both early as well as more recent developments in the field of 1D TLLs, including nonlinear and interaction effects. Most of this chapter has been adapted from [123]. Chapter 3 introduces the experimental technique behind most measurements reported in this thesis, magnetunnelling spectroscopy (MTS). Here, we show how MTS can be performed with both energy and momentum resolution, and discuss how the spectral function of a system can be inferred from the resulting tunnelling dispersion maps. We conclude by modelling the capacitive effects which affect our measurement, estimating their magnitude. Chapter 4 reports on the semiconductor nanodevices used in this work, including design and material considerations, cleanroom fabrication, and measurement setup. In this chapter we also discuss the implementation of a novel electron-

beam-lithography technique for fabricating suspended air-bridge structures, which has since been published in [58]. Chapter 5 reports on the observation of two separate Fermi seas for spin and charge excitations respectively. Here, we start by characterising the 1D wire array before discussing the measured dispersion maps. After ruling out a single Fermi sea as a possible explanation for the observed spectra, we interpret the results based on the 1D Fermi-Hubbard model. All data discussed in this chapter was obtained with only a single 1D subband occupied, with most of the results reported in [124]. Chapter 6 then expands from the previous chapter by going into the multiple-subband regime. The first half of the chapter discusses 1D-1D intersubband screening effects, showing how both Fermi seas are seen to emerge as interaction strength is varied. The second half of the chapter applies the 1D Fermi-Hubbard model to the extraction of the bare mass of electrons in GaAs (*i.e.*, free from many-body effects) as reported in [125]. Finally, chapter 7 discusses additional observed signatures indicative of interaction effects in 1D. Here, we report on the observation of higher-order 1D 'replica' modes, as predicted by the hierarchy of modes picture for nonlinear Luttinger liquids. Chapter 8 summarises all main results reported in this thesis and provides a perspective on future work.

Chapter 2

The many-body problem

Interactions between electrons in solids are often behind exciting novel effects such as magnetism, superfluidity, and superconductivity. All these phenomena break away from the single-electron picture, instead having to take into account the collective, correlated behaviour of the system as a whole. In this chapter, we discuss the many-body problem and its many manifestations within the specific context of condensed matter physics. We start by discussing the Fermi liquid paradigm for a system of interacting electrons at low temperatures, showing how it can be used to describe a vast array of systems in both three and two dimensions (section 2.1). We then introduce the Tomonaga-Luttinger liquid (TLL) model, valid for electron liquids in one dimension, showing how it marks a clear departure from Fermi liquid theory, and discuss some of the early experimental evidence in support of it (section 2.2). We conclude with an overview of more recent experimental results in support of the TLL model, as well as its nonlinear counterparts, obtained using a variety of experimental techniques (sections 2.3), as well as briefly commenting on some other 1D effects reported in the literature (section 2.4).

The review presented in this chapter has been adapted from [123].

2.1 The Fermi liquid paradigm

Fermi liquid theory is probably one, if not the most well-known, theoretical model in many-body condensed matter physics. Proposed by Lev Landau in 1956 [78], and later justified microscopically by Abrikosov and Khalatnikov using the Green's function formalism [3], it describes the normal state of many metals at low temperatures. Interestingly, the initial motivation was not to describe metals but instead liquid ^{3}He, whose heat capacity, despite being a liquid, had been found to be very similar to that of an ideal (*i.e.*, non-interacting) gas. The resulting theory was capable of not only explaining why so many interacting fermionic

systems often have properties resembling that of an ideal Fermi gas, but also why, how, and when these can start to break down.

Landau's model essentially relies on two underlying assumptions, the Pauli exclusion principle and adiabaticity. The basic idea is that, for a system of interacting fermions with repulsive interactions (such as, for example, electrons in solids), the low-energy spectra can be constructed by directly mapping onto that of a non-interacting system. In other words, starting with an hypothetical (ideal) system where no interactions are present, one can establish a one-to-one correspondence between its excited states and those after interactions are turned on, after which the approximate eigenstates and eigenenergies of the interacting system can be obtained. Since a noninteracting system can always be specified by a set of occupation numbers $\{\mathcal{N}_{\mathbf{k},\sigma}\}$, it follows that these can also be used to describe the equivalent excitations in the interacting scenario. In order for this argument to be valid, however, the transition from ideal to interacting system needs to occur slowly. As we will see, this sets a maximum lifetime for the type of excitations that can be described using this model.

Let us start with an ideal gas. Here, any excited state can be described by the deviation of its distribution function n from ground state,

$$\delta n_{\mathbf{k},\sigma} = n_{\mathbf{k},\sigma} - n^0_{\mathbf{k},\sigma} \tag{2.1}$$

where $n_{\mathbf{k},\sigma}$ represents the probability of a state of momentum $\mathbf{k}$ and spin state $\sigma = \{\uparrow, \downarrow\}$ being occupied. For fermions at zero temperature, $n^0_{\mathbf{k},\sigma}$ is given by the Fermi-Dirac distribution, $\Theta(k_\mathrm{F} - k)$, see Fig. 2.1. This allows us define the Fermi wavevector, k_F, as the boundary between occupied and unoccupied states.

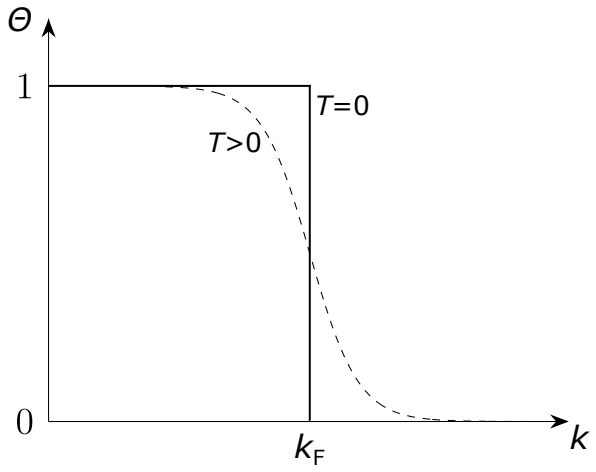

Fig. 2.1 The Fermi-Dirac distribution, showing the probability of a state being occupied, for $T = 0$ and $T > 0$.

We can also compute the change in total energy caused by this excitation as

$$\delta E[\delta n] = E[n] - E_0 = \sum_{\mathbf{k},\sigma} \varepsilon_{\mathbf{k}} \delta n_{\mathbf{k},\sigma} \tag{2.2}$$

where $\varepsilon_{\mathbf{k}} = \hbar k^2/2m$ is the energy of a free particle. More generally, the energy of a particle can be defined as

$$\varepsilon_{\mathbf{k}} = \frac{\delta E[n]}{\delta n_{\mathbf{k},\sigma}}. \tag{2.3}$$

An arbitrary excitation will then consist of adding or removing particles from the ground state, in other words, creating electron-hole pairs. Close to the Fermi surface, equation (2.3) can be expanded to give

$$\varepsilon_{\mathbf{k}} = \varepsilon_{\mathrm{F}} + v_{\mathrm{F}}\hbar(k - k_{\mathrm{F}}) + \mathscr{O}((k - k_{\mathrm{F}})^2) \tag{2.4}$$

where ε_{F} is the Fermi energy and $v_{\mathrm{F}} = \nabla_{\mathbf{k}}\varepsilon_{\mathbf{k}}|_{\mathbf{k}=\mathbf{k_F}} = \hbar k_{\mathrm{F}}/m$ is the Fermi velocity.

The crucial insight of Fermi liquid theory is realising that electron-electron scattering is incredibly ineffective in changing the electron's momentum close to the Fermi energy, since most of the states in which it could end up after collision have already been occupied (see Fig. 2.2). As such, because of the Pauli exclusion principle, these will be unavailable, making the scattering rate $\tau^{-1} \propto |k - k_{\mathrm{F}}|^2$ effectively vanish as $k \to k_{\mathrm{F}}$. Note that this argument is valid irrespective of the strength of the interactions.

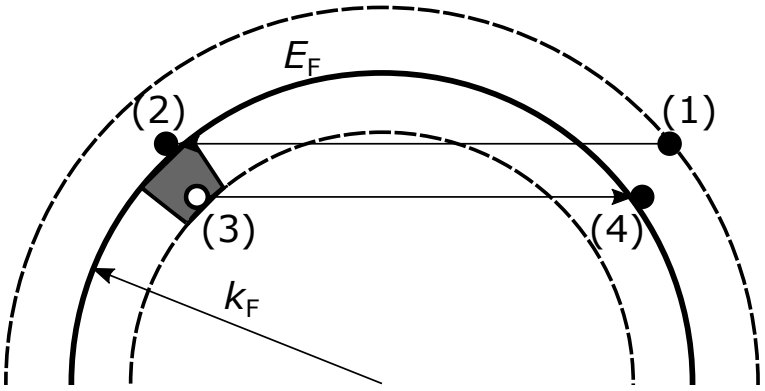

Fig. 2.2 Schematic representation of a decay process for a quasiparticle near the Fermi energy E_{F}. Here, quasiparticle (1) transitions to (2) (no. of available states $\propto |k - k_{\mathrm{F}}|$), creating in the process an electron-hole pair (3) and (4) (no. of possible states also $\propto |k - k_{\mathrm{F}}|$). The shaded area marks the region from which the hole state may be created based on conservation of energy and momentum.

Based on the above argument, it is then expected that for excitations whose lifetime is shorter than τ, the occupation numbers describing them when interactions are present should

not differ that much from the ideal gas scenario. In other words, $\mathcal{N}_{\mathbf{k},\sigma}$ will still be good (albeit approximate) quantum numbers. Using Landau's language, a low-energy excitation in a Fermi liquid can then be described in terms of these quasi-excitations (creating what he coined as a *quasiparticle*), in a similar fashion to how a low-energy excitation in an ideal gas is described in terms of particles. This way, the model is capable of explaining why the properties of an interacting system apparently resemble those of an ideal gas.

A quasiparticle is not an exact eigenstate of an interacting system. Rather, it can be seen as a superposition of closely packed eigenstates of the ideal Fermi gas which, on a timescale shorter than $\tau_{\mathbf{k}}$, are essentially stationary. Physically, it is best visualised as a dressed particle, that is, a particle which, when injected into a system, creates a disturbance around itself— a composite of many other interacting particles— which effectively screen it from its surroundings. This allows it to move around and only very weakly interact, effectively as if interactions were not present.

Following from above, we can write the dispersion of a quasiparticle in analogy to that of a free particle as

$$\varepsilon_{\mathbf{k}} = \mu + v_{\mathrm{F}}\hbar(k-k_{\mathrm{F}}) + \mathcal{O}((k-k_{\mathrm{F}})^2) \tag{2.5}$$

where μ is now the chemical potential and $v_{\mathrm{F}} = \hbar k_{\mathrm{F}}/m^{\star}$ is the effective Fermi velocity of the quasiparticle, with $m^{\star}$ being the effective mass. Similarly, the excitation (quasi)energy is given by

$$\delta E[\delta n] = \sum_{\mathbf{k},\sigma} \varepsilon_{\mathbf{k}} \delta n_{\mathbf{k},\sigma} + \frac{1}{2V} f(\mathbf{k},\mathbf{k}^{'}) \delta n_{\mathbf{k}\ ,\sigma}\ \delta n_{\mathbf{k}^{'},\sigma^{'}} \tag{2.6}$$

where $f(\mathbf{k},\mathbf{k}^{'})/V = \delta^2 E[n]/\delta n_k \delta n_{k^{'}}$ is known as the Landau interaction function. Rewriting equation (2.6), we can then define the energy of a quasiparticle as

$$\tilde{\varepsilon}_{\mathbf{k}} = \frac{\delta E[\delta n]}{\delta n_{\mathbf{k},\sigma}} = \varepsilon_{\mathbf{k}} + \frac{1}{V} \sum_{\mathbf{k}^{'},\sigma^{'}} f(\mathbf{k},\mathbf{k}^{'}) \delta n_{\mathbf{k}^{'},\sigma^{'}} \tag{2.7}$$

The beauty of Fermi liquid theory is that all properties of this new composite entity can now be easily encapsulated in just two parameters: the effective mass $m^{\star}$ and the Landau function $f(\mathbf{k},\mathbf{k}^{'})$. Note that, having constructed $\tilde{\varepsilon}_{\mathbf{k}}$, similar equilibrium properties such as specific heat, compressibility and susceptibility can easily be derived from here. As expected, these have a similar form to those of an ideal gas, apart for modifications due to $m^{\star}$ and higher-order corrections from $f(\mathbf{k},\mathbf{k}^{'})$.

There is, however, one caveat about Fermi liquid theory which we have so far not discussed. Effectively, the argument used above when justifying that the scattering rate should vanish close to the Fermi level is only valid in three (3D) or two (2D) dimensions.

Indeed, it can be shown that in 3D $\tau^{-1} \propto (k-k_F)^2$ while in 2D $\tau^{-1} \propto (k-k_F)^2 ln|k-k_F|$ (that is, slightly slower than in bulk but nevertheless still vanishing) [41]. In one dimension (1D), however, this behaviour is completely different. That is because, in 1D, the Fermi surface becomes discrete (in fact, just two points), instead of a continuous circle or sphere as is the case for higher dimensions.

A simple way of understanding why Fermi liquid theory fails is realising that its construction inherently assumes single-particle type excitations. In contrast, when confined to 1D, geometry alone imposes that all types of excitations must be collective responses of the entire system, and as such, the notion of a quasiparticle, as defined by Landau, naturally breaks down. As we will see in the next section, the correct paradigm in this situation is what is called a Tomonaga-Luttinger liquid. This is an example of a non-Fermi liquid.

2.2 Electrons in one dimension

Many-body systems of electrons in three and two dimensions can, generally speaking, be treated using Fermi liquid theory, discussed in the previous section. Non-Fermi liquids, on the other hand, mark the departure from this paradigm which, in general, can occur in one of two situations:

- in higher dimensions, such as a two- or three-dimensional system, if the electron liquid is highly correlated, for instance, when the energy of the Coulomb interaction greatly exceeds the kinetic energy;
- in lower dimensions, like one-dimensional wires, where spatial confinement alone dictates strong correlations regardless of the strength of the interactions in question.

It is the purpose of this thesis to explore the later situation.

The fundamental problem of 1D physics is that electrons confined to this geometry can no longer be modelled as Fermi quasiparticles (see Fig. 2.3). Effectively, unlike a normal Fermi liquid where electrons are free to move around and remain screened from its surroundings, essentially still behaving as free particles, in 1D spatial confinement alone blocks this from occurring. That is because it is now impossible to go over, under or around other electrons, the only option left being to try to go through, were this not prevented by the diverging Coulomb repulsion at short distances. Hence, strong correlations arise.

One-dimensional wires then mark a drastic departure from their higher-dimensional counterparts as, unlike the latter, there is no longer such a thing as locality of interactions. Instead, the motion of one electron necessarily has to cause a collective response of the whole system. This is why single-particle properties, on which Fermi liquid theory rests, break down

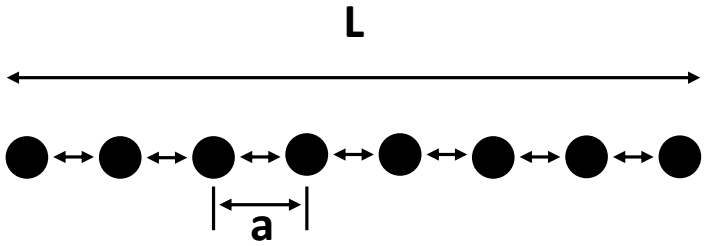

Fig. 2.3 Schematic representation of a one-dimensional electron system with density per unit length $N/L = 1/a$, where L is the length of the system and a is the inter-particle spacing.

completely. What emerges instead are the hydrodynamic modes of the Tomonaga-Luttinger liquid (TLL) model, which as we will see exhibit bosonic statistics.

Proposed by Tomonaga is 1950 [116] and later refined by Luttinger in 1963 [89], the TLL model was introduced as an attempt to describe interacting 1D electron systems at arbitrary interaction strength. Unlike most other many-body models, it allows for a full analytical rather than approximate solution to be obtained, as shown by Mattis and Lieb in 1965 [91] and later improved by Luther and Peschel in 1974 [88]. The current version of the model is credited to Haldane, who finalised it in 1981 [47].

The basic idea was that, in order to explain highly correlated interacting electrons in 1D without having to resort to perturbation theory (as this would only be valid in the limit of weak interactions), electron excitations should in principle be treatable using a Bose field, in analogy to Bloch's theory of sound waves. This effectively laid the ground-work for what today is known as the method of bosonisation and indeed, in a TLL, the collective modes of the system exhibit bosonic rather than fermionic statistics.

The model starts from two key assumptions, that the dispersion is linear near the Fermi points, and that the 1D system is infinitely long, see Fig. 2.4. Starting with the first, note that even though it is well established that for free electrons the dispersion is indeed parabolic, $E_k = \hbar^2 k^2/(2m^\star)$, this can be approximately treated as being linear when in the low-energy regime (*i.e.*, close to the Fermi energy). In other words, a TLL is by construction a linear model, valid in principle only as long as the curvature of the dispersion can be neglected and electrons only move from just below to just above the Fermi level. The second assumption is, as we will see in chapter 7, more subtle. For now, let us simply say that as long as end effects in the wires do not play a significant role, and one can take the long wavelength limit of the system, it should remain valid. A final assumption is that the wire is infinitely narrow, *i.e.*, the subband spacing is infinite and so there is no mixing with higher 1D subbands. Note that, in practice, this last point makes it hard to be sure whether the theory is applicable to any particular experimental observation (where subband spacing is never huge compared with

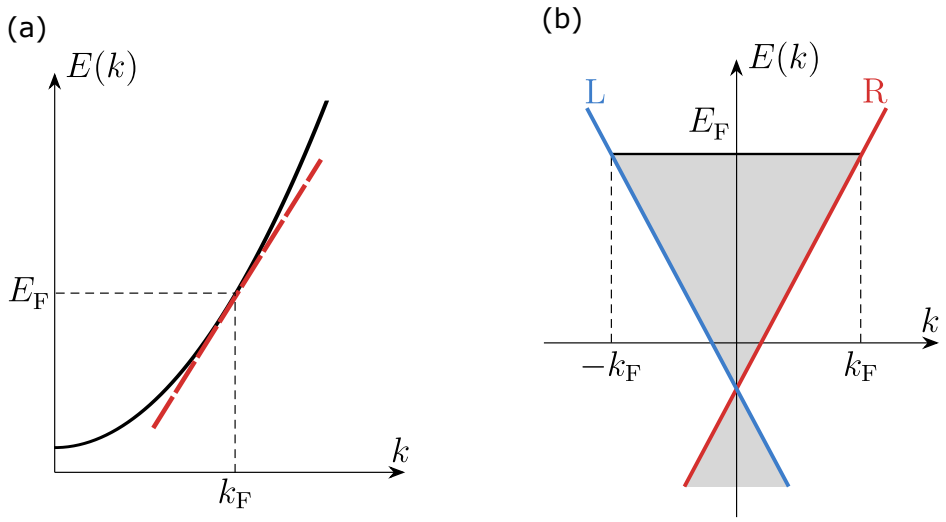

Fig. 2.4 The Tomonaga-Luttinger-liquid (TLL) model. (a) The original energy dispersion relation is shown in black. For electrons in free space, this is parabolic. According to the TLL picture, this can be approximated by a linear dispersion close to the Fermi points (red dashed lines). (b) The linear dispersion used in the TLL model. Red and blue curves correspond, respectively, to right- and left-moving electrons, while the shaded area marks the filled Dirac sea below the Fermi energy.

the interaction energy). Single- and multiple-subband occupancy regimes will nevertheless be discussed in chapters 5 and 6, respectively.

2.2.1 The Tomonaga-Luttinger liquid model

Let us start by assuming a system of spinless interacting fermions. In three or two dimensions, low-energy excitations with arbitrarily low momenta can occur [40], as in both cases the Fermi surface is well defined and as such electrons are free to occupy any state within it. In 1D, however, this is no longer the case, as the Fermi surface is now not only discontinuous but also consists of only two specific points, at k_F and $-k_F$, respectively.

Following from the TLL assumptions, one can then write the Hamiltonian of a 1D interacting electron system as

$$\hat{H} = \hat{H}_0 + \hat{H}_{\text{int}}. \tag{2.8}$$

where $\hat{H}_0$ represents the kinetic energy, whilst $\hat{H}_{\text{int}}$ refers to the interaction energy of the system. They can be written, respectively, as

$$\hat{H}_0 = \sum_{k,\alpha=\pm 1} \upsilon_F(\alpha k - k_F)\hat{a}^\dagger_{k,\alpha}\hat{a}_{k,\alpha} \tag{2.9}$$

with $\upsilon_F = \hbar k_F/m$ being the Fermi velocity, and $\hat{a}^\dagger_{k,\alpha}$ and $\hat{a}_{k,\alpha}$ the creating and annihilation operators at the right ($\alpha = 1$) and left ($\alpha = -1$) branches of the dispersion, and

$$\hat{H}_{\text{int}} = \frac{1}{2L}\sum_{q\neq 0} \upsilon_q \hat{\rho}_{-q}\hat{\rho}_q \tag{2.10}$$

where $\hat{\rho}_q$ is the electron density fluctuation operator, and υ_q the Fourier transform of the interaction potential. Together, $\hat{H}$ accounts for particles moving in either of the right (R) and left (L) branches, as well as for inter- and intra-branch interactions [41].

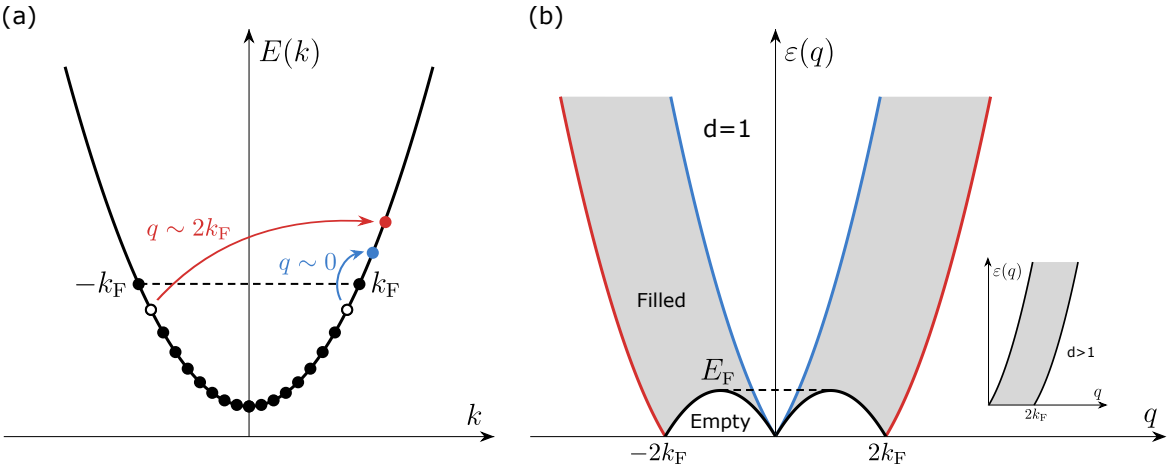

Fig. 2.5 Excitation spectrum for 1D fermions. (a) Single-particle excitations constituting forward (blue) and backward (red) scattering for small and large momentum change across the Fermi points, respectively. Occupied states are represented by filled dots and holes by empty circles. (b) Electron-hole pair spectrum. Only shaded areas are energetically accessible. The forbidden region indicated by the gap is unique to the 1D geometry and is not present at higher dimensions (see inset). The position of the spectral edge, separating the accessible and forbidden regions, is marked by the black curve. It can be observed directly, for instance, by neutron scattering in some magnetic materials [77, 95, 76].

Generally speaking, it is $\hat{H}_{\text{int}}$ that characterises the type of interactions present. For a 1D electron system with spacing a, these will be Coulomb in nature and of two types (see Fig. 2.5a): if an electron is excited within the same branch (left or right) from a state just below the Fermi energy, then only a small change of momentum is required, $q \sim 0$, with the direction of motion remaining unchanged. This is called forward scattering. On the other hand, if there is an exchange involving both branches, then a larger change in momentum will be necessary, $q \sim 2k_F$, with the direction of motion now being reversed. This constitutes backward scattering. All of these processes appear naturally from the density fluctuation operator when the particles are split into the left and right moving subbands around the $\pm k_F$

points,

$$\hat{\rho}_q \simeq \begin{cases} \sum_k (\hat{a}^\dagger_{k-q,\mathrm{R}} \hat{a}_{k,\mathrm{R}} + \hat{a}^\dagger_{k-q,\mathrm{L}} \hat{a}_{k,\mathrm{L}}) & \text{for } |q| \sim 0, \\ \sum_k \hat{a}^\dagger_{k-q,\mathrm{L}} \hat{a}_{k,\mathrm{R}} & \text{for } q \sim 2k_\mathrm{F}, \\ \sum_k \hat{a}^\dagger_{k-q,\mathrm{R}} \hat{a}_{k,\mathrm{L}} & \text{for } q \sim -2k_\mathrm{F}. \end{cases} \tag{2.11}$$

By substituting equation (2.11) into equation (2.10), the interaction term in the Hamiltonian can be divided into two terms depending on the direction of motion of the interacting electrons. Taking the long-wavelength limit, *i.e.*, by considering a system of infinite length or, in other words, by assuming arbitrarily high excitation energies, we find that the total TLL Hamiltonian is given by

$$\begin{aligned} \hat{H}_\mathrm{TLL} = \hat{H}_0 &+ \frac{1}{2L} \sum_{q \neq 0} V_1(q) (\hat{\rho}_{-q,\mathrm{R}} \hat{\rho}_{q,\mathrm{R}} + \hat{\rho}_{-q,\mathrm{L}} \hat{\rho}_{q,\mathrm{L}}) \\ &+ \frac{1}{2L} \sum_{q \neq 0} V_2(q) (\hat{\rho}_{-q,\mathrm{R}} \hat{\rho}_{q,\mathrm{L}} + \hat{\rho}_{-q,\mathrm{L}} \hat{\rho}_{q,\mathrm{R}}), \end{aligned} \tag{2.12}$$

with $V_1(q) = \upsilon_q$ and $V_2(q) = \upsilon_q - \upsilon_{2k_\mathrm{F}}$. Note that the choice of V_1 and V_2 is, in general, completely arbitrary and highly dependent on the interaction process in question. Attempts to verify their form have been made by Dash *et al.* assuming a Gaussian-dependence [32], by Creffield *et al.* using Monte-Carlo simulations [30, 29], and by Haüsler *et al.* [52] and Matveev *et al.* [92] analytically.

It can also be shown that the TLL Hamiltonian is diagonalisable if written in a bosonic basis. This means that every operator, including the fermionic creation and annihilation operators, can be represented in terms of boson operators together with operators that raise or lower the *total* number of particles. This is in stark contrast with the representation used so far, which assumed action on individual electrons and not on the system as a whole. This is, however, not surprising. As argued before, in 1D systems, collective response replaces individual behaviour.

A full review of the bosonisation method can be found in Apostol [6] or von Delft and Schoelle [128] as well as in several textbooks [5, 40]. The main result is that a one-dimensional system, following the TLL assumptions, is equivalent to a system of independent massless bosons, where the dispersion is given by $\omega_q = v|q|$, see Fig. 2.5b , with the velocity

$$v = \lim_{q \to 0} \sqrt{\left| \upsilon_\mathrm{F} + \frac{V_1(q)}{2\pi\hbar} \right|^2 - \left| \frac{V_2(q)}{2\pi\hbar} \right|^2}. \tag{2.13}$$

Rewriting $v = v_F/K$ in equation (2.13) allows one to extract the TLL parameter K as

$$K = \lim_{q\to 0} \frac{1}{\sqrt{\left|1+\frac{V_1(q)}{2\pi\hbar\upsilon_F}\right|^2 - \left|\frac{V_2(q)}{2\pi\hbar\upsilon_F}\right|^2}}. \tag{2.14}$$

Here, K encapsulates both the interaction potentials $V_1(q)$ and $V_2(q)$ as well as the Fermi velocity υ_F. Note that all of these parameters are independent of temperature.

2.2.2 Spinful Tomonaga-Luttinger liquids

Any model attempting to describe electron behaviour must account for spin. Indeed, as was shown by Luther *et al.* [87, 88], this can play an important role when considering the interaction process given by forward and backward scattering, since both parallel and anti-parallel configurations are now possible. One can generalise both the kinetic $\hat{H}_0$ and the interaction $\hat{H}_{\text{int.}}$ terms to include spin, see section 9.12 of [41]. The Hamiltonian for the spinful Tomonaga-Luttinger liquid (sTLL) then becomes

$$\begin{aligned}\hat{H}_{\text{sTLL}} = \hat{H}_0 &+ \frac{1}{2L}\sum_{q\neq 0} V_1(q)\left(\hat{\rho}_{-q,\text{R}}\hat{\rho}_{q,\text{R}} + \hat{\rho}_{-q,\text{L}}\hat{\rho}_{q,\text{L}}\right) \\ &+ \frac{1}{2L}\sum_{q\neq 0,\sigma}\left[V_2(q) - V_1(q)\right]\left(\hat{\rho}_{-q\sigma,\text{R}}\hat{\rho}_{q\sigma,\text{L}} + \hat{\rho}_{-q\sigma,\text{L}}\hat{\rho}_{q\sigma,\text{R}}\right),\end{aligned} \tag{2.15}$$

where $\hat{\rho}_{q,\alpha} \equiv \hat{\rho}_{q\uparrow,\alpha} + \hat{\rho}_{q\downarrow,\alpha}$ is the electron density operator and $\sigma = \uparrow,\downarrow$ is the spin index.

Note the similarities between the spinless (equation (2.12)) and the spinful (equation (2.15)) Hamiltonians, the only difference being the potential prefactor of the last term. This result suggests that the bosonisation method should remain applicable as long as both bosonic operators and the density fluctuation operator are also modified to include spin.

One of the most striking features of the spinful TLL is what came to be known as spin-charge separation. Once $\hat{H}_{\text{sTLL}}$ is rewritten in terms of the spinful bosonic operators, one sees that it decouples into two independent Hamiltonians,

$$\hat{H}_{\text{sTLL}} = \hat{H}_{\text{C}} + \hat{H}_{\text{S}}, \tag{2.16}$$

which can be associated with charge and spin modes, respectively. This result is analogous to the one discussed in the spinless case. Now, however, one has two independent collective

excitations given by the characteristic frequencies $\omega_q^{\mathrm{C}} = |q|v^{\mathrm{C}}$ and $\omega_q^{\mathrm{S}} = |q|v^{\mathrm{S}}$, where

$$v^{\mathrm{C}} = \lim_{q\to 0} \sqrt{\left(\upsilon_{\mathrm{F}} + \frac{V_1(q)}{\pi\hbar}\right)^2 - \left(\frac{V_1(q)+V_2(q)}{2\pi\hbar}\right)^2} \tag{2.17}$$

is the velocity of the charge-density wave (CDW) and

$$v^{\mathrm{S}} = \lim_{q\to 0} \sqrt{\upsilon_{\mathrm{F}}^2 - \left(\frac{V_1(q)-V_2(q)}{2\pi\hbar}\right)^2} \tag{2.18}$$

is the velocity of the spin-density wave (SDW). These are, generally speaking, different.

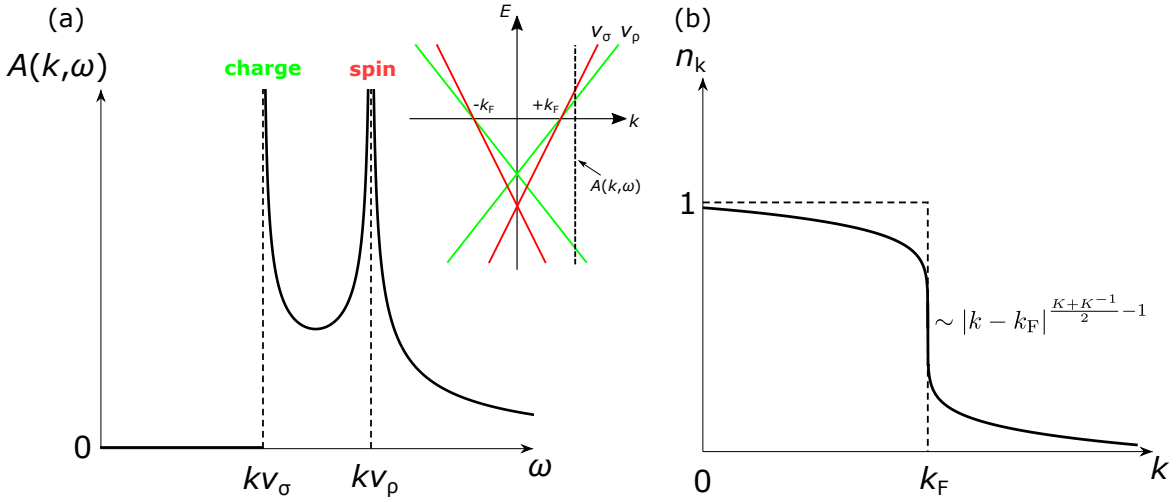

Fig. 2.6 Spectral function of the spinful TLL and occupation numbers. (a) Spectral function $A(k,\omega)$ of a spinful TLL, evaluated at fixed k, showing charge and spin power-law singularities at different energies [127, 93]. From [107]. Inset: elementary excitations of a spinful TLL with $v_\rho \neq v_\sigma$. Green and red lines mark charge- and spin-type modes, respectively. (b) Occupation numbers n_k within the TLL theory without spin. From [57].

Similarly to the spinless scenario, one can also define two interaction parameters for the spinful TLL, $K_{\rho,\sigma}$ given by $v_\rho \equiv v^{\mathrm{C}} = v_{\mathrm{F}}/K_\rho$ and $v_\sigma \equiv v^{\mathrm{S}} = v_{\mathrm{F}}/K_\sigma$ for the charge and spin modes, respectively. A spinful TLL is therefore fully determined by four parameters, υ_ρ, υ_σ, K_ρ and K_σ, compared to just two, υ and K, in the spinless scenario.

2.2.3 Spectral functions and power-law behaviour

In many-body physics, the spectral function, $A(k,\omega)$ is a rigorous way of describing single-particle properties of a system and corresponds to the probability density of adding or removing a single particle from a state characterised by a momentum k and energy ω, see

an example in Fig. 2.6a for a spinful TLL. For comparison, in the absence of interactions, $A(k,\omega)$ takes the form of a δ-function in frequency [41], *i.e.*, $A(k,\omega) \propto \delta(\omega - E_k)$, where $E_k = \hbar^2 k_x^2/2m$. This means adding or removing a particle to/from a plane-wave state always results in an exact eigenstate of the system. Note, however, that we are implicitly assuming here zero disorder. In reality, as we will see later in section 3.4 , $A(k,\omega)$ is more accurately described by a Lorentzian function.

Spectral functions naturally emerge out of the Green's function formalism. A full analysis of many-body dynamics using this formalism is outside the scope of this thesis but can be found in [2, 41]. In summary, it can be shown that $A(k,\omega)$ is derived from the retarded Green's function as

$$A(k,\omega) = -\frac{1}{\pi} Im G_{\mathrm{ret}}(k,\omega) \tag{2.19}$$

with the system's momentum distribution function n_k also being related to $A(k,\omega)$ via the Fourier transform of the real-space Green's function

$$n(k) = \int \mathrm{d}x e^{-ikx} G_{\mathrm{R}}(x, \tau = 0). \tag{2.20}$$

In chapter 3 we will derive the spectral function of a non-interacting 1D system. For now, let us simply introduce it as

$$A_{1,non-int}(k_x^{'}, k_y, E, \Gamma) = \sum_n \frac{\Gamma}{\pi} \frac{H_n(k_y a) e^{-(k_y a)^2}}{\Gamma^2 + (\mu - \xi)^2} \tag{2.21}$$

where $a = m_{1\mathrm{D}}\omega/\hbar$ is the finite width of the wire, $H_n(x)$ are the Hermite polynomials, Γ is the spectral line width associated with the single-particle disorder broadening, μ is the chemical potential, and ξ is the energy spectra of the system. The latter is equal to

$$\xi = E_n + \frac{\hbar^2 k_x^{'2}}{2m^\star} + E_0 \tag{2.22}$$

with $E_n = (n + 1/2)\hbar\omega_0$ being the energy of the nth subband and E_0 the bottom of the 2D band. It then follows that, at $T = 0$, and using equation (2.21), $n(k)$ takes the form

$$n(k) \propto |k - k_{\mathrm{F}}|^{\frac{K+K^{-1}}{2} - 1} \tag{2.23}$$

meaning that, at $k = k_{\mathrm{F}}$, the decay is characterised by an exponent $\alpha = (K + K^{-1})/2 - 1$, see Fig. 2.6b.

The importance of this result is that is establishes a natural connection between the interaction parameter K, derived previously in the context of a spinless TLL, and correlation

functions like $n(k)$ [127]. Indeed, as we will see in the next section, early experimental studies looking for TLL-type behaviour focussed exactly on this property, by trying to establish the existence of an interaction parameter K by looking for power-law behaviour in the density of states around the Fermi points.

2.2.4 Early signatures of Tomonaga-Luttinger liquid behaviour

Before proceeding onto more general forms of the Luttinger liquid model, let us first review some of the early results in support of this theory. As discussed in the previous sections, two clear signatures of TLL-type behaviour, as opposed to that of a Fermi liquid, include power-law discontinuities near the Fermi points, with the decay exponent α being defined in terms of the interaction parameter K, and separation of the spin and charge degrees of freedom. Early experimental work therefore focused on measuring the spectral function $A(k,\omega)$ of a 1D interacting system, where all the relevant information about the energy and momentum of the elementary excitations, both for particles and holes (*i.e.*, when a particle is removed), at arbitrary interaction strength, is combined. A distinct prediction of the TLL model is, for example, that the spectral function should be double-peaked, leading as we saw, to spin-charge separation, and that the height of those peaks should follow a power law in both temperature T and source-drain bias V_{dc}.

Following the experimental technique used, early evidence for TLL dynamics was found using photoemission spectroscopy, momentum-resolved tunnelling spectroscopy, and transport measurements. The range of systems utilised is large, and their claims to a 1D geometry vary significantly. Nevertheless, important progress has been made using GaAs quantum wires [10, 61], carbon nanotubes [16, 55, 72], the high T_{c} superconductor $SrCuO_2$ [70], the 1D metal $Li_{0.9}Mo_6O_{17}$ [46], 1D organic conductors [135, 102], and quantum Hall edge states [25, 44], to name but a few.

Photoemission spectroscopy

The most direct way of measuring a system's spectral function is by photoemission spectroscopy. This is a difficult experiment to do with high resolution and as such made it difficult to know if the 1D system was truly behaving as given by the TLL model. Nevertheless, it provided some of the early evidence in support of both spin-charge separation and power-law behaviour.

The basic principle of operation is relatively straightforward, see Fig. 2.7a. Here, an incident photon $E_\gamma = \hbar\omega$ of known energy causes the transition of an electron from an initial band state at energy E_{i} to a final, plane-wave, state at energy E_{f} above the vacuum energy,

where $E_f = \hbar^2 k_f^2 / (2m) = E_i + \hbar\omega - \phi$ and ϕ is the work function of the material. This photo-emitted electron then leaves the crystal before being collected by a detector, giving the emission intensity $I(k,\omega)$ as

$$I(k,\omega) = M(k)A(k,\omega). \tag{2.24}$$

Here, $A(k,\omega)$ is the spectral function of the system and $M(k)$ is the photoemission matrix element involving the initial and final states of the emitted photoelectrons. By mapping the system's response of photo-emitted electron energies as a function of analyser angle, information about the band structure can be obtained. For a review of angle-resolved photoemission spectroscopy (ARPES) experiments, see [109].

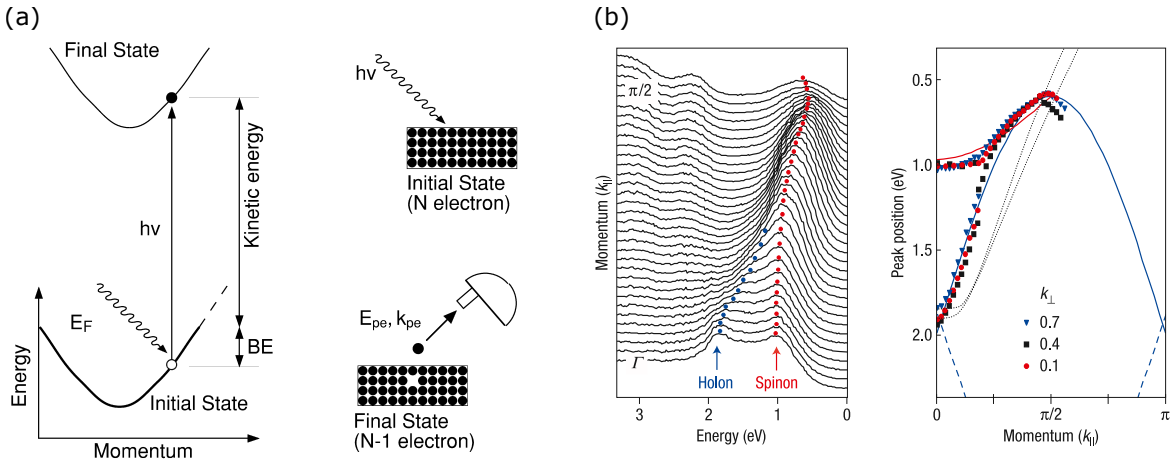

Fig. 2.7 (a) Schematic representation of direct photoemission spectroscopy, used in mapping the band structure of a system. From [69]. (b) Left: ARPES data showing the many-body spectrum of $SrCuO_2$, where a two-peak spinon-holon structure can be seen, as predicted by the spinful Tomonaga-Luttinger model. Right: comparison between experimental (symbols) and theoretical (solid and dashed lines) dispersions. From [68].

This technique is, however, limited on two fronts. First, it assumes the 1D system is relatively close to the surface on which the light is incident. While this is true for certain classes of materials, such as anisotropic layered structures and specific high-temperature superconductors, surface effects often require samples to have been prepared specifically *in situ*, making otherwise the data also harder to interpret. On the other hand, by its very nature, only occupied states can be probed using ARPES. While it is in principle possible to map unoccupied bands by inserting an electron of known energy into an empty band state and measuring the outgoing, ejected photon (this is known as *inverse* photoemission spectroscopy), little work has been carried out in the 1D field using this technique.

Photoemission spectroscopy was first applied by both Kim *et al.* [70, 69, 68] and Fujisawa *et al.* [38, 37] in studying the high-temperature superconductor $SrCuO_2$. Here,

good agreement to the experimental data was obtained by solving for the band structure using the Hubbard model, with the broadness of the observed peak being interpreted as resulting from the separation of the spinon and holon modes, see Fig. 2.7b. This work provided early evidence of spin-charge separation in a 1D Mott insulator which, although not metallic, still behaved as a 1D system as described by the TLL model.

Another experiment using photoemission spectroscopy was carried out by Gweon *et al.* [46] using the quasi-1D metal $Li_{0.9}Mo_6O_{17}$, with results similar to those shown above (*i.e.* spectral separation between the spinon and holon modes in the observed dispersion) also being obtained. From the spectral functions, the velocities of each mode were also estimated, giving $v_\rho/v_\sigma = 2$. Their experiment also yielded good theoretical agreement, with a power-law exponent of about $\alpha = 0.9$, characteristic of a system with strong backscattering.

Transport measurements

Another set of results showing early TLL-type signatures concerns measuring electrical transport along a 1D system, such as the work on TLL power-law behaviour by Bockrath *et al.* [16] and Yao *et al.* [133] using carbon nanotubes. These experiments consisted of measuring electrical transport along single-walled carbon nanotubes (SWNTs) with different contact geometries, either bulk or end. Taking the Luttinger-liquid parameter as being approximately equal to

$$K_\rho = \left[1 + \frac{2U}{\Delta}\right]^{-1/2}, \tag{2.25}$$

where U is the charging energy of the nanotube and Δ is the single-particle level spacing. Bockrath *et al.* showed that, in a 1D system, the conductance along the system is suppressed at zero bias, vanishing as a power-law dependence with temperature T for small biases $|eV| \ll k_B T$,

$$G(T) \propto T^\alpha, \tag{2.26}$$

while with source-drain bias V_{dc} at larger biases $|eV| \gg k_B T$,

$$\mathrm{d}I/\mathrm{d}V \propto V^\alpha, \tag{2.27}$$

as predicted by the TLL model. Here, α depends on the number of 1D channels and on whether the tunnelling is happening into the bulk of the system or whether it is affected by the ends. This can be found from the TLL theory by calculating the momentum distribution function once the spectral function is known. In SWNTs, depending on the contact geometry,

the power-law exponent α can then be related to K_ρ as either

$$\alpha_{\text{end}} = (K_\rho^{-1} - 1)/4 \tag{2.28}$$

or

$$\alpha_{\text{bulk}} = (K_\rho^{-1} + K_\rho - 2)/8 \tag{2.29}$$

as different contact geometries slightly change the prominence of the long-range Coulomb interactions.

In the experiment, sometimes individual nanotubes were placed on top of two metallic contacts, perturbing the nanotube only weakly and therefore yielding a long 1D system and hence 'bulk' tunnelling. Alternatively, contact metal was deposited on top of the nanotube, yielding a short 1D system in which any tunnelling excitation would propagate to the ends and be affected by the boundary condition there, producing 'end' tunnelling. Whether the tunnelling is 'bulk' or 'end' can be determined by comparing the energy of the tunneling electron to $\Delta E = 2v_{\text{F1D}}/(K_\rho L)$, which is related to the inverse time scale that it takes the TLL quasi-particles to travel to the end of a wire of length L [118, 65]. For $k_{\text{B}}T$, $eV_{\text{dc}} \gg \Delta E$, and as such, the ends are unimportant.

Conductance measurements as a function of temperature T and source-drain bias V_{dc} were then performed at zero magnetic field, resulting in $\alpha_{\text{end}} \approx 0.6$ and $\alpha_{\text{bulk}} \approx 0.3$, in good agreement with the theoretical predictions for SWNTs, $\alpha_{\text{end}}(\text{theory}) = 0.65$ and $\alpha_{\text{bulk}}(\text{theory}) = 0.24$ [64, 35], see insets in Fig. 2.8. Most importantly, while different contact geometries translated into different transport mechanisms, both systems were observed to still follow a power law in temperature once the data was rescaled using the universal relation

$$\frac{\mathrm{d}I}{\mathrm{d}V} = AT^{\alpha}\cosh\left(\gamma\frac{eV}{2k_{\text{B}}T}\right)\left|\Gamma\left(\frac{1+\alpha}{2} + \gamma\frac{\mathrm{i}eV}{2\pi k_{\text{B}}T}\right)\right|^2, \tag{2.30}$$

where $\Gamma(x)$ is the gamma function, γ takes into account the voltage drops at the two tunnel junctions, and A is an arbitrary constant (see Fig. 2.8). Note that this result assumed that the leads were at $T = 0$. From here, the bulk-contacted nanotubes were observed to follow $\gamma_{\text{bulk}} \approx 0.46$, while end-contacted nanotubes gave $\gamma_{\text{end}} \approx 0.63$, in good agreement with the theoretical predictions of Fisher and Kane [66], where $\gamma_{\text{bulk}}(\text{theory}) = 0.50 \pm 0.10$ and $\gamma_{\text{end}}(\text{theory}) = 0.60 \pm 0.10$. This was the first experimental evidence that electrons in a metallic nanotube behaved as a TLL.

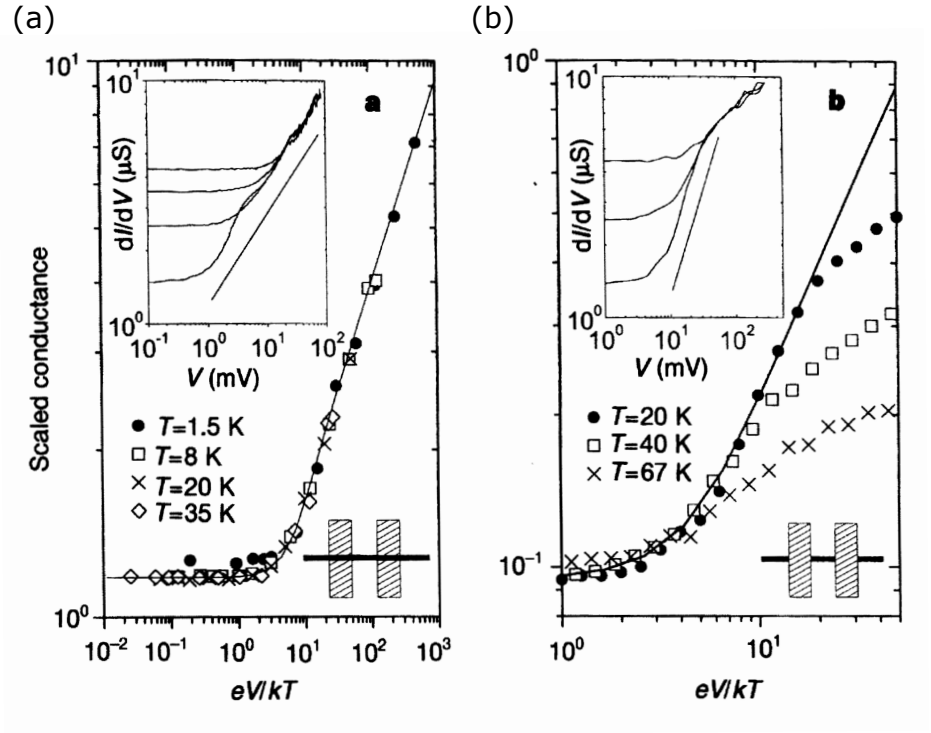

Fig. 2.8 Differential conductance $\mathrm{d}I/\mathrm{d}V$ taken at various temperatures for both (a) bulk- and (b) end-contacted carbon nanotubes. Insets show $\mathrm{d}I/\mathrm{d}V$ on a log-log plot where power-law behaviour, $\mathrm{d}I/\mathrm{d}V \propto T^{\alpha}$, can be seen in both geometries (see straight line). Main panels show the same data collapsed onto a single curve after using the scaling relation described in equation (2.30). The extracted values of γ were (a) $\gamma = 0.46$ and (b) $\gamma = 0.63$. From [16].

Tunnelling spectroscopy

Following Haldane's suggestion in 1981 and after initial measurements done on the 1D spectral function by Kardynal *et al.* [67], Barnes proposed in 1999 a novel method for probing TLL behaviour [4].

The idea was to measure the tunnelling conductance between a quantum wire and a parallel two-dimensional electron system (2DES) as a function of both the potential difference between them, V, and an in-plane magnetic field, B, see Fig. 2.9a. The dependence on wave vector k and frequency ω of the spectral function $A(k,\omega)$ could then be determined by analysing the differential tunnelling conductance $\mathrm{d}I/\mathrm{d}V$. In particular, the authors argued that presence of spin-charge separation should manifest itself as emerging singularities in the $I-V$ characteristics, in a markedly different fashion from what would be expected in a non-interacting system. This idea was later further refined by Grigera *et al.* [45], who extended it to arbitrary values of the interaction parameter K_ρ while accounting for the effects of Zeeman splitting in both the TLL and the 2DES.

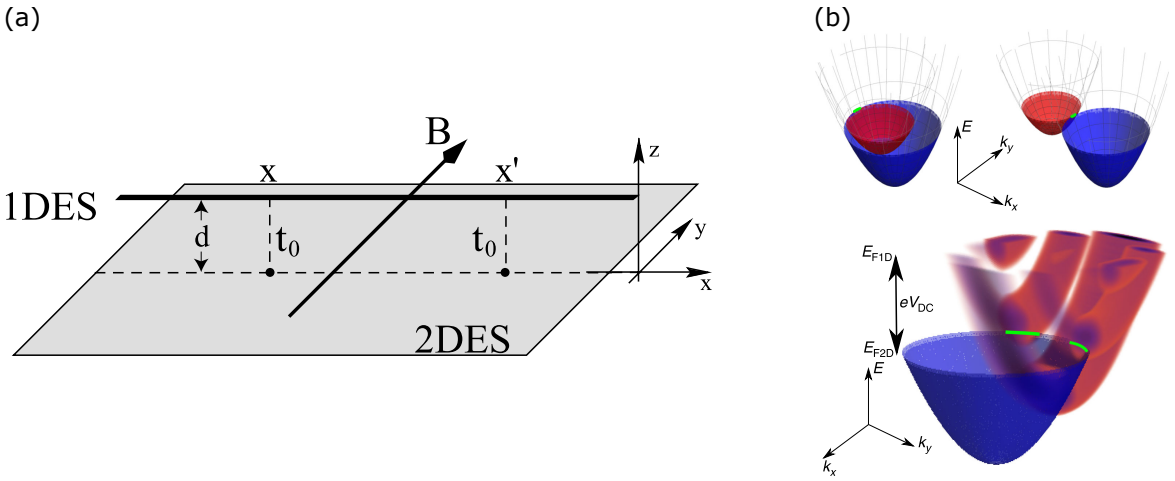

Fig. 2.9 (a) Device configuration for mapping the dispersion of a 1D system by measuring tunnelling of electrons from it to a nearby 2DES. From [4]. (b) Magnetotunnelling spectroscopy. Top panels show the overlap of the spectral functions of two 2D systems. Magnetic field B displaces the blue paraboloid to the right, making the Fermi circles touch from the inside (top left) or from the outside (top right). This allows the states of the red paraboloid near $-k_F$ and k_F to be probed at the Fermi energy E_F. Bottom panel shows tunnelling between a 2D (blue) and a 1D (red) system at finite bias V_{dc}. Multiple 1D subbands can be probed by varying both B and V_{dc}. From [59].

When an electron tunnels quantum-mechanically through a barrier between two regions, it must conserve energy and momentum transverse to the barrier (modulo a reciprocal-lattice vector, in a crystal). It must also obey the Pauli exclusion principle, so it cannot tunnel into an occupied state. In a solid at low temperatures, nearly all the states below the Fermi energy E_F are occupied, providing therefore a reference energy below which tunnelling is forbidden. We will focus on semiconductor heterostructures where a planar barrier separates two parallel quantum wells containing electrons, which are free to move in two (or fewer) dimensions, so that in those directions their wave functions are described by plane-wave Bloch states with wave vector $\mathbf{k}$. The tunnelling probability then depends on the overlap of the wave functions on either side of the barrier, integrated perpendicular to the barrier, at a rate given by Fermi's golden rule [13, 108, 112]. A full derivation and analysis of this result will be done in chapter 3. For now, let us simply say that in order for tunnelling to occur, both initial and final states must match in $\mathbf{k}$, ensuring conservation of momentum, with resonances in I being observed each time the 2D band and the nth 1D subband dispersions are aligned.

This, however, is unlikely to happen under equilibrium conditions, and therefore they need to be offset in both energy and momentum in order for each dispersion to be fully mapped. By applying a magnetic field B parallel to the layers, a Lorentz force is produced as the electrons tunnel, boosting the momentum by an amount $\Delta k = eBd/\hbar$, where d is the

tunnelling distance (the distance between the centres of the wave functions). Similarly, a voltage V_{dc} applied across the barrier can provide an extra energy eV_{dc} to one of the systems. Putting it all together, we obtain

$$\begin{aligned} I \propto \int \mathrm{d}\mathbf{k}\mathrm{d}E[f_T(E-E_{\mathrm{F1D}}-eV_{\mathrm{dc}})-f_T(E-E_{\mathrm{F2D}})] \\ \times A_1(\mathbf{k},E)A_2(\mathbf{k}+ed(\mathbf{n}\times\mathbf{B})/\hbar,E-eV_{\mathrm{dc}}). \end{aligned} \tag{2.31}$$

Here, e is the electronic charge, $f_T(E)$ is the Fermi-Dirac distribution, $\mathbf{n}$ is a unit normal to the plane, $\mathbf{B}=-B\hat{\mathbf{y}}$ is the (in-plane) magnetic-field vector, and $A_1(\mathbf{k},E)$ and $A_2(\mathbf{k},E)$ are the corresponding spectral functions of the 1D and 2D systems, together with their Fermi energies, E_{F1D} and E_{F2D}, respectively (see Fig. 2.9b). One can then map the dispersion of one system with respect to the other by measuring the differential tunnelling conductance $G=\mathrm{d}I/\mathrm{d}V$ in both energy and momentum space.

Both the 1999 proposal of Barnes (Altland *et al.* [4]) and the subsequent work of Grigera *et al.* [45] in 2004 concerned the idea of detecting spin-charge separation in a quantum wire. Neither, however, made any attempt at modelling the anomalous suppression of tunnelling current at zero bias, as predicted by the TLL model. This feature, commonly referred to as the zero-bias anomaly (ZBA), is expected to depend strongly on the strength of the interactions and to follow a power-law behaviour in both bias V and electron temperature T, see equations (2.26) and (2.27).

The first experimental realisation of tunnelling from a 1D wire in the single-subband regime was achieved by Auslaender *et al.* [11, 10], with later theoretical analysis done by Carpentier *et al.* [22]. Here, the authors used a pair of coupled quantum wires grown via cleaved-edge overgrowth (CEO), meaning that the tunnelling process took place between two 1D systems instead of between a wire and a 2DES as discussed before, see Fig. 2.10a and b. The CEO technique allowed very strong confinement to be obtained, equal to roughly the width of the well itself, and as such in principle well suited for observing interaction effects. Unfortunately, the probe layer was now also of the same nature as the system being probed, meaning that interpretation and disentanglement of each wire's response became significantly more complicated. These experiments, nevertheless, showed early evidence in support of the TLL picture by observing an enhancement of the excitation velocity relative to the bare electron velocity v_{F}, see Fig. 2.10c and d. Previous work, done by the same authors, also observed power-law behaviour of the tunnelling density of states around the zero-bias suppression region [117, 118].

In 2009, Jompol *et al.* reported the first clear observation of spin-charge separation together with power-law suppression of the tunnelling current at zero bias. In contrast to

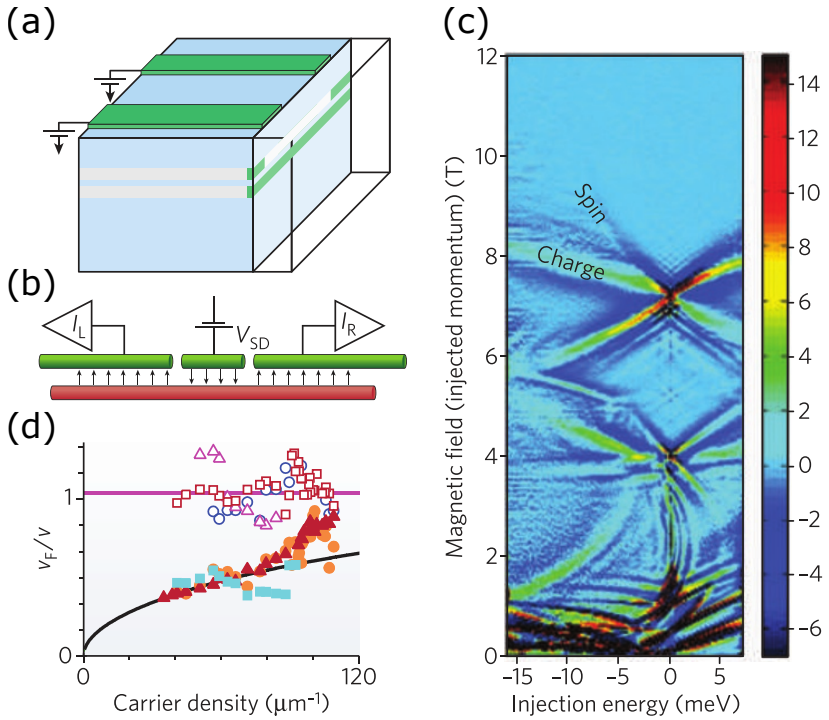

Fig. 2.10 Probing spin-charge separation via momentum-resolved magnetotunnelling spectroscopy between two interacting 1D wires. (a) Schematic representation of double-wire structure made via cleaved-edge overgrowth (CEO). The system resides at the edge of a GaAs/AlGaAs double-well heterostructure. (b) Schematic of the circuit used in the 1D–1D tunnelling process. Here, I_L is the left-moving current, I_R the right-moving current and V_{SD} the source-drain bias voltage. (c) Differential conductance $G = dI/dV$ plotted as a function of both V_{SD} ($\propto$ energy) and B ($\propto$ momentum). Two features, labelled charge and spin, can be seen branching away from each other at around zero energy and a magnetic field of 7 T. (d) Measured spin velocities (open symbols) and charge velocities (filled symbols), plotted as a function of carrier density and normalised with respect to the Fermi velocity v_F. At lower densities, repulsion between the electrons is stronger and hence the charge excitation velocity larger, unlike the spin mode, which remains largely unaffected. Solid curves show the theoretical fits. From [33].

the CEO samples, the authors fabricated an electrostatically gated 1D system and measured tunnelling between it and a nearby 2DES. Thus, the probe layer used was now a well-understood system, making interpretation therefore much more straightforward.

Figure 2.11 shows the tunnelling conductance G as a function of both inter-layer bias V_{dc} and in-plane magnetic field B at lattice temperatures of 1 K and ~ 40 mK, when only one 1D subband is occupied. The dashed and solid black curves mark the expected 1D and 2D parabolic dispersions, respectively, arising from single-particle tunnelling in the absence of interactions. A parasitic 2D–2D tunnelling signal originating from the ungated injection

region is also shown, as green dash-dotted lines. From the crossing points at $V_{\mathrm{dc}} = 0$, B^- and B^+, the 1D Fermi wavevector $k_{\mathrm{F1D}} = ed(B^+ - B^-)/2$ together with the 1D electron density $n_{\mathrm{1D}} = 2k_{\mathrm{F1D}}/\pi$ can be extracted. For the data shown, the approximate electron density in the wires was $n_{\mathrm{1D}} \cong 40\,\mu m^{-1}$.

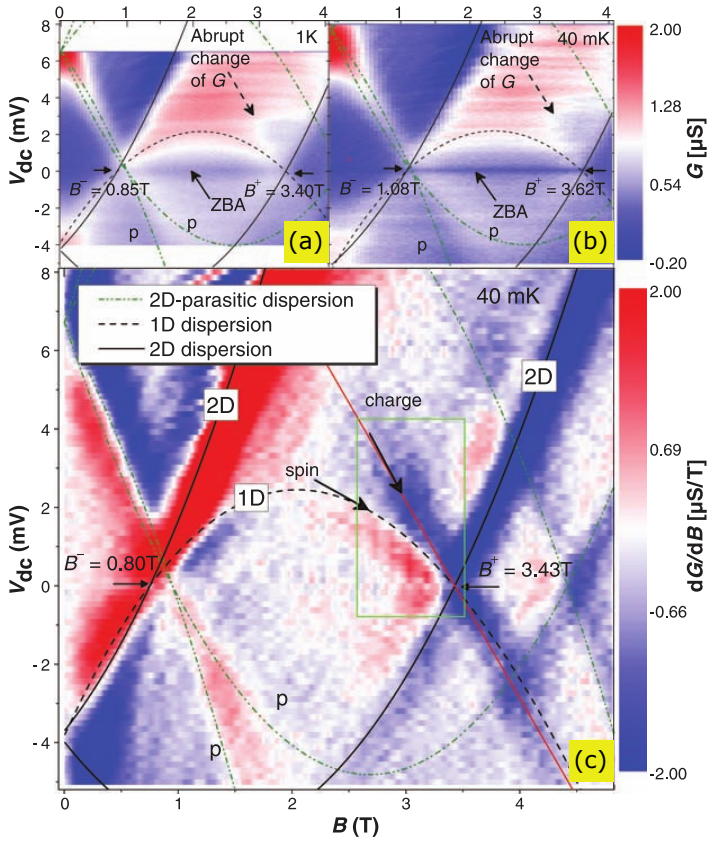

Fig. 2.11 Tunnelling conductance G *vs* dc-bias V_{dc} and magnetic field B, at lattice temperatures T of (a) 1 K and (b) 40 mK. Tunnelling resonances between a system of 1D wires and a 2DES as predicted by the non-interacting model are marked by solid and dashed black lines while green dash-dotted curves indicate the location of unavoidable parasitic 2D–2D tunnelling 'p'. In addition, signs of interactions can be seen in the suppression of G around zero bias (ZBA) and its abrupt drop at positive biases around B^+. (c) $\mathrm{d}G/\mathrm{d}B$ differential of the data shown in (b). The non-interacting parabolae shown in (a) and (b) are labelled 1D, 2D, or p, depending on which system's dispersion is being probed. The straight red line, marking the position of the abrupt drop in G, is ~ 1.4 times steeper on this plot than the 1D parabola at $V_{\mathrm{dc}} = 0$. According to the TLL model, we identify the first as a charge-type mode (holon) while the second as a spin-type excitation (spinon). From [62].

In both Fig. 2.11a and b, an additional region of high conductance at positive biases near B^+ can be observed. This can be more clearly seen in Fig. 2.11c by looking at the differential $\mathrm{d}G/\mathrm{d}B$. In both cases, a feature moving diagonally up and to the left of B^+ is visible. Fig.

2.12b shows detailed measurements taken around the same region, for a different device, also in the single-subband regime.

For comparison, Fig. 2.12a and d show the theoretical prediction for a non-interacting system. Here, a strong dark-blue feature of negative $\mathrm{d}G/\mathrm{d}B$ can be seen. However, it follows the 1D parabola, unlike what is observed experimentally, where it moves away from it (dashed red line). It follows therefore that the 1D parabola and the dashed red line track the dispersion of two independent features which, according to the TLL picture, can be associated with spin- and charge-type excitations, respectively. The velocity of the charge mode was estimated to be $v_\rho = 1.4 v_\sigma$, resulting, under the linear approximation, in an interaction parameter $K_\rho \approx 0.71$. For completeness, Fig. 2.12c and e show the theoretical result as expected for 1D interacting electrons tunnelling to and from a 2D system according to the TLL model, where a similar feature to that observed can also be seen.

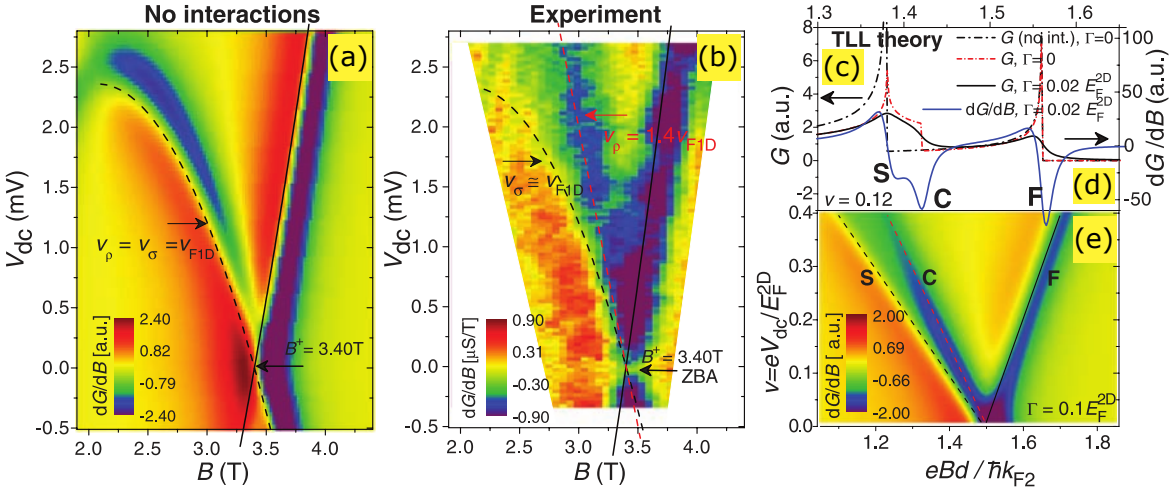

Fig. 2.12 Spin-charge separation around the $+k_\mathrm{F}$ point: comparison between experiment and theory. (a) $\mathrm{d}G/\mathrm{d}B$ for a system of non-interacting electrons with disorder broadening $\Gamma = 0.6\,\mathrm{meV}$. (b) High-resolution mapping of $\mathrm{d}G/\mathrm{d}B$. The red dashed line marks a feature that does not follow the non-interacting parabola (black dashed) and is absent in (a). The spinon velocity is given by $v_\sigma \equiv v_\mathrm{F1D}$. The extracted holon velocity was $v_\rho = 1.4 v_\mathrm{F1D}$. (c) and (d) show, respectively, the calculation of G and $\mathrm{d}G/\mathrm{d}I$ for both a non-interacting and a TLL system of electrons. Spin and charge excitations are labeled by S and C, respectively, while F labels the non-interacting 2D dispersion curve. The cuts were taken at a bias of $\nu = eV_\mathrm{dc}/E_\mathrm{F}^\mathrm{2D} = 0.12$ (given here in dimensionless units). (e) $\mathrm{d}G/\mathrm{d}B$ as a function of B and ν according to the TLL model. Note how, unlike (a), this model predicts a charge feature C as seen in (b). From [62].

Another observation that cannot be explained by the non-interacting model is the zero-bias anomaly (ZBA), visible as a dark blue horizontal line in Fig. 2.11a and b. As discussed before, this anomalous suppression in the tunnelling current results from interaction effects

and is likely to be associated with the extra energy cost for an electron to tunnel in or out of the wire, at zero bias, as it inevitably disturbs the remaining electrons already present. The tunnelling conductance G as a function of $V_{\rm dc}$ for different temperatures T can be seen in Fig. 2.13a, at a field B approximately midway between B^- and B^+. Similarly, Fig. 2.13b and c show $G(V_{\rm dc}=0,T)$ and $G(|V_{\rm dc}|,T<70\,{\rm mK})$, respectively, on a log-log plot. Here, clear variation as a power law in both $V_{\rm dc}$ and T over a range of orders of magnitude is observed. Both $V_{\rm dc}$ and T play a similar role in smearing the energy, as illustrated in Fig. 2.13d.

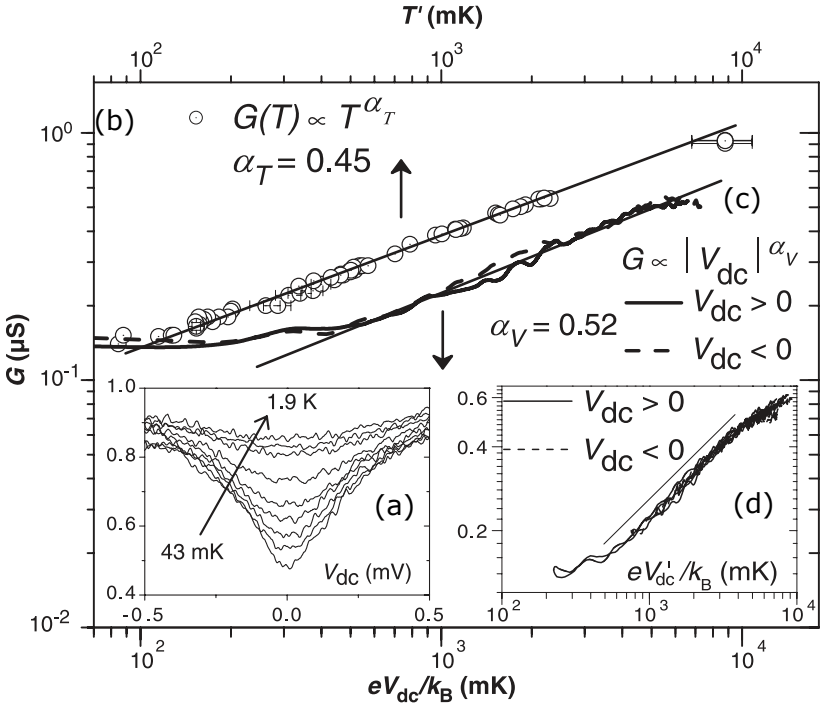

Fig. 2.13 The zero-bias anomaly. (a) Tunnelling conductance G as a function of bias $V_{\rm dc}$, taken at a field $B=2.33\,{\rm T}$, for different temperatures T ranging from 43 mK to 1.9 K. (b) Log-log plot of $G(V_{\rm dc}=0)$ versus T, showing power-law behaviour $\propto T^{\alpha}$ with $\alpha_{\rm T}\approx 0.45$. (c) Same as in (b) but showing $G(|V_{\rm dc}|)$ versus $V_{\rm dc}$ with $\alpha_{\rm V}\approx 0.52$. (d) $G(|V_{\rm dc}|)$ versus $V'_{\rm dc}=\sqrt{|V_{\rm dc}|^2+(3k_{\rm B}T/e)^2+V_{\rm ac}^2}$, obtained by adding different sources of energy smearing as noise in quadrature. The value of $3k_{\rm B}T$ was chosen so that the curves in (b) and (c) and all the curves in (d) would superpose. For comparison, using the scaling relation in Eq. (2.30) results in a universal curve with $\alpha\approx 0.51$. From [62].

The interaction parameter K_ρ was obtained from the ZBA using the extracted power-law exponents, $\alpha_{\rm T}\approx 0.45\pm 0.04$ and $\alpha_{\rm V}\approx 0.52\pm 0.04$, depending on whether excitations from electrons tunnelling into or out of the wire generally propagated as far as the ends ('end tunnelling') or not ('bulk tunnelling'), see section 2.2.4. For the latter, the measured exponents gave $K_\rho\approx 0.28$ and 0.26 respectively, significantly smaller than the value extracted from the holon branch in Fig. 2.12b. By considering 'end' tunnelling instead, the values

obtained were of $K_\rho = 0.53$ for α_T and $K_\rho = 0.49$ for α_V, considerably closer to that obtained in Fig. 2.12. However, this implies that the wire length was shorter than the thermal length $L_T = 2v_{\mathrm{F1D}}/(K_\rho k_\mathrm{B} T)$ at all temperatures measured (100 mK to 10 K), or else the power-law exponent would change at some temperature, as observed in 1D–1D tunnelling by Tserkovnyak *et al.* [118].

Overall, the work carried out by Jompol *et al.* showed decise evidence in support of the TLL model. It was surprising, though, that the 'charge' line observed persisted far beyond the energy range over which the dispersion could be approximately treated as being linear, suggesting that spin-charge separation might be a phenomenon more robust than that expected from the range of validity of the TLL model. This naturally raised the question of what happens to both spin and charge modes in the nonlinear region, that is, far from the Fermi points, where the linear approximation should break down. The role of interactions in 1D wires at arbitrary energy and momentum has only recently started to be understood. Such nonlinear Tomonaga-Luttinger liquids are the topic of the next section.

2.3 Away from the Fermi points

The Tomonaga-Luttinger liquid theory works remarkably well in describing the low-energy behaviour of one-dimensional systems. As we have seen in section 2.2, these exhibit a number of unusual properties, including long-lived plasmonic excitations, the separation of the spin and charge degrees of freedom, and interaction-driven power-law behaviour [47]. In general, however, the 1D spectrum is curved, *i.e.* nonlinear, meaning that deviations from linearity are expected to occur away from the Fermi points. We will now focus our attention on two particular nonlinear theories.

2.3.1 The mobile-impurity model of nonlinear Tomonaga-Luttinger liquids

The first attempt at describing high-energy excitations in a 1D system came from what is now known as the mobile-impurity model, see Fig. 2.14 [53, 54]. The idea behind this framework is actually reminiscent of an early problem on X-ray scattering in metals, where it was shown that nonlinear hydrodynamics could be used in describing the creation of a hole far below the Fermi energy after adsorption of a high-energy photon. As in the TLL scenario, this system was shown to also have power-law singularities around the Fermi level. However, when applied in 1D, the model still failed in obtaining the resulting dynamics, as interaction between the deep holes and the low-energy quasiparticles remained divergent.

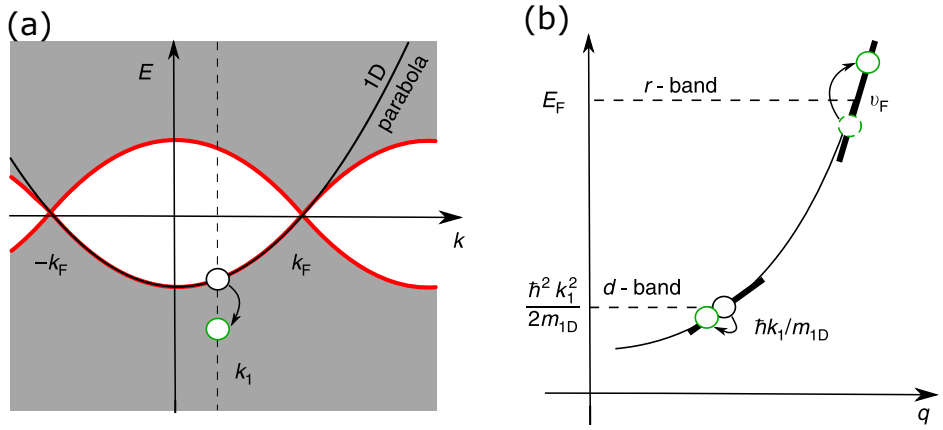

Fig. 2.14 (a) Dispersion of an interacting 1D system. Kinematically forbidden regions are shown in white while the grey shaded area represents the many-body continuum of excitations. The spectral edge marks the border between these two regions and is shown in red. A higher-energy excitation (green circle) is obtained by changing the state of a heavy hole (black circle) deep below the Fermi energy and simultaneously creating some linear TLL excitations around the Fermi energy. This moves the total energy of the many-body state away from the spectral edge as described by the mobile-impurity model—see text. (b) Splitting of the fermionic dispersion into two subbands, one for a heavy hole deep in the Fermi sea, with characteristic velocity given by k_1/m_{1D}, and one for excitations close to the Fermi point k_F, with velocity v_F. From [59].

Nozières and De Dominicis [96] solved this problem by introducing the so-called heavy-impurity model. This construction, unlike the previous one, considered Fermi-liquid-like quasiparticles interacting with a hole state deep below the Fermi level, with the resulting Hamiltonian being now diagonalisable, in a framework analogous to that of a TLL system. As for the (linear) TLL, it succeeded in predicting power-law behaviour away from the Fermi energy. Most interestingly, however, the 1D spectral function, as derived from the mobile-impurity model, was shown to be

$$A_1(k_x,E) \propto \frac{1}{|E+\mu-\xi_1|^{\alpha(k_x)}}, \tag{2.32}$$

implying that there was now a momentum dependence in the threshold exponent $\alpha(k_x)$ of the interacting 1D system [54]. The explicit expression for spinful fermions that is applicable for electronic systems was found to be [120]

$$\alpha(k_x) = 1 - \frac{(1-C(k_x))^2}{4K_\rho} - \frac{K_\rho\,(1-D(k_x))^2}{4}, \tag{2.33}$$

where $C(k) = \left(k^2 - k_{\mathrm{F}}^2\right) / \left(k^2/K_\sigma - k_{\mathrm{F}}^2 K_\sigma/K_\rho^2\right)$ and $D(k) = (k - k_{\mathrm{F}}) \left(k_{\mathrm{F}}/K_\rho^2 + k/K_\sigma^2\right) / (k^2/K_\sigma^2 - k_{\mathrm{F}}^2/K_\rho^2)$.

One then observes that, having extended the universality of the TLL model from the low- to the finite-energy regime, a momentum-dependent power law appears. This is a unique feature of nonlinear hydrodynamics in 1D, and can be seen as a direct consequence of the curvature of the spectral edge which had, until now, been neglected. Observation of such behaviour would be a hallmark of nonlinear Tomonaga-Luttinger liquid (NLL) dynamics.

Another implication of this theory is the emergence of higher-order 'replica' modes (or 'shadow bands'), in addition to the principal 1D dispersion, see red lines in Fig. 2.14a. These features will be further discussed in the next section when discussing the hierarchy of modes picture. Note, for now, that the mobile-impurity model simply states their existence, making no predictions about what their relative spectral strengths might be.

Finally, yet another prediction from the NLL model is the drastic reduction of the plasmon's lifetime. Let us show this by analogy with the linear case. If the spectrum is linear, each electron-hole pair can be identifiable by an energy linear in its momentum. If, instead, the spectrum is curved, the possibility exists of having different electron-hole pairs with different energies yet the same momentum. These can morph into a plasmon (for example, a spinon and/or a holon) with wave number q once the interactions are turned on, with the finite spectral width then being approximately equal to the spread in the energy, that is

$$\delta\omega(q) = \omega_+(q) - \omega_-(q). \tag{2.34}$$

Hence, the resulting lifetime is reduced by $\tau \propto 1/\delta\omega$.

The mobile-impurity model paved the way in releasing the Luttinger liquid from the constraints of linearity, by introducing new tools for dealing with curved *i.e.*, more realistic, dispersions. Nevertheless, it still suffered from a number of limitations. For instance, as constructed, it is a spinless theory, and as such unable to predict already observed phenomena such as spin-charge separation. It also does not provide a description for arbitrary nonlinear excitations as, similarly to the edge singularity in the X-ray scattering problem, the nonlinear hydrodynamics become less well defined away from the spectral edge separating the forbidden zone from the many-body continuum, making such approach inconsistent. Finally, it also still takes into account infinite length systems which, as we will see in the next section, suppresses the natural length scale at which 'replicas' emerge.

2.3.2 A hierarchy of modes

A more systematic understanding of the general picture for nonlinear excitations came from a microscopic analysis via the Bethe ansatz. This is a method for finding the wavefunctions of certain one-dimensional quantum many-body systems by making it two-body reducible, that is, assuming many-body collisions happen as a sequence of two-body collisions and, as such, the many-body wavefunction can be written in terms of two-body wavefunctions. It was then found that [119, 121], when applied to a 1D fermionic system, an exponentially large number of excitations are separated into levels of a mode hierarchy according to their respective spectral strengths, which are proportional to integer powers of a small parameter R^2/L^2, with R being the radius of the two-body interaction potential and L the length of the system. Note that now, unlike before, the system is no longer taken to be infinite. A detailed analysis of these amplitudes revealed formation of a parabola-like dispersion, see Fig. 2.15a, similar to that of the original noninteracting fermions but with some renormalisation due to interactions, by the strongest excitations with the zeroth power of R^2/L^2. All other many-body modes have powers of R^2/L^2 greater than zero, with the general trend being of increasing the integer by one with each discrete step of $2k_\mathrm{F}$ away from the principal parabola.

As an example, let us analyse the hole part of the principal parabola between the $\pm k_\mathrm{F}$ points. This has the largest amplitude, but its mirror in the particle sector—a 'replica' or 'shadow band' in the shape of a dome marked as $p0b$ in Fig. 2.15a—has a parametrically smaller amplitude proportional to the first power of R^2/L^2. In the spectral function, the strength of this mode is predicted to be

$$A_1\left(k_x, E\right) \propto \frac{R^2}{L^2} \frac{k_\mathrm{F}^2 k_x^2}{\left(k^2 - k_\mathrm{F}^2\right)^2} \delta\left(E - \mu + \xi_1\right). \tag{2.35}$$

Therefore, for almost all momenta, this mode will be unobservable in the thermodynamic limit. The only exceptions are the regions around the $\pm k_\mathrm{F}$ points, where the singularity in the denominator starts to compete with the parametric smallness, resulting in an amplitude overall large enough so that the mode is, in principle, observable. On the other hand, the measurement of the whole mode requires using smaller systems, in which the R^2/L^2 parameter still leaves the amplitude of the whole mode above the background from the other processes.

Whilst the mode hierarchy emerges away from the Fermi points, close to them (where the spectrum is almost linear), it transitions into the usual linear TLL, see Fig. 2.15b. The hydrodynamic modes of the latter consist of a huge number of many-body modes, all of which are of similar spectral strengths, making the two regimes distinct already on the

microscopic level. The change from one into the other can be traced using a macroscopic quantity, the density of states, which is calculated exactly by numerical means using the Bethe ansatz. The result exhibits both the power-law suppression around the Fermi energy E_{F} predicted by the TLL model as well as a crossover into a finite density, $\propto 1/\sqrt{E}$, predicted by the mode hierarchy away from the linear region, where the nonlinearity of the single-particle dispersion already destroys the hydrodynamic modes of the TLL.

The hierarchy of modes model and, specifically the prediction that extra, higher-order 'replica' modes should emerge as the system length L is made progressively smaller, was the main motivation behind the fabrication of progressively smaller and smaller 1D systems. A full study on the length-dependence will be discussed in detail in chapter 7. Before this, however, we briefly overview some of the other recent experimental work done on NLLs.

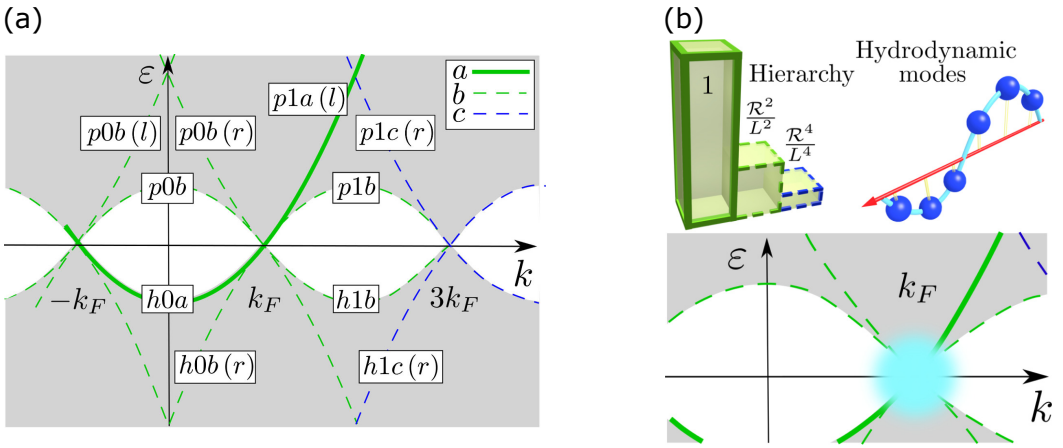

Fig. 2.15 (a) Spectral function of spinless fermions according to the mode-hierarchy picture. First (second)-level modes are shown in the region $-k_{\mathrm{F}} < k < k_{\mathrm{F}}$ ($k_{\mathrm{F}} < k < 3k_{\mathrm{F}}$) and are labelled by 0 (1), where k_{F} is the Fermi wave vector. Accessible and forbidden regions are marked by grey and white, respectively. Particle (hole) sectors are marked by p (h) for positive (negative) energies, a, b and c correspond respectively to the level in the mode-hierarchy in powers of 0, 1 and 2 of R^2/L^2 and (r,l) correspond to the origin in the range, right or left. From [119]. (b) Bottom, regions of validity for different theories on the energy-momentum plane. Top right, TLL hydrodynamic modes, where the deviations from the red line mark a variation in density and which dominate at low energies (see cyan region in the bottom panel). Top left, mode-hierarchy up to third order, where the bars denote qualitatively the amplitude of different many-body modes and which is relevant for the rest of the plane. From [121].

2.3.3 Recent work on nonlinear effects

Experimentally speaking, nonlinear effects in one-dimensional systems have been traditionally challenging to probe, in great part due to both the difficulty in measuring at high energies, and the problem of creating a system where interactions are strong enough so that these effects can be distinctively observed in the first place. To date, only two experimental platforms have claimed observation of nonlinear Luttinger behaviour: semiconductor quantum wires using tunnelling spectroscopy, and carbon nanotubes using infrared nano-imaging and electrical transport measurements. Below we discuss their main conclusions.

Higher-order 'replica' modes

In 2015, the first observation of structure resembling higher-order excitations, as predicted by the mode-hierarchy model, was reported in Tsyplyatyev *et al.* [119] in devices similar to that used by Jompol *et al.* [62] but with air-bridges [58], see Fig. 2.16. The experiment consisted of measuring momentum-resolved tunnelling to and from an array of one-dimensional wires to a 2DES in a GaAs/AlGaAs heterostructure, for a variety of different wire lengths down to $10\,\mu$m. The authors observed structure resembling second-level spinon excitations, near the $+k_{\mathrm{F}}$ point, branching away from the 1D mode and dying away rapidly at high momentum, in line with the theoretical predictions. Most interestingly, however, this feature was observed to emerge as a function of system length, its spectral weight increasing for shorter channels. It was also noted to be visible even when more subbands started being occupied. A comprehensive review on the mode-hierarchy picture, highlighting both theoretical and experimental progress, can be found in Tsyplyatyev *et al.* [121].

In 2016, Moreno *et al.* [94], also using tunnelling spectroscopy, found evidence for the existence of another higher-order mode, this time a first-level inverted spinon band (see Fig. 2.17). The tunnelling device used consisted of an array of 6000 GaAs wires, $1\,\mu$m in length, considerably shorter than previously used in Tsyplyatyev *et al.* [119, 121], which were $10\,\mu$m and $18\,\mu$m in length. The mode reported by Moreno *et al.* could not be observed in the longer-length wires, further establishing the mode-hierarchy picture as one of the main nonlinear TLL theories.

Momentum-dependent power law

As was discussed in section 2.3.1, the mobile impurity model, developed in the context of 1D quantum fluids at finite energy and momentum, makes a remarkable prediction regarding the power-law behaviour of the observed density of states near the spectral edge. Here, due to the finite curvature of the 1D dispersion, the exponent becomes momentum dependent, in clear

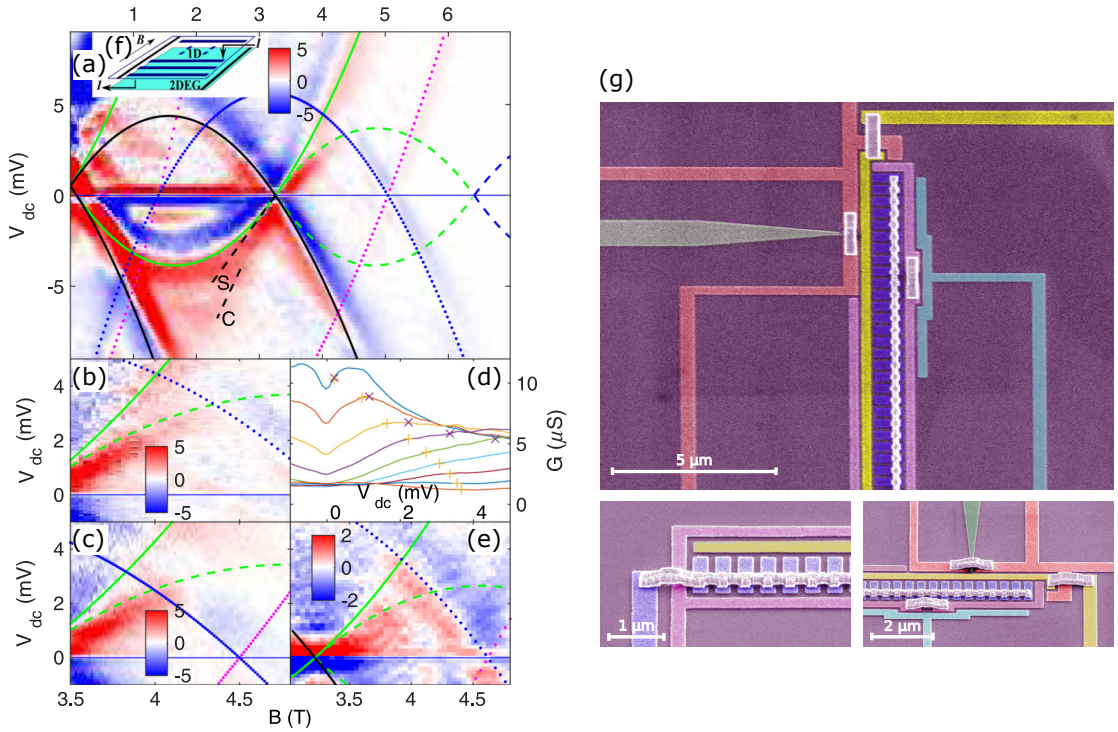

Fig. 2.16 Tunnelling differential conductance $G = \mathrm{d}I/\mathrm{d}V$ for two samples, consisting of a set of identical wires of length $L = 10\,\mu$m (a)–(d) and $L = 18\,\mu$m (e). A schematic representation of the device measured can be seen in inset (f). (a) $\mathrm{d}G/\mathrm{d}V_{\mathrm{dc}}$ map obtained at a lattice temperature of $T = 300\,$mK. The 1D signal is marked by solid green curves for the a modes, dashed green for the b modes and dashed blue for the c modes, see Fig. 2.15 for details. Magenta and blue curves indicate the parasitic 2D–2D signal while the black curve follows the dispersion of the 2D system as probed by the 1D wires. Spin and charge modes are labelled by the S and C lines, respectively. (b) and (c) show an enlargement of the replica region to the right of $+k_{\mathrm{F}}$, as seen in (a), for $v_{\mathrm{PG}} > 0$ and $v_{\mathrm{PG}} = 0$, respectively, where PG is a gate running over most of the parasitic 'p' region, see blue curves. (d) G vs V_{dc} at various fields B, around the replica region. The symbols $+$ and $\times$ on each curve mark, respectively, the dashed and solid green curves in (a) and (b). (e) $\mathrm{d}G/\mathrm{d}V_{\mathrm{dc}}$ map for a second device obtained at $T < 100\,$mK, showing a similar feature to that observed in (a)–(c). From [119]. (g) Scanning electron micrographs of a tunnelling device with air-bridges, showing how air-bridges are used not only to connect gates together across other gates, but also to link together all the finger gates defining the 1D wires, which avoids variation of the gate potential along each of these very short wires, as happens when the gates are joined together at one end [58, 124]

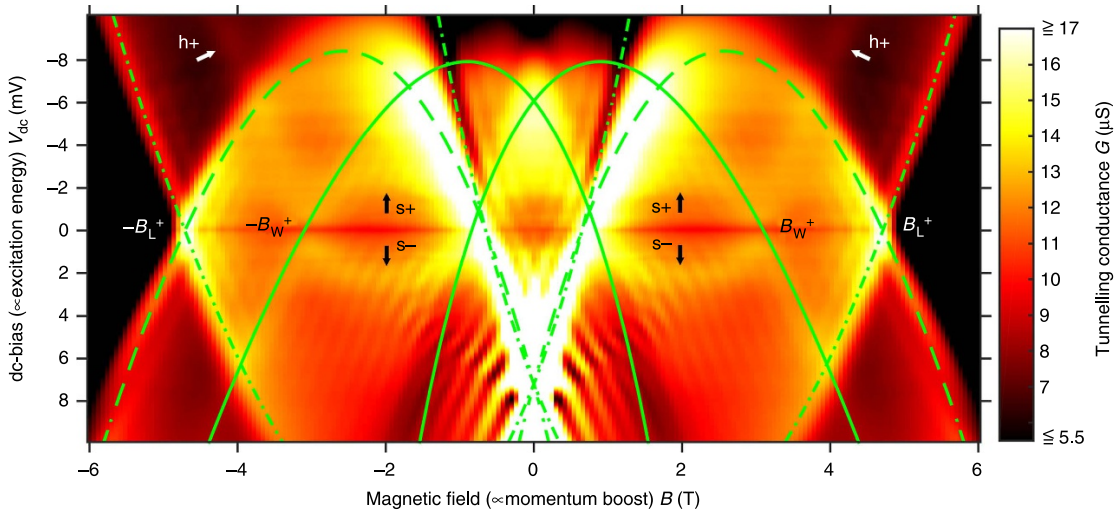

Fig. 2.17 Tunnelling conductance G plotted as a function of dc-bias V_{dc} and in-plane magnetic field B, for the regime of a single 1D subband occupied. The electron density in the wires is $n_{1\mathrm{D}} \approx 35\,\mu m^{-1}$. The solid green curves mark the dispersion of the 2D system as mapped by the 1D wires, while the green dashed and dash-dotted lines indicate the resonances arising from 2D–2D parasitic tunnelling. Spinon bands can be seen in the hole (s–) and particle (s+) sectors, while a holon band is present in the particle sector (h+). The labels $\pm B^{+}_{\mathrm{W,L}}$ indicate specific magnetic fields at which each resonance crosses the $V_{\mathrm{dc}} = 0$ axis. From [94].

contrast with the linear model, where no such dependence is expected. For electrons, *i.e.* spin-1/2 fermions, the observation of a momentum dependence of the threshold exponent away from the Fermi points would therefore constitute a hallmark of 1D nonlinear hydrodynamics.

In 2019, Jin *et al.* [59] reported the first observation of this new type of power-law using a system of interacting electrons in a quantum wire, probed via tunnelling spectroscopy. Here, a finite length-scale was present—given by the particle's wavelength—in contrast to, for example, what is the case in the usual physical picture of phase transitions where length-scales become infinite. This was the first time a power law was observed in the absence of scale invariance.

The authors observed that an enhancement of the tunnelling conductance below the bottom of the 1D dispersion (see Fig. 2.18) could not be explained solely by considering either a non-interacting or linear Luttinger framework (*i.e.* a momentum-independent power law). Instead, the best fits to the data were obtained by considering a momentum-dependent power law as predicted by the mobile-impurity model. In addition to the interaction effects, the effects of disorder-induced broadening were also considered, with the result being observed in multiple devices, of different wire length and measured at different temperatures. The extracted Luttinger parameter from the nonlinear regime was then of $K_\rho = 0.70 \pm 0.03$, in good agreement with the values obtained from other 1D interaction effects, most notably

the ZBA ($K_\rho = 0.59 \pm 0.13$ assuming end-tunnelling) and the spin-charge separation ($K_\rho = 0.76 \pm 0.07$), both also present in this experiment. Note that throughout this analysis the authors considered $K_\sigma = 1$, in accordance to renormalisation-group arguments [40].

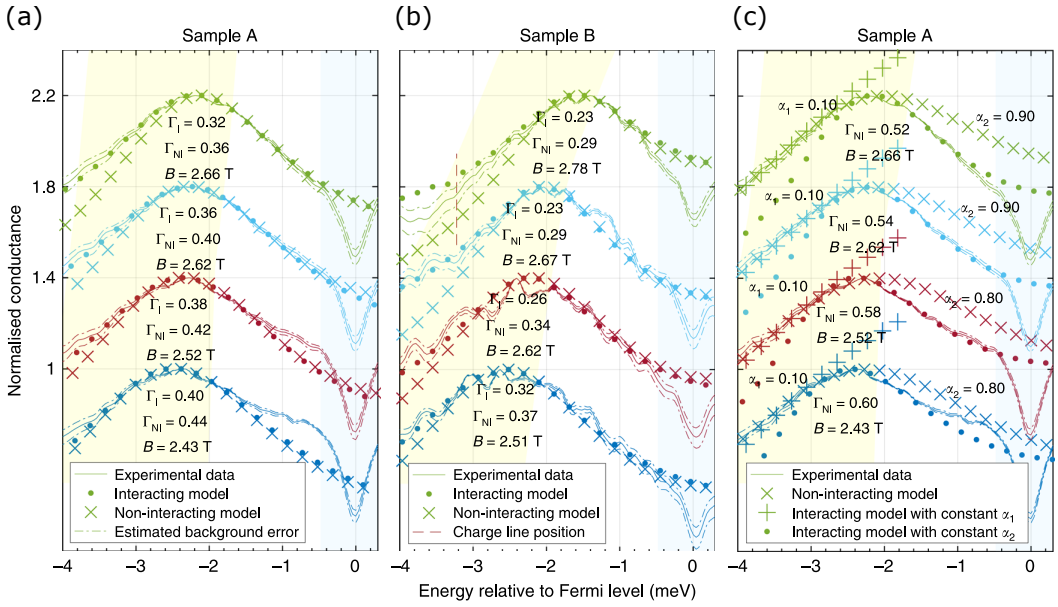

Fig. 2.18 Momentum-dependent power law. (a) and (b) Fits to the tunnelling conductance of two different samples, around the bottom of the 1D subband, for a variety of different fields, normalised to their peak value and shifted vertically for clarity. Two different models, non-interacting ($\times$) and interacting with a momentum-dependent exponent ($\cdot$), were used when fitting the data. The effects of disorder-induced broadening were also considered. Sample A, consisting of 18 μm long wires, was measured at 50 mK in a He^3/He^4 dilution refrigerator, while sample B, with 10 μm, was measured at 330 mK in a He^3 cryostat. (c) Fittings obtained using a momentum independent power law ($\cdot$ and $+$) and a non-interacting model ($\times$), matched to specific parts of the data. From [59].

Lifetime of spinons and holons at high energies

One of the early studies of NLL dynamics was done by Barack *et al.* [12] also using tunnelling spectroscopy but instead on CEO wires. Here, the authors selectively injected holes and particles into a quantum wire in order to study its relaxation properties. Their measurements concluded that while energetic particles underwent a rapid thermal relaxation, holes remained largely unchanged, in clear contrast with the linear TLL theory, in which energy relaxation is largely forbidden. This set the limits on the relaxation times to $\tau < 10^{-11}$ s for particles and $\tau \gg 10^{-11}$ s for holes.

It is important to highlight that while these results were important, they rest on the assumption that the interactions were weak. Previous work done by the same authors on

similar samples, for instance, obtained a Luttinger parameter for the electrons of $K_\rho \approx 0.55$, comfortably sitting in the strongly interacting regime. This apparent contradiction was explained by suggesting that relaxation dynamics are largely independent of the strength of the interactions as, indeed, the model derived showed good agreement with the data. Its phenomenological nature, however, illustrated the clear need for a microscopic description of kinetics and energy relaxation in the strongly interacting limit.

Plasmon lifetime in nonlinear carbon nanotubes

Recent work by Wang *et al.* [129] has provided further experimental evidence of nonlinear TLL dynamics. By growing long and clean semiconducting carbon nanotubes (CNTs), the authors were able to utilise low-noise near-field scanning optical measurements to map the plasmonic excitations in a nanotube, even when in the low-density limit. Semiconducting CNTs have a bandgap and as such the linear approximation is expected to break as one approaches the bottom of the conduction band. By coupling the nanotube to a gate electrode, the authors were able to tune the position of the Fermi level and use it to probe the effect of the nonlinear dispersion on the plasmons. Similar measurements were also carried out on metallic CNTs, where the band structure is gapless and so well captured by the linear model.

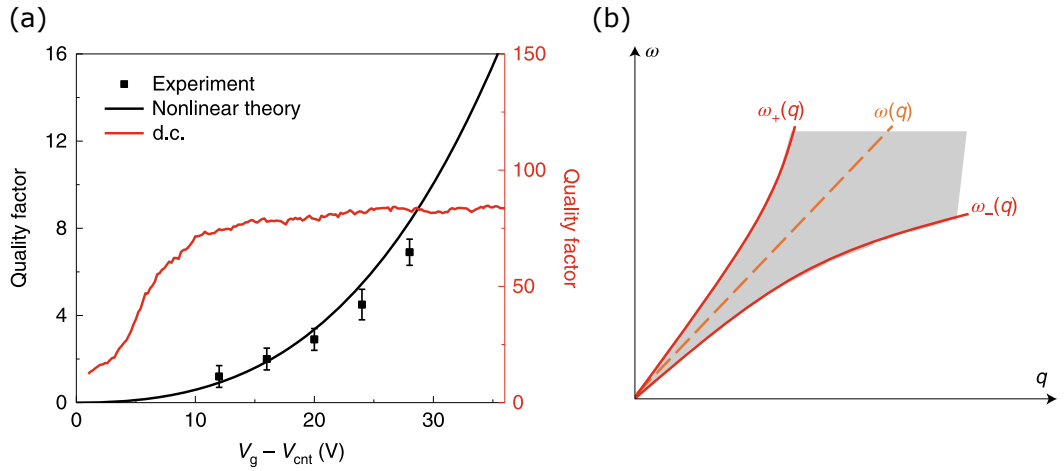

Fig. 2.19 Nonlinear Luttinger plasmons in carbon nanotubes. (a) Plasmon quality factor as a function of gate voltage. The experimental results match the NLL well (black) and cannot be captured by alternative mechanisms like impurity scattering (red). (b) DSF diagram characteristic of the NLL model. In a nonlinear TLL, the plasmon mode is not an exact eigenstate of $\omega(q) = v_p q$ (dashed) but instead is broadened with upper and lower bounds given by $\omega_\pm(q)$, respectively. The spectral width, $\delta\omega(q) = \omega_+(q) - \omega_-(q)$, therefore increases with q, indicating a reduction in the plasmon lifetime, as observed. From [129].

One of the key predictions of the NLL theory is a drastic reduction of the plasmon lifetime. By injecting a plasmon wave into the nanotube, Wang and collaborators were able to observe the interference between the incident and reflected excitations at one end of the nanotube and from there extract the quality factor and the wavelength of the mode in the system. This led them to observe the increase of the quality factor (and consequently, of the plasmon lifetime) as a function of the electron density, see Fig. 2.19a. By contrast, the linear model predicts a drastically different scenario, with infinitely lived excitations and as such no intrinsic relaxation mechanism, meaning that the quality factor should remain gate-independent unlike what was observed. Optical and transport measurements on similar samples also confirmed that the decay was indeed associated with nonlinear dynamics rather than, for example, scattering off impurities.

These results can be understood from the dynamic structure factor (DSF) of a NLL, see Fig. 2.19b. For a linear TLL, such as in a metallic nanotube, the DSF takes the form $S(q,\omega) = 2K|q|\delta(\omega - v_{\mathrm{p}}q)$. This results in a linear dispersion for the plasmon mode, given by $\omega(q) = v_{\mathrm{p}}q$. Here, K is the Luttinger parameter, v_{p} is the plasmon velocity (charge mode), and q is its wave vector.

In contrast, for a nonlinear TLL, as in a semiconducting CNT, the DSF is given by

$$S(q,\omega) = 2\frac{\tilde{m}K}{|q|}\theta\left(\frac{q^2}{2\tilde{m}} - |\omega - v_{\mathrm{p}}q|\right), \tag{2.36}$$

where $\tilde{m}$ is an interaction-dependent effective mass and θ is the Heaviside function. This means that the plasmon mode is no longer an exact eigenstate of the system but instead is broadened, with upper and lower limits given by $\omega_{\pm} = v_{\mathrm{p}}q \pm q^2/(2m)$. Consequently, for a given frequency, *i.e.* energy, there will now be multiple available plasmons with different momenta. A high-energy plasmon can then easily decay into multiple low-energy plasmons, with the damping and lifetime associated with this process being determined by the width of the broadening $\delta\omega(q) = q^2/\tilde{m}$.

2.4 Other work on one-dimensional interaction effects

Before we conclude, let us briefly mention some other important results obtained using 1D systems which, although not directly related to the work discussed in the present thesis, nevertheless complement its main conclusions, and further contextualise the current state of the field.

2.4.1 Coulomb drag

It is often the case that free carriers in semiconducting devices cannot screen each other very efficiently with, indeed, the Coulomb interaction between them only being expected to be screened out at finite, often rather long, distances. Interestingly then, when two parallel conducting wires come together, separated only by a thin insulating barrier, it is possible for a current through one of them to induce a net charge displacement in the other. This is the so-called Coulomb drag effect which, while often negligible for large systems, can play an important role in the electrical transport properties of nanoscale devices. Here, the drag resistivity $R_{\mathrm{D}} = -V_{\mathrm{drag}}/I_{\mathrm{drive}}$ is determined by the drive current in the inducing wire, I_{drive}, and the measured drag voltage in the induced wire, V_{drag}.

Initially, this phenomenon was thought to be due to electrons in the drive wire transferring their momentum to their counterparts in the other wire, via the Coulomb interaction, with the direction of motion remaining unchanged. However, Laroche *et al.* [81, 82] strongly challenged this picture. Here, the authors found that the drag resistance could be either positive or negative, something surprising since the momentum-transfer model could only account for the former. Negative Coulomb drag, however, had been predicted to exist in models where the drag is induced by charge fluctuations, therefore introducing a new transport paradigm in addition to the momentum-transfer picture.

Later work by the same group [83] also observed an upturn in drag resistance at a temperature $T^{\star}$. This confirmed a long-held prediction of the TLL model, wherein a crossover between drag dominated by forward (for $T > T^{\star}$) or backward scattering (for $T < T^{\star}$) should occur, thus establishing a 1D–1D drag dependence on temperature. Note, however, that in this experiment, both wires remained in the single-subband occupancy regime, in accordance with the assumptions of the TLL model. It then remains an open question how multiple-subband occupancy may change the screening profile of 1D systems. Results on 1D–1D intra-subband screening will be discussed in chapter 6 .

2.4.2 Helical current

Conductance along a ballistic, 1D quantum wire is quantised in units of $2e^2/h$, with the factor of 2 arising from the spin degenerancy of the electrons. After some initial debate [65, 66, 64, 35], it was shown [79, 122, 130] that this value is not affected by interactions in a clean system, but instead solely determined by the contact resistance of the Fermi leads. In the presence of disorder, however, it is reduced following a TLL power law.

An early problem in the CEO wires work was that, systematically, these structures showed a suppression of the height of the conductance plateau in a way which was not consistent

with the TLL model. Recently, however, work carried out using similar samples in the ultra-low-temperature regime ($T \sim 10\,\mathrm{mK}$) revealed promising new evidence on what might be helical nuclear magnetism in the TLL regime. Tracking the conductance of the first mode as a function of temperature, Scheller *et al.* [106] observed the expected value of $2e^2/h$ at $T \gtrsim 10\,\mathrm{K}$ drop to e^2/h as the temperature was lowered, becoming independent of T at $T \lesssim 0.1\,\mathrm{K}$. This behaviour was also seen to be independent of both density and magnetic field up to at least 3 T.

After ruling out several other potential interpretations, the authors concluded that the most likely explanation was the appearance of a nuclear spin helix—an ordered state of nuclear spins hosted by atoms of the same crystal—thus explaining the drop in conductance by a factor of 2 at lower temperatures, since the wire could now only transmit spin-down right- and spin-up left-movers. This interpretation is consistent with a recent theory proposed by Braunecker *et al.* [19, 20, 18]. Note, however, that the model predicts a sharp phase transition to occur at a given crossover temperature $T^\star$, rather than a broad reduction as observed in this experiment. Attempts to explain this were made in [8], but the question remains whether it truly was helical nuclear magnetism the most likely mechanism behind the observation, as $T^\star$ could not be extracted. A potential way of answering this would be using a 1D system where the interaction strength, on which $T^\star$ is expected to depend strongly, could be varied *in situ*. This, however, was not possible in CEO wires where the confinement in the wires is defined by the width of the well (or, in other words, MBE), and as such remains fixed.

2.4.3 Cold atoms

For completeness, we conclude by commenting on a different experimental platform, outside solid state, for studying the physics of strongly correlated many-body systems. In recent years, experiments have emerged reporting the formation of clean, disorder-free 1D chains by trapping ultracold atoms in optical lattices [98, 17, 132]. Here, the confinement potential is given by the laser field itself, therefore allowing the simulation of a very controlled Fermi-Hubbard model not otherwise accessible to material systems. Recent work using quantum gas microscopy, that is, probing the atomic chain with single-atom/single-lattice-site resolution, revealed signatures of spin-charge separation [51, 105], with real-space tracking of the deconfinement and evolution of each separate plasmon having also been reported [126]. These systems are particularly attractive because of the relative ease of varying the strength of the interactions within them, and because they also offer the prospect for tracking crossover from 1D to 2D physics. Nevertheless, while they allow for the simulation of what are essentially disorder-free, perfect lattices, and as such offer the possibility of testing the

available theories to new limits, the issue remains that, unlike solid-state systems, real-world integration in generally speaking not as straightforward.

2.5 Summary

In this chapter we have covered the many-body problem of electrons inside solid crystals. We started by briefly discussing the Fermi-liquid model, valid for non-correlated systems at higher dimensions, before introducing the Tomonaga-Luttinger liquid model for electron systems in 1D. Note that this model implicitly assumes a linear dispersion and, as such, is only strictly speaking valid at low-energies. Nevertheless, we showed how some of its seminal predictions, including separation of spin and charge modes and interaction-driven power-law behaviour, have since been observed experimentally in a variety of solid-state systems. In the second half of the chapter we moved on to nonlinear Luttinger liquids, where the dispersion of the electrons is no longer assumed to remain linear. Here, we reviewed some of the more recent experimental work performed at high energies, where both momentum-dependent power laws, short-lived plasmons excitations, and higher-order 'replica' modes, all of which go beyond the original Luttinger picture, have since been observed. We concluded by reviewing additional interaction effects reported in 1D systems, including spontaneous nuclear spin magnetism, Coulomb drag, and time-resolved dynamics.

Chapter 3

Energy- and momentum-resolved tunnelling spectroscopy

In this chapter, we introduce the experimental technique behind all measurements conducted in this thesis, and which we have now named as *magnetotunnelling spectroscopy*. This allows us to map the spectral function of one system with respect to a known, well-understood spectrometer, while both energy and momentum are being varied. We start by giving a brief overview of other, well-established, spectroscopy techniques, commenting on how their performance compares to our method (section 3.1). We then derive the tunnelling current and show how the measurement can be carried out with both energy (section 3.2) as well as momentum resolution (section 3.3), to map the respective spectral functions of each system. After that, we discuss how resonances in phase-space tunnelling dispersion maps can be interpreted based on the underlying spectral functions for both 1D and 2D systems (section 3.4). Finally, we conclude by discussing and modelling the capacitive effects which impact the measurement (section 3.5).

3.1 Beyond surface probing techniques

The ability to probe a system at smaller and smaller scales has often been associated with breakthroughs in science. The invention of the optical microscope, for example, gave us a new perspective into the biological world. Scanning tunnelling microscopy (STM), on the other hand, allowed for a level of resolution otherwise unachievable via optical means, giving us a fresh glimpse into the atomic landscape. The key development behind this discovery was the concept of quantum tunnelling, that is, the observation that in quantum mechanics,

subatomic particles can appear on the opposite side of a barrier that should, otherwise, be impossible for them to penetrate.

As we saw in chapter 2, and particularly, sections 2.2.4 and 2.3.3, there are a number of experimental techniques that can be employed when probing the underlying dynamics of a solid-state system. While each presents its own set of advantages and limitations, the choice of which one to use is often in practice determined by the experimental system being investigated. For instance, as discussed in section 2.2.4, early work on Luttinger-type behaviour and carbon nanotubes naturally suggested the use of ARPES (angle-resolved photoemission spectroscopy) and indeed, this led to some of the very earliest observations indicative of power-law behaviour and spin-charge separation. Later technological developments, like STM, and refinements such as STS (scanning tunnelling spectroscopy), have also since been successfully implemented in probing strongly-correlated systems and many-body dynamics, in systems such as topological insulators, superconductors, majorana channels, and edge states, amongst others.

As surface probes, however, their main limitation is that they are naturally subject to every potential anomaly which may occur at a surface of a material. Specifically, since only the top few layers of atoms are being probed, any amount of defects, impurities, and/or atmospheric phenomena can get greatly enhanced. As we will see below and later in chapter 5, the key advantage of magnetotunnelling spectroscopy is that it works for systems buried deep below the surface, and therefore, protected from the exterior. Unlike STS and ARPES, where crystals have to be specifically prepared *in situ* in order for clean and regular interfaces to be achieved, this is no longer the case for tunnelling spectroscopy. In other words, by having the spectrometer built into the device so that measurements can take place well below the surface, not only are the results less sensitive to surface effects, but also the system of interest of potentially much higher quality. Furthermore, interaction with the sample becomes much more flexibile as, for example, high vacuum is no longer required. One can then envision using tunnelling spectroscopy while simultaneously varying pressure or uniaxial stress, two other parameters often used when looking for new quantum materials, and something which neither STS or ARPES currently allow for. In the following sections we introduce the physical principles behind tunnelling spectroscopy, starting from a general overview of the technique before applying it to the specific geometry of our tunnelling device.

3.2 Energy-resolved tunnelling spectroscopy

Our experiment consists of a vertical tunnelling spectrometer device where two parallel quantum wells are placed in close proximity to one another. By appropriately engineering

the barrier, one can ensure that tunnelling of electrons to and from each system can be measured. In order to study 1D dynamics, one layer is modulated by a set of wire gates into forming an array of 1D channels, while the other remains largely unperturbed, thus acting as a well-understood 2D spectrometer. The dispersion of both systems can then be mapped by measuring tunnelling to and from the 1D array to the 2D layer. As we will show, this can be done while varying both energy as well as momentum. Before analysing the 1D-2D geometry in question, however, let us first derive the tunnelling current for the more general case of two fermionic 2D systems separated by a barrier.

In order to calculate this, we follow Bardeen's approach, initially developed to study metal-insulator-superconductor junctions [13]. It is well established that when an electron tunnels quantum-mechanically through a barrier between two regions, it must conserve both energy and momentum transverse to the barrier (modulo a reciprocal-lattice vector, in a crystal). Since electrons are fermions, they must also obey the Pauli exclusion principle, meaning they cannot tunnel into an occupied state. In a solid at low temperatures, nearly all the states below the Fermi energy E_F are occupied, so we can use this energy as a reference point below which tunnelling is forbidden.

In this work we focus on semiconductor heterostructures where a planar barrier separates two parallel quantum wells containing electrons. This allows us to use Fermi's golden rule in order to determine the rate of tunnelling as

$$\Gamma_{\mu\to\nu} = \frac{2\pi}{\hbar}|T_{\mu\to\nu}|^2\delta(E_\mu^\mathrm{UW} - E_\nu^\mathrm{LW}) \tag{3.1}$$

where $T_{\mu\to\nu} = \langle\psi_\mu|\,U\,|\psi_\nu\rangle$ is the transmission matrix and U the potential of the barrier. Note that here we are assuming that electrons tunnel from a state μ in the upper-well (UW) to a state ν the bottom-well (LW), though a simple change of sign can easily account for the reverse process. Furthermore, conservation of energy is effectively enforced through the δ-function, so that tunnelling is only possible between an occupied and an empty state of the same energy (*i.e.,* elastic tunnelling).

Fermi's golden rule is a general result of first-order time-dependent perturbation theory, and its derivation can be found in a number of textbooks [27]. The tunnelling current I is then proportional to $e\Gamma_{\mu\to\nu}$, where e is the elementary charge since we are describing single-electron processes.

While the above formula describes tunnelling from (occupied) state μ into (empty) state ν, we know that both wells are characterised by a continuum of states. Therefore, the probability of a state being occupied is given by the Fermi-Dirac distribution $f(E - E_\mathrm{F}) = (1+\exp[(E-E_\mathrm{F})/k_\mathrm{B}T])^{-1}$ meaning that, in other words, the probability of it being

unoccupied is simply described by $1-f(E-E_{\mathrm{F}})$, see Fig. 2.1. The tunnelling currents are then given by

$$\begin{aligned} I_{\mathrm{UW}\to\mathrm{LW}} &= \frac{4\pi e}{\hbar}\sum_{\mu\nu} f(E_\mu^{\mathrm{UW}}-E_{\mathrm{F}}^{\mathrm{UW}})[1-f(E_\nu^{\mathrm{LW}}-E_{\mathrm{F}}^{\mathrm{LW}})]|T_{\mu\to\nu}|^2\delta(E_\nu^{\mathrm{LW}}-E_\mu^{\mathrm{UW}}-eV) \\ I_{\mathrm{LW}\to\mathrm{UW}} &= \frac{4\pi e}{\hbar}\sum_{\mu\nu} f(E_\mu^{\mathrm{LW}}-E_{\mathrm{F}}^{\mathrm{LW}})[1-f(E_\nu^{\mathrm{UW}}-E_{\mathrm{F}}^{\mathrm{UW}})]|T_{\mu\to\nu}|^2\delta(E_\nu^{\mathrm{LW}}-E_\mu^{\mathrm{UW}}-eV) \end{aligned} \tag{3.2}$$

where the extra factor of 2 accounts for the two possible spin states of the tunnelling electron. The resulting net tunnelling current is obtained from the difference between the two currents above

$$I = \frac{4\pi e}{\hbar}\sum_{\mu\nu}[f(E_\mu^{\mathrm{UW}}-E_{\mathrm{F}}^{\mathrm{UW}})-f(E_\nu^{\mathrm{LW}}-E_{\mathrm{F}}^{\mathrm{LW}})]|T_{\mu\to\nu}|^2\delta(E_\nu^{\mathrm{LW}}-E_\mu^{\mathrm{UW}}-eV) \tag{3.3}$$

We can now substitute the summation over discrete states by replacing it with an integral over the density of states (DOS), n, running over all energies $n(E):\sum_\mu \to \int n(E)\mathrm{d}E$

$$\begin{aligned} I =& \frac{4\pi e}{\hbar}\int \mathrm{d}\varepsilon[f(E_{\mathrm{F}}^{\mathrm{LW}}-eV+\varepsilon)-f(E_{\mathrm{F}}^{\mathrm{UW}}+\varepsilon)] \\ &\times n^{\mathrm{LW}}(E_{\mathrm{F}}^{\mathrm{LW}}-eV+\varepsilon)n^{\mathrm{UW}}(E_{\mathrm{F}}^{\mathrm{UW}}+\varepsilon)|T(E_{\mathrm{F}}^{\mathrm{UW}}+\varepsilon,E_{\mathrm{F}}^{\mathrm{UW}}-eV+\varepsilon)|^2 \end{aligned} \tag{3.4}$$

Here, n^{UW} and n^{LW} are the density of states of the upper and lower layers, respectively.

As can be seen from equation (3.4), the tunnelling current depends directly on the electronic structure of both systems, via their respective DOS. This is, in fact, identical to the mechanism behind STM, which can be constructed in an analogous fashion simply by substituting UW, LW $\to$ sample, tip.

At zero temperature, or if $k_{\mathrm{B}}T \ll \Delta E$, where ΔE is the desired energy resolution, the Fermi distribution function is essentially given by a step function (see Fig. 2.1), simplifying the above expression to

$$I = \frac{4\pi e}{\hbar}\int_0^{eV} \mathrm{d}\varepsilon n^{\mathrm{LW}}(E_{\mathrm{F}}^{\mathrm{LW}}-eV+\varepsilon)n^{\mathrm{UW}}(E_{\mathrm{F}}^{\mathrm{UW}}+\varepsilon)|T|^2 \tag{3.5}$$

which, at small biases, reduces to

$$I = \frac{4\pi e^2}{\hbar}Vn^{\mathrm{LW}}(E_{\mathrm{F}}^{\mathrm{LW}})n^{\mathrm{UW}}(E_{\mathrm{F}}^{\mathrm{UW}})|T|^2. \tag{3.6}$$

In practice, what is measured, however, is often the differential conductance $G = \mathrm{d}I/\mathrm{d}V$, which following from (3.6), is given then by

$$\frac{\mathrm{d}I}{\mathrm{d}V} = \frac{4\pi e^2}{\hbar} n^{\mathrm{LW}}(E_{\mathrm{F}}^{\mathrm{LW}}) n^{\mathrm{UW}}(E_{\mathrm{F}}^{\mathrm{UW}} + eV) |T(E_{\mathrm{F}}^{\mathrm{UW}} + eV, E_{\mathrm{F}}^{\mathrm{LW}})|^2. \tag{3.7}$$

Note that both occupied and unocupied states can be accessed in the upper well simply by changing the sign of the bias V. The resolution in energy, on the other hand, is set by $\max(e\delta V, k_{\mathrm{B}}T)$.

3.3 Spectral functions and momentum-resolved tunnelling spectroscopy

So far we have only discussed tunnelling processes where by varying the applied bias between each layer one can probe both systems in energy-space. Let us know discuss how this can be expanded in order for tunnelling to occur between states separated in momentum as well.

In section 2.2.3 we introduced the spectral function $A(k,\omega)$ as a tool for describing single-particle properties in many-body systems. To recap, it represents the probability density of a state of momentum k and energy ω being occupied. The density of states $n(\omega)$ can then be defined in terms of $A(k,\omega)$ by summing over all possible k-states, that is

$$n(\omega) = \sum_k A_k(\omega). \tag{3.8}$$

Substituting this expression in equation (3.5), and doing a change of variable $E = E_{\mathrm{F}} - eV + \varepsilon$, we get

$$I = \frac{4\pi e}{\hbar} \sum_{k_1} \sum_{k_2} |T_{k_1 \to k_2}|^2 \int \mathrm{d}E A^{\mathrm{LW}}(k_1, E) A^{\mathrm{UW}}(k_2, E + eV) \times [f(\varepsilon^{\mathrm{LW}}) - f(\varepsilon^{\mathrm{UW}} + eV)]. \tag{3.9}$$

Following from Bardeen's approach [13], we also know that

$$T_{k_1 \to k_2} = \frac{\hbar^2}{2m^\star} \int \mathrm{d}x\mathrm{d}y \Big(\psi_{\mathrm{LW}} \frac{\partial \psi_{\mathrm{UW}}^\star}{\partial z} - \psi_{\mathrm{UW}}^\star \frac{\partial \psi_{\mathrm{LW}}}{\partial z} \Big), \tag{3.10}$$

meaning that all that is left to do is obtaining the respective wavefunctions for each system.

Let us now apply this framework to the specific geometry of our devices (see chapter 4 for details on device design). Defining the $x-y$ plane as parallel to the sample surface, with

the x-axis parallel to the 1D channels, we construct the electron wavefunctions of the two layers as

$$\psi_{\mathrm{UW}}(x,y,z) = e^{ik_x^{'}x}\phi_n(y)\chi_{\mathrm{UW}}(z) \qquad \psi_{\mathrm{LW}}(x,y,z) = e^{ik_x x}e^{ik_y y}\chi_{\mathrm{LW}}(z). \tag{3.11}$$

Here, $\chi(z)$ defines the confinement potential along the z-direction for both wells, while $\phi(y)$ is the confinement potential created by the wire-gate, which defines the 1D wire array. We get

$$T_{k_{\mathrm{UW}}\to k_{\mathrm{LW}}} = (2\pi)^2 t(z)\delta(k_x - k_x^{'})\tilde{\phi}_n(k_y) \tag{3.12}$$

where $t(z) = \frac{\hbar^2}{2m^\star}\left(\chi_{\mathrm{LW}}\frac{\partial\chi^\star_{\mathrm{UW}}}{\partial z} - \chi^\star_{\mathrm{UW}}\frac{\partial\chi_{\mathrm{LW}}}{\partial z}\right)$, and $\tilde{\phi}$ is the Fourier transform. Note that $\delta(k_x - k_x^{'})$ effectively imposes that momentum must be conserved in the x-direction during a tunnelling process, in an analogous role to the δ-function in energy in equation (3.1).

In order to determine $\phi(\tilde{k}_y)$, we start by treating the confinement potential induced by the gates and responsible for creating the 1D wire array as being parabolic, *i.e.*, $V(y) = \frac{1}{2}m^*\omega_0^2 y^2$. Note that, in our geometry, y is a coordinate transverse to the 1D channels. It is then well established that for a parabolic potential, the wavefunctions allowed are given by the eigenstates of a quantum harmonic oscillator [27]

$$\phi_n(y) = \frac{1}{\sqrt{2^n n! l\sqrt{\pi}}}H_n\left(\frac{y}{l}\right)exp\left(-\frac{y^2}{2l^2}\right) \tag{3.13}$$

with $l = \sqrt{\hbar/m^\star\omega_0}$ being the natural length and H_n the nth degree Hermite polynomial. Functions of the form of $\phi_n(y)$ form an orthogonal eigenbasis to the Fourier transform operator, meaning that the probability distributions given by $|\phi(y)|^2$ and $|\tilde{\phi}(k_y)|^2$ are mathematically the same. Physically, $\phi_n(k_y)$ represents the wavefunction in momentum space, which can also be directly probed via our tunnelling technique.

So far we have seen that in order for a tunnelling process to occur, both the initial and final electron states must match in energy as well as momentum along the x-direction. While the first can be accounted for by applying a DC-bias between the wells, thus offsetting the respective spectral functions in energy, a momentum offset along the x-direction can also be achieved by applying an in-plane magnetic field along the y-direction, that is, transverse to the wires. Indeed, it can be easily verified that, for a magnetic field vector $\mathbf{B} = (0,B,0)$, satisfying the Landau gauge $\mathbf{A} = (zB,0,0)$ so that $\mathbf{B} = \nabla\times\mathbf{A}$, the electron canonical momentum $\mathbf{p} = \hbar\mathbf{k} + e\mathbf{A}$ is boosted by $\hbar\Delta\mathbf{k} = e\mathbf{A} = (eBd,0,0)$, where d is the separation between the centres of the wavefunctions of the two states.

Putting everything together, the tunnelling current between the two systems is then given by

$$I \propto \int \mathrm{d}E\mathrm{d}\mathbf{k}[f(\varepsilon_{\mathrm{LW}}) - f(\varepsilon_{\mathrm{UW}} + eV)]|\tilde{\phi}_n(k_y)|^2 A^{\mathrm{LW}}(\mathbf{k},E)A^{\mathrm{UW}}\left(\mathbf{k} + \frac{ed}{\hbar}\tilde{\mathbf{n}} \times \mathbf{B}, E + eV\right). \tag{3.14}$$

where $\tilde{\mathbf{n}}$ is the unit vector along the direction of the injected current in the wires, and $V = V_{\mathrm{DC}} + V_{\mathrm{AC}}$, with V_{AC} being the additional AC signal introduced by the lock-in amplifier when measuring.

Equation (3.14) essentially underpins all measurements reported in this thesis, effectively establishing the foundations of the technique we have now coined as *magnetotunnelling spectroscopy*. This is both an energy- and momentum-resolved tunnelling probe, whereby measuring tunnelling to and from a system of interest (in our case a 1D wire array, $A^{\mathrm{UW}} \equiv A_{\mathrm{1D}}$) to a well-understood probe (such as a 2D Fermi liquid, $A^{\mathrm{LW}} \equiv A_{\mathrm{2D,FL}}$), one can map the dispersion of both systems in all of the energy-momentum plane. Note, however, that strictly speaking, I is proportional to the convolution of the spectral functions, not the spectral functions themselves. In the next section, we will see how the conditions of maximum overlap in both $\mathbf{k}$ and E can be used to infer the shape of $A(\mathbf{k},E)$.

3.4 Tunnelling conductance and resonance conditions

We measure the tunnelling current between the two quantum wells via a phase-sensitive lock-in detection technique,. This means that, effectively, the quantity being measured is not I but instead the tunnelling conductance G,

$$G = \frac{\mathrm{d}I}{\mathrm{d}V} \propto \frac{\mathrm{d}}{\mathrm{d}V}\int \mathrm{d}E\mathrm{d}\mathbf{k}A^{\mathrm{LW}}(\mathbf{k},E)A^{\mathrm{UW}}(\mathbf{k}+\Delta\mathbf{k},E+eV) \tag{3.15}$$

Because G is proportional to the convolution of the spectral functions, and not the spectral functions themselves, an interesting question to ask is whether the maximum in the convolution stays at the maximum of the probed function. In order to do so, let us now discuss the form of $A(\mathbf{k},\omega)$ for the various systems of interest.

2D Fermi liquid

Let us assume, for now, that the electron gas in the lower well can be treated as a Fermi liquid. It is then well-known that, in the absence of interactions, $A(\mathbf{k},\omega)$ takes the form of a δ-function, $A(\mathbf{k},\omega) \propto \delta(\omega - E_k)$, where $E_k = \hbar^2(k_x^2 + k_y^2)/(2m)$. In other words, adding or

removing a particle to/from a plane-wave state always results in an exact eigenstate of the system.

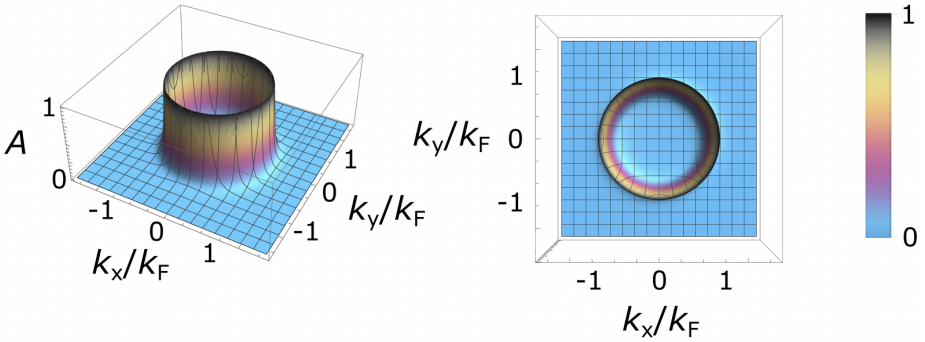

Fig. 3.1 Normalised spectral function of a 2D Fermi liquid, evaluated at $eV_{DC} = 0$, $B = 0$, for $\Gamma = 0.25$ meV and $\hbar\omega = 1.7$ meV. Note the high-degree of symmetry, as expected for a system with translational invariance along two directions.

In order to account for broadening arising from disorder, the spectral function can be convolved with a Lorentzian function. Following from the notation used in Kardynal *et al.* [67], we have

$$A_{\mathrm{2D,FL}}(k_x,k_y;\mu) = \frac{\Gamma/\pi}{\Gamma^2 + (\mu - \xi_{\mathrm{2D,FL}})^2} \tag{3.16}$$

where Γ is the spectral line width associated with the single-particle disorder broadening, μ is the chemical potential, and $\xi_{\mathrm{2D,FL}}$ is the energy spectra of a Fermi liquid, given by

$$\xi_{\mathrm{2D,FL}} = \frac{\hbar^2(k_x^2 + k_y^2)}{2m^\star} + E_{0,\mathrm{LW}} \tag{3.17}$$

where $E_{0,\mathrm{LW}}$ denotes the bottom of the 2D band in the lower well, see Fig. 3.1.

Non-interacting 1D system

A *perfect*, *i.e.*, infinitely narrow, non-interacting 1D system can be modelled in the same way as a 2D Fermi liquid, with $\xi_{\mathrm{2D,FL}}$ being instead replaced by

$$\xi_{\mathrm{1D,non\text{-}int.}} = E_n + \frac{\hbar^2 k_x'}{2m} + E_{0,\mathrm{UW}} \tag{3.18}$$

where $E_n = (n + 1/2)\hbar\omega_0$

Experimentally, however, all (quasi-)1D materials do indeed have some sort of finite transverse extension. In order to account for such, we treat the confinement potential as being parabolic, with electron wavefunctions in the transverse direction being given by the eigen-

states of a quantum harmonic oscillator, see section 3.3. Consequently, $A_{\text{1D,non-int.}}(\mathbf{k},n;\mu)$ must be modified to account for a harmonic dependence along the y-direction, resulting in energy levels known as 1D subbands. These are given by

$$\begin{aligned} A_{\text{1D,non-int.}}(k_x^{'},k_y,E,\Gamma) &= \int \sum_n \delta(\mu-\xi_{\text{1D, non-int.}}-z)\frac{\Gamma}{\pi}\frac{H_n^2(k_y a)e^{-(k_y a)^2}}{\Gamma^2+z^2} \\ &= \sum_n \frac{\Gamma}{\pi}\frac{H_n^2(k_y a)e^{-(k_y a)^2}}{\Gamma^2+(\mu-\xi_{\text{1D, non-int.}})^2} \end{aligned} \tag{3.19}$$

where $a = m_{\text{1D}}\omega/\hbar$ is the finite width of the wire and $H_n(x)$ are the nth degree Hermite polynomials, see Fig. 3.2.

Interacting 1D system

Finally, let us consider a 1D system of interacting electrons according to the Luttinger liquid model. Here, it is known (see Fig. 2.6) that the spectral function must exhibit power-law singularities near the spectral edge. It then follows that $A(\mathbf{k},E)$ can be obtained by substituting the δ-function in equation (3.19) by a power-law

$$A_{\text{1D,int.}}(k_x^{'},k_y,E,\Gamma) = \int \sum_n \frac{\theta(\mu-\xi_{\text{1D, non-int.}}-z)}{(\mu-\xi_{\text{1D, non-int.}}-z)^{\alpha}}\frac{\Gamma}{\pi}\frac{H_n^2(k_y a)e^{-(k_y a)^2}}{\Gamma^2+z^2}. \tag{3.20}$$

In a linear system, the threshold exponent α above is constant, see Fig. 3.3. For a nonlinear TLL, however, and as discussed in section 2.32, $\alpha \equiv \alpha(k)$, meaning it will have a momentum dependence, see equation (2.33).

Fig. 3.1-3.3 show the normalised spectral functions at $B = 0$, $eV_{\text{DC}} = 0$ for each of the three systems discussed above, calculated assuming $\Gamma = 0.25$ meV, $\hbar\omega = 1.7$ meV, and a subband occupancy value from one to four. As we will see later in chapter 5, these are representative of the experimental systems measured in our experiment.

As expected, the degree of symmetry between 2D and 1D systems varies significantly. Furthermore, note that once interactions are turned on, spectral features tend, in general, to become less sharp. Because equation (3.15) is proportional to the convolution of two spectral functions rather than the spectral functions themselves, this means that the points of maximum conductance do not necessarily have to correspond to the points of maximum spectral weight. Overall, this effectively translates into a small deviation, though more

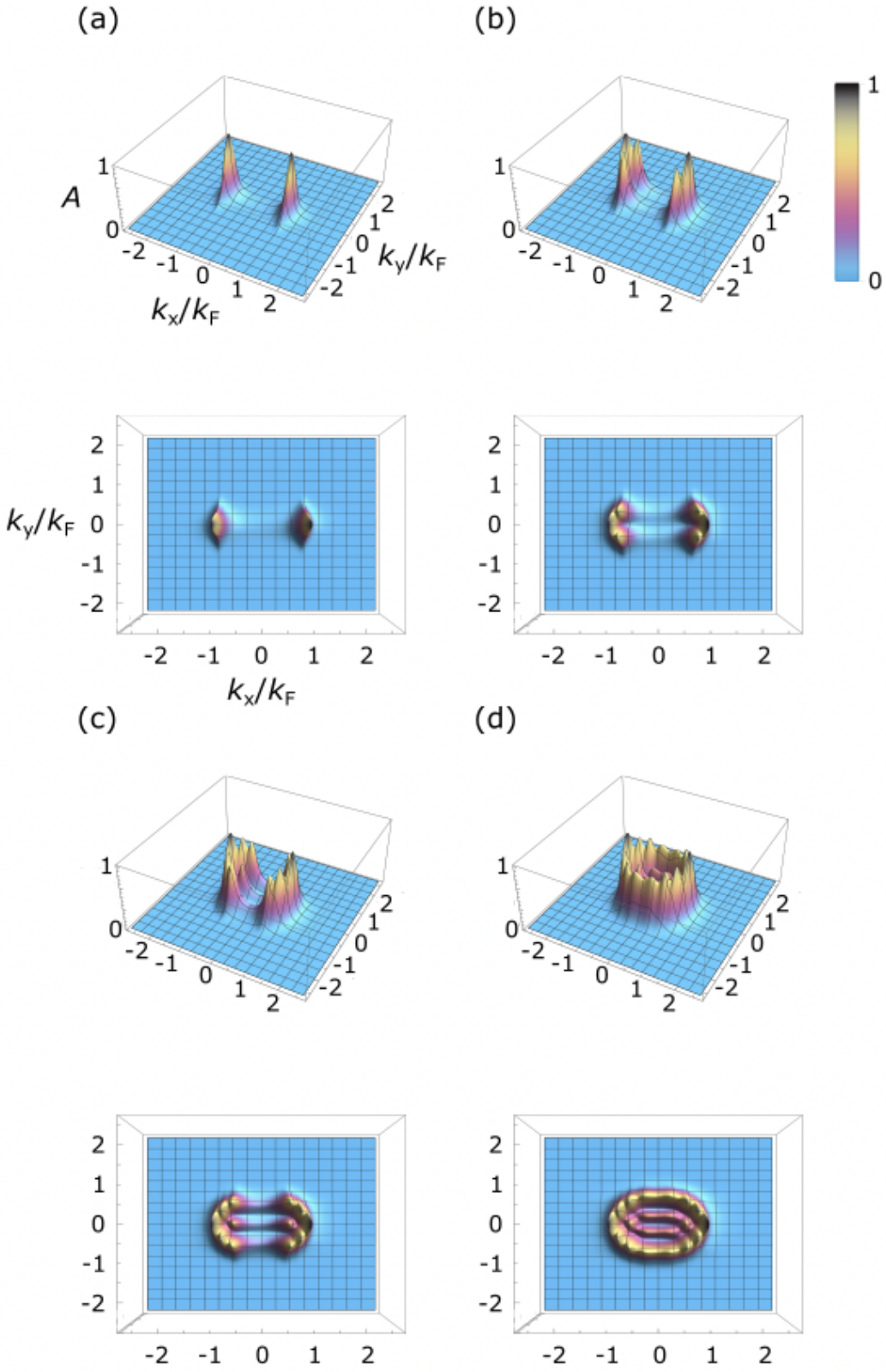

Fig. 3.2 Normalised spectral functions of a non-interacting 1D system, evaluated at $eV_{DC} = 0$, $B = 0$, for $\Gamma = 0.25$ meV and $\hbar\omega = 1.7$ meV. The number of occupied subbands is varied from one to four, see (a) to (d).

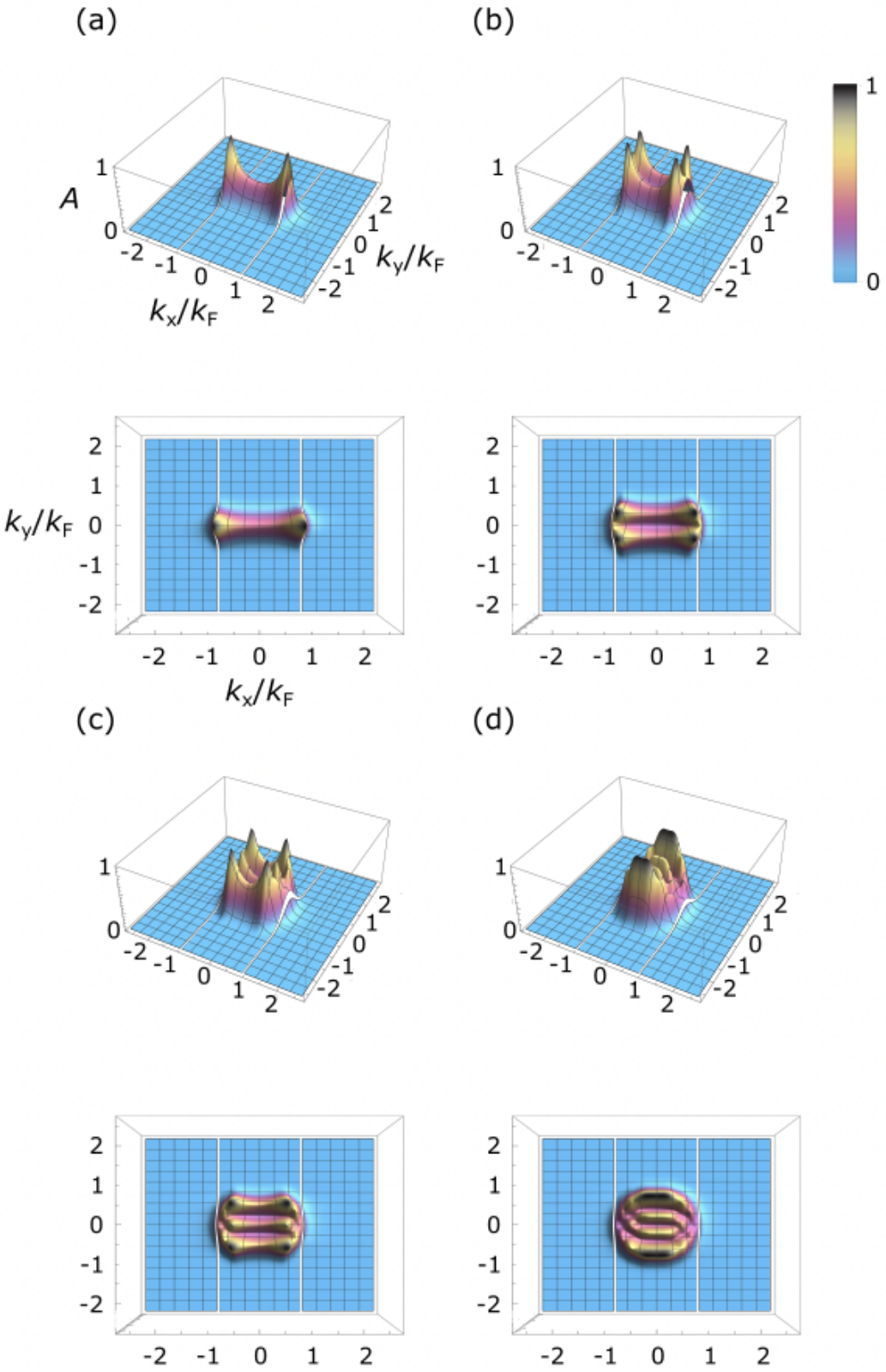

Fig. 3.3 Normalised spectral functions of an interacting 1D system according to the (linear) TLL model, evaluated at $eV_{DC} = 0$, $B = 0$, for $\Gamma = 0.25$ meV and $\hbar\omega = 1.7$ meV. Here, the white lines mark the position of the Fermi wavevector k_F. The number of occupied subbands is varied from one to four, see (a) to (d). Note how the spectral weight moves away from the spectral edge when compared to the non-interacting scenario.

pronounced the stronger the interactions in question. We will return to this point later in this section. First, however, let us introduce the energy-momentum tunnelling maps.

As shown from Figs. 3.1-3.3, the probability of there being any significant overlap, and therefore any measurable tunnelling conductance, between the spectral functions of two systems of different densities in close proximity to one another at $B = 0$, $eV = 0$, is quite small. Note that, from equation (3.14), a necessary condition for tunnelling to occur between a filled and an empty state is matching in both energy and momentum; however, no overlap necessarily means such is not possible.

In order to map the dispersion of both systems, an alternative workaround consists of measuring the non-equilibrium tunnelling current as both energy and momentum of the tunnelling electrons is being varied. Effectively, this is equivalent to offsetting the spectral function of one system with respect to the other in both energy and momentum, whereby the measured conductance tracks the amount of spectral overlap.

Fig. 3.4 illustrates this scenario for two 2D systems assuming $V_{\mathrm{DC}} = 0$ (*i.e.* in momentum-space only). Here, the Fermi surface of each system in the absence of interactions is a simple Fermi circle, concentric at $B = 0$, with the difference in radius accounting for the difference in density between the two. Let us take $n_1 > n_2$, and therefore, A_1 with a larger radius than A_2. We then define B_- and B_+ as, respectively, the magnetic field strength required to offset A_2 with respect to A_1 so that both circles touch from the inside or outside. The relative offsets in k-space are

$$\Delta k_- = k_{\mathrm{F2}} - k_{\mathrm{F1}} = \frac{ed}{\hbar} B_- \qquad \Delta k_+ = k_{\mathrm{F2}} + k_{\mathrm{F1}} = \frac{ed}{\hbar} B_+ \tag{3.21}$$

which, rearranging, gives us the respective Fermi wavevectors as

$$k_{\mathrm{F},1} = \frac{ed}{2\hbar}(B_+ - B_-) \qquad k_{\mathrm{F},2} = \frac{ed}{2\hbar}(B_+ + B_-) \tag{3.22}$$

We can also repeat the above procedure but now offsetting in energy rather than just momentum. In general terms the positions where maximum overlap occurs in energy-momentum space are then given by

$$eV_{\mathrm{DC}} = \frac{\hbar^2}{2m^\star}\left[k_{\mathrm{F},1}^2 - \left(k_{\mathrm{F},2} \pm \frac{eBd}{\hbar}\right)^2\right] \tag{3.23}$$

and

$$eV_{\mathrm{DC}} = \frac{\hbar^2}{2m^\star}\left[\left(k_{\mathrm{F},1} \pm \frac{eBd}{\hbar}\right)^2 - k_{\mathrm{F},2}^2\right] \tag{3.24}$$

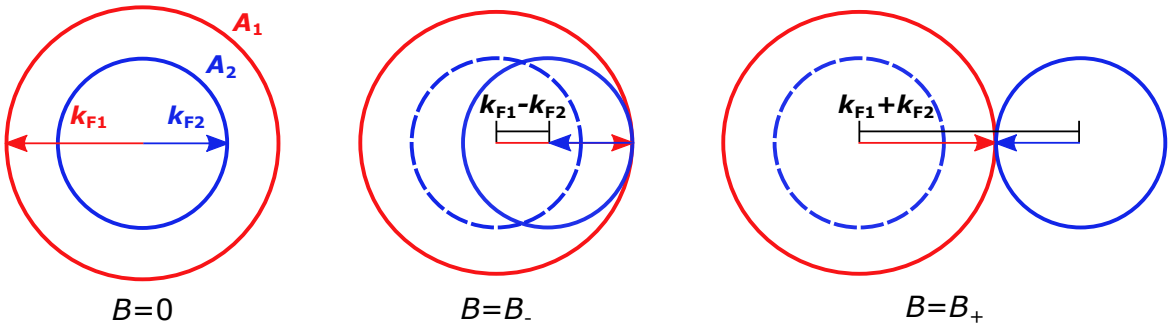

Fig. 3.4 Zero-bias field intercepts, showing the two field magnitudes, B_- and B_+, for which tunnelling resonances are obtained as one spectral function is shifted in momentum-space. The red and blue circles represent, respectively, the 2D spectral functions of the upper and lower layers. Note how $k_{F1}>k_{F2}$ given that $n_1>n_2$.

where equations (3.23) and (3.24) refer, respectively, to A_1 being probed by A_2, and *vice versa*. Note that here $m^\star$ is the effective electron mass in both systems, which we assume, for now, to be the same.

Physically speaking, the curves traced by the two equations above mark the dispersion of each system as mapped by one another. In chapters 5 and 6 we will analyse in detail tunnelling dispersion maps and show how they allow us to infer the dynamics taking place in both systems. For now, and as an example, Fig. 3.5 shows the dispersion curves when tunnelling is occurring between two 2D systems.

Before we conclude, let us just go back to the initial point discussed at the beginning of this section regarding the symmetry of $A(\mathbf{k},\omega)$. The analysis done above and, particularly, illustrated in Fig. 3.4, assumes that a certain degree of symmetry is present in the spectral function, so that k_F can be well defined. If the spectral function and, therefore, the Fermi surface, is asymmetric about E_F, k_F will naturally vary, though with an analogous construction similar to that discussed above being nevertheless possible. In both cases, however, the key prerequisite is that the boundaries of these functions are sharp (within the limits of disorder broadening Γ), so that tunnelling resonances indeed occur when they touch. While this is true for 2D-2D tunnelling measurements, where the dispersion curves are mapped using the other 2D spectral function as a probe (which, accordingly, is a symmetric function of energy), the same is no longer true in 1D, particularly as interactions are turned on. Here, when the 2D dispersion is probed by the spectral function of, for example, interacting fermions in 1D, the maximum is shifted significantly even if no Γ is included. This is because, for example, taking the spinful (linear) TLL model, $A(\mathbf{k},\omega)$ is known to be pronouncedly asymmetric in energy about E_F, having a double-peaked structure due to spin-charge separation, see Fig. 2.6.

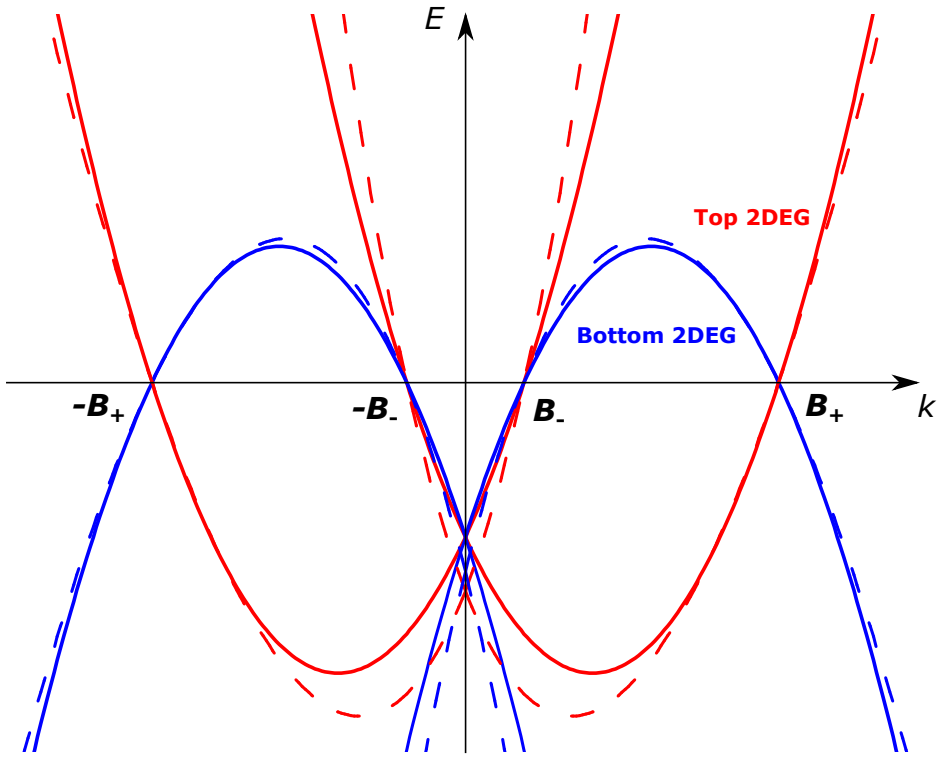

Fig. 3.5 Energy-momentum tunnelling dispersion map of two 2D systems. Here, the red and blue curves mark the positions where tunnelling resonances are expected to occur, as given by equations (3.23) and (3.24). They correspond, respectively, to the dispersion of the upper and lower layers as mapped by one another. The dashed curves account for the same dispersions once capacitance is accounted for, see equations (3.29) and (3.30).

This effect has been quantified and shown to be, at most, of the order of a few meV (typically, $\sim 0.2\,\text{meV}$, see Fig. 3E in [60]), which, therefore, in comparable to the typical energy broadening Γ present in our experiment.

3.5 Modelling of the capacitive effects

In the previous section, we discussed how offsetting the spectral function of one system with respect to another in both energy and momentum space, while also tracking the tunnelling conductance between the two, allows their respective dispersions to be mapped. Indeed, we will use this formalism later in chapter 5 when analysing the tunnelling data between an array of 1D wires and a 2D layer. Before that, however, it is important to note that our tunnelling measurement is subject to capacitive effects, not only between the two systems to and from which tunnelling is occurring (in our case, the two quantum wells), but also between these

and any existing surface gates. Therefore, equations (3.23) and (3.24) must first be modified so that capacitive coupling can be taken into account.

When tunnelling across a dielectric barrier electrons are affected by its capacitance. In our setup, for instance, owing to the finite capacitance C between each layer, a small increase or reduction of the electron density $\pm\delta n_{\mathrm{2D/1D}}$ occurs at each side of the barrier, which in turn results in small distortions to the observed dispersions (making them no longer perfectly symmetric), as we will now derive for the 1D and 2D scenarios.

Let us start by considering that a bias V_{DC} is applied across a dielectric barrier, the corresponding change in electron density then being given by $e\delta n = V_{\mathrm{DC}}C$. In our geometry, we have $e\delta n_{\mathrm{2D}} = V_{\mathrm{DC}}C/A$ for a 2D system (of area A), and $e\delta n_{\mathrm{1D}} = V_{\mathrm{DC}}C/L$ for the corresponding 1D system (of total length L). The electron densities for 1D and 2D systems are in turn given by

$$n_{\mathrm{1D}} = \frac{\mathrm{d}N}{\mathrm{d}L} = \frac{2k_{\mathrm{F,1D}}}{\pi} \tag{3.25}$$

and

$$n_{\mathrm{2D}} = \frac{\mathrm{d}N}{\mathrm{d}L} = \frac{k_{\mathrm{F,2D}}^2}{2\pi} \tag{3.26}$$

where $k_{\mathrm{F,1D}}$ and $k_{\mathrm{F,2D}}$ are, respectively, the Fermi wavevectors in the 1D system (in the absence of interactions), and the 2D system below it.

One can determine the Fermi wavevectors of each layer using the zero-bias crossing points, B_+ and B_-, as seen in Fig. 3.4 for the 2D-2D tunnelling scenario. For the 1D-2D configuration, on the other hand, $k_{\mathrm{F1}} \equiv k_{\mathrm{F,1D}}$ while $k_{\mathrm{F2}} \equiv k_{\mathrm{F,2D}}$, with $k_{\mathrm{F,1}} < k_{\mathrm{F,2}}$ as, indeed, the 1D wire array, once defined (electrostatically) by the wire-gate, does have a Fermi wavevector smaller than that of the 2D system below it.

Putting everything together, we get

$$\delta n_{\mathrm{1D}} = n_{\mathrm{1D}}(V_{\mathrm{DC}}) - n_{\mathrm{1D}}(0) = \frac{\eta_i C V_{\mathrm{DC}}}{eL} = \frac{2}{\pi}(k_{\mathrm{F,1D}}(V_{\mathrm{DC}}) - k_{\mathrm{F,1D}}(0)) \tag{3.27}$$

and

$$\delta n_{\mathrm{2D}} = n_{\mathrm{2D}}(V_{\mathrm{DC}}) - n_{\mathrm{2D}}(0) = \frac{\eta_i C V_{\mathrm{DC}}}{eA} = \frac{1}{2\pi}(k_{\mathrm{F,2D}}^2(V_{\mathrm{DC}}) - k_{\mathrm{F,2D}}^2(0)) \tag{3.28}$$

which, when reorganised, gives the new Fermi wavevectors as a function of inter-layer bias as

$$k_{\mathrm{F,1D}}(V_{\mathrm{DC}}) = k_{\mathrm{F,1D}}(0) + \frac{\pi\eta_i C V_{\mathrm{DC}}}{2eL} \tag{3.29}$$

and

$$k_{\mathrm{F,2D}}(V_{\mathrm{DC}}) = \sqrt{k_{\mathrm{F,2D}}^2(0) + \frac{2\pi\eta_i C V_{\mathrm{DC}}}{eA}}. \tag{3.30}$$

Here, $\eta_i = \pm 1$, with $i = 1, 2$ corresponding to the upper and lower layers, respectively. This is a sign factor associated with the polarity of the applied inter-layer bias, which results in the electron density being increased in one layer and decreased in the other. In our experiment, $\eta_1 = -1$ and $\eta_2 = 1$, since for $V_{\mathrm{DC}} > 0$ the upper well is more positive than the lower well, see dashed curves in Fig. 3.5.

As we will see in section 4.1 regarding device design, the lower well is always 2D in nature, which means that $k_{\mathrm{F2}} = k_{\mathrm{F,2D}}(V_{\mathrm{DC}})$ with $\eta_2 = 1$. The upper well, on the other hand, can behave as either 2D, in the 'parasitic' injection region, or 1D, in the wires. For the latter, we have $k_{\mathrm{F1}} = k_{\mathrm{F,1D}}(V_{\mathrm{DC}})$ with $\eta_1 = -1$. For the former, note that the measured upper-well density is roughly double that in the lower well (as we will show in chapter 5, see Fig. 5.5), so $k_{\mathrm{F1}} \equiv k_{\mathrm{F,2D}}^{\mathrm{p,UW}}$ and $k_{\mathrm{F2}} \equiv k_{\mathrm{F,2D}}^{\mathrm{p,LW}}$.

Finally, note that equation (3.30) also reduces to equation (3.29) when expanded in the low-capacitance limit,

$$k'_{\mathrm{F,2D}} = k_{\mathrm{F,2D}} \left(1 + \frac{2\pi\eta_i C V_{\mathrm{DC}}}{e A k_{\mathrm{F,2D}}^2} \right)^{1/2} \tag{3.31}$$

$$\approx k_{\mathrm{F,2D}} + \frac{\pi\eta_i C V_{\mathrm{DC}}}{e A k_{\mathrm{F,2D}}}. \tag{3.32}$$

This means that, in the 1D wire region the capacitance correction can nevertheless be treated as for a 2D system, provided the capacitances are transformed as $C/L = C/A \times 2/k_{\mathrm{F,1D}}$. This result allows us to estimate the width of the wires as

$$C/L = w \times C/A \tag{3.33}$$

where both layers are assumed to be charge-neutral. For our wires, once defined, w can vary between $20 - 50$ nm, putting them strong-confinement limit.

3.5.1 Geometric and Quantum Capacitances

Having derived equations (3.29) and (3.30) for the modified Fermi wavevectors of, respectively, 1D and 2D systems once capacitive effects are taken into account, let us now discuss how such capacitive couplings may arise in the first place.

In a classical Coulomb system, the capacitance $C = \mathrm{d}Q/V_{\mathrm{DC}}$, where Q is the charge on the conductor, is a purely geometrical quantity. For example, it is well-known that for a parallel-plate capacitor $C = \varepsilon\varepsilon_0 A/d$, A being the surface area of the plates, d their separation, and ε the relative permitivity of the dielectric material in between [56]. In systems with a low density of states, however, such as the 2DEGs in our experiment, this result does not usually

apply, as here, unlike in a perfect metal plate, the density of states is no longer infinite. This results in a 2DEG being, in general, unable to perfectly screen the electric field generated by the surface gates, meaning that the parallel-plate approximation is usually no longer valid.

This effect can nevertheless be accounted for by considering the effects of band-filling/band-emptying as the gate voltages change the density of states in each system. Following from the initial proposal made in [86] regarding capacitive coupling between a surface gate and a nearby 2DEG, we start by modelling our system as two capacitors connected in series,

$$\frac{1}{C} = \frac{1}{C_{\mathrm{G}}} + \frac{1}{C_{\mathrm{Q}}} \tag{3.34}$$

where C_{G} is the usual geometric capacitance, and $C_{\mathrm{Q}} = e^2 \mathrm{d}n_{2\mathrm{D}}/\mathrm{d}E_{\mathrm{F}}A$ the new quantum capacitance per unit area (or alternatively, $C_{\mathrm{Q}} = e^2 \mathrm{d}n_{1\mathrm{D}}/\mathrm{d}E_{\mathrm{F}}L$, as appropriate), with $E_{\mathrm{F}} = \hbar^2 k_{\mathrm{F}}^2/2m^\star$ being the Fermi energy. The latter is measured relative to the bottom of the band and therefore varies as the occupation changes. Depending on dimensionality, and using equations (3.25), (3.26), and (3.33), the ratio of the two capacitances is then given by

$$\frac{C_{\mathrm{G}}}{C_{\mathrm{Q}}} = \begin{cases} \dfrac{\hbar^2 \pi^2 \varepsilon \varepsilon_0 w}{4m^* e^2 D} n_{1\mathrm{D}} & \text{for gate-wire system,} \\ \dfrac{\hbar^2 \pi \varepsilon \varepsilon_0}{m^* e^2 D} & \text{for gate-2DEG system,} \end{cases} \tag{3.35}$$

where D is the distance from the wells to the surface, w is the width of the wire, and m^* is the electron effective mass in GaAs. Here, we assumed $n_{1\mathrm{D}} = n_{2\mathrm{D}} \cdot w$, with $n_{1\mathrm{D}}$ and $n_{2\mathrm{D}}$ as defined in equations (3.25) and (3.26), respectively. Taking $w = 50\,\mathrm{nm}$, $D = 85\,\mathrm{nm}$, $m^* = 0.067 m_{\mathrm{e}}$, $\varepsilon = 12$, and $n_{1\mathrm{D}} = 33\,\mu\mathrm{m}^{-1}$ as representative values, we get $C_{\mathrm{G}}/C_{\mathrm{Q}} = 0.036$ and $C_{\mathrm{G}}/C_{\mathrm{Q}} = 0.028$ for 1D and 2D systems, respectively. In both cases $C_{\mathrm{Q}} \gg C_{\mathrm{G}}$, and so the geometric contribution is expected to largely dominate in any capacitance measurement. In the next section, we will use the COMSOL Multiphysics software package, which takes into account only the geometrical contributions, to simulate these effects.

3.5.2 Numerical simulations

Our system consists of a GaAs/AlGaAs double quantum-well heterostructure with translational invariance along the x- and y-directions. For reference, the wells are, roughly, 70 and 100 nm below the surface. A set of surface gates is used in defining an array of quantum wires in the upper well only. There is then a capacitve coupling between the wells, and between each well and the surface gates.

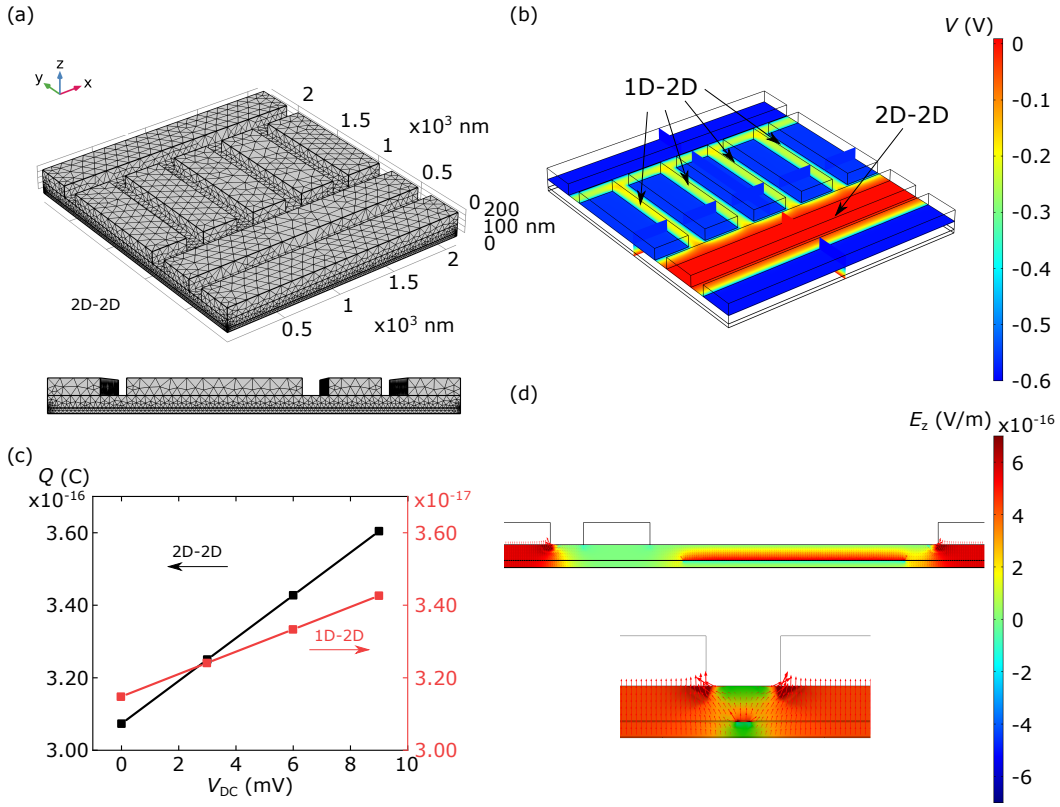

Fig. 3.6 COMSOL numerical simulations. (a) Mesh grid utilised in our calculation. Note how the size of each node decreases as one approaches the quantum wells. (b) Potential distribution. Here, we assumed $V_{BG} = -0.6$ V, $V_{WG} = -0.57$ V, and V_{PG}=0 as boundary conditions (see chapter 4 for details on device design and operation). There are two regions relevant for our tunnelling measurements, marked as '2D-2D' and '1D-2D'. (c) Simulation results. From here, the capacitance (per unit area) was extracted, see text. (d) Electrical field profile [z-component (colourbar) and total field (arrows)] along (top) and across (bottom) the wires.

Using the COMSOL Multiphysics 5.5 software package [1] to simulate our device electrostatically (not self-consistently), we computed the potential distribution (see Fig. 3.6b) and the electrical field (see Fig. 3.6d) in the dielectrics, given the known charge distributions in each well, one of which had wires defined by the surface gates (see chapter 4 for details on device design and geometry). Specifically, we took $U(\mathbf{r})$ in the Poisson equation as the potential induced by the gates, and solved by equating to either $U(\mathbf{r}) = V_{SG}$ at the gates, or Neumann boundary conditions otherwise. In our simulation, we also accounted for the finite width of the 2D electron systems, though this made little difference to the results. Poisson's equation was then solved using a finite-element grid, the number of nodes chosen so that the computation was free from finite-size effects (see Fig. 3.6a). Finally, in our model, the effect

of ionised donor layers on both sides of the wells was ignored, since these form a static layer of charge which is not affected by changes to the gate voltages. The results are shown in Fig. 3.6c for both 2D-2D and 1D-2D tunnelling scenarios. The capacitance values (per unit area), $C = Q/V_{\mathrm{DC}}A$, obtained were $C_{\mathrm{G}}/A = 0.0047\,\mathrm{Fm}^{-2}$ for the 2D injection region and $C_{\mathrm{G}}/A = 0.0103\,\mathrm{Fm}^{-2}$ for the 1D wire region in the single-subband regime (assuming a width $w \sim 30\,\mathrm{nm}$ for a characteristic density of $\sim 33\,\mu\mathrm{m}^{-1}$). In chapter 5 we will see that, while the first result does indeed match the experimental data quite well, the second is about 4 times larger than the extracted value, implying that $C_{\mathrm{Q}}/A = 0.0035\,\mathrm{Fm}^{-2}$. This is not surprising, as screening is less efficient in 1D than 2D geometries, meaning that quantum capacitance contributions, not accounted for in the COMSOL simulation, should become more prevalent.

3.6 Summary

Tunnelling spectroscopy has proven itself over the past years as a powerful technique capable of mapping the dynamics of many-body systems across the whole spectrum of momentum and energy. This has been shown to be extremely important, for not only has it allowed the confirmation of many of the predictions made by the original, linear TLL model, but also, more recently, it has provided much-needed evidence in support of its nonlinear counterparts. Improvements in wafer quality, nanofabrication and tunnelling resolution have also recently allowed for a full mapping to occur at high energies, with early results suggesting signs of physics beyond the Tomonaga-Luttinger paradigm. We anticipate that, provided that two conductors lie close together with a well-controlled tunnel barrier in between, this technique can be applied to study different classes of materials, such as topological insulators, superconductors, and itinerant magnets, therefore offering itself as a powerful tool for probing novel emerging many-body physics in new systems. Note that, because it is not a surface probe, it can in principle be carried out whilst varying both temperature, chemical composition, hydrostatic pressure, and/or uniaxial stress.

Chapter 4

Device design, fabrication, and measurement

Having now introduced the main framework behind magnetotunnelling spectroscopy, our aim is to use it in mapping the dynamics of a one-dimensional strongly-correlated system which, as argued in chapter 2, is expected to behave in a pronouncedly different way from a Fermi liquid. In order to do so, we use a semiconductor double-quantum-well heterostructure to create a vertical tunnelling spectrometer device where tunnelling to and from a (quasi-)1D array to a 2D layer (*i.e.*, the spectrometer) can be measured. We start this chapter by discussing the design considerations as well as the principle of operation behind this device (section 4.1). We then give an overview of both the semiconductor materials utilised (section 4.2), as well as the fabrication techniques employed (section 4.3). For details on wafer assessment and step-by-step fabrication protocols, see Appendix A and B, respectively. A particular unique feature of our devices is the presence of microscopic air-bridge interconnections between the surface gates. Since nanofabrication usually takes place in two rather than three dimensions, we discuss in detail how these structures, suspended about 100 nm from the surface, can be fabricated with high yield. We conclude by discussing how the measurement was performed electronically, as well as the cryogenic systems utilised (section 4.4).

The fabrication protocol for producing air-bridge structures has been reported in [58].

4.1 Design of a vertical tunnelling spectrometer

All experimental work presented in this thesis was obtained using a series of vertical spectrometer devices embedded into a semiconductor heterostructure. This consisted of two

two-dimensional electron gases (2DEGs) in close proximity to one another, separated by a barrier, so that electrons could tunnel back and forth between the two systems. As we saw in chapter 3, tunnelling spectroscopy can then be used in tracking the shape of the respective spectral functions, as both energy and momentum of the tunnelling electrons are varied.

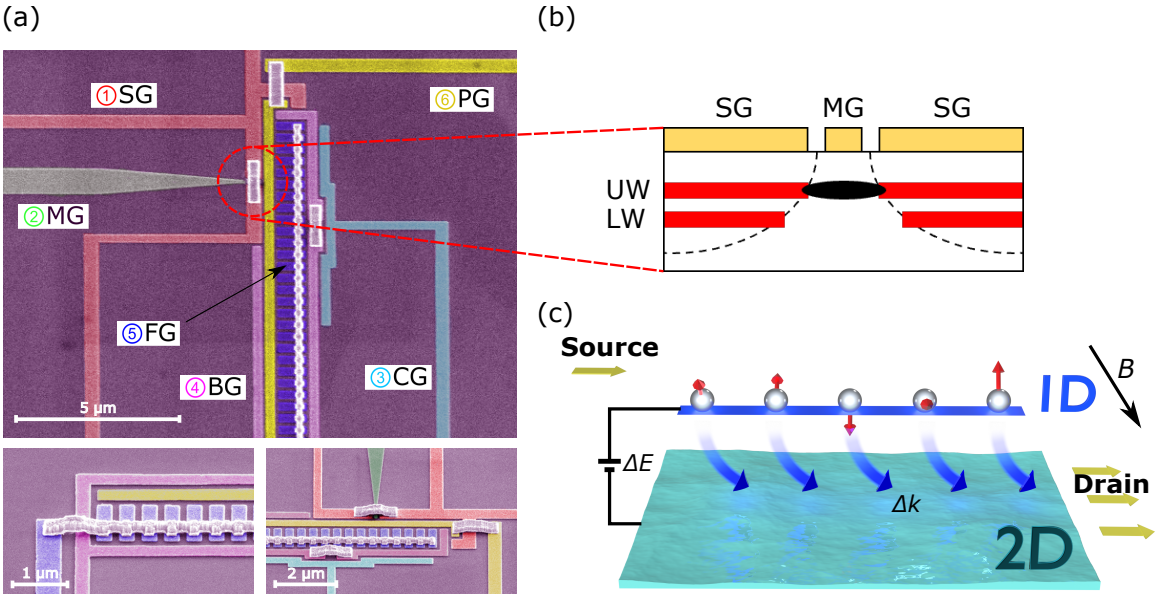

Fig. 4.1 A vertical tunnelling spectrometer device. (a) Scanning electron microscopy (SEM) images of a tunnelling device, showing the various surface gates used in setting up the experimental conditions. See text and section 5.1 for details on gate operation. The white-shaded region corresponds to air-bridge interconnections, see section 4.3.4 for further details. (b) Split-gate/mid-gate architecture, used to selectively inject current in the top well only. (c) Schematic representation of tunnelling between the 1D array (only one wire shown for simplicity) and the 2D spectrometer. We measure momentum-resolved tunnelling to and from these two systems, and map the elementary excitations in each by measuring the tunnelling conductance while varying both energy $\Delta E \propto V_{\mathrm{DC}}$ and momentum $\Delta k \propto B$. Electrons flow from the source into the wire and tunnel between the layers in order to reach the drain.

Fig. 4.1a shows some scanning electron microscopy (SEM) images of a 1 μm tunnelling device. It consists of a total of 6 electron-beam-defined surface gates, used in setting up both the tunnelling conditions as well as defining the experimental 1D system. In order to observe resonant tunnelling, we start by establishing independent electrical contact to each 2DEG. Note that, since the quantum wells are just $\sim$ 14 nm apart (see section 4.2 for material details), this has to be done using selective surface-gate depletion techniques, as the wells are too close to one another for individual ohmic contacts to be feasible. Our method also avoids the use of back gates. We use a split gate (SG)/mid-gate (MG) architecture in order to inject electrical current into the top well only (see Fig. 4.1b), while simultaneously using a

barrier gate (BG) on the other side to deplete just the top well. Under this configuration, the source ohmic is then only connected to the top 2DEG, and the drain ohmic only to the bottom 2DEG, meaning that any current measured between the two cannot arise from transport but rather has to be due to tunnelling between the two layers, see Fig. 4.1c and Fig. 4.2a.

We use a set of wire-gates (WG), interconnected via air-bridges, in order to squeeze the top 2DEG only into forming an array of 1D channels. As argued in section 3.5, and as we will later show in chapter 5 once we determine the density range for the 1D system, capacitive measurements put the width of our gated wires at around $20-50\,\text{nm}$, depending on the V_{WG} applied, and as such comparable with other semiconductor quantum-wire structures *e.g.*, CEO-wires. Use of an array averages out impurities, length resonances, and charging effects, as well as increasing the overall signal-to-noise ratio in our experiment. Here, most of the devices fabricated consisted of ~ 400 1D wires in single-column arrangements. A natural question that arises then is how do we ensure that the 1D wire array is indeed uniform and that it is conducting as a whole. We will discuss this issue again in chapter 5 when analysing the tunnelling data. For now, let us simply highlight that use of air-bridges is crucial in ensuring that short-wire devices (*i.e.*, $< 5\,\mu$m in length) remain uniform across the entirety of the 1D channel. For future reference, we will refer to the tunnelling signal coming from the WG region (*i.e.*, between the 1D channels and the bottom 2DEG) as '1D-2D tunnelling signal'.

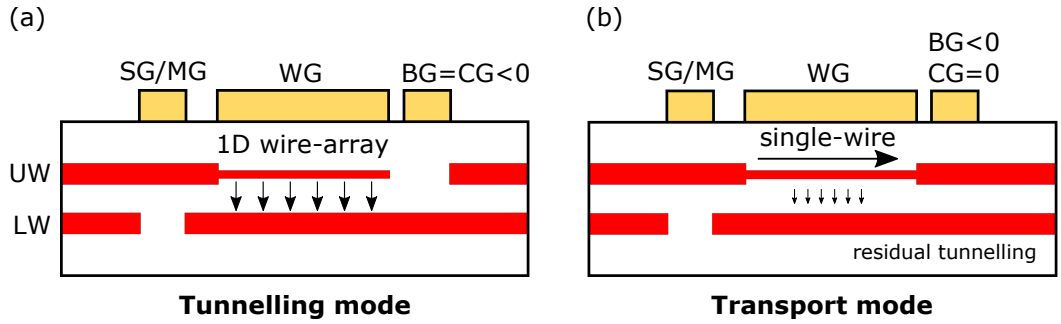

Fig. 4.2 Device operation modes. (a) Tunnelling mode. We measure tunnelling to and from a 1D wire-array to a 2DEG by establishing independent ohmic contact to each quantum well. This is achieved by selectively biasing both split-/mid-gate and barrier gates so that source and drain are only connected to the top and bottom wells, respectively. (b) Transport mode. Use of a cut-off gate allows us to locally open a gap in the barrier-gate potential. This enables transport to be measured in the top well along one wire only. Note that while tunnelling to the bottom well still occurs, it contributes to less than 1% of the total signal.

Another design consideration has to do with how electrons are injected into the wires. Note that, as seen in Fig. 4.1a, current flows from the SG/MG point into the 1D channels via a region running parallel to the length of array. This region is wide enough ($0.45-0.6\,\mu$m)

that the electron gas is not significantly confined here, and as such can be treated as being 2D. Nevertheless, since current does have to flow through it in order to reach each wire, electrons will also be able to tunnel from here into the bottom 2DEG. We collectively refer to this region of the device as 'parasitic', for it will account for a constant background of 2D-2D tunnelling signal when mapping the wires. Accordingly, the gate running over it is called the 'parasitic' gate (PG), and while it does not allow us to eliminate the additional, undesirable 2D-2D background, it can be used to slightly modulate the electron density of the 2DEG underneath it. This allows us to shift all background features in k-space, therefore readily distinguishing them from those coming from the 1D array. Indeed, as we will see later in chapter 7, use of a PG is crucial in establishing that 'replica' features are coming from the 1D channels, instead of some form of background artifact. Note also that, when the bias on WG is sufficiently negative, the wires will be pinched off and therefore unable to conduct. Under these circumstances, the only region under which current can flow is exactly that covered by PG. We will see in chapter 5 how this can be used in separately mapping the 2D-2D background signal, which can then be used to isolate the 1D-2D signal of interest.

A final gate also present in some of our devices is the 'cut-off' gate (CG). For most of this work, this gate will be biased together with BG, fulfilling the same role of depleting the top layer so that current is forced to tunnel in order to reach the drain. However, when set to zero, CG allows us to locally open a gap in the BG, meaning that current can now flow from source to drain along the top well only, without having to tunnel (see Fig. 4.2b). For reference, since the transport resistance is typically of the order of kΩ while the tunnelling resistance ∼MΩ, the latter will be largely negligible with respect to the first. Using CG therefore, we can measure the transport properties of a single wire rather than tunnelling in the entire array.

4.2 Wafer materials

As stated in section 4.1, we use a semiconductor double-quantum-well heterostructure, grown via molecular-beam epitaxy (MBE), in order to fabricate our vertical spectrometer. In total, two different wafers were used across all devices present in this work, see Appendix A for details on structure and characterisation results. In summary, each wafer comprised of two identical 18 nm GaAs quantum wells separated by a 14 nm $Al_{0.165}Ga_{0.835}As$ superlattice tunnelling barrier [10 pairs of $Al_{0.33}Ga_{0.67}As$ and GaAs monolayers], and with 20 nm and 40 nm $Al_{0.33}Ga_{0.67}As$ spacer layers above and below the wells, respectively. These were followed in both cases by 40 nm Si-doped layers of $Al_{0.33}Ga_{0.67}As$ (donor concentration $1\times10^{24}\,m^{-3}$). Wafer 1, however, differed from Wafer 2 by having a 100×2.5 nm/2.5 nm

GaAs/AlGaAs superlattice below the 350 nm AlGaAs under the lower quantum well. The distance from the top of the upper well to the surface was ∼70 nm, including a GaAs cap layer to prevent oxidation. The composition of both wafers is shown in Table A.1. Fig. 4.3 shows the profile of the conduction band.

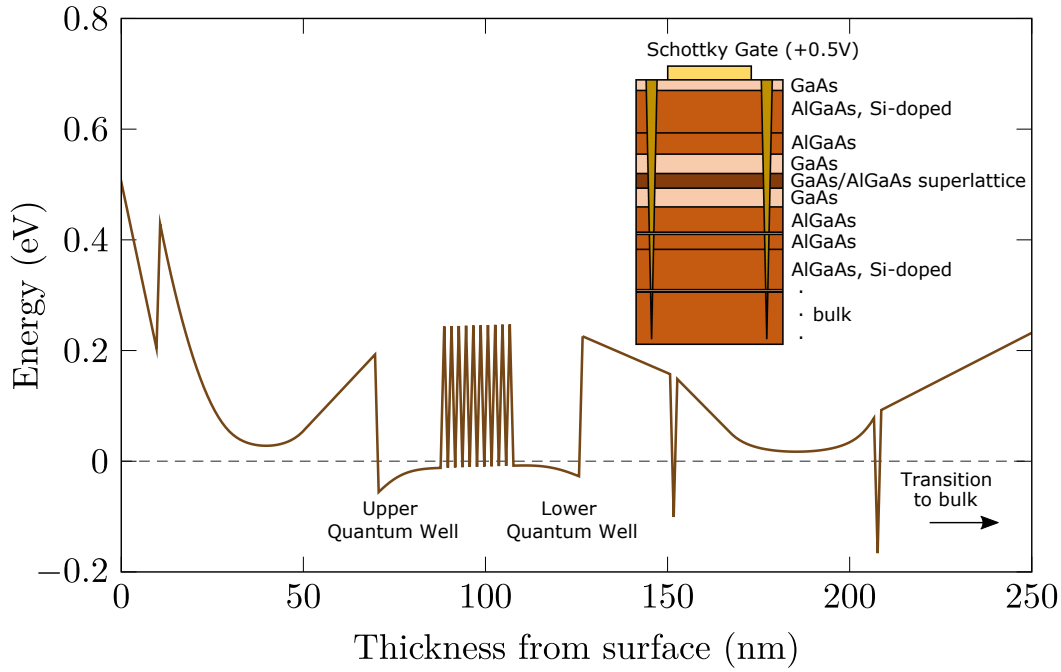

Fig. 4.3 Conduction-band structure of the semiconductor heterostructure used. Note than the top and bottom wells are roughly 70 and 100 nm below the surface. The calculation was run assuming a +0.5 eV Schottky barrier at the surface as well as fully ionised donors [adapted from [57]]. Inset: side profile of the GaAs/AlGaAs heterostructure used. See Table A.1 for details.

Note that, in order for this type of device to work, a crucial aspect of the design is appropriate engineering of the (superlattice) tunnelling barrier. This is because, on one hand, tunnelling spectroscopy requires that the barrier is thin enough so that a measurable signal can be obtained. Indeed, it is well-established that the tunnelling probability typically decays exponentially with barrier thickness. On the other hand, and as derived in section 3.3, the boost in momentum of the tunnelling electrons when subject to an in-plane field is $\Delta k = eBd/\hbar$. Depending on the size in momentum of the system which we wish to map (*i.e.*, its spectral function $A(k,\omega)$, characterised by the Fermi wavevector k_{F}), one is then forced to go to either higher magnetic fields or, instead, use thicker barriers. By using a superlattice we are able to find a compromise between these two competing conditions, simultaneously increasing the physical separation between the two quantum wells, hence minimising screening/inter-layer interactions, while also having a potential barrier low

enough so that tunnelling signal can nevertheless still be detectable. This also ensures that the maximum available momentum boost is increased and that both systems are kept separate from one another.

Before starting device fabrication, transport characteristics, such as carrier density and mobility, were also assessed in order to ensure good material quality. We measured 4-terminal quantum-Hall and Shubnikov-de Haas effects using standard Hall-bar geometries, see Appendix A for details. The electron concentrations obtained were of 3 (2.2)$\times 10^{15}$ m^{-2} with mobilities of 120 (165) m^{2}V^{-1}s^{-1} for the top (bottom) wells for Wafer 1, and 2.85 (1.54)$\times 10^{15}$ m^{-2} and 191 (55) m^{2}V^{-1}s^{-1} for Wafer 2, as measured at 1.4 K.

4.3 Nanofabrication

A significant challenge when fabricating nanodevices, such as the ones discussed here, is that they all have components whose dimensions are significantly smaller than particles of airborne contamination, often present in a standard laboratory environment. If many such particles were to be present during fabrication, then the yield of the entire process would be severely reduced. This can, however, be easily solved by fabricating in an environment where concentration of contaminants is reduced to a minimum. Such controlled environment is called a cleanroom.

The first three steps of fabrication, specifically development of the mesa, ohmics, and optical gates, were all carried out using photolithography. This is a standard microfabrication process which allows a pattern to be transferred from a pre-manufactured photomask, usually a piece of quartz glass coated with a layer of chromium, onto a photo-sensitive coating called a photoresist. A series of chemical treatments then allows for either the exposed or unexposed regions to be removed, after which metal can be deposited, thus imprinting the desired pattern onto the substrate. A photoresist is said to be positive if the region exposed to light becomes soluble, and negative if the opposite. Because of its optical nature, the dimensions of the smallest features that can be patterned using photolithography are limited by the diffraction limit. Current state-of-the-art tools, using deep ultraviolet light, allow for minimum feature sizes of about 50 nm. In practice, however, manual mask aligners are much more commonly used and here, user errors can play a big role. Consequently, the lower limit of pattern dimensions is more realistically placed at about $\sim 1\,\mu$m. Below we outline the main steps involved in the fabrication of our devices. For a detailed step-by-step protocol, see Appendix B.

4.3.1 Mesa

A mesa is a type of structure commonly used in microelectronics where part of the substrate is etched back, thus allowing a device to be isolated in the non-etched region. This is usually done so as to reduce possible alternative current paths, as well as potential parasitic capacitances arising from connections to the external world.

The surface structure of all devices present in this work was fabricated on a $200 \times 1000\,\mu$m long Hall bar, aligned so that the long edge would be parallel to the major flat *i.e.*, the high-mobility direction of the wafer. Prior to all photolithography, all samples were cleaned in acetone and IPA (isopropyl alcohol) while under ultrasonic agitation, before being dried in nitrogen and baked on a 115°C hotplate to ensure all solvents dried out. They were then coated with Shipley Microposit S1813 positive photoresist, spun so as to achieve an approximate thickness of ~ 150 nm, after which the Hall bar pattern was exposed, see Fig. 4.4a. The chips were then developed using Microposit MF-319 developer (Fig. 4.4b), with the exposed resist being removed, while the unexposed regions remained to protect the mesa.

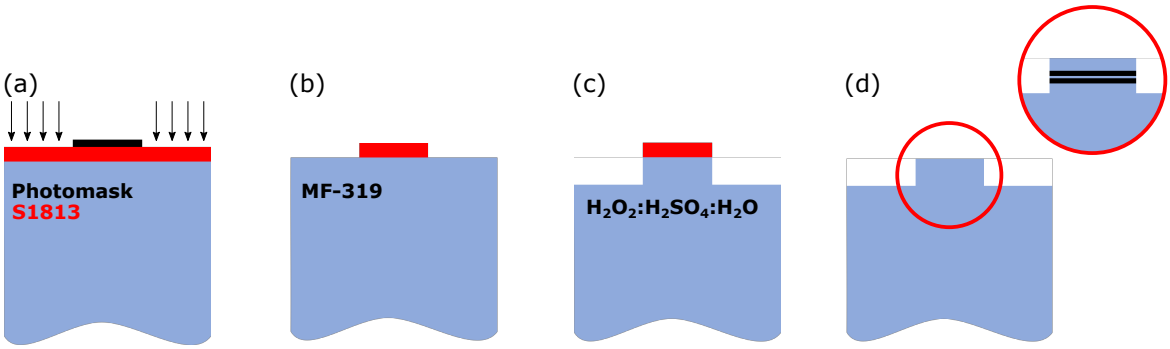

Fig. 4.4 Fabrication of the mesa using photolithography. (a) Exposure of the pattern. (b) Development of the (exposed) photoresist. (c) Etching of the exposed region. (d) Removal of the left-over resist. Note that both quantum wells have been etched away in every region except the mesa.

We used a wet-etch process in defining the mesa. Here, the surface covered by the (undeveloped) photoresist was protected from the chemicals, while the exposed regions were dissolved away. There are several choices of etchant available for use in semiconductor materials, the differences usually being etching speed (which controls the precision of the etching depth) and, most importantly, etching profile (under-cut, over-cut, vertical, etc). Because both of our quantum wells are quite deep below the surface, we aimed for a shallow, over-cut profile in order to avoid possible discontinuities over the mesa edges. The etchant used consisted of a 1:8:1000 H_2O_2:H_2SO_4:H_2O solution, see Fig. 4.4c. Since we wanted both 2DEGs to remain isolated in the mesa, and since the lower quantum well is approximately

100 nm below the surface, we aimed at etching between 150-170 nm. The etch rate was determined using an iteration of DekTak surface profile measurements. For the present volume ratio, the total etch time at room temperature (21°C) was usually 5-6 min. Once etching was concluded, the sample was again cleaned in acetone and IPA to remove any left-over resist, see Fig. 4.4d.

4.3.2 Ohmic contacts

In order for current to be injected into our devices, electrical contact to both 2DEGs must be established. We achieved this by annealing an alloy of AuGeNi (gold-germanium-nickel) into the crystal. This process is well established in the literature and allows for low-resistivity contacts to be obtained at low temperatures. Because the metal-semiconductor junction formed has a linear current-voltage response, these are commonly known as ohmic contacts.

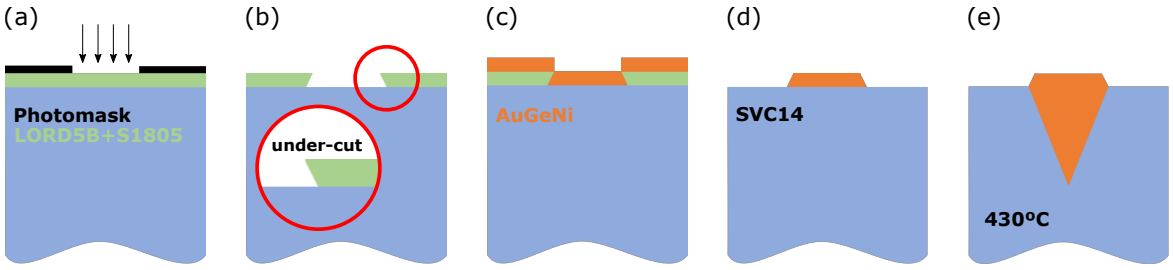

Fig. 4.5 Fabrication of the ohmic contacts. (a) Exposure of the pattern onto a LOR5B+S1805 resist stack. (b) Development of the photoresist. Note that the choice of resists was made so to ensure an under-cut profile. (c) Evaporation of the AuGeNi alloy. (d) Lift-off using positive resist remover SVC14. (e) Rapid thermal annealing of the evaporated alloy. This is done so that the metal can diffuse into the sample, therefore establishing contact to both wells.

The first half of the process used to fabricate the contacts was relatively similar to that described in section 4.3.1. We patterned a total of four contacts so that current could be injected both along and across the mesa. For the purposes of this work, however, source and drain were normally chosen as the two contacts at the end of the mesa, meaning that injected current flow along the major flat. We started by spinning two layers of photoresist onto the sample, MicroChem LOR5B followed by Microposit S1805, before exposing the pattern (Fig. 4.5a). These two resists differ from one another in that LOR5B has a higher sensitivity to UV radiation than S1805, resulting in an under-cut profile when developed, see Fig. 4.5b. This was crucial for ensuring good metal lift-off. After development, the samples were plasma etched in order to remove any leftover resist, in a process known as descum, followed by an

HCl dip (1:9 HCl:H_2O), before being placed in a high-vacuum thermal evaporator, where approximately 150-200 nm of AuGeNi alloy was deposited, see Fig. 4.5c.

Following evaporation, the chips were then immersed in positive resist remover SVC14 in order to separate the deposited metal from the photoresist (Fig. 4.5d). Only the metal in direct contact with the substrate (*i.e.*, evaporated onto the exposed regions) remained. Finally, in order for the alloy to diffuse into the sample, we used a rapid-annealing oven, heating the sample quickly up to 430°C, for about 80 seconds. This ensured that the alloy diffused well into the heterostructure, establishing contact to both quantum wells, see Fig. 4.5e.

In order to check the quality of the electrical contacts obtained, we then tested these at both room and nitrogen (77 K) temperatures using a probe station, with typical values being of about $\sim$6 kΩ and <1 kΩ, respectively. Because GaAs is a photovoltaic material, these values can change significantly if exposed to light. In order to increase the thickness of the bond pads to the optical gates (discussed in section 4.3.3), ohmic metal was also deposited off the mesa in the regions where the optical pads will later be defined. Note that here both 2DEGs have already been etched away (see section 4.3.1), and therefore these should not be connected to the quantum wells. In order to check that this was indeed the case, typical resistance values between the ohmic contacts and the ohmic gate pads should be of the order of a few MΩ, with anything significantly below this usually indicating that some 2DEG remains outside the mesa and, therefore, was not successfully etched away.

The ohmic contacts fabricated typically have a (surface) contact resistance of $R_C \approx 0.8\,\Omega$ at 4 K, the highest temperature at which the devices are assessed, as reported in [15]. In this work, using high-mobility GaAs/AlGaAs samples very similar to our own, a drop in resistance to about $R_C \approx 0.2\,\Omega$ was observed when below 0.9 K, which the authors attributed to the presence of a superconductor in the AuGeNi contact. Since superconductors typically have low thermal conductivities, this result effectively limits one's ability to cool down the 2DEG to ultra-low temperature regimes (<10 mK) if using AuGeNi contacts. We highlight, however, that this result does not hinder the analysis or conclusions of the present thesis, as no measurements have been carried out below $\sim$ 300 mK.

4.3.3 Surface gates

The final step of optical lithography is the optical gates, which allow electrical contact to be established between the electron-beam-defined gates (discussed in section 4.3.4) and the external world. The fabrication process is identical to that of the ohmic contacts up to the metallisation stage (see Fig. 4.7a-d). Here, however, we instead evaporate gold (Au), thus forming a Schottky barrier at the metal-semiconductor interface. In order to improve adhesion, a thin layer of titanium (Ti) is usually also evaporated first, as it adheres strongly

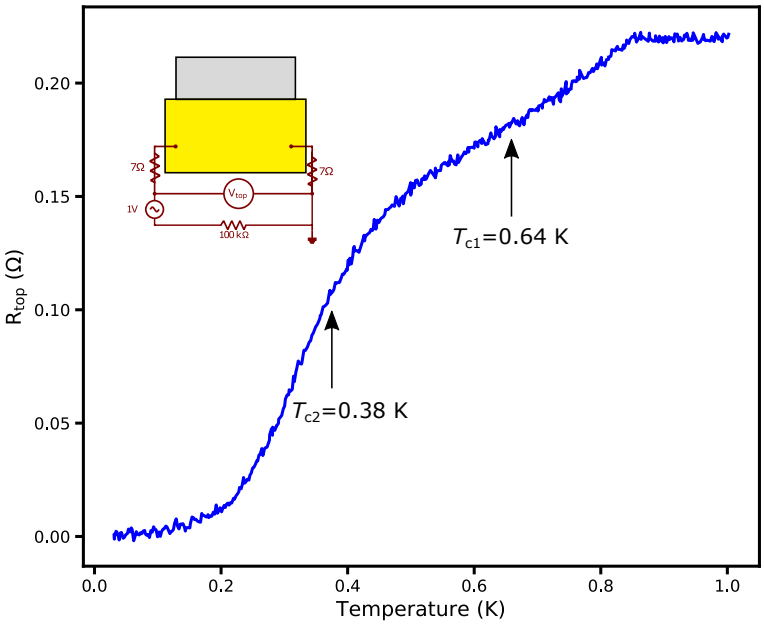

Fig. 4.6 Measurement of the surface resistance R_{top} of an Ohmic contact used in this work, courtesy of C. Beauchamp (Royal Holloway, University of London). Here, a current of $I = 0.1$ mA is driven through the contact while V_{top} is being measured. The dimensions of the ohmic contact are $210 \times 300\,\mu$m. Note that in two-terminal measurements the resistance of the leads, in this case the cryostat wiring connected to the sample, needs to be subtracted. For this setup, that value was $14\,\Omega$. The ohmic contact is then observed to undergo what seems like a broad transition into a superconducting phase, see [15] and text for discussion. Adapted from [14].

to both the Au as well as to the GaAs surface. For the devices fabricated in this work, 25 nm of Ti followed by 120-150 nm of Au was usually applied. Note that, in principle, one aims to evaporate as much gold as possible (given, of course, the limits of the thickness of the resist double-layer), to facilitate the bonding process.

4.3.4 Electron-beam lithography

As was discussed above, photolithography is limited in the size of the smallest features it can pattern by the wavelength of the radiation used. For deep UV, this usually corresponds to about $\sim 1\,\mu$m at its finest. In order to fabricate at sub-micron scales, electron-beam lithography (EBL) can then be used for patterning an electronic device. The principle of operation is identical to that of photolithography, whereas resist is spun onto a substrate after which selective exposure allows for a pattern to be imprinted. Here, however, instead of radiation (*i.e.*, photons), which are constrained by the diffraction limit, a beam of highly-energetic electrons is used instead. All EBL done in this work was carried out using a fully

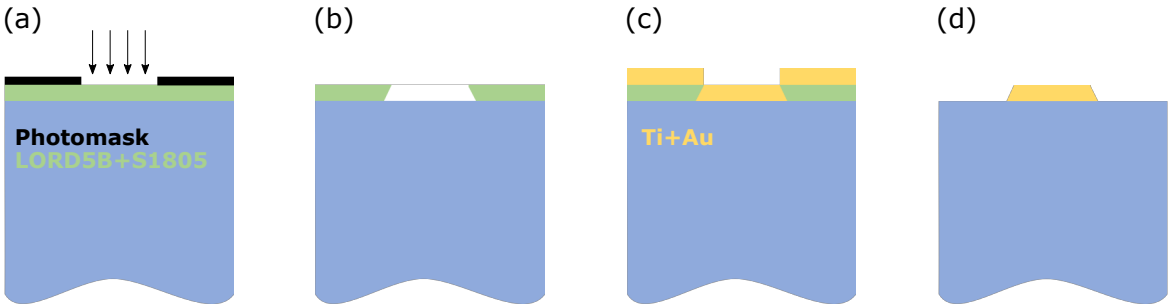

Fig. 4.7 Fabrication of the *optical* surface gates. All steps are similar to those used for the ohmics. These are (a) exposure of the pattern, (b) development of the exposed regions, (c) metal evaporation (here, Ti followed by Au), and (d) lift-off.

automated Vistec VB6 UHR EWF system operating at 100 kV with a 4 nm spot size. The best alignment precision of this system is < 15 nm. The primary sub-micron features present in our device are the tunnelling device itself which, as we saw in section 4.1, is made up of a number of surface gates used in establishing both independent electrical contact to each 2DEG as well as defining an array of 1D channels. A set of air-bridge interconnections is also used to connect the wire array in a way that ensures channel uniformity. In order to fabricate these structures, two stages of EBL were required. We will now outline each of these in detail.

First EBL stage: surface gates

All surface gates, including split-, mid-, barrier-, cut-off, 'parasitic', and wire-gates, used in setting up the tunnelling conditions and defining the 1D wire array, were patterned using EBL (see Fig. 4.1a for SEM micrographs of a 1 μm device). For reference, the mid-gate corresponds to a 0.1 μm wide gate in between two $0.1-0.2$ μm gaps (see Fig. 4.8a). The wire-gates, on the other hand, can be $1-18$ μm in length and $0.15-0.3$ μm wide, with their separation varying between $0.15-0.17$ μm (see Fig. 4.8b). Overall, these correspond to the smallest lithographic features present in these devices. Note that change of the lithographical dimensions, particularly regarding the wire-region, only slightly alters the voltage values at which the devices are operated. This has been characterised and optimised (see [60]) as to ensure that $3-4$ 1D subbands can be defined in the top well before pinch-off, while the bottom well remains unperturbed.

We started by spinning a layer of MMA(8.5)MAA copolymer (diluted 1:1 in ethyl-lactate), followed by A4 (4% solid content in anisole) PMMA with a molecular weight of 950k [diluted 2:1 to methyl isobutyl ketone (MIBK)]. The spin speeds were calibrated so as to result in a double-layer stack approximately 125 and 100 nm thick, respectively. After each

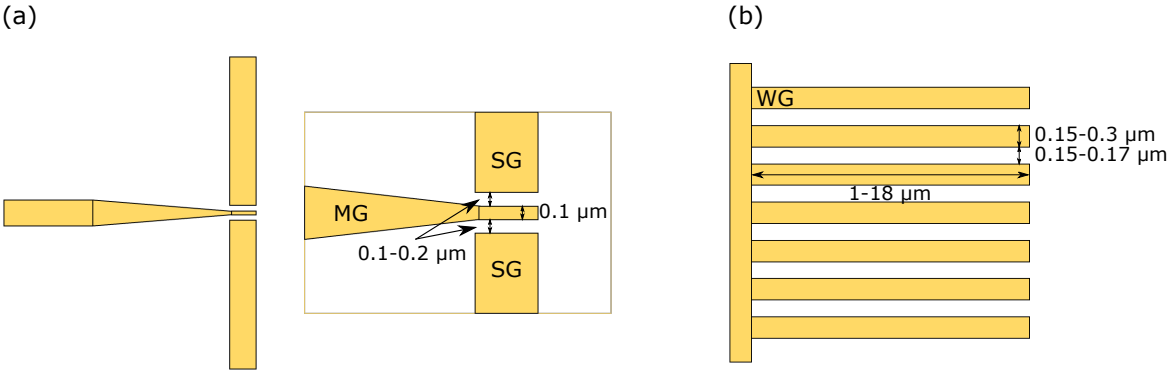

Fig. 4.8 Electron-beam-defined gates and dimensions, showing (a) split-/mid- and (b) wire-gate regions.

layer was applied and baked, the sample was exposed to a 100 kV ebeam (dose 550 μCcm^{-2}). The pattern was then developed using a H_2O:IPA (3:7 ratio) mixture at 5°C.

After development, the remaining steps were identical to those done already under normal photolithography: first, the sample was plasma etched to descum, followed by an HCl dip to remove oxide and any scum remaining on top of it; after that, it was placed in a thermal evaporator to be metallised. In order to ensure good lift-off, a standard rule of thumb when it comes to EBL patterning is to not evaporate more metal than about a third of the thickness of the base layer. In our samples, therefore, all surface gates were formed by evaporating about 5 nm of Ti, followed by 20 nm of Au. Lift-off was carried out overnight in acetone. Note that at this stage, use of an ultrasonic bath to remove any excess metal was avoided as it was found to damage many of the electron-beam-defined gates. For alignment reasons, the first EBL stage was also often done before the optical gate lithography.

Second EBL stage: air-bridges

As will be discussed in chapter 7, one of the main experimental results presented in this thesis has to do with the emergence of extra 1D 'replica' modes, in addition to the main 1D subband, in one-dimensional systems at finite length. In order to explore such regime, however, it became necessary to be able to fabricate wires at progressively shorter and shorter lengths: for reference, the work done in [60] used tunnelling devices both 37.5 μm and 17.5 μm in length, while [57] brought this value down to 10 μm; [94], on the other hand, managed to fabricate a 1 μm array, though in order to do so a multi-column geometry was required, and so 'parasitic' and fringing effects were also greatly enhanced. In contrast, the results presented in this thesis were all obtained using $1-5$ μm-long single-column wire arrays, in a way that 'parasitic' background effects could be reliably suppressed and/or subtracted.

Fabricating an array of 1D wires this short naturally then raised the question of how to ensure that the channels remained uniform along their entire length. Indeed, initial use of a backbone to connect all wire gates led to significant levels of non-uniformity being observed, as expected, since the channels were being made significantly narrower towards one end. We solved this problem by developing a novel electron-beam lithography technique for patterning air-bridges, *i.e.*, three-dimensional connections suspended above the surface. While the initial motivation for developing this method was fabrication of uniform, shorter wire arrays, air-bridge applications are vast and widespread. For instance, it is often the case that when fabricating nanoscale devices, one ends up having to overlap different layers of conductor, a way of doing so being via depositing insulating material in between layers to prevent shorts. This is both complicated as well as detrimental to device operation, as both insulator and metal need to be separately patterned. On the other hand, by using air-bridges, one would have access to a straightforward and reliable process for connecting isolated control gates and/or reducing the number of external leads by wiring two or more gates in parallel, making it therefore a more desirable technique to use.

Our technique corresponds to a single-exposure, multi-resist EBL process capable of forming air-bridge structures with strong metal-metal and metal-substrate adhesion, at very high yield. These correspond to microscopic metallic bridges, suspended about 100 nm above the surface, and which can be used to interconnect both surface gates defined in a first EBL stage, as well as going over other gates. The latter greatly increases the flexibility in device design, as one is now effectively fabricating in three, rather than the usual two, dimensions. Using our technique we were able to fabricate up to 6000 bridges on each chip, as well as individual bridges up to 10 μm in length. Another advantage of air-bridge interconnections is that, as the name suggests, they are suspended in air rather than on top of a solid dielectric. This minimises the capacitive coupling between the bridge and the underlying 2DEG, which for a given bridge height d, and taking into account the parallel-plate approximation, is given by

$$C = \frac{\varepsilon_0 A}{d/\varepsilon + d_{\text{sub}}/\varepsilon_{\text{sub}}} \tag{4.1}$$

where d_{sub} and ε_{sub} are the equivalent substrate properties. Therefore, C can be minimised by either maximising d or, alternatively, minimising ε, for instance by having an air gap rather than PMMA.

Fig. 4.9 outlines the fabrication procedure. We started by coating the sample with PMMA with a molecular weight of 950k (4% solid content in anisole diluted to a 2:1 ratio in MIBK), followed by MMA(8.5)MAA copolymer (9%, 1:1 ratio in ethyl lactate), and finally 100k PMMA (undiluted) (Fig. 4.9a). Note that, in between each layer being applied, the sample

was baked at 110°C for 10 min. in order to dry off solvents and harden the resists. The sample was then patterned by selective exposure to two doses, D_p and D_b, referred to as the pedestal and bridge doses, respectively (Fig. 4.9b). While D_p was high enough so that all resist layers could be removed by the developer, D_b only removed the top two layers, leaving the bottom layer in place. The base doses used, after accounting for proximity correction, were 880 and 600 μC/cm^2, respectively. In the resist profile after development, therefore, the regions exposed to D_b remained covered with 950k as this has a much lower sensitivity than the other resists. This is where the deck of the bridge will be formed. We also highlight that because copolymer is much more sensitive than PMMA, the middle layer will be under-cut with respect to the top layer. The next step was to evaporate metal in order to form the bridges (Fig. 4.9c). We evaporated approximately $110-130$ nm of gold (*i.e.*, roughly equal to the thickness of the bottom-most resist layer), after which the sample was left overnight in a bottle of acetone before being placed in a water bath at 45°C for about 90 min. before final lift-off (Fig. 4.9d). The resulting air-bridges were suspended over the substrate at a height roughly equal to the thickness of the bottom layer, as confirmed by SEM.

In order to achieve a reliable process, it was necessary to be able to control the thickness and uniformity of the resists. We calibrated the thickness of each layer as a function of spinner rotation speed for each type of resist used in the process. Using ellipsometry, we then confirmed that the obtained values were within $\pm 10\%$ of the target values: ~ 130 nm for 950k, ~ 300 nm for copolymer, and ~ 130 nm for 100k. We note, however, that there is flexibility to change these numbers, with successful working samples having been obtained within $\pm 20\%$ of these values, after adjustment of the e-beam dose. Fig. 4.10 and Fig. 4.11 show some SEM micrographs of air-bridge interconnections. We successfully fabricated over 6000 bridges on-chip as well as individual bridges up to 10 μm in length, with average yields of about 90%.

By far the most challenging, and most common, cause of failure, in the air-bridge process was achieving good adhesion between the pedestals and the underlying material. Because the choice of developer has a significant impact on the surface roughness of the developed region, we used a H_2O:IPA (3:7 ratio) mixture at (5 ± 0.5)°C as this was found to reduce the amount of residue left behind. Numerical calculations using the average development rates predicted an optimum development rate of about 35 s. In reality, however, this was found to be closer $60-70$ s. A potential explanation for this mismatch might be due to changes in the development rate of different resists as development progresses and solute accumulates, something which was not accounted for in our model. While no significant cases of over-development were detected, development times under 55 s were also found to lead to poor metal adhesion. In practice, therefore, a simple way to home in on the optimum

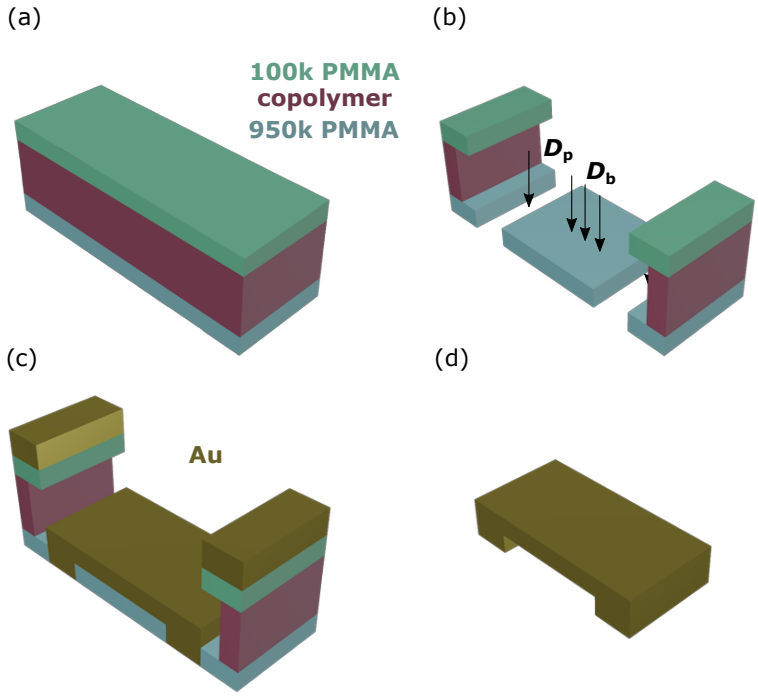

Fig. 4.9 Air-bridge fabrication via a three-layer PMMA single-exposure process. (a) Triple-layer spin-coating of the sample. (b) Selective exposure by electron beam, followed by development. Two EBL doses are used: the pedestal dose, D_p, whose regions are completely cleared from resist after development, and the bridge dose, D_b, which only affects the top two layers, leaving the bottom layer intact. (c) Metallisation via thermal evaporation. (d) Lift-off. The air-bridges are formed at a height slightly less than the original thickness of the bottom layer.

development time for a particular sample, thickness profile, and/or device was to divide the chip into multiple batches and proceed iteratively.

As a final comment, the integrity of the air-bridge structures can often be easily checked using optical microscopy. Here, even though individual bridge resolution is not possible, the whole structure should nevertheless be visible as a thin, iridescent and, most importantly, uniform stripe, making potential breaks and/or regions of poor adhesion easy to detect. Note that, apart from sacrificial samples, we refrained from using SEM so as to avoid potential contamination by electron-beam-induced deposition. Furthermore, samples were also tested for electrical continuity between contacts, as well as potential shortages to nearby gates. For the purpose of our tunnelling devices, there are a set number of tests which can be carried out in order to ensure good bridge adhesion and continuity while simultaneously avoiding having to image them directly. These will be discussed later when analysing and discussing the main results in chapter 5.

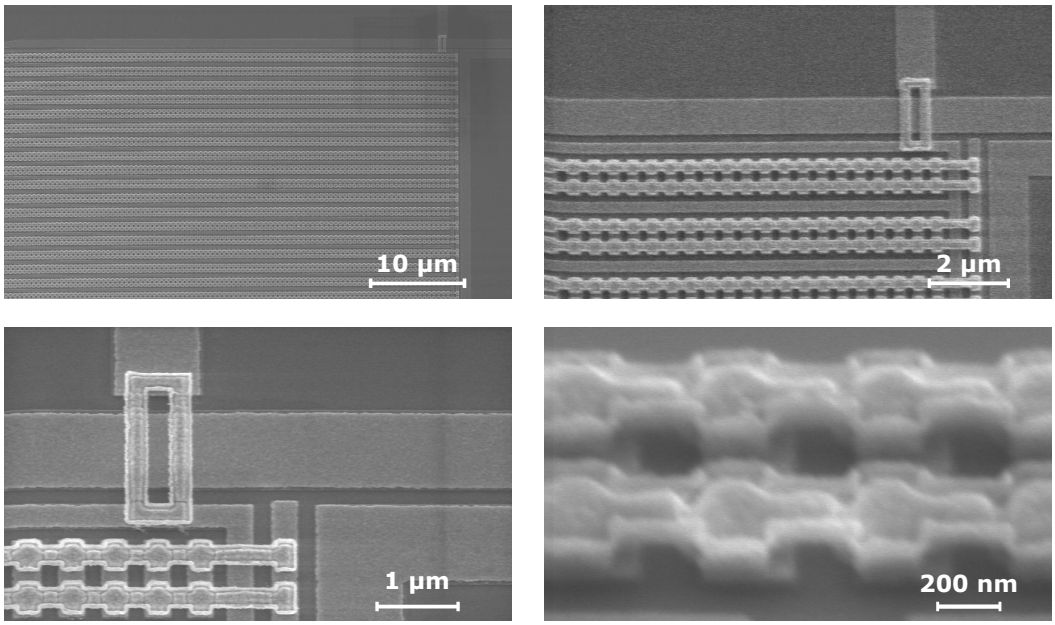

Fig. 4.10 SEM micrographs of an air-bridge device. Once calibrated, the process can be repeated and scaled up in number to very high yields, with devices containing over 6000 on-chip air-bridges having successfully been fabricated.

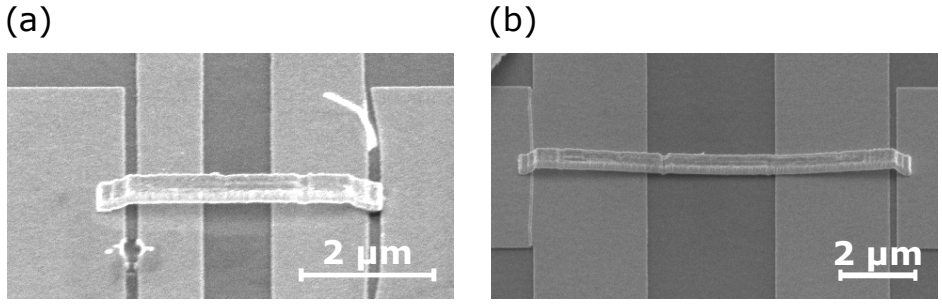

Fig. 4.11 SEM micrographs showing (a) a 5 μm and (b) 10 μm air-bridge interconnection. The air-bridge process can therefore also be scaled up in length. Note that in (a) accidental misalignment put the right-hand pedestal in a gap. On the other hand, the curvature seen in (b) is suspected to result from surface tension with the developer during the development and drying process. Presence of a shadow, nevertheless, establishes that the structure is still suspended.

4.3.5 Sample packaging and bonding

The final step of the fabrication process concerns bonding the sample onto a package so that it could be loaded into a cryostat in order to be measured. Overall, all the steps described above were usually done on a 12 mm$\times$12 mm chip, which allowed a 5$\times$5 chip array to be patterned, each containing 4 separate tunnelling devices, giving a total of 100 potential working devices. Typical yields of the entire process usually ran between $40-50$ %. Individual chips were

then separately scribed off and cleaved away from the processed chip before being glued onto a 20-pin ceramic lead-less chip carrier (LCC) with GE varnish, see Fig. 4.12. Bonding to the LCC pins was done using gold wires on a wedge-bonding machine. Use of a wedge bonder, as opposed to, for example, a ball bonder, was crucial to ensure that the electron-beam gates were not damaged by possible electrostatic discharges. In order to further minimise this risk, an air ioniser was also utilised whilst bonding was taking place. Note that by far the most common cause of device failure was damage to the mid-gate, one of the smallest features patterned in our devices. Therefore, it was important that both during bonding as well as every time the device was handled from there onwards, care was taken so that the sample remained grounded, in order to minimise static.

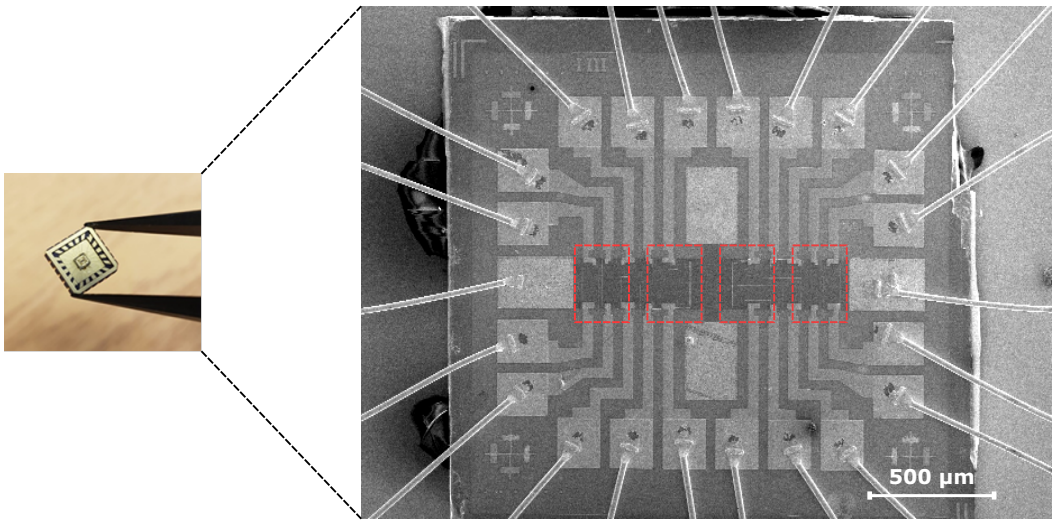

Fig. 4.12 Images of a complete device. All devices were bonded to an LCC package before being measured in a cryostat. Care was taken so as to minimise the risk of electrostatic discharge. For reference, each chip contains a total of 4 potentially working tunnelling devices, see red dashed boxes.

4.4 Low-noise and low-temperature measurement setup

Having now outlined both the considerations that went into the design of our experimental device, as well as how it was fabricated, we conclude this chapter by discussing the measurement setup. As seen before, the 1D system of interest in our experiment corresponds to an array of, approximately, 400 wires, of variable length ($1-18\,\mu$m) and carrier density ($n_e \sim 15-60\,\mu\text{m}^{-1}$), meaning that, at its lowest density and length, the dynamics being probed arise from, at most, 6000 electrons. This results in a signal of interest which is, unsur-

prisingly, quite small. Overall, the total current is of the order of 10^{-10} A, making therefore both data acquisition as well as noise filtering techniques of incredibly high importance.

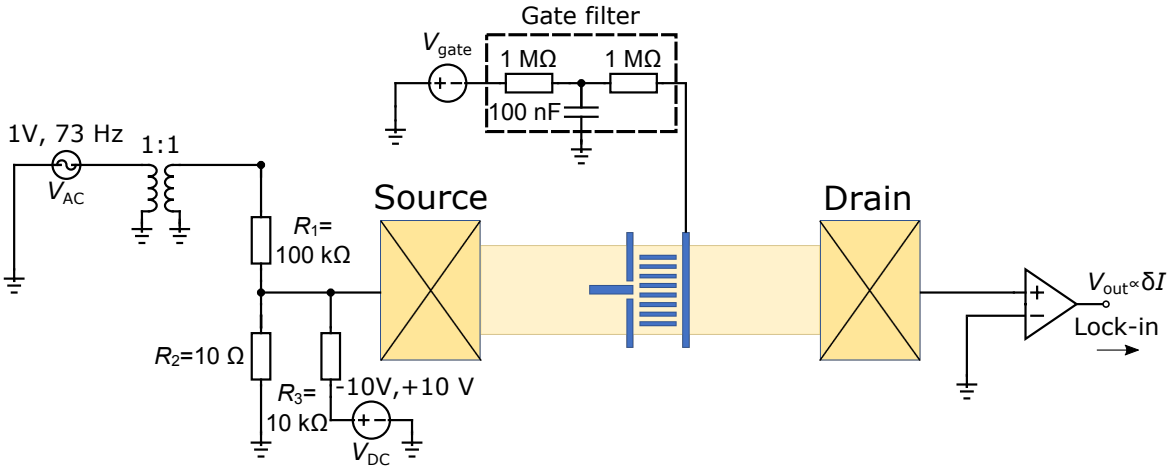

Fig. 4.13 Schematic of the circuit used for measuring the tunnelling conductance. See text for details.

All measurements present in this work were carried out at temperatures between 300 mK and 4 K using a sorption-pumped ^{3}He cryostat. The circuit setup used can be seen in Fig. 4.13. Here, a sinusoidal excitation voltage $V_{AC} = 1$ V at 73 Hz was used to drive a current across the sample, with the frequency having been selected to avoid pickup from the mains. Note that a 1:1 transformer was used so to decouple the DC and the AC grounds, so as to minimise mains pickup due to earth loops. The AC signal then went through a potential divider in order to be reduced by a fraction $R_2/R_1 = 10^{-4}$ before reaching the sample. We then performed our tunnelling spectroscopy measurement (see chapter 3 and section 4.1 for details), with a DC bias $V_{DC} = \pm 10$ V being applied in order to offset the Fermi energies of each system in the sample, after having also been reduced by $R_2/R_3 = 10^{-3}$. This measurement was repeated as an external, in-plane magnetic field B was varied, so that momentum-resolution could also be achieved, with the highest field used in our experiment being 7 T. The outgoing, tunnelling current was then converted into a voltage using a current pre-amp at $10^6 - 10^7$ V/A gain, before being measured by a lock-in amplifier. Note that this introduces an input offset voltage V_{DC}, which has been accounted for in all measurements shown. V_{gate} is the voltage bias applied to each surface gate, each coupled to its own gate filter (two 1 MΩ resistors and one 100 nF capacitor) to protect from voltage surges such as electrostatic discharges. All electronic devices were disconnected from the main electrical network and ran on battery power to minimise noise. The cryogenic system inside which the measurements were performed also sat on low vibration supports.

4.5 Summary

Since its inception, one of the biggest challenges in the field of one-dimensional strongly-correlated systems has been the development of experimental devices capable of emulating Luttinger-liquid-like behaviour. In the absence of perfect 1D systems, several candidates where quasi-1D geometries are present, such as carbon nanotubes, edge states, and particular classes of superconductors have since been explored. This thesis focuses on a different platform for exploring 1D physics, that of semiconductor quantum wires. In this chapter we have discussed the considerations that went into the design and fabrication of all devices presented in this thesis, together with the measurement protocol employed. One of the key outputs of this work has been the development of a novel electron-beam-lithography technique for fabricating microscopic air-bridge structures suspended above the surface. This allowed for much-improved flexibility in both design as well as number of gates implemented on each device. We expect that due to its simplicity, together with potential scalability both in number and in length (having successfully fabricated over 6000 bridges on a single device and single bridges up to 10 μm), this technique should be of use to anyone involved in nanofabrication. A straighforward and reliable way for bridging between regions is a particularly needed solution in areas such as quantum computing, where interconnecting qubits can often prove challenging.

Chapter 5

Two Fermi seas for spin and charge

In this chapter we report on the main experimental finding of this work, the observation of two separate Fermi seas for spin and charge excitations respectively. We start by giving an overview of how independent electrical contact can be established to each layer so that tunnelling spectroscopy can be performed (section 5.1). The discussion in this section follows largely from that started in section 4.1, where we discussed device design. We then characterise the 1D wire array by mapping the 1D subbands and extracting the respective electron densities (section 5.2), before using them to estimate the interaction strength in our systems via the interaction parameter r_s (section 5.3). We then analyse the full dispersion maps obtained from performing tunnelling spectroscopy on our devices. We start by discussing the 2D-2D 'parasitic' tunnelling signal, showing how it can be used to calibrate for a number of known parameters (section 5.4), before analysing the 1D-2D tunnelling signal of interest (section 5.5). Here, we show how a single Fermi sea, even when assuming separate dispersions for spin and charge, is unable to fully capture the observed resonances. Next, we introduce the 1D Fermi-Hubbard model, using it to calculate the full dispersion spectra (*i.e.*, both at low and high energies) of our system (section 5.6). We conclude by showing how the 1D signal discussed before can now be fully explained if two Fermi seas, rather than the usual one, are assumed, as predicted by Hubbard (section 5.7). Note that all data presented and discussed in this chapter were obtained in the single-subband regime. Multiple-subband occupancy data will be discussed later in chapter 6.

All the material and results reported in this chapter can be found in [124]. The theoretical discussion and numerical simulations presented in section 5.6 and later applied to our data were carried out by O. Tsyplyatyev.

5.1 Setting up of the tunnelling conditions

In section 4.1 we discussed the design considerations that went into the fabrication of the vertical tunnelling spectrometer devices. In particular, we saw how selectively biasing a number of electron-beam-defined surface gates could be used in setting both tunnelling as well as transport configurations (see Fig. 5.1a). Let us now discuss in more detail how tunnelling mode was achieved

In order for tunnelling spectroscopy to be used in mapping the dynamics of both 2D and 1D systems, current must only be allowed to flow from source to drain via inter-layer tunnelling. When ohmic contacts are annealed into the sample, however, electrical contact is established to both layers. This means that, in the absence of any biases applied to the surface gates, most of current will instead flow along each individual layer, bypassing tunnelling. In order to establish independent contact to each layer (while avoiding the use of alternative structures such as back gates), we therefore use a combination of split-gates (SG)/mid-gates (MG), barrier gates (BG) and cut-off gates (CG).

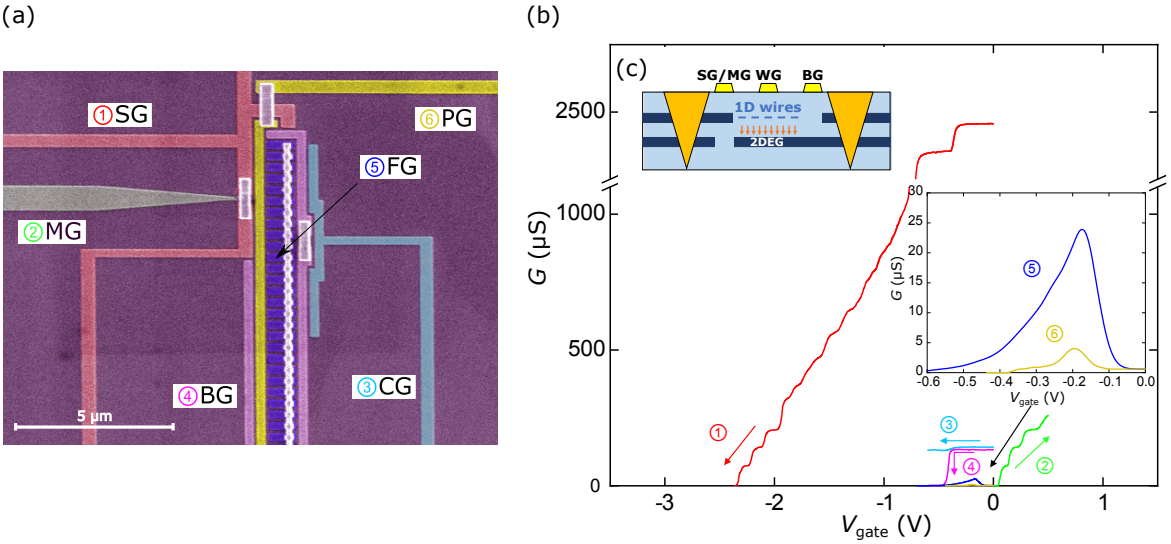

Fig. 5.1 Setting of the device in tunnelling mode. (a) Scanning electron microscopy (SEM) micrograph of a tunnelling device, showing all relevant electron-beam-defined surface gates. (b) Gate operation and setting of tunnelling conditions. We start by negatively biasing SG (1), followed by positively biasing MG so that conductance is only allowed in the upper well (2). Next, we negatively bias both CG (3) and BG (4) but enough to only deplete the upper well. In this configuration, any signal measured between source and drain must result from direct tunnelling between each well. Inset: by varying WG and/or PG one can observe, respectively, 1D-2D and 2D-2D tunnelling between the wells (5 and 6). (c) Side profile of a device in tunnelling mode.

We start by first negatively biasing the SG so that both layers are depleted underneath it, see sweep (1) in Fig. 5.1b. Two sharp drops in conductance are observed, first at ~ -0.3 V followed by ~ -0.7 V, each corresponding to the point at which the electron gas is depleted in the upper and lower layers, respectively. The fact that the conductance value does not drop immediately to zero past ~ -0.7 V reflects the fact that there is a gap in SG, see also Fig. 4.8a. Beyond this point, as V_{SG} is made progressively more negative, a series of conductance plateaux start being observed. These can be understood within the context of the Landauer-Büttiker formalism, where each plateau corresponds to a conduction channel contributing $G_0 = 2e^2/h$ to the total conductance. Therefore, as the confinement potential in the gap is made progressively stronger, fewer channels are allowed to conduct until eventually G hits zero. The MG can then be positively biased so that a narrow conduction channel opens in the top layer only, see sweep (2). Under this configuration, one of the ohmics is now only connected to the top layer.

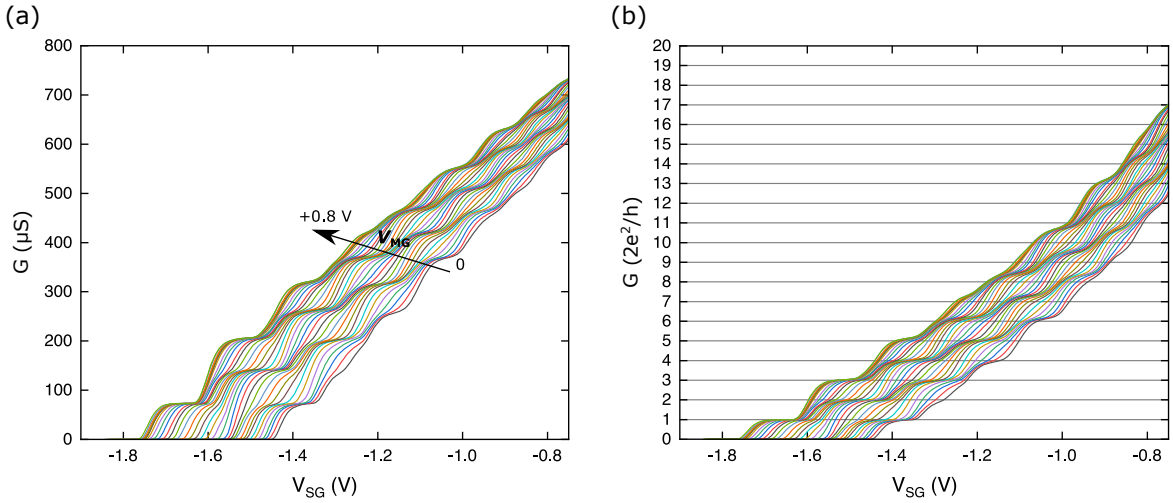

Fig. 5.2 Split-gate/mid-gate characterisation. (a) Conductance G *vs* split-gate voltage V_{SG} as mid-gate voltage V_{MG} is increased from 0 to +0.8 V in increments of 0.02 V. (b) Same data as that shown in (a) but now normalised in units of the conductance quantum $G_0 = 2e^2/h$, after having subtracted a series conductance of $G_s = 1650\,\mu$S. Note how the conductance increases in steps of G_0 up to about $(7-8)G_0$, as expected from a ballistic channel.

In order to ensure that current is indeed only being injected into the top layer, we can further analyse the use of a SG/MG geometry. Fig. 5.2a shows a series of G *vs* V_{SG} sweeps as V_{MG} is increased from 0 to $+0.8$ V. Fig. 5.2b, on the other hand, shows the same data in units of G_0 once a series resistance ($R_s = 606\,\Omega$, $G_s = 1650\,\mu$S in units of conductance) has been subtracted. Note how the conductance signal increases in steps of either G_0 or $2G_0$, depending on whether one channel, in either layer, or two channels, one per layer, are being activated. This can be more easily visualised from Fig. 5.3, where three different regions,

each corresponding to either the top, bottom, or a mix of both layers, are observed. In order to ensure that only channels in the top layer are able to conduct, therefore, we choose V_{SG} and V_{MG} so that they lie in upper-well region.

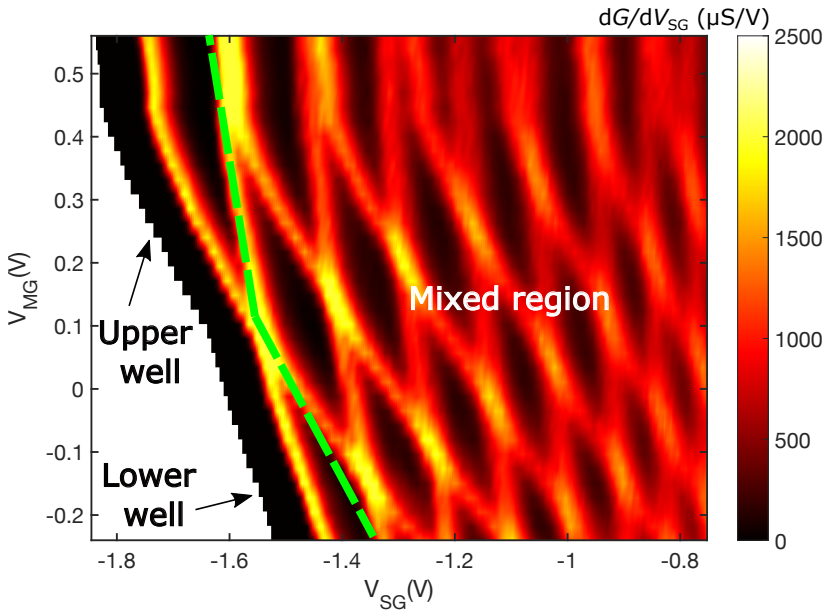

Fig. 5.3 Independent ohmic contacts. Conductance differential $\mathrm{d}G/\mathrm{d}V_{SG}$ *vs* mid-gate voltage V_{MG} and split-gate voltage V_{SG} of the data shown in Fig. 5.2. Here, three regions can be identified, based on whether the device is conducting in only one or both wells. Note that this can already be seen from Fig. 5.2b where G is observed to increase in units of either G_0 or $2G_0$. Based on this map, the values of V_{SG} and V_{MG} are chosen so that current is only being injected into the top well.

Once the SG/MG are set up, at the other end of the device, the BG and the CG are biased together so that only the top layer is depleted. This makes the ohmic contact on this side now only connected to the bottom layer, see sweeps (3) and (4). Under these conditions, any current measured between source and drain must then have tunnelled between the layers, see Fig. 5.1c. Note, however, that at $B = 0$, $V_{DC} = 0$, the overlap between the spectral functions of each layer is negligible, reason why $G \approx 0$.

In order to increase the amount of tunnelling signal observed, two gates going over the experimental tunnelling area, the wire-gate (WG) and the 'parasitic' gate (PG), are used to control, respectively, the 1D system as well as the (2D) injection region. Sweeps (5) and (6) show therefore, both 1D-2D and 2D-2D tunnelling between the upper and lower layers as the bias on each is varied. Comparing the magnitude of sweep (1) with sweeps (5) and (6), we estimate the tunnelling resistance to be of the order of MΩ while transport across each layer of the order kΩ. Once the biases on the SG/MG and the BG/CG are set-up, they remain fixed for the remainder of the experiment.

5.2 Characterising the 1D wire-array

Before analysing the tunnelling dispersion maps, let us first discuss how the 1D wire array has been characterised.

Fig. 5.4a shows the tunnelling conductance differential $\mathrm{d}G/\mathrm{d}V_{\mathrm{WG}}$ as a function of both wire-gate voltage V_{WG} and in-plane magnetic field B. As can be seen, a number of resonant features are observed. In section 3.4 (and specifically, Fig. 3.4), it was argued that in k-space (*i.e.*, along B) two tunnelling resonances should occur as the spectral functions of each well (effectively, two 2D systems) touch from both the inside and the outside. Indeed, this is what is observed, with both B_{+}^{2D} and B_{-}^{2D} moving closer to each other as V_{WG} is decreased up to about -0.3 V. For this voltage range, therefore, the electron gas in the upper layer is still largely 2D in nature, with the observed resonances marking the position of the 2D band.

As V_{WG} is made more negative, however, and as expected, at some point the electron gas underneath the wire gates will become fully depleted. When this happens, the only states that remain populated are those in-between the wire gates, forming a 1D channel, reason why the upper layer can no longer be described as a simple 2DEG. Instead, from -0.3 V to about -0.6 V, additional resonances are observed, each corresponding to a 1D subband arising from the wire array. The number, as well as the spacing between each subband can be tuned based on the lithographic dimensions, see [60]. For this work, however, the maximum number of subbands will always be three or four. Note that, by tuning V_{WG}, the number of 1D subbands occupied can then be progressively changed. As we will show later in chapter 6, this will be used to study 1D dynamics under different subband occupancy values, as well as inter-subband screening effects. Beyond -0.6 V, the signal drops to zero, marking the point at which the wire-array pinches off, with no current being injected into the wires.

Fig. 5.4a, therefore, sets the range in V_{WG} over which the electron gas in the upper layer under the wire-gate array can be tuned to behave as either 2D or 1D (with variable number of occupied subbands), before being fully depleted. A zoom in around the subband region can be seen in Fig. 5.4b. Note that, when looking at the $\mathrm{d}G/\mathrm{d}B$ differential, two additional vertical features can be seen in conductance, at $\sim$1 and $\sim$4.7 T. These arise from the 'parasitic' 2D injection region and, as expect, show no dependence on V_{WG}.

Another important analysis that can be done based on measurements such as those shown in Fig. 5.4a and b has to do with the uniformity of the wire-array. As argued in section 4.1, use of an array allows us to both increase the signal-to-noise ratio as well as average out any potential disorder effects. The question that naturally arises then is how to ensure that this geometry indeed results in a uniform 1D system, with each channel being roughly identical to one another. As can be seen from the data, the fact that well-defined resonances in conductance can be observed strongly suggests that this is the case. Note that here the

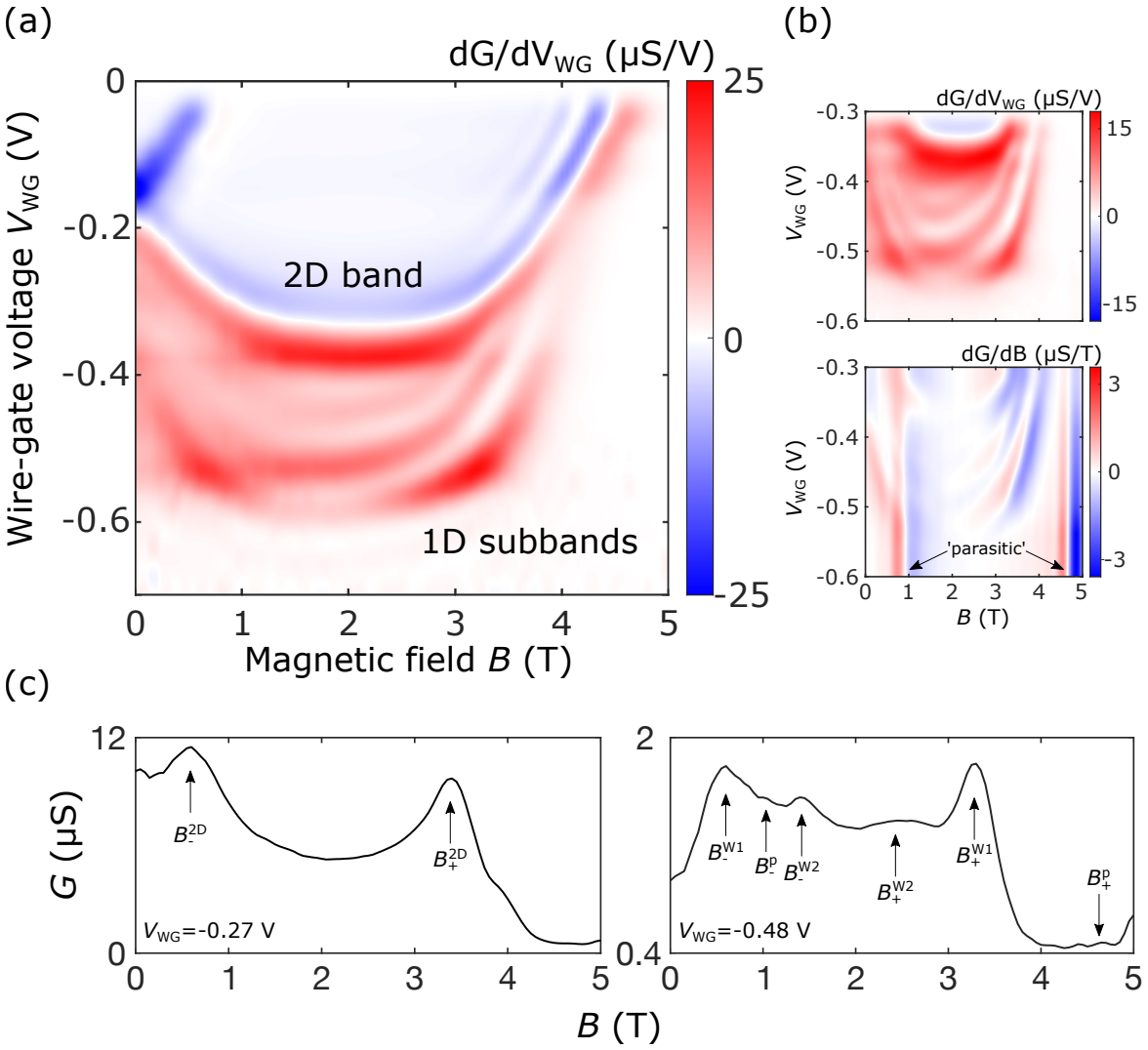

Fig. 5.4 Characterisation of the 1D wire system. (a) Tunnelling conductance differential $\mathrm{d}G/\mathrm{d}V_{\mathrm{WG}}$ as a function of both wire-gate voltage V_{WG} and in-plane magnetic field B, obtained under equilibrium conditions $V_{\mathrm{DC}} = 0$ for a 1.7 μm device. Here, three fully developed 1D subbands can be seen below the 2D band at $V_{\mathrm{WG}} \approx -0.35$ V and up to about the pinch-off point $V_{\mathrm{WG}} \approx -0.55$ V, below which the wires cannot conduct. (b) Zoom in of the data shown in (a) around the 1D subband region, showing both $\mathrm{d}G/\mathrm{d}V_{\mathrm{WG}}$ and $\mathrm{d}G/\mathrm{d}B$. Note how, for the latter, two vertical tunnelling features (*i.e.*, independent of V_{WG}) can be seen, corresponding to the tunnelling resonances coming from the 2D 'parasitic' injection region. (c) Line-cuts of the data shown in (a) and (b) at voltages where either the 2D band (left) or two 1D subbands (right) are defined. From here, the tunnelling resonance fields B_- and B_+ for the respective 2D, 1D (W1, W2) or parasitic (p) regions can be extracted.

resulting signal arises from a total of, approximately, 400 wires meaning that if there was significant non-uniformity along the channels, then the different minima and maxima of the signal coming from each would effectively end up overlaping completely in the total tunnelling signal, with the 1D parabolae becoming consequently impossible to observe. Of course, effects of disorder due to averaging, charge traps, lithographic roughness, and well-width fluctuations by one atomic layer should also cause some level of blurring in the observed spectra. Nevertheless, data like that shown in Fig. 5.4a allows for a quantitative assessment of the array uniformity to be made.

Fitting the lineshapes of *G vs B* gives a minimum broadening Γ of $0.2-0.3$ meV, even when only one 1D subband is occupied, see [57]. Therefore, by measuring the current from all wires in parallel, each wire with different impurity configurations and wire-width fluctuations, we conclude that if the spread of wire widths were too large, then no signs of 1D subbands would be observable. Given that this is not the case, each 1D channel must then be, on average, approximately equal to one another, within Γ. Furthermore, as we will see later in chapter 7, for $1-18\,\mu$m wires, the conductance in such arrays scales with both length as well as total number of wires, whilst leaving the conductance structure unchanged. This further suggests that most wires, and indeed most of each wire, is contributing to tunnelling.

Extracting both B_+ and B_- for each subband as the confinement in the wires is made progressively stronger, allows us to extract both the 1D (in the upper well) and 2D (in the lower well) electron densities, n_{1D} and n_{2D}, in terms of V_{WG}, see equations (3.22), (3.25) and (3.26), and Fig. 5.4c. From here, the Fermi wavelength λ_F can also be obtained which, for our wires, is usually $70-150$ nm, resulting in a estimated wire width of $20-50$ nm. Similarly, the 2D densities in both wells in the 'parasitic' region can also be extracted.

Our tunnelling device, therefore, allows us to create a 1D system where both the number of occupied subbands as well as the electron density in each, can be tuned *in situ* by changing V_{WG}. In the next section we introduce the interaction parameter r_s, showing how it allows us to obtain an initial estimate of the interaction strength in a system irregardless of dimensionality.

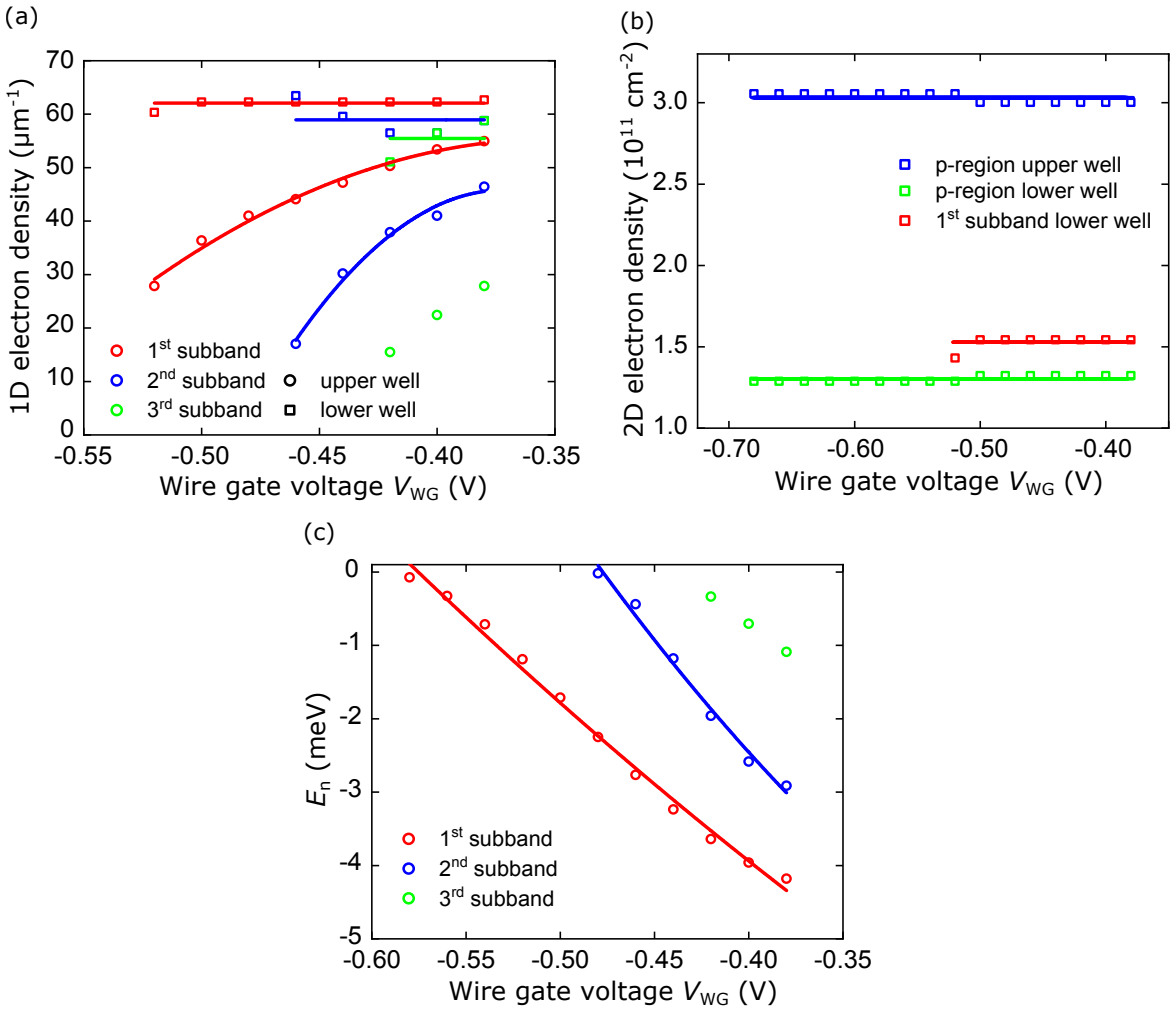

Fig. 5.5 1D wire subbands. (a) Equilibrium 1D densities in both the upper (circles) and lower (squares) wells for each occupied subband. Note that the electrons are not laterally confined in the bottom well and as such the lower well 1D densities have no physical meaning and are only shown for comparison. (b) 2D electron densities in both upper (blue) and lower (green) wells' 'parasitic' regions. The overall independence of the 2D densities on the wire-gate voltage and the proximity of the (now physical) 2D electron density of the bottom well below the wire region (red) to that of the injection region shows that the bottom 2DEG remains largely unaffected by V_{WG}. This allows us to use this layer as a well-understood 2D probe. (c) Subband energies relative to the chemical potential $\mu = 0$ as a function of V_{WG}.

5.3 Interaction parameter r_s

The Wigner-Seitz radius r_s is often used as a generic interaction parameter for Fermi systems. While multiple constructions of this parameter are often found in the literature, the most common definition is usually done in terms of the ratio of the potential to the kinetic energies. Here, while the kinetic energy (*i.e.*, the Fermi energy) in a Fermi system is inversely proportional to the inter-particle distance squared, $\langle K.E.\rangle \sim k_F^2 \sim 1/\lambda_F^2$, the Coulomb energy, on the other hand, is $\langle I.E.\rangle \sim e^2/\langle x\rangle$ (assuming two-body dynamics only), where $\langle x\rangle \simeq \lambda_F$ is the average distance between two particles, therefore resulting in

$$\frac{\langle I.E.\rangle}{\langle K.E.\rangle} \sim \lambda_F \cong \langle x\rangle \tag{5.1}$$

It can then be seen that, once the density is low enough (and, therefore, $\langle x\rangle$ is high), interactions will always dominate over the kinetic energy. Indeed, in the extreme scenario, this can even force the electrons to crystallise in place, as they try to remain as far away as possible from one another, in what is known as a Wigner crystal. The main advantage of this parameter, however, is that it works in all dimensions, including 1D, making it therefore ideally suited for comparing the magnitude of interactions in systems of different geometries.

We parameterise the average inter-particle distance in units of the Bohr radius a_B, so that $\langle x\rangle = r_s a_B$. Note that under this definition r_s is now dimensionless. Taking n as the electron density and V_D as the volume of a D-dimensional sphere of radius $r_s a_B$, we can write

$$V_D(a_B r_s) = \frac{1}{n} \tag{5.2}$$

which gives

$$n = \begin{cases} \frac{1}{2a_B r_s} & \text{1D} \\ \frac{1}{\pi a_B^2 r_s^2} & \text{2D} \\ \frac{3}{4\pi a_B^3 r_s^3} & \text{3D,} \end{cases} \tag{5.3}$$

In other words, r_s is simply a re-parameterisation of density

Let us now focus on the energy ratio. For a Fermi system, we know that the kinetic energy is given by

$$E_K = \frac{\hbar^2 k_F^2}{2m} \tag{5.4}$$

while a Coulomb energy scale is

$$E_C = \frac{k_e e^2}{\lambda_F}. \tag{5.5}$$

Note that here $k_\mathrm{e} = 1/(4\pi\varepsilon_0)$ is the Coulomb constant, while $\lambda_\mathrm{F} = 2\pi/k_\mathrm{F}$ is the Fermi wavelength.

The ratio of these energies is then given by

$$\frac{E_\mathrm{C}}{E_\mathrm{K}} = \frac{k_\mathrm{e}e^2}{\lambda_\mathrm{F}} \frac{2m\lambda_\mathrm{F}^2}{\hbar^2(2\pi)^2} = \frac{2mk_\mathrm{e}e^2}{(2\pi)^2\hbar^2}\lambda_\mathrm{F} \tag{5.6}$$

Finally, we need to relate λ_F to r_s. We know that the density of electrons in a Fermi sea is given by the integral over the Fermi function

$$n = 2\int \frac{\mathrm{d}^\mathrm{D}k}{(2\pi)^\mathrm{D}} n_\mathrm{k}, \tag{5.7}$$

where the occupation numbers are a step function, $n_\mathrm{k} = \theta(k_\mathrm{F} - |k|)$. Here, we have included the electron spin degeneracy 2, as this quantity is evaluated for free particles. This gives

$$n = \begin{cases} \frac{2k_\mathrm{F}}{\pi} \\ \frac{2k_\mathrm{F}^2}{\pi} \\ \frac{k_\mathrm{F}^3}{3\pi^2} \end{cases} = \begin{cases} \frac{4}{\lambda_\mathrm{F}} & \text{1D} \\ \frac{8\pi}{\lambda_\mathrm{F}^2} & \text{2D} \\ \frac{8\pi}{3\lambda_\mathrm{F}^3} & \text{3D.} \end{cases} \tag{5.8}$$

Equating equation (5.3) to equation (5.8), we get

$$\lambda_\mathrm{F} = \begin{cases} 8a_\mathrm{B}r_\mathrm{s} & \text{1D} \\ 2^{3/2}\pi a_\mathrm{B} r_\mathrm{s} & \text{2D} \\ \frac{2^{4/3}\pi^{2/3}}{3^{2/3}} a_\mathrm{B} r_\mathrm{s} & \text{3D.} \end{cases} \tag{5.9}$$

Finally, inserting the above result in equation (5.6)

$$\frac{E_\mathrm{C}}{E_\mathrm{K}} = \frac{2mk_\mathrm{e}e^2}{(2\pi)^2\hbar^2} a_\mathrm{B} r_\mathrm{s} \times \begin{cases} 8 & \text{1D} \\ 2^{3/2}\pi & \text{2D} \\ \frac{2^{4/3}\pi^{2/3}}{3^{2/3}} & \text{3D,} \end{cases} \tag{5.10}$$

together with the Bohr radius of electrons in GaAs

$$a_\mathrm{B} = \frac{4\pi\varepsilon_0\hbar^2}{me^2} \tag{5.11}$$

results in

$$\frac{E_C}{E_K} = r_s \times \begin{cases} \frac{4}{\pi^2} \simeq 0.41 & \text{1D} \\ \frac{\sqrt{2}}{\pi} \simeq 0.45 & \text{2D} \\ \frac{2^{1/3}}{3^{2/3}\pi^{4/3}} \simeq 0.13 & \text{3D.} \end{cases} \tag{5.12}$$

Therefore, while E_C/E_K is proportional to the average distance between particles in all dimensions, the proportionality coefficient depends on dimensionality.

As a final comment, note that while r_s can be seen as a measure of density, it does not account for details of the interactions, meaning it has no knowledge of the interaction dynamics (two-body or otherwise) and/or the screening potential. Indeed, it is worth highlighting that the biggest uncertainty in the numbers of equation (5.12) comes from how E_C was defined in the first place, see equation (5.5). Indeed, note that the shape of the screening potential is, generally speaking, unknown, and can differ significantly from the Thomas-Fermi solution, meaning (5.5) should be used with caution. This problem will be solved later in section 5.6.3 for 1D once the interaction parameter γ is introduced based on a microscopic analysis of the Hubbard model using the Bethe *ansatz*. In the meantime, we will use equation (5.3) to calculate r_s given the electron density n.

In this chapter, all data discussed will be in the range $r_s = 1 - 1.5$, with chapter 6 being dedicated to multiple-subband data where $r_s = 1.5 - 4$.

5.4 Fitting of the tunnelling resonances

Having shown how the upper layer can be tuned to display both 2D and 1D dynamics, and having characterised the resulting 1D wire-array, we will now use tunnelling spectroscopy to map the full dispersion of each layer in both energy and momentum space. Here, multiple tunnelling resonances are expected to be observed, as the overlap of the spectral function of each system is changed, see section 3.4. We will analyse all observed tunnelling dispersions based on this interpretation, including the capacitive corrections discussed in section 3.5. Let us start by discussing the 2D-2D tunnelling maps before proceeding to the 1D-2D measurements.

5.4.1 2D-2D tunnelling signal

It is inevitable that, when mapping a device, in addition to the tunnelling processes happening between the wire array and the 2D spectrometer (which will be discussed in the next section), some tunnelling will also occur between the 2D leads in the upper well and the spectrometer

in the lower well. This is because, in order for current to be injected in the wires, an injection region running parallel to the array needs to be present. This region is set by design and is always wide enough ($\sim 0.45-0.6\,\mu$m) so that the 2DEG underneath it is not significantly confined. This means that, as we will see, it can safely be treated as a 2D system. Nevertheless, the resulting outcome is that, in addition to the 1D-2D signal of interest coming from the wire-region, some 2D-2D 'parasitic' signal will also be present in the data.

In order to separate the 'parasitic' signal from the overall tunnelling data, we map it separately so that it can later be subtracted. This is achieved by setting the wire-gate voltage V_{WG} negative enough (*i.e.*, below the bottom subband) so that the wires do not conduct. Under these conditions, only the injection region in the upper well is allowed to conduct, meaning that all the tunnelling signal must arise from there. Fig. 5.6 shows some representative data of the 2D-2D tunnelling signal measured, with $\mathrm{d}G/\mathrm{d}V_{\mathrm{DC}}$ and $\mathrm{d}G/\mathrm{d}B$ corresponding to the tunnelling conductance differentials with respect to in-plane magnetic field B and inter-layer bias V_{DC}. Dashed and dash-dotted curves correspond, respectively, to the capacitance corrected and uncorrected dispersion curves for each layer.

Following from the discussion in sections 3.4 and 3.5, the location of the tunnelling resonances can be fully determined given seven parameters. These are: the capacitances (per unit area) of both the upper and lower wells, $c^{\mathrm{2D}}_{\mathrm{UW}}$ and $c^{\mathrm{2D}}_{\mathrm{LW}}$, their respective effective electron masses, m_{UW} and m_{LW}, the separation between the centres of the wavefunctions in the two wells, d, and the zero-bias field intercepts, B^{p}_{-} and B^{p}_{+}. Let us now discuss each individually, showing how strong constraints can be obtained for all.

Starting with $c^{\mathrm{2D}}_{\mathrm{UW}}$ and $c^{\mathrm{2D}}_{\mathrm{LW}}$, it was found that the best results were obtained taking $c^{\mathrm{2D}}_{\mathrm{UW}} = (0.0047 \pm 0.0003)\,\mathrm{Fm}^{-2}$ and $c^{\mathrm{2D}}_{\mathrm{LW}} = (0.0033 \pm 0.0003)\,\mathrm{Fm}^{-2}$. Note that this is in very good agreement with the COMSOL simulation results discussed in section 3.5.2, where $c = 0.0047\,\mathrm{Fm}^{-2}$. We attribute the slight asymmetry in values, $c^{\mathrm{2D}}_{\mathrm{LW}}/c^{\mathrm{2D}}_{\mathrm{UW}} \approx 0.7$, to the likely presence of screening effects between both wells, as well as capacitive coupling to the surface gates.

Similarly, regarding the effective electron masses, both m_{UW} and m_{LW} were found to be equal to $0.93m_{\mathrm{b}}$, where $m_{\mathrm{b}} = 0.067m_{\mathrm{e}}$ is the electron band mass in GaAs. The extracted 2D effective mass, $m^{*}_{\mathrm{2D}} = 0.93m_{\mathrm{b}} = 0.062m_{\mathrm{e}}$, measured using tunnelling spectroscopy, is also in very good agreement with independent work carried out in GaAs/AlGaAs heterostructures with similar densities and mobilities to our own, probed using a variety of techniques, such as Shubnikov–de-Haas oscillations [49, 28, 115], microwave-induced resistance oscillations [48], quantum Monte-Carlo calculations [75], and cyclotron-resonance measurements [74]. We will come back to the effect of dimensionality on electron mass renormalisation later in chapter 6 when discussing the extraction of the bare (1D) electron mass.

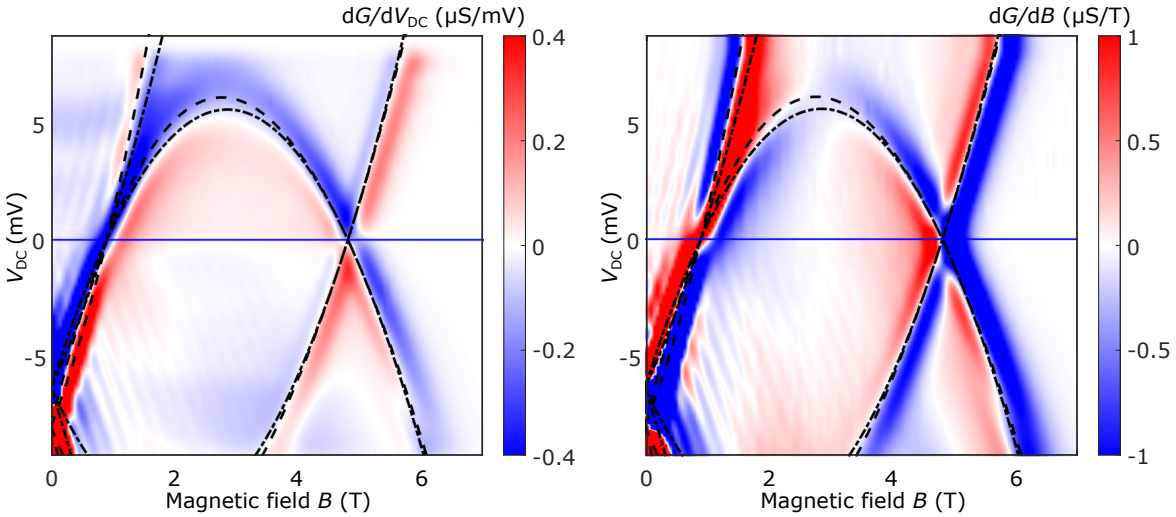

Fig. 5.6 2D-2D background signal. (a) Conductance tunnelling differentials $\mathrm{d}G/\mathrm{d}V_{\mathrm{DC}}$ and $\mathrm{d}G/\mathrm{d}B$ *vs* DC-bias V_{DC} and in-plane magnetic field B of a 1.7 μm-long device, mapped at $V_{\mathrm{WG}} = -0.57$ V. At this voltage, the wires are pinched off and cannot conduct. The spectrum observed arises, therefore, solely from tunnelling between both wells in the 2D 'parasitic' injection region. Dashed- and dash-dotted curves mark the positions of, respectively, the capacitance corrected and uncorrected resonance curves, as discussed in section 3.4, see also Fig. 3.5.

The next parameter that needs to be determined is d, the separation between the wavefunctions in the two wells. For this, we know from the MBE growth data that each well is $\approx$18 nm thick, with the superlattice barrier in between being $\approx$14 nm, making therefore $d \approx 32$ nm. Even though it is reasonable to expect deviations from this value to occur due to, for example, monolayer fluctuations, the current status of MBE technology means that the resulting structures are unlikely to differ from the target by more than a few nanometres. Indeed, it was found that a systematic value of $d = 31$ nm worked best for all devices fabricated from wafer W939, while $d = 33$ nm for devices coming from wafer C2617. It is worth also noting that, particularly at high fields where the sign of k changes while tunnelling, one could argue that a Lorentz force could act in such a way as to force the carriers in each well further apart, effectively increasing d. This would, in practice, translate into having $d \equiv d(B)$. While we cannot rule out such an effect, it can be seen from Fig. 5.6 that no such correction was required up to at least 7 T, the highest field used in this experiment.

Finally, the zero-bias crossing points B_{-}^{p} and B_{+}^{p}, corresponding to the field magnitudes at which tunnelling resonances are observed (see Fig. 3.4), can be easily determined by visual inspection of both the DC-B (see Fig. 5.6) and WG-B (see Fig. 5.4) tunnelling maps.

As can be seen from Fig. 5.6, the level of agreement between experiment and theory allows us to confidently treat the signal arising from the 'parasitic' injection region as being

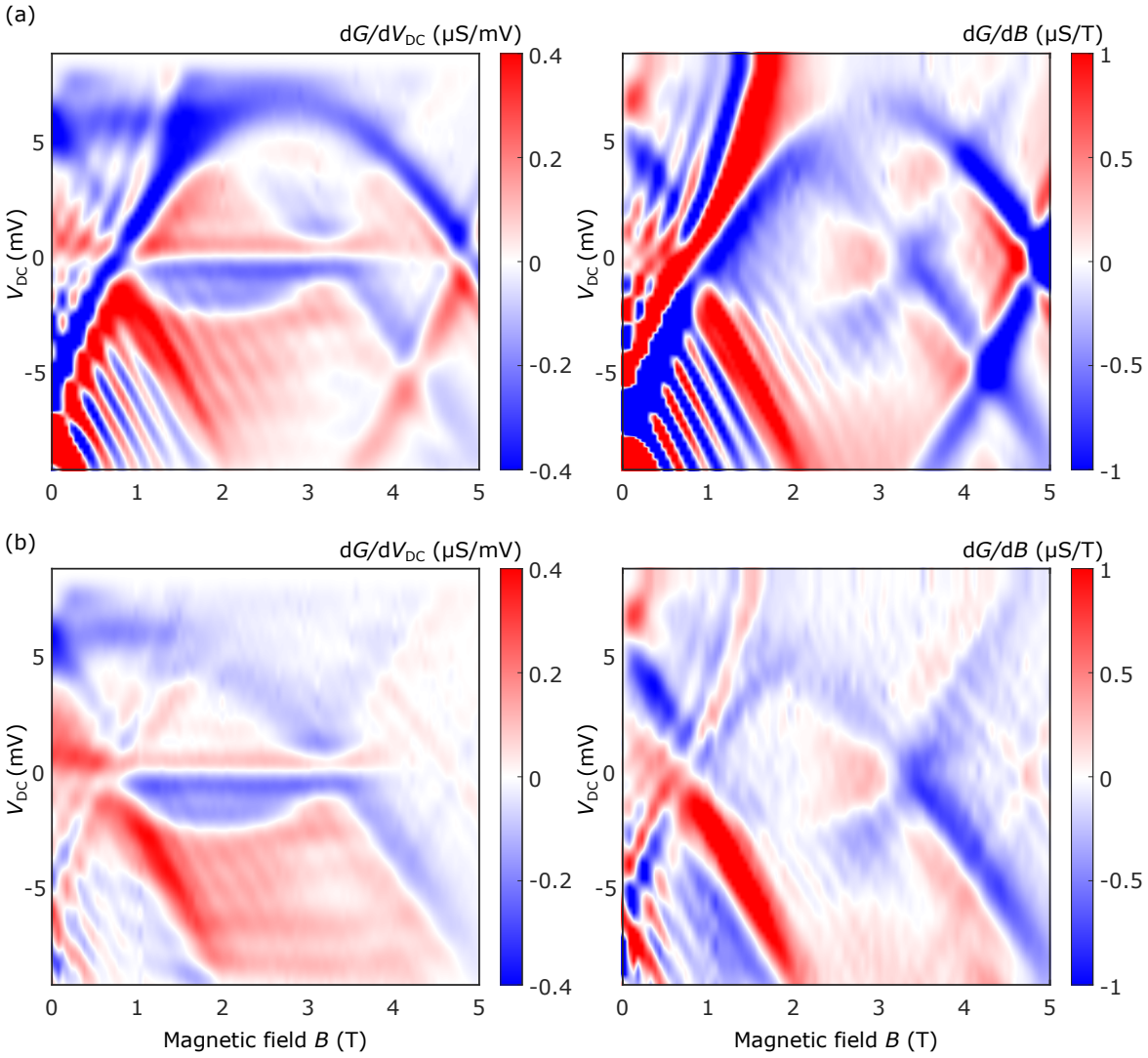

Fig. 5.7 Subtraction of the 'parasitic' 2D-2D tunnelling signal. Here, (a) and (b) show, respectively, data from a 1.7 μm-long device in the single-subband regime, before and after the 2D-2D background (shown in Fig. 5.6) was subtracted.

2D-2D in nature, with the set of parameters used having been reproduced across a total of 5 devices. For the remainder of this work we will refer to the 2D-2D tunnelling maps as 'background'. Every tunnelling map that follows will have had this data subtracted from it (see Fig. 5.7 for an example) unless mentioned otherwise, so that the only signal remaining comes from the wire-region. This is the topic of the next section.

5.5 1D-2D tunnelling signal

In the previous section we discussed how to constrain $c_{\mathrm{UW}}^{\mathrm{2D}}$, $c_{\mathrm{LW}}^{\mathrm{2D}}$, $m_{\mathrm{2D}}^{\star}$, and d from the background data, *i.e.,* using the tunnelling-conductance maps with the wires past pinch-off. We will now focus on the signal arising from the wire-region, where 1D dynamics are expected to be present. In order to isolate this signal and analyse it free from 'parasitic' 2D influences, we subtract the 2D-2D background as discussed in the previous section. Note that this is possible because the modulation of the wire gate to the injection region is observed to be negligible, even as the wires start conducting. Furthermore, the density under the parasitic and wire regions also closely matches across a range of V_{WG} (see Fig. 5.5b), making the 2D-2D signal therefore very weakly dependent on V_{WG}.

We characterise the 1D system by mapping its subbands as discussed in section 5.2. As can be seen, under our chosen geometry, most devices display between three and four subbands, that is, after the 2DEG in between the lithographic wires has been depleted. Using maps such as that of Fig. 5.4 allows us to map the dispersion of the 1D system at any subband occupancy value by choosing appropriate values for V_{WG}. In this chapter, we will focus on the single-subband regime, with chapter 6 being dedicated to multiple-subband occupancy.

The procedure followed when analysing the tunnelling signal arising from the wire region is analogous to what was done for the 2D injection region. Since $c_{\mathrm{UW}}^{\mathrm{2D}}$, $c_{\mathrm{LW}}^{\mathrm{2D}}$ and d have already been obtained, the only free/unknown parameters in this region are: the zero-bias field intersects, B_{-}^{W} and B_{+}^{W}, the effective mass of the 1D electrons in the upper well, $m_{\mathrm{UW}} = m_{\mathrm{1D}}^{\star}$, and the capacitances per unit area of both wells in this region, $c_{\mathrm{UW}}^{\mathrm{1D}}$ and $c_{\mathrm{LW}}^{\mathrm{1D}}$.

The capacitance values found to work best were $c_{\mathrm{UW}}^{\mathrm{1D}} = c_{\mathrm{LW}}^{\mathrm{1D}} = (0.0026 \pm 0.0005)\,\mathrm{Fm^{-2}}$. These are significantly lower than those predicted in COMSOL, where $c = 0.0103\,\mathrm{Fm^{-2}}$, see section 3.5.2. Using larger values for the capacitance (and indeed taking $c_{\mathrm{UW}}^{\mathrm{2D}}$ and $c_{\mathrm{LW}}^{\mathrm{2D}}$ as an upper bound) completely distorts the dispersions, even when accounting for larger errors in the remaining parameters (which have already been calibrated using the background data). We interpret the observed deviations as arising from the quantum capacitance, C_{Q}, since in a 1D wire, interactions effectively push down the band, reducing the rate of filling of the wire, that is, $\mathrm{d}n_{\mathrm{1D}}/\mathrm{d}E_{\mathrm{F}}$. This means that the energy required in order to add an extra electron to the 1D chain is increased, leading to a decrease of $C_{\mathrm{Q}} \propto \mathrm{d}n_{\mathrm{1D}}/\mathrm{d}E_{\mathrm{F}}$. Note that this is essentially the same mechanism as that behind the zero-bias anomaly (see Fig. 2.13), where conductance is strongly suppressed at zero bias since it is no longer energetically favourable to tunnel in or out of the wire.

Using the framework presented in section 3.5.1, we estimate $C_{\mathrm{Q}}/A = 4e^2m^{\star}/\pi^2\hbar^2 w n_{\mathrm{1D}} = 0.0326\,\mathrm{Fm^{-2}}$, where $m^{\star} = 0.067m_{\mathrm{e}}$, $n_{\mathrm{1D}} = 33\,\mu m^{-1}$, and $w = 50\,\mathrm{nm}$ were chosen as rep-

resentative values in the single-subband regime. Similarly, using the data shown in Fig. 5.5, and taking $\mathrm{d}n_{1\mathrm{D}}/\mathrm{d}E_{\mathrm{F}} \approx \Delta n_{1\mathrm{D}}/\Delta E_{\mathrm{F}}$, we get $C_{\mathrm{Q}}/A = 0.0218\,\mathrm{Fm}^{-2}$. While both estimates agree in magnitude, C_{Q} is still about ten times larger than what experiment suggests ($C_{\mathrm{Q}}/A = 0.0035\,\mathrm{Fm}^{-2}$, see section 3.5.2), suggesting a larger effect of the interactions than accounted for in our model. Nevertheless, because the total capacitance C is determined by the sum of both geometrical and quantum capacitances, $1/C = 1/C_{\mathrm{Q}} + 1/C_{\mathrm{G}}$, and since $C_{\mathrm{Q}} \lesssim C_{\mathrm{G}}$, there is no reason to expect the results of the COMSOL simulation done in section 3.5.2 to remain valid, since this only took into account electrostatics. Note that, in comparison, the results from COMSOL closely matched the experiment when in the 2D-2D tunnelling regime, as expected since here the effects from C_{Q} are largely negligible.

Regarding B_{-}^{w} and B_{+}^{w}, these can be obtained as before, that is, by visual inspection of both the DC-B and WG-B maps.

The last parameter that remains to be determined is then $m_{1\mathrm{D}}^{\star}$.

5.5.1 Single Fermi sea and single plasmon

As a starting point, the simplest assumption one can make is that the 1D dispersion is completely described by a single 1D effective mass, $m_{1\mathrm{D}}^{\star}$. This should, in principle, be able to take any value. Let us start by assuming it matches the 2D non-interacting effective mass, *i.e.*, $m_{1\mathrm{D}}^{\star} = m_{2\mathrm{D}}^{\star}$. We will refer to the $V_{\mathrm{DC}} > 0$ sector as the particle sector, corresponding to electrons tunnelling *into* the wire, while $V_{\mathrm{DC}} < 0$ is the hole sector, corresponding to the reverse process whereby electrons tunnel *out*.

From Fig. 5.8 it can be seen that while the behaviour of the 1D mode is nicely captured in the hole sector ($V_{\mathrm{DC}} < 0$), the same does not happen in the particle sector ($V_{\mathrm{DC}} > 0$), particularly at high biases, even when correcting for mass. It is therefore our experimental statement that the 1D dispersion cannot be fully accounted for by a single parabola (*i.e.*, a single mass) in both hole and particle sectors.

5.5.2 Single Fermi sea and two plasmons

We now assume that there are both spin- and charge-type excitations in the 1D system. Note that based on previous work, most specifically well-established observations such as spin-charge separation [10, 60], this is the natural starting point, as spin and charge modes are known to propagate along a 1D wire at different velocities, therefore suggesting different masses. We label these masses m_{s} and m_{c} referring, respectively, to spin-type and charge-type excitations.

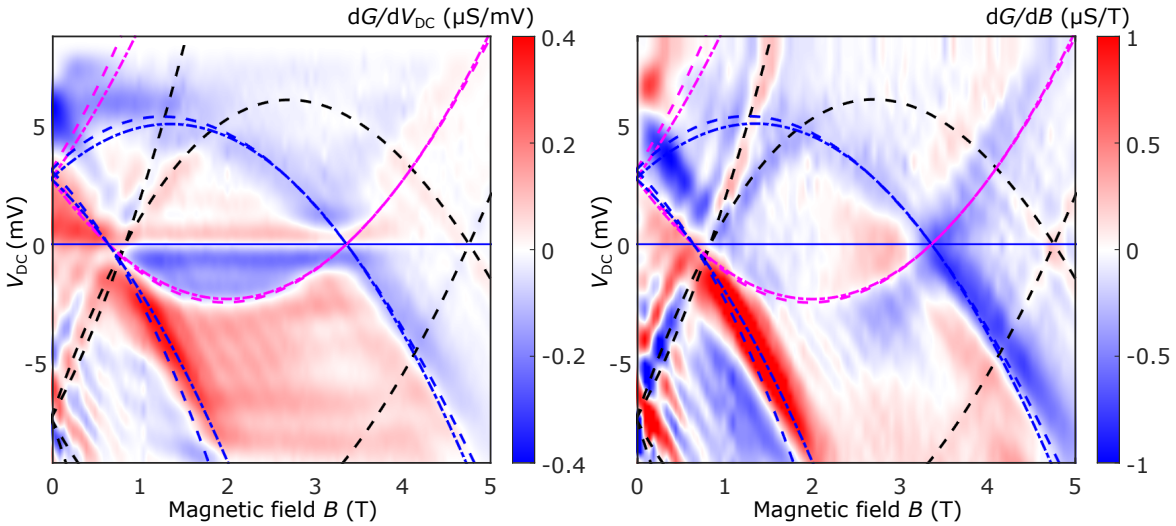

Fig. 5.8 One Fermi sea and one plasmon. Tunnelling conductance differentials $\mathrm{d}G/\mathrm{d}V_{\mathrm{DC}}$ and $\mathrm{d}G/\mathrm{d}B$ as a function of DC-bias V_{DC} and in-plane magnetic field B, for a 1.7 μm device, mapped at $V_{\mathrm{WG}} = -0.515$ V. Here, the 1D signal was fitted assuming a single plasmon type, where $m^{\star}_{\mathrm{1D}} = m^{\star}_{\mathrm{2D}} = 0.93 m_{\mathrm{b}}$. The dashed black curves indicate the location of the subtracted 2D-2D 'parasitic' signal mapped in Fig. 5.6. The dashed- and dashed-dotted magenta curves mark the capacitance corrected and uncorrected resonances arising from the tunnelling between the lower-well (LW) ground states and the upper-well (UW) wire region. They reveal the dispersion of the elementary excitations in the 1D UW wire region. Similarly, the dashed and dash-dotted blue curves mark the location of the resonances resulting from the reverse tunnelling process, between the UW ground states and the LW, revealing the dispersion of the 2D LW.

As can be seen from Fig. 5.9, while $m_{\mathrm{s}} = m^{\star}_{\mathrm{2D}}$ provides a good match to the data, even when taking $m_{\mathrm{c}} < m^{\star}_{\mathrm{2D}}$ one still fails to fully capture the observed behaviour for this mode. This is particularly noticeable in the particle sector when taking the $\mathrm{d}G/\mathrm{d}B$ differential. Furthermore, note that any dispersion for the holon branch in this sector should also catch the low-energy charge mode, that is, the holon branch in the hole sector, when extended back to it, something which is clearly not the case, see Fig. 5.9 inset.

Both models introduced above have proven insufficient in fully capturing the observed 1D tunnelling dispersions. While it is clear that a single parabola cannot satisfactorily account for the observed dynamics, separating the dispersion in two, for spin and charge modes respectively, still does not fully explain the position of the measured resonances. In the next section we will introduce the 1D Fermi-Hubbard model, which will be used to further analyse the 1D-2D tunnelling maps.

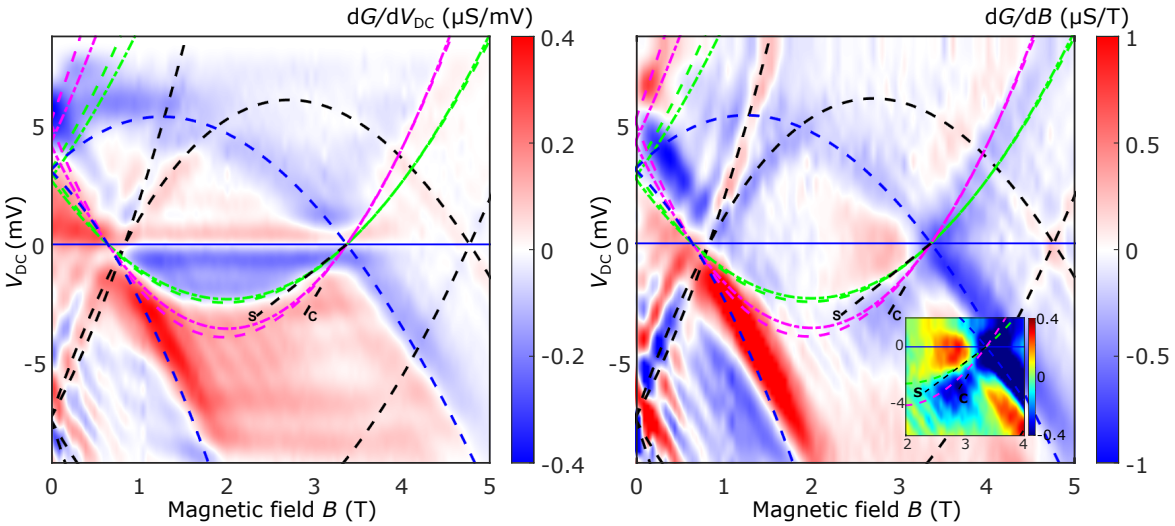

Fig. 5.9 One Fermi sea and two plasmons. Same data as that shown in Fig. 5.8 but now fitted assuming two different dispersions, for spin and charge respectively. The dashed black and blue lines have the same interpretations as in Fig. 5.8. The green curves correspond to the spinon mode with $m_s = m^\star_{2D}$. The magenta lines, on the other hand, mark the location of the holon mode with $m_c < m^\star_{2D}$. Inset: spin-charge separation, marked by dashed black 'S' and 'C' lines, near the $+k_F$ point, at low bias.

5.6 The Hubbard model

The Hubbard model is a microscopic model used in treating interacting particles, usually fermions, subject to a periodic potential (*i.e.*, in a lattice). At its core, it consists of only two parameters, one kinetic term which allows 'hopping' of particles between nearby sites, and one potential term reflecting on-site interactions. Nevertheless, for its apparent simplicity, it has been successfully applied in explaining a wide range of phenomena, including the transition between conducting and Mott insulating systems, the study of high-temperature superconductors, quantum magnetism, and charge-density waves. For the purposes of this work, however, the advantage of this model stems from the fact that it is fully integrable in 1D, meaning that it allows full analytical solutions of the dispersion spectra, both in the linear (*i.e.*, low-energy) and nonlinear (*i.e.*, high-energy) regimes to be obtained. We begin our discussion by introducing second-quantisation operators, in terms of which the Hubbard model can be written.

5.6.1 Creation and annihilation operators

Creation and annihilation operators are often used in many-body physics as an alternative to having to deal explicitly with many-body wavefunction symmetry, providing a simple

and straightforward language for constructing the Hamiltonian. Their most well-known application is probably in the context of the quantum harmonic oscillator (QHO), which we will use to start our analysis. For a QHO, the creation and annihilation operators are defined in terms of the position $\hat{x}$ and momentum $\hat{p}$ operators as

$$\hat{a} = \sqrt{\frac{m\omega}{\hbar}}\hat{x} + i\sqrt{\frac{1}{2m\omega\hbar}}\hat{p} \qquad \hat{a}^\dagger = \sqrt{\frac{m\omega}{2\hbar}}\hat{x} - i\sqrt{\frac{1}{2m\omega\hbar}}\hat{p}. \tag{5.13}$$

From here, and using the commutation relation $[\hat{x},\hat{p}] = i\hbar$, one can rewrite the QHO Hamiltonian as

$$\hat{H} = \frac{1}{2m}\hat{p}^2 + \frac{1}{2}m\omega^2\hat{x}^2 = \hbar\omega\left(\hat{a}^\dagger\hat{a} + \frac{1}{2}\right) = \hbar\omega\left(\hat{n} + \frac{1}{2}\right) \tag{5.14}$$

where $[\hat{a},\hat{a}^\dagger] = 1$ and $\hat{n} = \hat{a}^\dagger\hat{a}$ is defined as the number operator.

Let us now construct the eigenstates of this system. For the ground state, $|0\rangle$, we define it such that

$$\hat{a}\,|0\rangle = 0 \qquad \hat{H}\,|0\rangle = \frac{\hbar\omega}{2}\,|0\rangle\,. \tag{5.15}$$

The remaining excited states can then be constructed by repeatedly applying the creation operator to $|0\rangle$,

$$\hat{a}^\dagger\,|n\rangle = \sqrt{n+1}\,|n+1\rangle \qquad \hat{H}\,|n\rangle = \hbar\omega\left(n + \frac{1}{2}\right)|n\rangle\,. \tag{5.16}$$

Knowing that the finite-temperature expectation value of a quantum mechanical operator $\hat{A}$ is given by $\langle\hat{A}\rangle = Z^{-1}\mathrm{Tr}[\hat{A}\exp-(\beta\hat{H})]$, where Z is the partition function and $\beta = 1/\mathrm{k_B}T$ with $\mathrm{k_B}$ being the Boltzmann constant, we obtain $\langle\hat{n}\rangle = 1/(e^{\beta\hbar\omega} - 1)$, that is, the Bose-Einstein distribution function, thus confirming that the states created/destroyed follow Bose statistics.

The Hubbard model for electrons in solids differs from this paradigm in the sense that it deals with fermions and therefore needs to be defined in terms of fermionic creation and annihilation operators. We introduce them as $\hat{c}^\dagger_{j\sigma}$ and $\hat{c}_{j\sigma}$, referring, respectively, to the creation and destruction of a fermion of spin σ on site j, where $\sigma = \{\uparrow,\downarrow\}$. Note that these differ from $\hat{a}$ and $\hat{a}^\dagger$ in a number of ways, starting with the fact that they are not defined in terms of either $\hat{x}$ or $\hat{p}$. Most interestingly, the new degrees of freedom σ and j also imply a certain level of locality to the model, with the occupation number states no longer being defined by a single value n, but instead by a collection of numbers $n_{j\sigma}$, where $|n_{1\uparrow}n_{2\uparrow}n_{1\downarrow}n_{2\downarrow}\ldots\rangle$ corresponds to sites 1, 2, …, respectively.

We define $\hat{c}_{j\sigma}$ as second-quantisation fermionic operators, which obey the following anticommutation relations

$$\{\hat{c}_{j\sigma}, \hat{c}^{\dagger}_{l\sigma'}\} = \delta_{j,l}\delta_{\sigma,\sigma'} \qquad \{\hat{c}^{\dagger}_{j\sigma}, \hat{c}^{\dagger}_{l\sigma'}\} = 0 \qquad \{\hat{c}_{j\sigma}, \hat{c}_{l\sigma'}\} = 0 \tag{5.17}$$

Like before, a fermion can simply be created by acting on the vacuum state, $\hat{c}^{\dagger}_{j\sigma}|0\rangle = |1\rangle$. Note, however, that now as a consequence of the anticommutation relations above, $\hat{c}^{\dagger}_{j\sigma}|1\rangle = \hat{c}^{\dagger}_{j\sigma}\hat{c}^{\dagger}_{j\sigma}|0\rangle = 0$. This is, of course, nothing more than the Pauli exclusion principle, where the maximum occupation of a site with a particular spin state is limited to 1. Another property of these fermionic operators is that they ensure that the wavefunction remains antisymmetric when exchanging labels of two particular states, *i.e.*, $\hat{c}^{\dagger}_{j\sigma}\hat{c}^{\dagger}_{l\sigma} = -\hat{c}^{\dagger}_{l\sigma}\hat{c}^{\dagger}_{j\sigma}$.

5.6.2 The Hubbard Hamiltonian

We are now ready to write down the Hubbard Hamiltonian. In 1D, it takes the form of

$$\hat{H} = -t \sum_{j=1,\sigma=\uparrow,\downarrow}^{L/a} (\hat{c}^{\dagger}_{j\sigma}\hat{c}_{l\sigma} + \hat{c}^{\dagger}_{l\sigma}\hat{c}_{j\sigma}) + U \sum_{j=1}^{L/a} n_{j\uparrow}n_{j\downarrow} - \mu \sum_{j=1}^{L/a} (n_{j\uparrow} + n_{j\downarrow}), \tag{5.18}$$

where $c_{j\sigma}$ are the second-quantisation operators as defined in section 5.6.1, $n_{j\sigma} = c^{\dagger}_{j\sigma}c_{j\sigma}$ is the local density operator, L is the length of the wire, and a is the crystal's lattice parameter.

The key assumption of the Hubbard model is that it simplifies the positions of atoms in a crystal to a number of lattice points, each with a single energy level, therefore ignoring any possible sub-atomic structure. When imposing the Pauli exclusion principle, this results in each site only being allowed one out of four configurations: empty, single up fermion, single down fermion, or double occupancy (by different spin states necessarily). While electrons moving around naturally interact with one another via a screened Coulomb interaction, it is expected that this will be at its strongest for those that are forced to occupy the same site. Therefore, in the Hubbard model, the interaction energy U is zero for an empty or singly occupied site, and U when double occupied. This property is naturally captured by the term $Un_{j\uparrow}n_{j\downarrow}$. Furthermore, note that, in addition to on-site interactions, nearest- or second-nearest neighbours interactions between electrons in different sites can also be included, via terms such as $Vn_{j,\sigma}n_{j\pm1,\sigma'}$ and $Vn_{j,\sigma}n_{j\pm2,\sigma'}$. These, however, will not be considered here.

Looking at equation (5.18), the Hubbard model is then fully determined by just two microscopic parameters, the hopping amplitude t, and the two-body interaction energy U. Here, the first term, associated with the kinetic energy, describes the destruction of a fermion of spin σ in lattice site l and its creation on site j (or vice-versa). Physically, its magnitude

is determined by the amount of overlap between the wavefunctions of any pair of electrons. These normally decay exponentially fast away from the lattice points and, therefore, only nearest-neighbour hopping is generally accounted for. The second term, on the other hand, is associated with the interaction energy and, as discussed above, is only non-zero for doubly occupied sites. Finally, the last term is the system's chemical potential, which controls the filling. For a lattice of N sites, the total filling will be $2N$ given spin degenerancy, while a half-filled state will correspond to N.

The local nature of U means that it is sensitive to both the Coulomb interaction strength, via the electronic charge e, and the interaction radius R, the latter of which we can vary in our experiment (see chapters 6 and 7). Furthermore, note that even though Coulomb interactions between same-charge fermions are normally repulsive (*i.e.*, $U < 0$), the Hubbard model can also be used in attractive regimes simply by flipping the sign of the interaction parameter.

Let us now construct the many-body eigenstates of the Hubbard model in 1D following the approach used in [39, 131]. For a given N-particle state described by lattice positions $j_1, \ldots, j_\mathrm{N} = \mathbf{j}$ and spin configuration $\alpha_1, \ldots, \alpha_\mathrm{N} = \alpha$, the wavefunction can be constructed as

$$\sum_{\mathbf{j}\alpha} a_{\mathbf{j}\alpha} c^\dagger_{j_1\alpha_1} \ldots c^\dagger_{j_\mathrm{N}\alpha_\mathrm{N}} |0\rangle \,, \tag{5.19}$$

where the amplitudes are given by a superposition of plane-waves

$$a_{\mathbf{j}\alpha} = \sum_P A_{PQ\alpha} e^{i(P\mathbf{k}a)\cdot(Q\mathbf{j})}. \tag{5.20}$$

Here, Q is the permutation that orders all N coordinates such that $Q_{j_1} < \cdots < Q_{n_N}$, $\mathbf{k} = k_1, \ldots, k_N$ is the momentum of all N particles, A is a phase factor (see equation (5.21)), and $\sum_P$ is the sum over all possible permutations P of the charge momenta, similar to the Slater determinant for free particles.

Unlike the Slater determinant, however, when exchanging two electrons, this does not simply result in a sign change but instead introduces a phase factor $A_{PQ\alpha}$ which depends on the spin configuration $Q\alpha$ as

$$\begin{aligned} A_{PQ\alpha} = (-1)^{PQ} \sum_R \left(\prod_{1\le l<m\le M} \frac{R\lambda_l - R\lambda_m - \frac{iU}{2t}}{R\lambda_l - R\lambda_m} \right) \\ \times \prod_{l=1}^{M} \frac{\frac{iU}{2t}}{R\lambda_l - \sin Pk_l a + \frac{iU}{4t}} \prod_{j=1}^{s_l-1} \frac{R\lambda_l - \sin Pk_j a - \frac{iU}{4t}}{R\lambda_l - \sin Pk_j a + \frac{iU}{4t}}, \end{aligned} \tag{5.21}$$

where $\mathbf{s} = s_1, \ldots, s_M$ are the coordinates of the M spins $\uparrow$ in the configuration α of all spins of N particles, $\lambda = \lambda_1, \ldots, \lambda_M$ are the respective spin momenta, and $\sum_R$ is the sum over all possible permutations of these.

Let us consider a simple example. For a spin configuration of $N = 8$ electrons where 5 spins are $\downarrow$ and 3 spins are $\uparrow$, we have

$$\alpha_1, \ldots, \alpha_N = \downarrow\downarrow\uparrow\downarrow\uparrow\uparrow\downarrow\downarrow \,. \tag{5.22}$$

Here, the positions of the $\uparrow$ spins are $\mathbf{s} = 3, 5, 6$ which, following from above, are interpreted as coordinates of $M = 3$ excitations in the spin chain of total length $N = 8$. In order to change these spins, one can consider electrons of opposite spin interacting via the Coulomb interaction, which changes their coordinates along the wire, making the spin eigenmodes extended, at least when in the low-density limit (*i.e.*, less than half-filling) away from the Mott-insulator regime. Alternatively, electrons with the same momentum can also interact with one another, making their spins also interact with each other and causing many-spin states consisting of M individual spins to be correlated in their own right.

The allowed momenta are quantised by boundary conditions. If periodic, these give the Lieb-Wu equations

$$k_j L - \sum_{m=1}^{M} \varphi\left(\lambda_m - k_j a\right) = 2\pi I_j, \tag{5.23}$$

$$\sum_{j=1}^{N} \varphi\left(\lambda_m - k_j a\right) - \sum_{l=1}^{M} \left(\lambda_m/2 - \lambda_l/2\right) = 2\pi J_m, \tag{5.24}$$

$$\text{with} \quad \varphi(x) = -2\arctan\left(\frac{4tx}{U}\right), \tag{5.25}$$

with N non-equal integers I_j and M non-equal integers J_m defining the solution for the orbital k_j and the spin momenta λ_m of an N-electron state for a given value of the microscopic parameter U/t. Note that the simultaneous quantisation of both the spin and charge degrees of freedom results in a system of $N + M$ connected nonlinear equations for any finite interaction parameter U. Here, the eigenenergy of the many-body state is $E = ta^2 \sum_{j=1}^{N} k_j^2$, while its momentum is $k = \sum_{j=1}^{N} k_j$.

5.6.3 Two Fermi seas and the interaction parameter γ

Having now obtained the many-body eigenstates and eigenenergies of the 1D Hubbard model we can start analysing the emerging picture.

The 1D wavefunction in equations (5.19) and (5.20) is zero for any equal pair of either k_j or λ_m, meaning that both the charge and spin momenta always correspond to non-equal integer numbers I_j and J_m. This can be described by two different Fermi seas, with both kinds of modes being filled with spin or charge excitations up to some finite density. For comparison, the usual Fermi sea is filled with non-interacting fermions up to a finite Fermi energy. The difference here is that interactions give rise to a non-trivial relation between the occupation numbers I_j and J_m, as well as the momenta k_j and λ_m. These are the solutions of a system of nonlinear coupled equations for any finite interaction U, making the resulting dispersions generally dependent, therefore, on the interaction strength. From now on we will refer to this emerging picture as the two-Fermi-sea model.

In our experiment, the maximum applied field is $\sim 7\,T$. This means that the numbers of spin-up and spin-down electrons in our wires are equal within 10%, and therefore, these can be treated as remaining largely unpolarised, with $M = N/2$ spin states. This then implies that the holon Fermi sea has approximately twice as many filled states as the spinon Fermi sea, in other words, it has twice the density. The Lieb-Wu equations can then be used to give the two distributions of their momenta at the infinite-interaction point $U = \infty$.

We define the Fermi wavevector k_{F} as the maximum momentum allowed in a free-electron system, *i.e.*, when $N/2$ fermions are doubly degenerate with respect to spin for $U = 0$. As U is increased, however, this degeneracy is naturally broken. By making the interactions stronger, the charges delocalise, increasing its density by up to a factor of two, and thus giving rise to a second Fermi sea. The spin Fermi sea, on the other hand, is a type of Heisenberg spin chain, where the spin-momenta have a pronounced higher density towards the Fermi points than at the bottom of the band. Note that Fermi seas of this kind have already been observed in neutron scattering experiments of non-itinerant magnets [77, 76, 95].

Numerical solutions of the Lieb-Wu equations for various interaction energies U away from the infinite point are given in Fig. 5.10. Down to an intermediate value, both Fermi seas remain stable. When the interactions are made weak, however, the free-fermion picture is recovered, with the holon Fermi sea becoming doubly degenerate, and the spinon Fermi sea giving the spin part of the free-electron function that describes ± 1 permutation signs for electrons of different or the same spin.

The dimensionless parameter that controls this phase transition emerges from the Hubbard model itself microscopically and was first identified in [120] as

$$\gamma = \frac{\lambda_{\mathrm{F}}}{16a}\frac{U}{t}\frac{1}{1-\frac{1}{N}\sum_{l=1}^{N/2}\frac{\lambda_l^2(\infty)-\left(\frac{U}{4t}\right)^2}{\lambda_l^2(\infty)+\left(\frac{U}{4t}\right)^2}}. \tag{5.26}$$

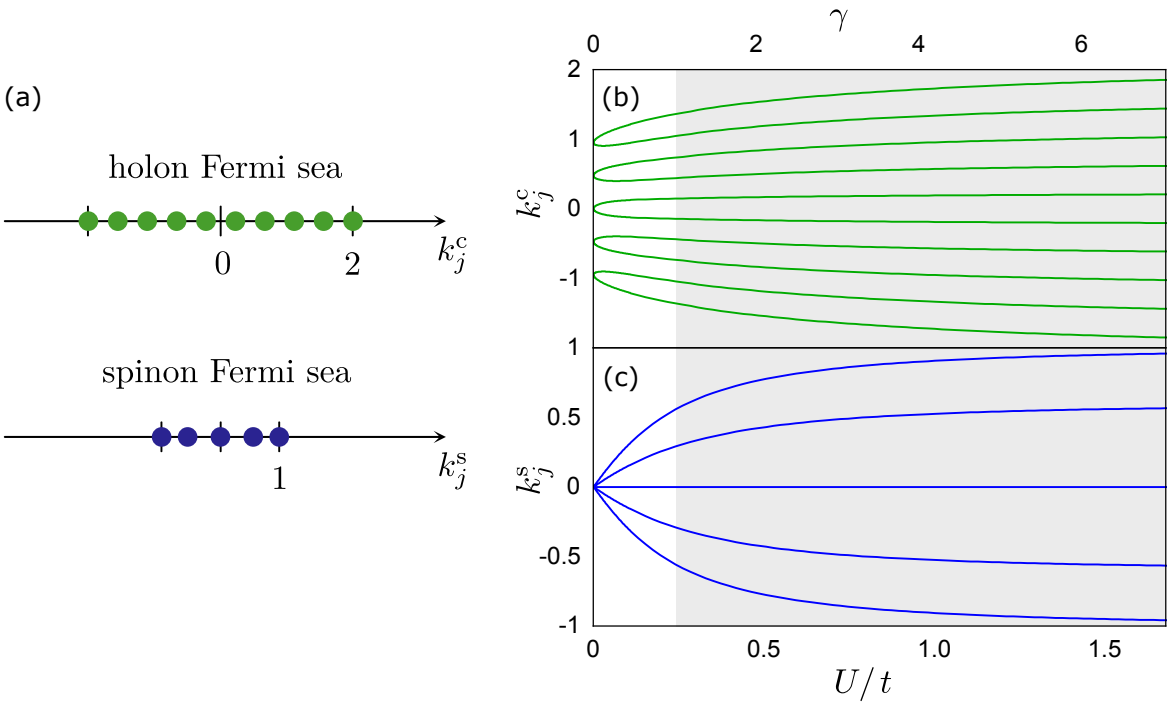

Fig. 5.10 The 1D Fermi-Hubbard model. (a) Solutions of the Lieb-Wu equations (5.23) and (5.24) for the charge and the spin degrees of freedom of the ground state in the infinite interactions limit $U = \infty$. (b) and (c) then show, respectively, the evolution of the charge and spin Fermi seas, as a function of U/t, for a system of $N = 10$, $M = 5$ unpolarised electrons. Note that the charge momenta are normalised with respect to the free-electron Fermi wavevector, $k_j^c = k_j/k_F$, where $k_F = \pi N/(2L)$, while the spin momenta $k_j^s = -2\arctan[U/(4t\lambda_j)]/\Lambda$ are normalised with respect to the solution of the integral Orbach equation Λ. This plays the same role as the Fermi momentum for Heisenberg spin chains, see [97]. The dimensionless parameter γ, defined in equation (5.26), plays a role similar to r_s, see text for discussion. In the grey area, for $\gamma > 1$, interactions are strong enough so that the two Fermi seas are fully developed and can be separately resolved.

Here, $\lambda_F = 4L/N$ is the Fermi wavelength (of the 1D free-electron gas), a is the lattice parameter, and $\lambda_l(\infty)$ the spin part of the solution of equations (5.23) and (5.24) in the infinite-interaction limit $U = \infty$. Taking the thermodynamic limit and assuming an unpolarised Heisenberg chain, we determine the numerical value of the sum in the denominator to be $1 - \sum_l \ldots /N = 1.193(1)$, thus reducing to

$$\gamma = 0.032 \frac{\lambda_F}{a} \frac{U}{t}. \tag{5.27}$$

As we will see later, γ plays a role similar to the interaction parameter r_s, already introduced in section 5.3. Its construction, however, is more encompassing, for it has knowledge not only of the density of the system, via λ_F, but also of the Coulomb screening

potential, via U. When the interactions are strong, $\gamma > 1$, both the spinon and holon Fermi seas are fully developed. On the other hand, when $\gamma < 1$, the holon Fermi sea is still too close to the double occupancy of the free Fermi gas and cannot, therefore, be separately resolved.

5.6.4 Spin and charge excitations

Let us conclude by discussing the resulting dispersion spectra for both spin and charge excitations.

We saw in chapter 2 that for 1D systems, all allowed types of excitations must correspond to collective responses of the entire system. This means that, for example, when adding an electron into a wire, with its charge and spin, this must eventually lead to the creation of two new excitations, one holon and one spinon. With two Fermi seas, however, the question naturally becomes, where are these excitations being created, and with what properties.

Starting with states of energy $E = \mu$, the first option is adding a holon to its Fermi sea at the $2k_{\mathrm{F}}$ point and a spinon to its Fermi sea at $-k_{\mathrm{F}}$, resulting in a net momentum for the total excitation of $k = k_{\mathrm{F}}$. Alternatively, one can add the holon and the spinon on the same side of their respective Fermi seas, say $2k_{\mathrm{F}}$ and k_{F}, which produces a net momentum $k = 3k_{\mathrm{F}}$. Because our wires have inversion symmetry, the mirror of this argument also produces the $k = -k_{\mathrm{F}}$ and $k = -3k_{\mathrm{F}}$ points, see Fig. 5.11.

After identifying the Fermi points $\pm k_{\mathrm{F}}$, one can also consider pairs of excitations at some finite momenta, ΔP_c and ΔP_s, above (or below) these. For simplicity, let us consider the Fermi point $k = k_{\mathrm{F}}$. As described above, the set of nonlinear Lieb-Wu equations that governs these excitations results in distorted Fermi seas, with all states in the spinon Fermi sea becoming asymmetric and non-equidistant from the ground-state, while the holon Fermi sea as a whole shifts by the total spinon momentum. Most importantly, however, the total momentum of the electronic excitation remains a good quantum number, with $k = 2\pi(\sum_j I_j + \sum_m J_m)/L$ being summed over the entire set of quantisation integer numbers I_j and J_m. Note that k here is independent of U.

Since the total momentum is conserved in a many-body system, one can find the momentum of the holon and the spinon excitations as

$$k = k_{\mathrm{F}} + \Delta P_{\mathrm{c}} \qquad k = k_{\mathrm{F}} + \Delta P_{\mathrm{s}} \tag{5.28}$$

where $\Delta P_{\mathrm{c}} = 2_{N+1}/L$ and $\Delta P_{\mathrm{s}} = 2_{M+1}/L$. The distance in momentum between neighbouring points is then always equal to $2\pi/L$, which we define as the quantum of momentum. Because this is independent of U, the crossing points at $E = \mu$, $\pm k_{\mathrm{F}}$ and $\pm 3k_{\mathrm{F}}$, are always fixed, regardless of how strong or weak the interactions may be.

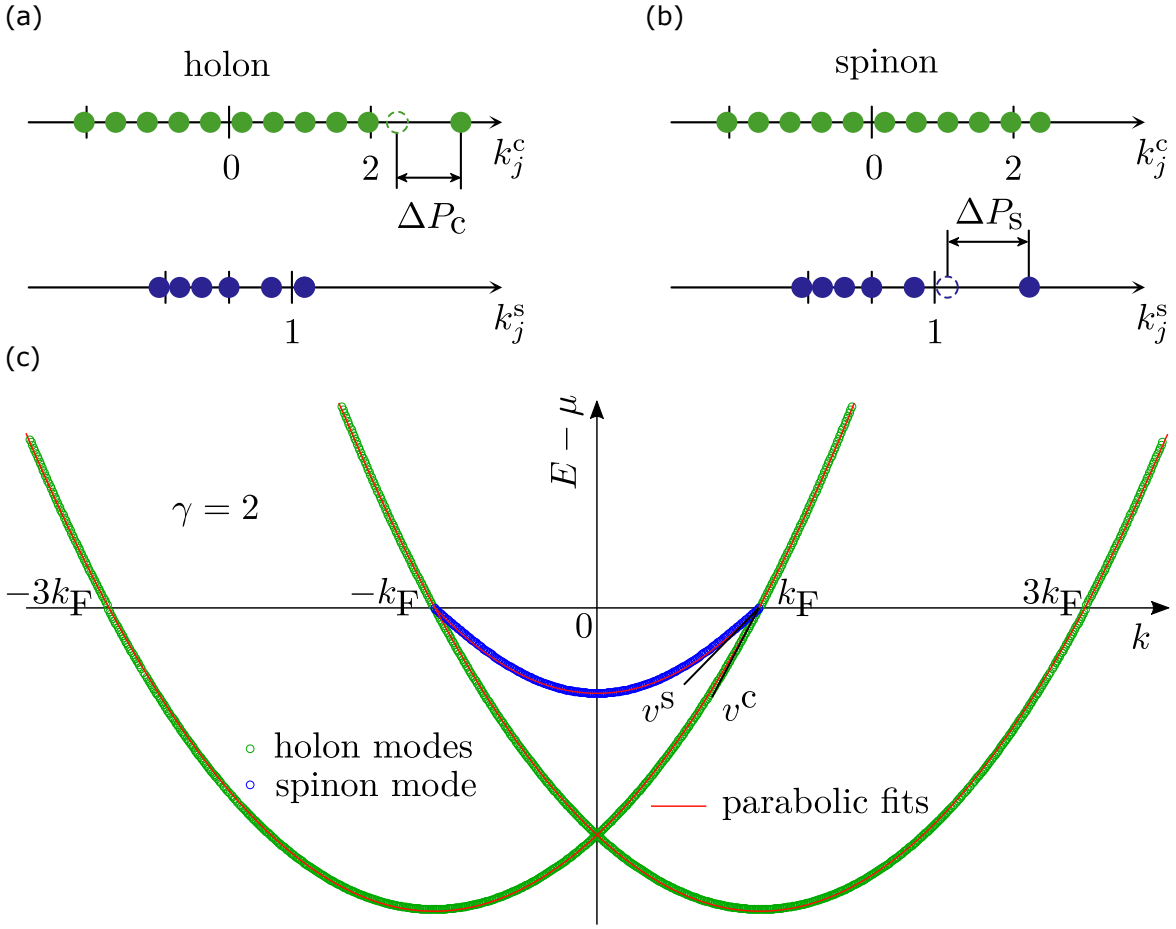

Fig. 5.11 Two Fermi seas for spin and charge. (a) Holon(-type) excitation. Here, the spinon mode is placed at the lowest possible momentum state while the holon is excited by some momenta ΔP_c over its lowest momenta configuration. (b) Same as (a) but now for spinon (type) excitations. (c) Full dispersion spectra for both holons (green) and spinons (blue) obtained by solving the Lieb-Wu equations (5.23) and (5.24) for $N = 550$ and $M = 275$, at an interaction strength $\gamma = 2$. The thin red lines mark parabolic fits to each mode. The black lines at the Fermi point $+k_F$, on the other hand, mark the linear dispersion of holons v^c and spinons v^s of the linear spinful Tomonaga-Luttinger model. Numerical calculations were performed by O. Tsyplyatyev.

In order to obtain the set of energies associated with these excitations, we solve the Lieb-Wu equations numerically for different values of U. At low energies (*i.e.*, $\Delta E \lesssim \mu$), the solutions form two linear dispersions with non-commensurate slopes, v^{c} and v^{s}. These are nothing more than the pair of Luttinger parameters already derived in the context of the spinful linear Tomonaga-Luttinger model, see section 2.2.2. When the interactions are weak (*i.e.*, in the limit of $U \to 0$), their ratio tends to $v^{\mathrm{c}}/v^{\mathrm{s}} = 1$, while for stronger U it increases. In the spectral function, these v^{c} and v^{s} are identified as a pair of divergences, see Fig. 2.6a.

Extending these modes in both momentum and energy away from the Fermi points provides their natural generalisation to the nonlinear regime. Note that, unlike before, where two branches would meet at $\pm k_{\mathrm{F}}$, there are now three. This is a manifestation of the different densities of the spinon and the holon Fermi seas discussed above, the latter which now has the second crossing point at $\pm 3k_{\mathrm{F}}$. It is also interesting to note that, even though the obtained dispersions are not, strictly speaking, parabolic, they are indeed very close to this for finite U. Because they are very close to parabolae, therefore, we can introduce two new masses, m_{c} and m_{s}, for holons and spinons respectively, which are given by the curvature of their respective dispersions.

5.7 Two Fermi seas and two plasmons

Let us now go back to the data first introduced in section 5.5. We have seen in section 5.6 that the 1D Fermi-Hubbard model predicts different dispersions for both charge and spin across the whole spectrum. These are, as seen in Fig. 5.11, very close to parabolae. Most interestingly, however, is the fact that they are also expected to have different degeneracies, with the degeneracy of spinons being twice that of holons, as seen in Fig. 5.11.

Starting from the assumption that the dispersion of each mode is parabolic, before correcting for capacitance, we get

$$E_{\mathrm{s}}(k) = \frac{\hbar^2 k^2}{2m_{\mathrm{s}}} - E_{\mathrm{F}}^{\mathrm{s}} = \frac{\hbar^2}{2m_{\mathrm{s}}}(k^2 - k_{\mathrm{F}}^2) \tag{5.29}$$

and

$$E_{\mathrm{c}}(k) = \frac{\hbar^2 (k + k_{\mathrm{F}})^2}{2m_{\mathrm{c}}} - E_{\mathrm{F}}^{\mathrm{c}} = \frac{\hbar^2}{2m_{\mathrm{c}}}\left[(k + k_{\mathrm{F}})^2 - 4k_{\mathrm{F}}^2\right]. \tag{5.30}$$

Here, $E_{\mathrm{F}}^{\mathrm{s}}$, m_{s} and $E_{\mathrm{F}}^{\mathrm{c}}$, m_{c} are the respective Fermi energies and renormalised masses for each mode, with $k_{\mathrm{F}} \equiv k_{\mathrm{F,1D}}$.

From each dispersion, one can then obtain the resulting group velocity at low energies. Since $v = \mathrm{d}\omega/\mathrm{d}k = \hbar^{-1}\mathrm{d}E/\mathrm{d}k$, this results in

$$v^{\mathrm{s}} = \frac{1}{\hbar}\frac{\mathrm{d}f_1}{\mathrm{d}k}\bigg|_{k=k_{\mathrm{F}}} = \frac{\hbar k}{m_{\mathrm{s}}}\bigg|_{k=k_{\mathrm{F}}} = \frac{\hbar k_{\mathrm{F}}}{m_{\mathrm{s}}} \tag{5.31}$$

and

$$v^{\mathrm{c}} = \frac{1}{\hbar}\frac{\mathrm{d}f_2}{\mathrm{d}k}\bigg|_{k=k_{\mathrm{F}}} = \frac{\hbar(k+k_{\mathrm{F}})}{m_{\mathrm{c}}}\bigg|_{k=k_{\mathrm{F}}} = \frac{2\hbar k_{\mathrm{F}}}{m_{\mathrm{c}}}, \tag{5.32}$$

giving

$$\frac{v^{\mathrm{c}}}{v^{\mathrm{s}}} = \frac{K_{\mathrm{s}}}{K_{\mathrm{c}}} = \frac{2m_{\mathrm{s}}}{m_{\mathrm{c}}}. \tag{5.33}$$

Equation (5.33) allows us to relate the spin-to-charge mass ratio to the phenomenological Luttinger parameters $K_{\mathrm{c,s}}$, first introduced in section 2.2.2 as $v^{\mathrm{c}} = v_{\mathrm{F}}/K_{\mathrm{c}}$ and $v^{\mathrm{s}} = v_{\mathrm{F}}/K_{\mathrm{s}}$. Note that, in general, $K_{\mathrm{c}} \neq K_{\mathrm{s}}$.

The ratio $K_{\mathrm{c}}/K_{\mathrm{s}}$ is a common figure of merit found in the literature for estimating the interaction strength in 1D systems. We highlight however that, strictly speaking, $K_{\mathrm{c,s}}$ are defined within the Luttinger model and are therefore only valid at low energies. Nevertheless, the beauty of equation (5.33) is that it relates a global quantity, the mass, found from fitting parabolae to the whole spectrum (*i.e.*, both at low and high energies), to a local one, the velocity, taken from the gradient of the dispersion around the $\pm k_{\mathrm{F}}$ points. It remains valid as long as the dispersions of each mode (as predicted from the Hubbard model) do not deviate significantly from parabolae. Furthermore, note that the extra factor of 2 in the last term of equation (5.33) essentially arises because k_{F} is twice as large for holons as it is for spinons. Specifically, for repulsive interactions, since $K_{\mathrm{s}} > 1$ and $K_{\mathrm{c}} < 1$, we have $m_{\mathrm{c}} < 2m_{\mathrm{s}}$.

Fig. 5.12 shows some example data of 1D-2D tunnelling in the single-subband regime fitted use the two-Fermi-sea model. Here, the dashed lines were obtained from the parabolic model described in this section while the open circles using the solutions of the Fermi-Hubbard model. Both models are in very good agreement across the whole momentum and energy range probed experimentally.

Let us analyse specific areas of the tunnelling map in more detail. In section 5.5.1 and 5.5.2 we saw that assuming a single Fermi sea, even when taking separate dispersions for spin and charge, still failed to explain the position of the tunnelling resonance observed at high energies in the particle sector (*i.e.*, $V_{\mathrm{DC}} > 0$). Specifically, it was observed that this could not be extended to either the spin mode or the charge branch in the hole sector (*i.e.*, $V_{\mathrm{DC}} < 0$). In contrast note how, unlike before, the holon mode emanating from $+k_{\mathrm{F}}$ is now fully captured both in the hole and particle sectors, see Fig. 5.13.

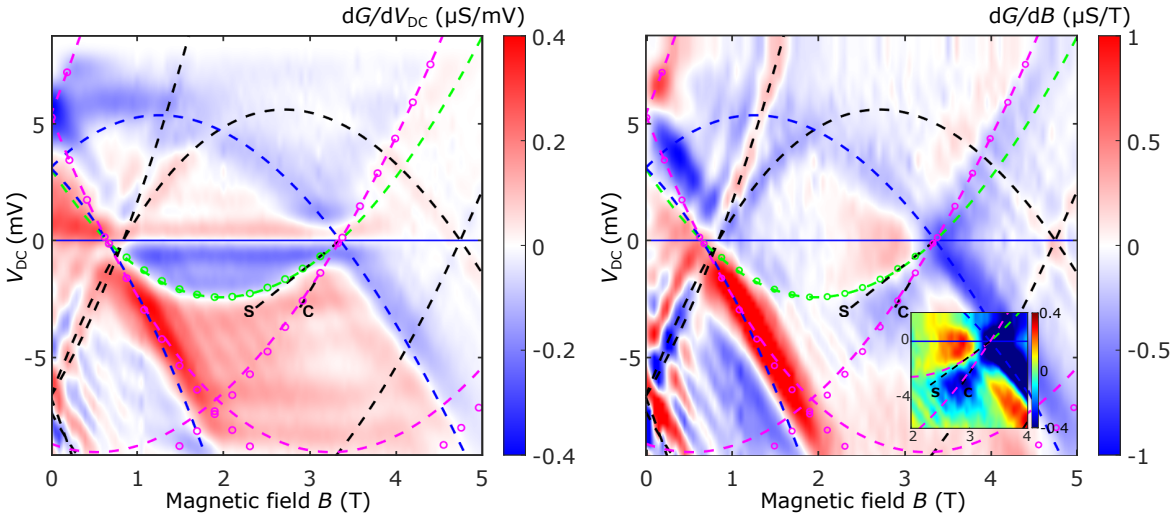

Fig. 5.12 Two Fermi seas with two plasmons. Same data as that shown in Figs. 5.8 and 5.9 but now fitted using two Fermi seas as predicted in section 5.6, see text for discussion. Dashed black and blue curves have the same meanings as before. The dashed green and magenta lines mark the 1D dispersions for spinons and holons, respectively. The open-circle curves are the corresponding solutions of the 1D Fermi-Hubbard model for $N = 54$. Inset: spin-charge separation near the $+k_F$ point at low bias.

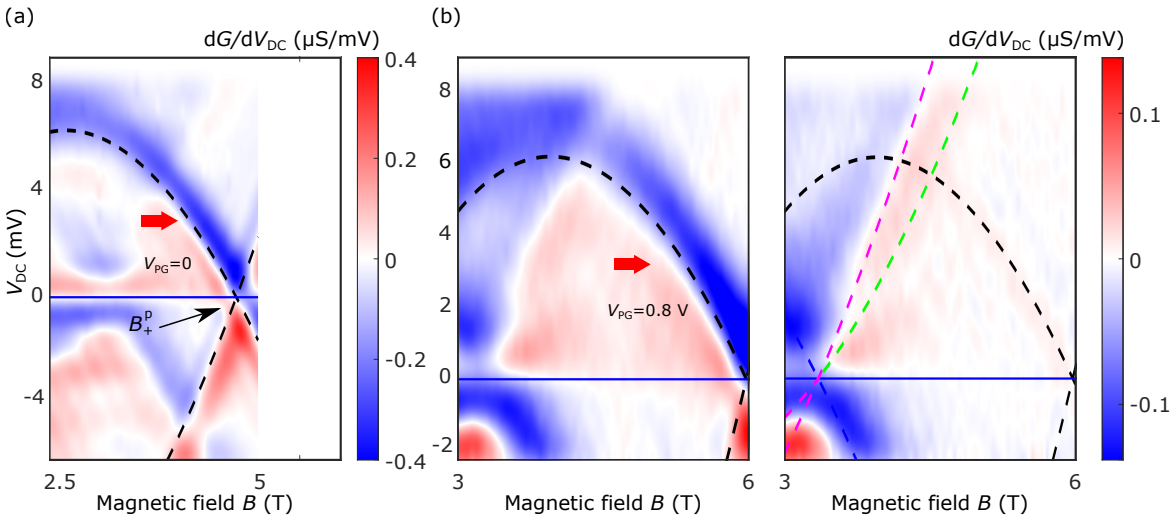

Fig. 5.13 The holon mode at $+k_F$. (a) Tunnelling conductance differential $\mathrm{d}G/\mathrm{d}V_{DC}$ around the $+k_F$ point for a device mapped at $V_{PG} = 0$. Note that $B_+^p < 5\,T$. (b) Same device as in (a) but now mapped with $V_{PG} = 0.8\,V$. Here, $B_+^p > 5\,T$, with the whole 2D-2D 'parasitic' tunnelling signal having now moved $\sim 1\,T$ to the right. This allows the region around $+k_F$ to be mapped free from 'parasitic' effects. Left and right panels show, respectively, the data before and after the background was subtracted. All curves have the same meaning as in Fig. 5.12.

Another tunnelling feature that can only be accounted for once two Fermi seas are assumed can be found by looking at the line-shape of the various tunnelling processes happening at zero magnetic field. Fig. 5.14a shows $\mathrm{d}G/\mathrm{d}V_{\mathrm{WG}}$ vs wire-gate voltage V_{WG} and DC-bias V_{DC} for two values of the 'parasitic'-region gate voltage, $V_{\mathrm{PG}} = 0$ and $V_{\mathrm{PG}} = +0.3\,V$. Note that PG is a gate going over the 'parasitic' (2D) injection region and, therefore, it allows us to modulate the electron density in this region without affecting the 1D wires.

By comparing both panels in Fig. 5.14a one can then see which features are 'parasitic' and which are coming from the 1D wires, by looking at how they respond to V_{PG}. For instance, all features at negative DC bias move away for positive V_{PG}, indicating that they are not related to the 1D wires themselves. They correspond to the 2D-2D 'parasitic' tunnelling coming from the injection region and already discussed in section 5.4.1. On the other hand, at positive V_{DC}, the main contribution comes from the superposition of both 1D and 2D tunnelling happening in the wire region. As expected, this is not affected by changes in V_{PG}. It also disappears at around $V_{\mathrm{WG}} = -0.6\,\mathrm{V}$, the same value at which the wires are known to pinch off, see Fig. 5.4.

At $B = 0$ it is expected that the tunneling current I should peak as V_{DC} is changed, corresponding to the 1D and 2D spectral functions coming in and out of alignment. The tunnelling conductance, $G = \mathrm{d}I/\mathrm{d}V$ should therefore have a peak and a trough (negative differential conductance, NDC) like that shown at small wire-gate voltages in Fig. 5.14b, which shows the line profiles of the data in Fig. 5.14a for $V_{\mathrm{PG}} > 0$. Further analysing the tunnelling signal, it can be seen that the tunnelling resonance slowly broadens as V_{WG} is made progressively more negative, that is, by making the confinement stronger. Simultaneously, higher 1D subbands and the small overlap of a large number of states in the two systems (note that at $B = 0$ they are not offset in momentum), enhance the tunnelling above the peak, moving it to higher bias while also suppressing the NDC.

As the wires are squeezed, from $-0.53\,\mathrm{V}$ onwards, first a kink, then two defined features can be seen. As discussed before, these are unaffected by V_{PG} and therefore cannot arise from the 'parasitic' region. While this feature could indicate tunnelling into an empty 1D subband, there is no sign of such anywhere else in our data. The splitting is also far too great to be explained as simple energy broadening (where typically $\Gamma \sim 0.2 - 0.3\,\mathrm{meV}$). Note also that Γ has always been observed to remain constant regardless of the confinement in the wires, while here we observe strong dependence on V_{WG}. Finally, the splitting can also not be explained by different masses of the 2D Fermi-liquid quasi-particles (determined in section 5.4.1) and/or the 1D spinon modes. Note that, for the latter case, the spinon mode would be equivalent to that coming from the $+k_{\mathrm{F}}$ point, which we observe to be systematically

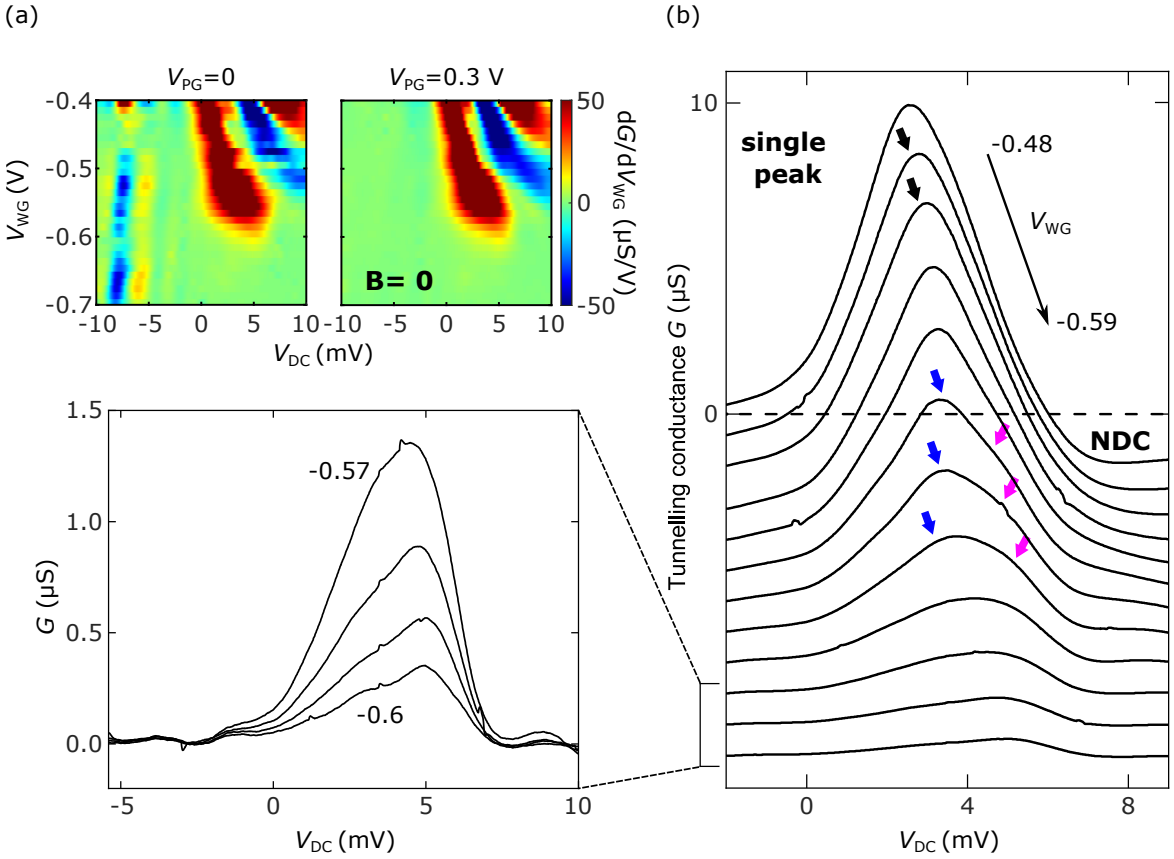

Fig. 5.14 Tunnelling processes at zero field. (a) $\mathrm{d}G/\mathrm{d}V_{\mathrm{WG}}$ *vs* wire-gate voltage V_{WG} and DC-bias V_{DC}, at $B = 0$, for both $V_{\mathrm{PG}} = 0$ and $V_{\mathrm{PG}} = 0.3\,\mathrm{V}$. Note how the latter moves the fringes arising in the 'parasitic' region out of the range of the plot. The conductance peak seen at $V_{\mathrm{DC}} > 0$ also disappears at $V_{\mathrm{WG}} \approx -0.6\,\mathrm{V}$, the same value at which the wires pinch off, see Fig. 5.5a. (b) Horizontal line-cuts of the conductance data shown in (a) for positive V_{PG}. Here, the signal can be seen to slowly broaden as V_{WG} is made progressively more negative (*i.e.*, by increasing the level of confinement in the wires and hence decreasing the density), eventually separating into two distinct features, with a similar spacing to that of the 2D and 1D holon modes in the particle sector (see blue and magenta arrows which mark, respectively, the centre of each dispersion according to the two-Fermi-sea model, and also Fig. 5.15). Every curve, except $V_{\mathrm{WG}} = -0.48\,\mathrm{V}$, has been offset for clarity. The left-hand panel shows, without any offsets, the line-cuts for $V_{\mathrm{WG}} \leq -0.57\,\mathrm{V}$, just as the 1D channels are about to pinch off.

absent in our data in the particle sector (see discussion below), and which is also therefore not expected here below $-k_F$.

We interpret the observed feature as resulting from the separation of the 1D holon mode coming from the $-k_F$ point and the 2D dispersion of the bottom well as mapped by the wires. This is in good agreement with the position of these modes at $B = 0$ as predicted from the full dispersion maps, see Fig. 5.15b. Furthermore, this feature is also completely missed when assuming just a single Fermi sea, see Fig. 5.15a. We note, however, that while NDC would in principle be expected to remain regardless of V_{WG}, its observed suppression could instead be indicative of a power-law similar to what has already been reported in [57] near the bottom of the 1D subband. Such interpretation, however, is far too speculative given the lack of knowledge of the shape of these modes which, we highlight, is still unknown theoretically. Nevertheless, the fact that the splitting is observed to strongly depend on V_{WG} rules out disorder effects. A tentative explanation instead can be found in a analogous way to spin-charge separation already reported in [60] around the $+k_F$ point, but where now the holon mode coming from $-k_F$ is seen to separate from the 2D dispersion.

As we have seen, the dispersion of the strongest features observed in the tunnelling of the experimental 1D signal cannot simply be interpreted as a single parabola, corresponding to a single Fermi sea (see section 5.5.1), even if separate modes for spin and charge are considered (see section 5.5.2). If, instead of one parabola we use two, corresponding to two Fermi seas, such as those predicted by the 1D Fermi-Hubbard model, then we can match the result of the experiment well. Note that the two modes observed in the data mark the dispersions of the pure (*i.e.*, single-particle-like) excitations, with each Fermi sea being formed by the nonlinear spinon and holon quasi-particles out of the many-body continuum away from the Fermi points.

As one final point, let us comment on the fate of the spinon mode in the particle sector. As seen from Fig. 5.12, we observe two separate dispersions (for spin and charge) in the hole sector, but only one (for charge) in the particle sector, the latter being identified as its gradient matches that of the charge line in the hole sector. No fourth dispersion, in principle expected for spin in the particle sector, is observed in any of the devices measured. Indeed, taking a naïve extension from the hole sector (green dashed), we see that it is systematically absent in the data. A tentative explanation can be found in particle-hole asymmetry in relaxation times as previously reported in [12]. Here, even though spin and charge excitations were not separately resolved (indeed, the authors took a perturbative approach, assuming a weakly interacting regime), if we assume that the spinon branch in the particle sector is unstable (so that we do not observe it), then it would be expected that hot electrons have an accelerated relaxation as they split between holons and spinons.

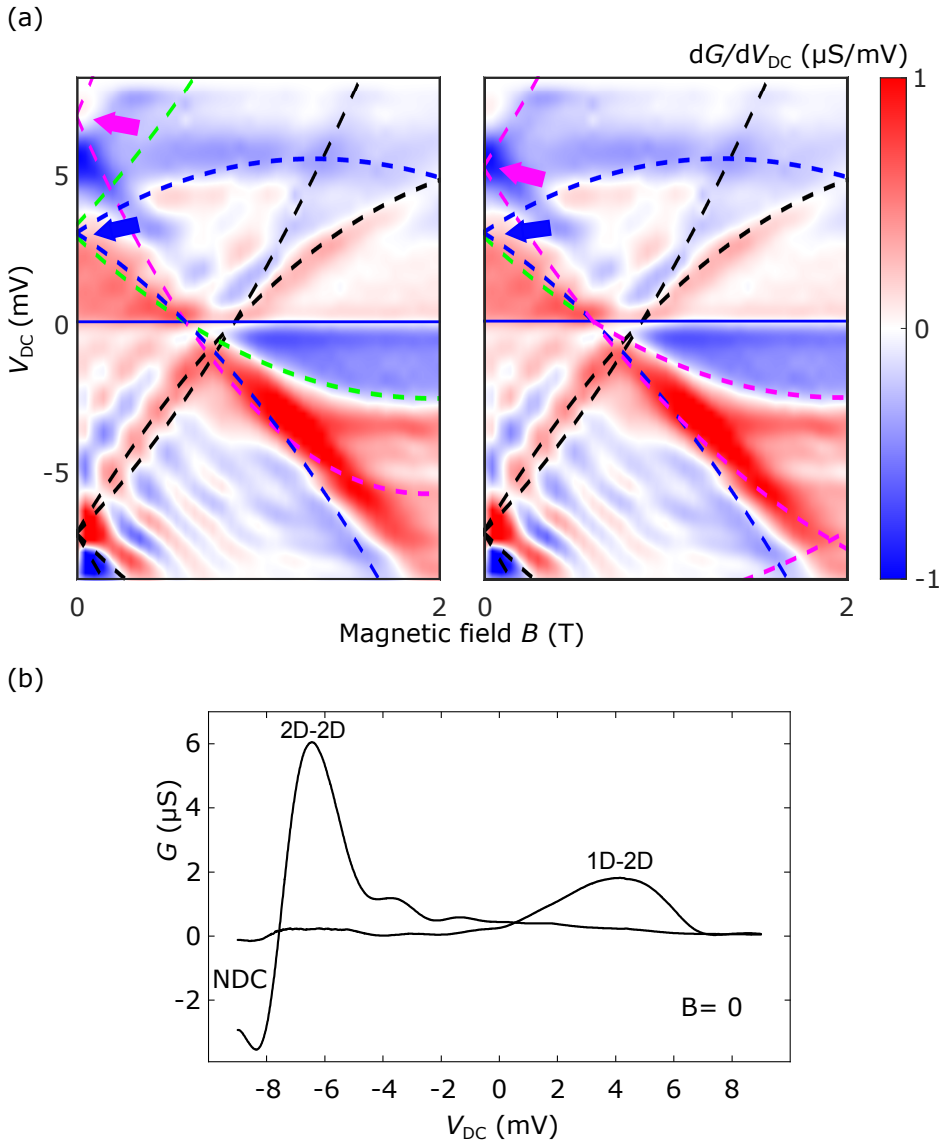

Fig. 5.15 Tunnelling modes at zero field. (a) Maps of the tunnelling conductance differential $\mathrm{d}G/\mathrm{d}V_{\mathrm{DC}}$ for a 5 μm device. Here, we analyse the data assuming one Fermi sea and two plasmons (left, see also Fig. 5.9), and two Fermi seas (right, see also Fig. 5.12). Note how the position of the holon mode (magenta) at $B = 0$ axis varies significantly between the two models. (b) Line-cuts of conductance G as a function of DC-bias V_{DC}, showing both 2D-2D (subtracted from the data in (a)) and 1D-2D tunnelling resonances. Note how, unlike in the 1D-2D case, negative differential conductance (NDC) is present in the 2D-2D signal. Nevertheless, assuming two Fermi seas, the position of the holon and the 2D modes is compatible with the observed line-shape.

Further evidence that this might indeed be the case can also be found from neutron scattering experiments in antiferromagnetic spin chains realised in insulating materials [77, 95, 76]. Here, probing the dynamic structure factor instead of the spectral function measured in the present work, the spinon Fermi sea was observed as a spectral edge with a nonlinear dispersion separating the multi-spinon continuum from a forbidden region [43, 23]. In these experiments the spectral power of the available excitations dropped very rapidly towards the particle part of the spinon dispersion, likely justifying why we are not detecting it. Unlike in these experiments, however, in our experiment the charges are delocalised, and this is the reason why we can see two Fermi seas.

Below we summarise the main figures of merit, extracted from fitting the tunnelling maps from a total of five different devices in the single-subband regime.

$\mathbf{L}$ (μm)	$n_{\mathbf{1D}}$ ($\mu\mathrm{m}^{-1}$)	$\lambda_{\mathbf{F}}$ (nm)	$r_{\mathbf{s}}$	$E_{\mathbf{F}}$ (meV)	$v^{\mathbf{s}}$ ($\times 10^5\,\mathrm{ms}^{-1}$)	$v^{\mathbf{c}}$ ($\times 10^5\,\mathrm{ms}^{-1}$)	$v^{\mathbf{s}}/v^{\mathbf{c}}$	$m_{\mathbf{s}}/m_{\mathbf{e}}$	$m_{\mathbf{c}}/2m_{\mathbf{e}}$	$m_{\mathbf{c}}/2m_{\mathbf{s}}$	γ
1	38.8	103.1	1.36	2.11	0.87	1.89	0.46	0.067	0.037	0.55	2.04
1.7	40.5	98.8	1.30	2.30	0.95	1.99	0.48	0.067	0.038	0.57	1.97
3	40.3	99.3	1.31	2.28	0.89	1.91	0.47	0.065	0.039	0.60	1.93
5	42.0	95.2	1.26	2.48	0.97	2.02	0.48	0.065	0.037	0.57	1.97
18	42.3	94.6	1.25	2.51	0.96	1.94	0.49	0.069	0.039	0.57	1.91

Table 5.1 Different parameters, extracted from a total of five different devices, by using the two-Fermi-sea model while in the single-subband regime.

5.8 Summary

In this chapter we have discussed the 1D spectra measured using tunnelling spectroscopy. We started by characterising the 1D wire-array, showing how the density as well as number of occupied 1D subbands could be tuned *in situ*. Note that all data presented in this chapter was obtained exclusively in the single-subband regime. We then discussed the fitting to the 2D-2D 'parasitic' tunnelling signal, showing how it could be used to calibrate a number of experimental parameters independently of the 1D signal. We showed how assuming a single Fermi sea, even with separate dispersions for spin and charge, proved insufficient for explaining the observed spectra. We then introduced the 1D Fermi-Hubbard model from which the many-body spectra, both at low and high energies, was obtained. Our results are compatible with a picture where two Fermi seas, for spin and charge excitations respectively, are seen to emerge. These are also observed to follow approximately parabolic dispersions. This is quite remarkable, for it establishes that in 1D, out of the many-body continuum, some single-particle-like properties still remain, and that composite excitations such as spinons and holons can take place both at low as well as high energies.

Chapter 6

Screening and mass renormalisation effects

In the previous chapter we introduced the two-Fermi-sea model, showing how two dispersions with different degeneracies are required in order to fully capture the observed spin and charge dynamics. All data presented and discussed in chapter 5 were obtained in the single-subband regime. In our devices, however, we can change the number of occupied subbands, up to four, by changing the degree of confinement in the wires. This chapter is divided into two parts, both relating to multiple-subband occupancy regimes. We start the first part by discussing how tunnelling dispersion maps can be analysed when more than one subband is occupied (section 6.1). We then show how, by varying the interaction parameter γ from the weakly to the strongly interacting regimes, one can follow the emergence of both Fermi seas separately, simultaneously quantifying the amount of 1D-1D inter-subband screening present in the system (section 6.2). We conclude this part by briefly commenting on the applicability of the 1D Fermi-Hubbard model in analysing our 1D semiconducting system (section 6.3). In the second part, we use the two-Fermi-sea picture to extract the electron mass in 1D (section 6.4), comparing it with previous results already reported in the literature for GaAs samples of higher dimensionality. This chapter follows from the discussion started in chapter 5, and establishes the overall robustness of the two-Fermi-sea picture by going beyond the single-subband regime.

All the material discussed in this chapter can be found in [125], apart from sections 6.1 and 6.2 which are reported in [124].

6.1 Multiple-subband occupancy regime

As was seen in section 5.2, by changing the level of confinement in the wires (*i.e.*, V_{WG}) we can change the number of 1D subbands that take part in the tunnelling process. In particular, once the 1D wires have been characterised (see Fig. 5.4), one can choose V_{WG} so that either two, three, or even four subbands are occupied. From here, tunnelling spectroscopy can be performed in an identical fashion to what was done before, when only one 1D subband was occupied.

Every time a new subband starts being occupied, another four parameters, B_{-}^{W}, B_{+}^{W}, m_{s}, and m_{c}, relative to that new subband, need to be added. The capacitances of each layer, $c_{\mathrm{UW}}^{\mathrm{1D}}$ and $c_{\mathrm{LW}}^{\mathrm{1D}}$, also need to be updated, with their values now lying somewhere in between the single-subband 1D-2D and the 2D-2D regimes. This leads to, for example, a total of $6+4+4+4+2=20$ parameters when in the three-subband regime.

Fig. 6.1a and Fig. 6.1b show examples of tunnelling dispersion maps obtained with, respectively, two and three 1D subbands occupied. As can be seen from the data, progressively occupying more and more subbands translates into an increase of map complexity. Nevertheless, accurate parameters for both spin and charge Fermi seas can still be extracted, albeit with larger uncertainties, as we will now outline.

We have restricted our analysis to, when applicable, the bottom two subbands even when more are occupied. One of the difficulties in analysing the data is that, as the number of occupied subbands increases, it becomes visually more difficult to reliably extract B_{-}^{W}. We know, however, that the centres of all subbands must allign at $k=0$, as evidenced by the high degree of symmetry seen from Fig. 5.4. This is not surprising, as the 1D channels are created by, approximately, parabolic confinement potentials. Therefore, we expect that

$$\frac{B_{+}^{\mathrm{W2}}+B_{-}^{\mathrm{W2}}}{2}=\frac{B_{+}^{\mathrm{W1}}+B_{-}^{\mathrm{W1}}}{2} \tag{6.1}$$

where $B_{\pm}^{Wn}$ denotes the zero-bias field crossing points of the nth subband. This allows us to obtain an initial estimate of, for example, B_{-}^{W2}, given knowledge of B_{-}^{W1}, B_{+}^{W1}, and B_{+}^{W2}.

Similarly, we can look at the zero-field bias crossing points $V_0^{\mathrm{W}n}$ between the nth subband and the V_{DC} axis at $B=0$. This gives

$$eV_{0,n}=\pm\frac{\hbar^2}{2}\left(\frac{k_{\mathrm{F,LW}}^2}{m_{\mathrm{2D}}^{\star}}-\frac{k_{\mathrm{F,UW},n}^2}{m_{\mathrm{s}}}\right)\Longrightarrow V_0^{\mathrm{W}n}\simeq\pm\frac{ed^2}{4m_{\mathrm{2D}}^{\star}m_{\mathrm{s}}}B_{+}^{\mathrm{W}n}B_{-}^{\mathrm{W}n}(m_{\mathrm{2D}}^{\star}+m_{\mathrm{s}}) \quad . \tag{6.2}$$

Here, $k_{\mathrm{F,UW},n}$ corresponds to the Fermi wavevector of the spinon mode of the nth subband while $\pm$ labels the upper and lower layers, respectively. The second equality is obtained by

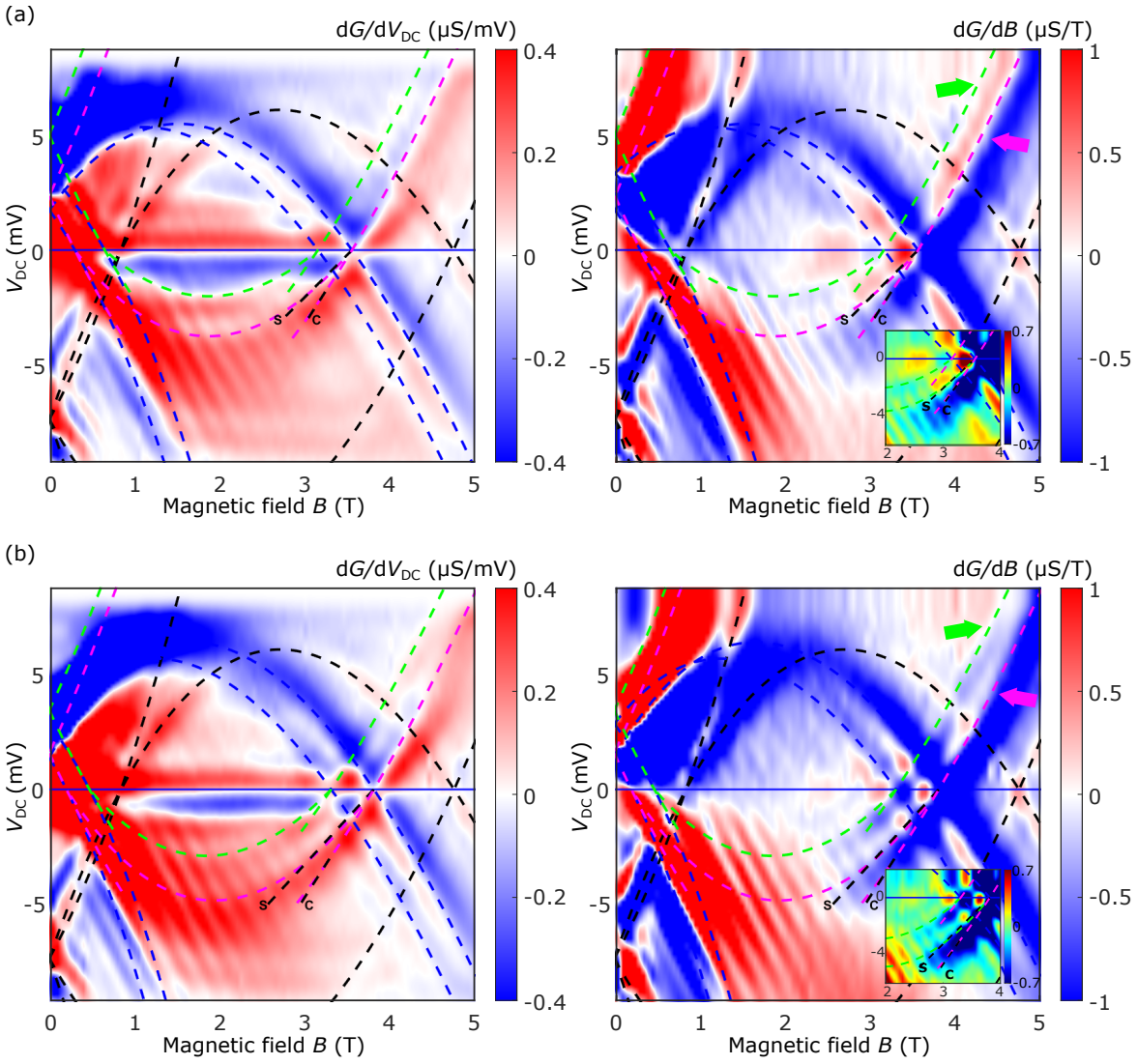

Fig. 6.1 Multiple-subband regime. Tunnelling conductance differentials $\mathrm{d}G/\mathrm{d}V_{\mathrm{DC}}$ and $\mathrm{d}G/\mathrm{d}B$ plotted as a function of DC-bias V_{DC} and in-plane magnetic field B, for a 1.7 μm device, mapped when (a) two ($V_{\mathrm{WG}} = -0.455\,\mathrm{V}$) and (b) three ($V_{\mathrm{WG}} = -0.405\,\mathrm{V}$) subbands are occupied. The dashed coloured curves have the same meaning as before, see Fig. 5.8 and 5.9. Insets show the $\mathrm{d}G/\mathrm{d}B$ differential near the $+k_{\mathrm{F}}$ point for the bottom-most occupied subband.

converting k_{F} into $B_{\pm}^{\mathrm{W}n}$ using equation (3.22). Combining both equations (6.1) and (6.2) we arrive at

$$\begin{aligned}(B_{+}^{\mathrm{W2}}-B_{-}^{\mathrm{W2}})^2 &= (B_{+}^{\mathrm{W2}}+B_{-}^{\mathrm{W2}})^2-4B_{+}^{\mathrm{W2}}B_{-}^{\mathrm{W2}} \\ &\Longrightarrow \frac{B_{+}^{\mathrm{W2}}-B_{-}^{\mathrm{W2}}}{2} = \sqrt{\left(\frac{B_{+}^{\mathrm{W1}}+B_{-}^{\mathrm{W1}}}{2}\right)^2 \mp 4V_0^{\mathrm{W2}}\frac{m_{\mathrm{2D}}^{\star}m_{\mathrm{s}}}{(m_{\mathrm{2D}}^{\star}+m_{\mathrm{s}})ed^2}}.\end{aligned} \tag{6.3}$$

Equation (6.3) allows us to determine the positions of the second subband by varying V_0^{W2} and plotting the dispersions with the resulting $B_{\pm}^{\mathrm{W2}}$ until the best match is obtained. Since B_{+}^{W2} is usually well-observed from the data, this effectively imposes a strong constraint on B_{-}^{W2}.

Having discussed how to obtain both B_{-}^{W2} and B_{+}^{W2}, let us now turn our attention to $m_{\mathrm{s}}^{\mathrm{W2}}$ and $m_{\mathrm{c}}^{\mathrm{W2}}$. Starting with the latter, $m_{\mathrm{c}}^{\mathrm{W2}}$ can normally be obtained by looking at the holon branch emerging from the B_{+}^{W2} point at high bias, see arrows in Fig. 6.3a and b. However, as more subbands come into play, these become progressively harder to resolve separately. As in the single-subband regime, we can obtain a second constraint on $m_{\mathrm{c}}^{\mathrm{W2}}$ by looking at the peak broadening at $B=0$. On the other hand, $m_{\mathrm{s}}^{\mathrm{W2}}$ can be extracted by looking at the spinon mode in the hole sector. This is usually clearly observed for at least the bottom two subbands, allowing us therefore to extract both masses similarly to what has already been done for the bottom-most 1D subband. Note, however, that unlike before, we can no longer compare the spin-to-charge mass ratio with the (independently) extracted velocity ratio (see insets in Fig. 6.3a and b showing the $\mathrm{d}G/\mathrm{d}B$ differential around the $+k_{\mathrm{F,UW,1}}$ region). This is because as more subbands become progressively occupied, v^{c} and v^{s} can no longer be accurately observed. Overall, this results into a slight increase of the uncertainty as the number of occupied subbands increases.

Tables 6.1 and 6.2 show, respectively, the extracted parameters for both the first and second subbands as either two or three subbands are occupied.

1st subband											
L (μm)	$n_{\mathbf{1D}}$ (μm^{-1})	$\lambda_{\mathbf{F}}$ (nm)	$r_{\mathbf{s}}$	$E_{\mathbf{F}}$ (meV)	$v^{\mathbf{s}}$ ($\times 10^5$ ms^{-1})	$v^{\mathbf{c}}$ ($\times 10^5$ ms^{-1})	$v^{\mathbf{s}}/v^{\mathbf{c}}$	$m_{\mathbf{s}}/m_{\mathbf{e}}$	$m_{\mathbf{c}}/2m_{\mathbf{e}}$	$m_{\mathbf{c}}/2m_{\mathbf{s}}$	γ
1	49.3	81.1	1.07	3.41	1.21	1.97	0.61	0.064	0.047	0.73	1.19
1.7	48.0	83.3	1.10	3.23	1.19	1.85	0.64	0.065	0.047	0.72	1.16
3	48.0	83.3	1.10	3.23	1.13	1.91	0.59	0.064	0.047	0.73	1.24
5	49.5	80.8	1.07	3.44	1.23	1.95	0.63	0.065	0.045	0.69	1.22
18	50.1	79.8	1.05	3.52	1.18	1.97	0.60	0.065	0.047	0.72	1.25

2nd subband								
L (μm)	$n_{\mathbf{1D}}$ (μm^{-1})	$\lambda_{\mathbf{F}}$ (nm)	$r_{\mathbf{s}}$	$E_{\mathbf{F}}$ (meV)	$m_{\mathbf{s}}/m_{\mathbf{e}}$	$m_{\mathbf{c}}/2m_{\mathbf{e}}$	$m_{\mathbf{c}}/2m_{\mathbf{s}}$	γ
1	37.6	106.4	1.40	1.98	0.073	0.043	0.59	1.92
1.7	37.5	106.7	1.41	1.97	0.072	0.041	0.57	2.05
3	37.0	108.1	1.43	1.92	0.069	0.041	0.59	1.89
5	35.4	113.0	1.45	1.76	0.069	0.041	0.59	1.84
18	36.7	109.0	1.44	1.89	0.070	0.040	0.57	2.01

Table 6.1 Different parameters, extracted from a total of five different devices, by using the two-Fermi-sea model while in the two-subband regime.

1st subband											
L (μm)	$n_{\mathbf{1D}}$ (μm^{-1})	$\lambda_{\mathbf{F}}$ (nm)	$r_{\mathbf{s}}$	$E_{\mathbf{F}}$ (meV)	$v^{\mathbf{s}}$ ($\times 10^5$ ms^{-1})	$v^{\mathbf{c}}$ ($\times 10^5$ ms^{-1})	$v^{\mathbf{s}}/v^{\mathbf{c}}$	$m_{\mathbf{s}}/m_{\mathbf{e}}$	$m_{\mathbf{c}}/2m_{\mathbf{e}}$	$m_{\mathbf{c}}/2m_{\mathbf{s}}$	γ
1	55.5	72.1	0.95	4.32	1.43	1.96	0.73	0.062	0.053	0.85	0.73
1.7	54.0	74.1	0.98	4.09	1.29	1.86	0.69	0.064	0.051	0.80	0.89
3	54.4	73.5	0.97	4.15	1.40	1.96	0.71	0.062	0.052	0.84	0.78
5	54.3	73.7	0.97	4.14	1.45	1.97	0.74	0.062	0.050	0.81	0.82
18	55.1	72.6	0.96	4.26	1.36	2.02	0.67	0.062	0.051	0.82	0.88

2nd subband								
L (μm)	$n_{\mathbf{1D}}$ (μm^{-1})	$\lambda_{\mathbf{F}}$ (nm)	$r_{\mathbf{s}}$	$E_{\mathbf{F}}$ (meV)	$m_{\mathbf{s}}/m_{\mathbf{e}}$	$m_{\mathbf{c}}/2m_{\mathbf{e}}$	$m_{\mathbf{c}}/2m_{\mathbf{s}}$	γ
1	43.0	93.0	1.23	2.59	0.064	0.048	0.75	1.13
1.7	42.4	94.3	1.24	2.52	0.066	0.047	0.71	1.32
3	44.2	90.5	1.19	2.74	0.067	0.048	0.72	1.27
5	44.4	90.1	1.19	2.77	0.066	0.048	0.73	1.26
18	44.7	89.5	1.18	2.80	0.064	0.048	0.75	1.13

Table 6.2 Different parameters, extracted from a total of five different devices, by using the two-Fermi-sea model while in the three-subband regime. Only the two bottom-most subbands were analysed.

6.2 Emergence of two Fermi seas and 1D-1D screening effects

Having discussed how to extract a variety of parameters for each Fermi sea, both in the single- and multiple-subband regimes, let us now analyse the collected statistics. Fig. 6.2a shows the mass and velocity ratios as the interaction parameter r_s is varied. The data shown has been summarised in Tables 5.1, 6.1, and 6.2 and corresponds to one or the two bottom-most occupied subbands as the occupancy value is changed from one to three.

As can be seen, the measured $m_c/2m_s$ ratio systematically deviates from the non-interacting limit (*i.e.*, $m_c/2m_s = 1$) as r_s increases, in other words as the 1D density is made progressively lower. A very similar dependence on r_s can also be observed from the ratio of the Luttinger parameters v^s/v^c, simultaneously extracted from the data. Fig. 6.2a allows us therefore to claim a 1D system where the strength of the interactions can be varied *in situ* by progressively changing the density and the number of occupied 1D subbands in the wires. In practice, as seen in section 5.2, this is achieved by changing the strength of confinement potential.

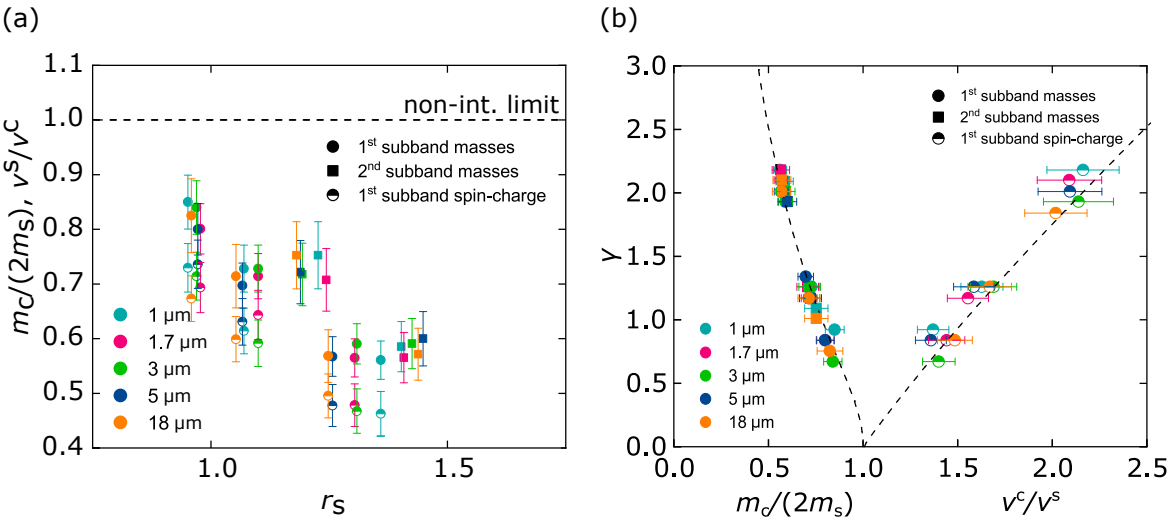

Fig. 6.2 A tunable 1D system. (a) Ratio of the holon-to-spinon masses and the spinon-to-holon velocities as a function of interaction parameter r_s (*i.e.*, density), for a variety of different-length devices. (b) Same data as in (a) but now plotted against the microscopic interaction Hubbard parameter γ. The Fermi-Hubbard model can reproduce the observed experimental dependence well, see black dashed line and text for discussion.

Going back now to the 1D Fermi-Hubbard model and, specifically, the discussion started in section 5.6.3, instead of r_s we can use γ as a way of estimating the interaction strength

between electrons in the system

$$\gamma = 0.032 \frac{\lambda_F}{a} \frac{U}{t}, \tag{6.4}$$

where a is the lattice parameter of the underlying crystal. Note that, unlike r_s, γ itself emerges from the Fermi-Hubbard model in 1D when taking a microscopic approach based on the Bethe *ansatz*. Therefore, while γ still retains knowledge of the system's density, via λ_F, it goes further in that it also takes into account the screening potential, via the Hubbard parameter U.

For $\gamma < 1$, the weakly interacting electrons are almost spin-degenerate, having double occupancy for each momentum state, as for free particles. Here, since the holon Fermi sea is still close to the double occupancy of the free Fermi gas, it cannot be separately resolved from the spinon Fermi sea. On the other hand, for $\gamma > 1$, each momentum state is occupied by only one electron due to strong Coulomb repulsion. Effectively, such a dependence of the system's behaviour on γ is qualitatively identical to that on r_s in all dimensions which, as we saw in section 5.3, reflects the ratio of the total interaction energy to the kinetic energy.

Analysing the same tunnelling maps shown before, but now with the dispersion solutions produced by the Fermi-Hubbard model, we can extract the evolution of each Fermi sea with respect to γ. Plotting the same mass and velocity ratios as shown in Fig. 6.2a, but now instead against γ rather than r_s, we are able to collapse all data points on to a set of universal curves, see Fig. 6.2b. Note that here the data shown corresponds to a total of five different devices, fabricated from two different wafers, measured at different density and subband occupancy values, and over independent thermal cycles. As can be seen, the agreement between experiment and theory further reinforces our claim of two separate Fermi seas for spinons and holons, having now observed their emergence as γ is varied from the weakly- to the strongly-interacting regime.

Let us now compare the extracted values of r_s with γ. Solely considering the single-subband data, we find that $\gamma \approx 1.5 r_s$, see dashed-line in Fig. 6.3a. Note that these values are consistent with the estimate performed in [42], where the long-range Coulomb interaction between the electrons was assumed to be screened by a conducting plate a certain distance away from the wire. We interpret the still-observable discrepancy of the remaining data points as a manisfestation of 1D-1D inter-subband screening, which is not captured by r_s but is taken into account explicitly in γ via the Hubbard two-body interaction energy U. This is proportional to the integral of the screened Coulomb potential, which we can change in our devices by changing the screening radius.

Using equation (6.4) we can extract the evolution of U as the number of occupied subbands is changed, see Fig. 6.3b. Here, two clear trends can be seen to emerge. First, U decreases as more subbands are progressively filled. This results in relative reductions of

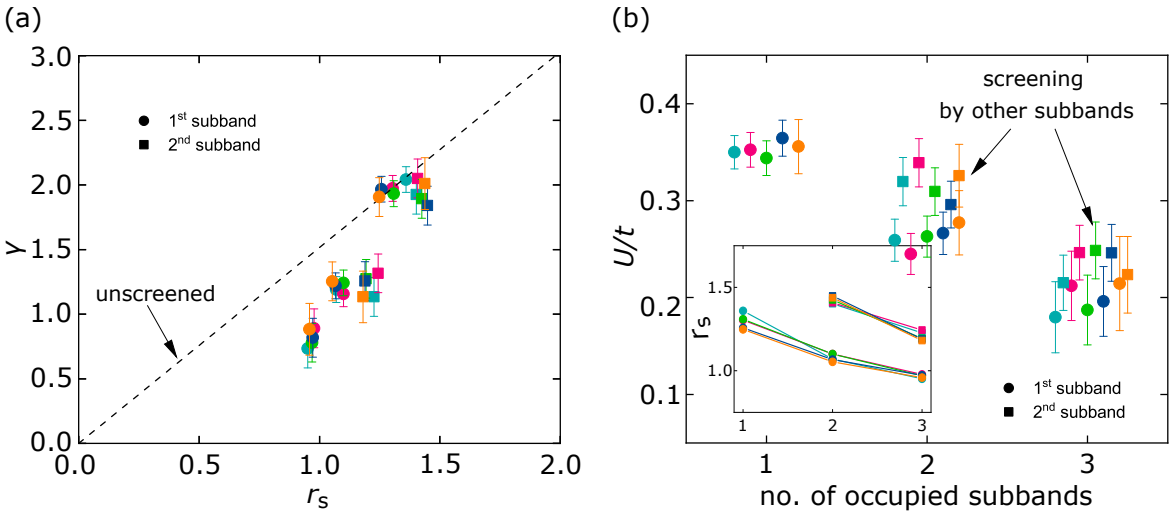

Fig. 6.3 1D-1D screening effects. (a) Microscopic parameter γ *vs* r_s where an approximate linear dependence can be seen. The dashed line corresponds to a fit using only the single-subband data and marks the minimal screening boundary. Note how every other point, corresponding to multiple-subband occupancy regimes systematically falls below this line. We interpret this as evidence of 1D-1D inter-subband screening, see text for discussion. (b) Hubbard parameter U/t *vs* number of occupied subbands, as extracted using equation (6.4). Data points have been offset horizontally from each other for clarity. Inset: r_s *vs* number of occupied subbands. We change r_s by tuning the confinement potential of the 1D wires, see Fig. 5.2.

$\sim 45\,\%$ for the 1st subband and $\sim 25\,\%$ for the 2nd subband. Second, the first subband is systematically more strongly screened than the second, result which we interpret as arising due to the difference in density between the two subbands. Furthermore, note that these trends are also visible from Fig. 6.3a, where all data points except those coming from the single-subband regime systematically fall below the minimal screening boundary. As far as the author is aware, this is the first report of observation of screening effects between two 1D systems, with a similar conclusion having also been reported in [71] for 2D systems.

6.3 Comments on the applicability of the Fermi-Hubbard model

Before we conclude, let us briefly comment on the applicability of the Fermi-Hubbard model to our particular 1D experimental system of choice.

The Fermi-Hubbard model is a particularly special microscopic construction in the sense that it is fully integrable. As we saw before, this means that the full dispersion spectra, both

at low and high energies, can be obtained. In fact, for 1D, it is currently the only available theoretical tool capable of calculating the dispersion of both pure holons and spinons outside the low-energy limit. In contrast, this is no longer possible if using a more generic finite-range interaction potential, even when in the weakly-interacting limit, as spin-charge separation is a nonperturbative effect.

It could be argued, however, that in our experiment, we are effectively applying the Fermi-Hubbard model to a 1D geometry of electrons created using a semiconductor material (GaAs) where the Fermi wavelength is $\sim 100-200$ times the size of the lattice parameter ($a = 5.6531$ Å), and the screening length of the Coulomb potential also at least some tens of lattice parameters. The Fermi-Hubbard model is based on an on-site tight-binding approach, something which would therefore *a priori* seem to not be valid on the microscopic level here.

Nevertheless, the spectra predicted with only on-site interactions still collapse the observed mass and velocity ratios of holon/spinon seas, extracted directly without any models for a large number of experimental points, onto a single curve with remarkably good accuracy, see Fig. 6.7b.

As one final point, note that a series of other 1D systems have been found to behave in a manner closely matching the predictions of the Fermi-Hubbard model. In section 2.2.4, when discussing the early results in Luttinger-liquid-type behaviour using ARPES, we saw how the works of both Kim *et al.* [70, 69, 68] and Fujisawa *et al.* [38, 37] found evidence of spin-charge separation when studying the high-temperature superconductor $SrCuO_2$. In both cases, the spectra was obtained using the 1D Fermi-Hubbard model in the strong interaction limit. More recently, Google AI Quantum has also reported the simulation of the 1D Fermi-Hubbard model using a 16-qubit superconducting quantum processor, with both spinon and holon modes being observed to separate beyond the low-energy regime, in a way compatible with our results [7]. Note, however, that here the simulation was carried out in a small system, whereas we instead do it using a real semiconducting material with hundreds of electrons.

6.4 Mass renormalisation effects

In the preceding sections we saw how two separate Fermi seas, for spin and charge excitations respectively, emerge from the mapped dispersion of the 1D wires, as interactions are tuned from the weakly to the strongly interacting regime. We will now show how expanding from the two-Fermi-sea model one can use it to extract the bare mass of electrons in GaAs. Before this, however, let us give an overview of some past results already reported for GaAs in samples of higher dimensionality.

6.4.1 Electron mass in 3D and 2D GaAs geometries

One of the basic parameters of any material is the band mass of its electrons, m_0. For GaAs, this is often quoted as the effective bulk, that is, three-dimensional (3D), mass value of $m^\star_{3D} = 0.067 m_e$ obtained at low densities, where m_e is the free-space electron mass. Fig. 6.4a shows the evolution of $m^\star_{3D}$ in terms of the electron density n_{3D}, as reported in [103].

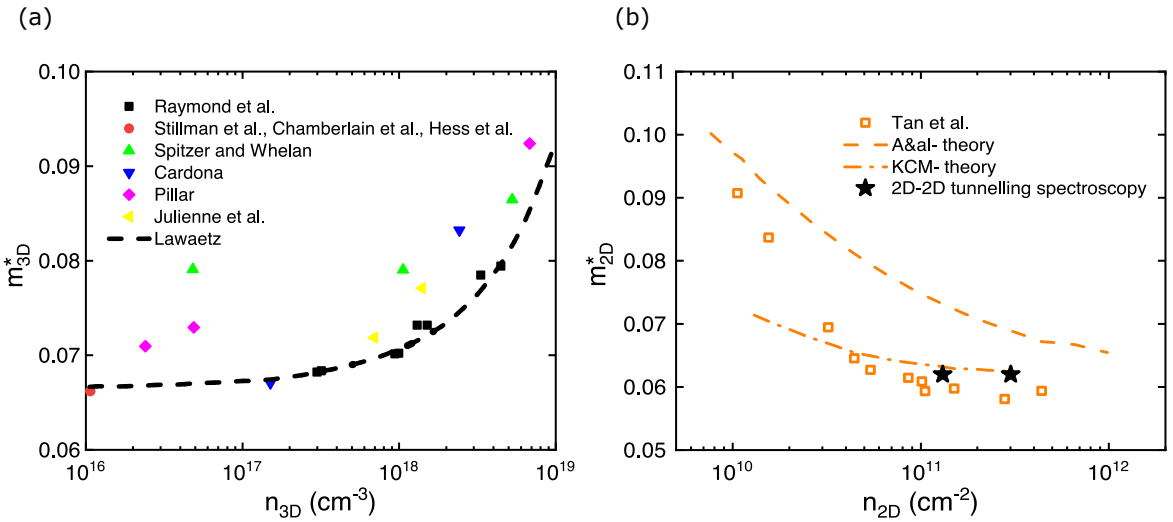

Fig. 6.4 Electron effective mass $m^\star$ in 3D and 2D GaAs geometries. (a) 3D (bulk) effective mass $m^\star_{3D}$ as a function of carrier density n_{3D}. Data reproduced from [103, 114, 24, 50, 113, 21, 101, 63, 84]. (b) 2D electron mass $m^\star_{2D}$ as a function of carrier density n_{2D}. Data reproduced from [115, 9, 75]. In addition, ★ marks the 2D mass result as extracted using tunnelling spectroscopy, see section 5.4.1 for details.

It is a well-established result that in a crystal the effective carrier mass often differs from its free-space counterpart as a direct consequence of the wavefunction interfering with the ionic lattice. Indeed, the enhancement or suppression of the effective electron mass has been measured in several materials, sometimes by up to several orders of magnitude. Additional degrees of freedom, such as phonons, spin waves, plasmons, spin-orbit coupling, and impurity scattering, have also been observed to play a role.

One can, however, enquire if, at a deeper level, the presence of electron-electron interactions could also affect the mass. These are known to be quite strong and, strictly speaking, unavoidable, yet as seen in section 2.1, Fermi liquid theory tells us that their effect should be indistinguishable from the renormalisation due to the band-structure of the material.

As argued in chapter 2, a way of exploring the effect of electron-electron interactions can be achieved via systems of reduced dimensionality. Note that, experimentally, by changing the dimensionality D of a system, one is effectively changing the coordination number, that is, the average number of neighbours that surround each electron.

After Esaki and Tsu's breakthrough with the invention of semiconductor quantum wells [36], two-dimensional electron systems became available, which have since been perfected to extremely high standards. In specific, regarding GaAs/AlGaAs heterostructures, a number of studies using techniques such as Shubnikov-de-Haas oscillations [49, 28, 115], microwave-induced resistance oscillations [48], quantum Monte-Carlo calculations [75], and cyclotron-resonance measurements [74], have since reported the extraction of the two-dimensional (2D) effective electron mass $m^{\star}_{\mathrm{2D}}$, see as an example Fig. 6.4b which reproduces the results reported in [115]. Note that here, ★ marks the $m^{\star}_{\mathrm{2D}}$ mass value as measured using tunnelling spectroscopy in the 2D regions of our devices (section 5.4.1), which is in excellent agreement with the results reported. In contrast to the 3D data, however, values both above and below the band-mass value of $0.067m_{\mathrm{e}}$ are observed as the electron density n_{2D} is varied.

Going further to a 1D geometry changes the effect of interactions drastically, from single-electron mass renormalisation, to collective spin and charge excitations, as seen before. Extracting the effective mass of electrons in 1D GaAs geometries is the topic of the next section.

6.4.2 Electron mass in 1D GaAs geometries

In 1D, geometry alone imposes strong correlations even when only at modest interaction strengths. As a result, the Fermi sea of electrons described by only one mass separates itself into two bands for excitations of spin and charge, which as we have seen, can in turn be described by two incommensurate masses m_{s} and m_{c}. This offers a new method for estimating m_0, in which it is given by the value where m_{s} and $m_{\mathrm{c}}/2$ converge in the non-interacting limit (*i.e.*, $\gamma = 0$). Note that here the extra factor of two arises from the difference in degeneracy between the spinon and holon Fermi seas already discussed in section 5.7.

In order to extract the dependence of the holon and spinon masses on γ, we repeat the calculation of the dispersion of these two bands based on the 1D Fermi-Hubbard model for γ varying from 0 to a large value, see Fig. 5.11 for an example for $\gamma = 2$. Fig. 6.5a shows the calculated dependence of each mass on γ, with Fig. 6.5b showing the evolution of the corresponding ratio. Note that, at large γ, the masses are very different from one another, with $2m_{\mathrm{s}}/m_{\mathrm{c}}$ becoming infinite as $\gamma \to \infty$. This is because, while m_{c} remains finite, the spinon band flattens out, with $m_{\mathrm{s}} \to \infty$. On the other hand, for small γ, the two masses are close to each other, approaching the single-particle mass m_0 as $\gamma \to 0$.

Our goal is to extract m_0 in 1D GaAs wires as the electron density n_{1D} is varied. Note than for all previously discussed data (see chapter 5 and section 6.1), $r_{\mathrm{s}} = 0.8 - 1.5$. In order to go to as low densities as possible or, in other words, higher r_{s}, we can instead map near the bottom of each 1D subband, just as it is about to become depleted. Ideally then, the

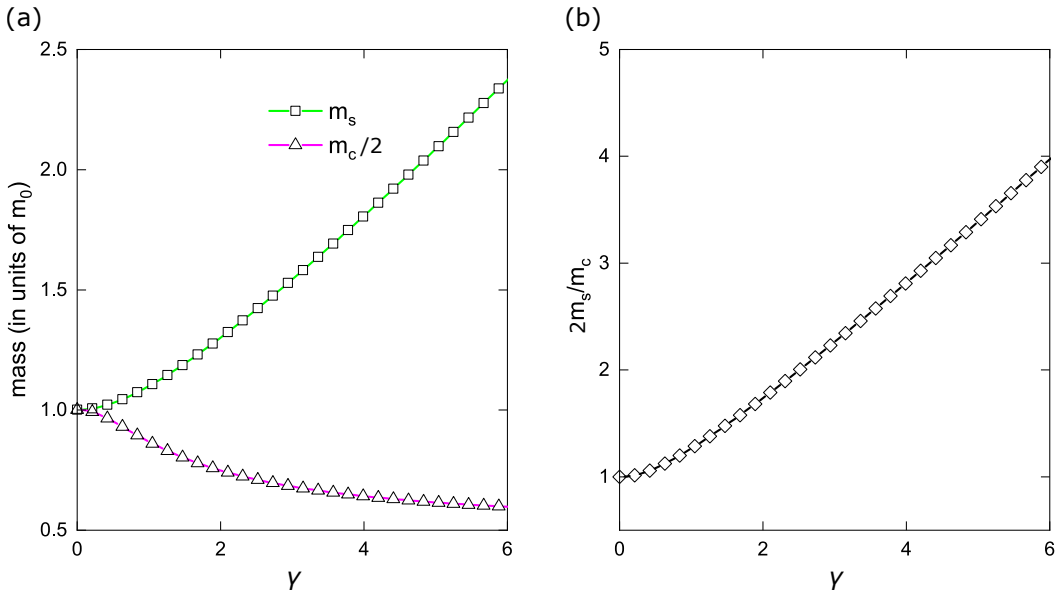

Fig. 6.5 Numerical calculation of the spinon (green) and holon (magenta) masses as a function of the microscopic Hubbard interaction parameter γ. (b) Dependence of the mass ratio $2m_s/m_c$ on γ obtained from (a).

best place to start would be when only a single subband is occupied, for here the number of tunnelling features to analyse is reduced; however, as the 1D channels approach pinch-off, the signal becomes largely dominated by the 'parasitic' 2D region, making it hard to accurately decouple 1D from 2D features. Another alternative would be to map at the bottom of the third, or even fourth, occupied subbands, for here the 1D signal would vastly outweigh any 'parasitic' contribution; similarly to before, however, proximity to the 2D band as well as overall increase in map complexity as more subbands become occupied makes this approach inadequate. The solution was found by mapping near the bottom of the second occupied subband, allowing us to raise r_s up to ~ 4, see Fig. 6.6.

For each dispersion map measured at a different density, we obtained γ from the directly extracted $2m_s/m_c$ ratio using the 1D Fermi-Hubbard model, see Fig. 6.5b. Note that, in addition, for the single-subband data, the observed v^s/v^c ratio was also used as a second, independent, estimate of γ. Fig. 6.7 shows the resulting individual evolution for each mass.

As can be seen, we are able to follow the evolution of the holon mass m_c across a large range of γ with good agreement with the theory. Similarly, we can also follow the evolution of the spinon mass m_s, as extracted from the same set of measurements, up to $\gamma \sim 3$. Above this point, the spinon mode becomes obstructed by the zero-bias anomaly (ZBA), first discussed in see Fig. 2.13, which greatly suppresses all signal falling within ± 0.5 mV of zero bias. Note further that, unlike the charge mode, the spinon mode can only be found in the

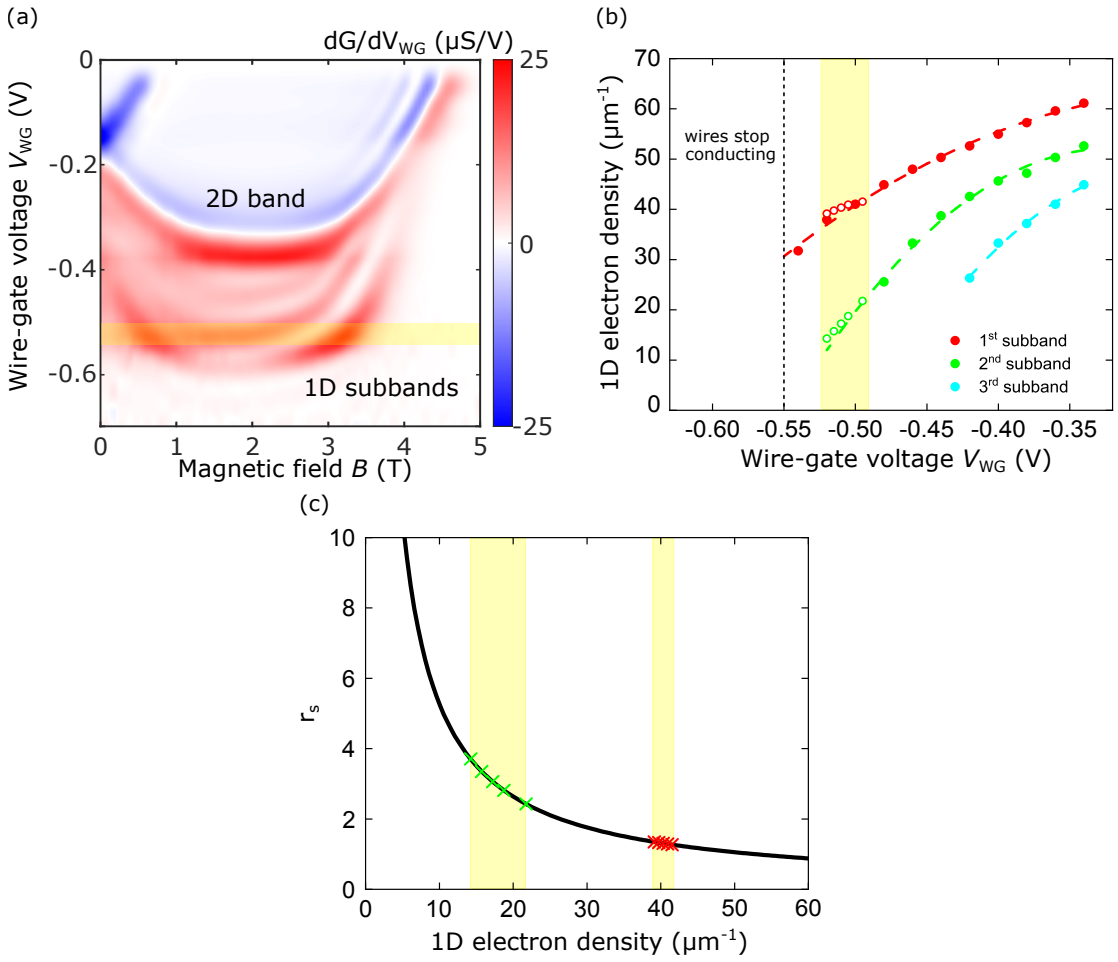

Fig. 6.6 Mapping a 1D system at low densities. (a) Tunnelling conductance differential $\mathrm{d}G/\mathrm{d}V_{\mathrm{WG}}$ as a function of wire-gate voltage V_{WG} and in-plane magnetic field B. The yellow shaded area marks the bottom of the second subband, where the device was mapped in order to reach $r_{\mathrm{s}} > 1.5$. (b) Equilibrium 1D electron density $n_{1\mathrm{D}}$ for each of the conducting subbands shown in (a), see closed symbols. Open symbols correspond to the equivalent density values as extracted from the full energy-momentum maps. (c) Interaction parameter r_{s} as a function of density.

hole sector, overall making the extraction of its mass more challenging. Nevertheless, the extracted values are also seen to evolve systematically with γ, in good agreement with our model. As the mass of each mode converges to the bare electron mass m_0 as interactions are turned off (*i.e.*, $\gamma = 0$), taking the interpolation from the best fit to the data we find $m_0 = (0.0525 \pm 0.0015) m_{\mathrm{e}}$. Note that this value is $\sim 22\%$ smaller than the band mass value of $0.067 m_{\mathrm{e}}$, suggesting that a sizeable percentage of the electron mass in GaAs may be due to electron-electron interactions.

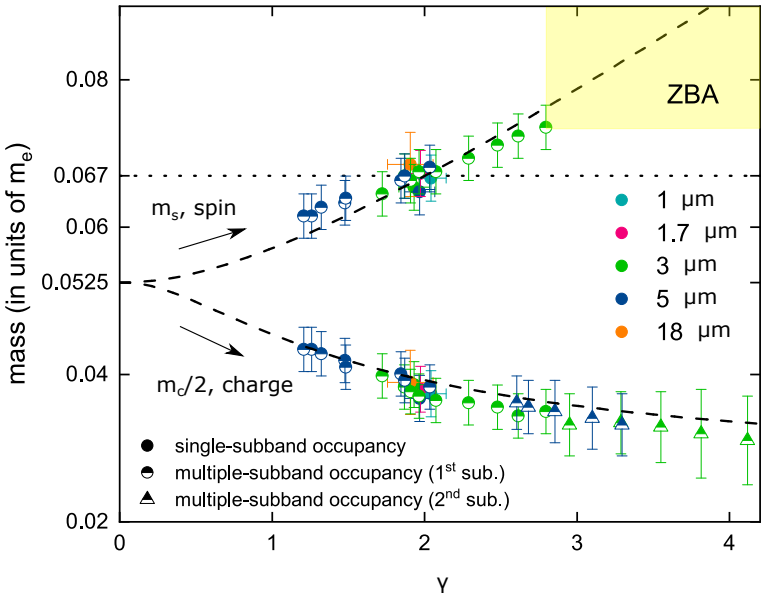

Fig. 6.7 Extraction of the bare electron mass m_0 in GaAs. We obtain both the spinon (m_s) and the holon (m_c) masses for a variety of different-length 1D devices at different interaction strengths γ, which is $\simeq r_s$ but also includes screening effects that are quite sizeable in our samples—see details below. In a 1D geometry, m_0 is then given as the convergence point of these two masses in the limit as interactions are turned off (*i.e.*, $\gamma \to 0$). Here, the dashed curves represent a one-parameter fit for the evolution of m_s and m_c according to the 1D Fermi-Hubbard model, see Fig. 6.5a. Note that the obtained value of m_0 is significantly below $0.067m_e$ (dotted line). The yellow shaded area marks the region in which m_s cannot be accurately determined, due to the presence of the zero-bias anomaly (ZBA), see text for details.

In addition to obtaining γ from the measured $2m_s/m_c$ ratio, we can use the Hubbard spectra to fit the observed tunnelling resonances, as first discussed in section 5.6.3, by scaling the overall energy axis by $1/m_0$, see Fig. 6.8. This allows us to obtain individual values of both m_0 per data set, rather than one cumulative extraction as seen in Fig. 6.7. The obtained average mass was $m_0 = (0.0515 \pm 0.0015)m_e$ for $r_s < 1.6$, see closed symbols in Fig. 6.9b. Across this range m_0 shows no dependence, within error, on density, being also in good agreement with the previously measured value.

At higher r_s (open symbols in Fig. 6.9b), and as discussed before, individual extraction of m_0 is hindered by the fact that m_s cannot be reliably observed due to the ZBA. In order to obtain a confidence interval on its value, we estimate m_0 by fitting the spinon mode up to the point where the ZBA takes over, from which we extract a minimal value for the interaction strength, γ_{min}. Similarly, assuming a minimal screening scenario allows us to extract γ_{max}, see Fig. 6.10, which follows from Fig. 6.3a but now also includes data for the bottom of

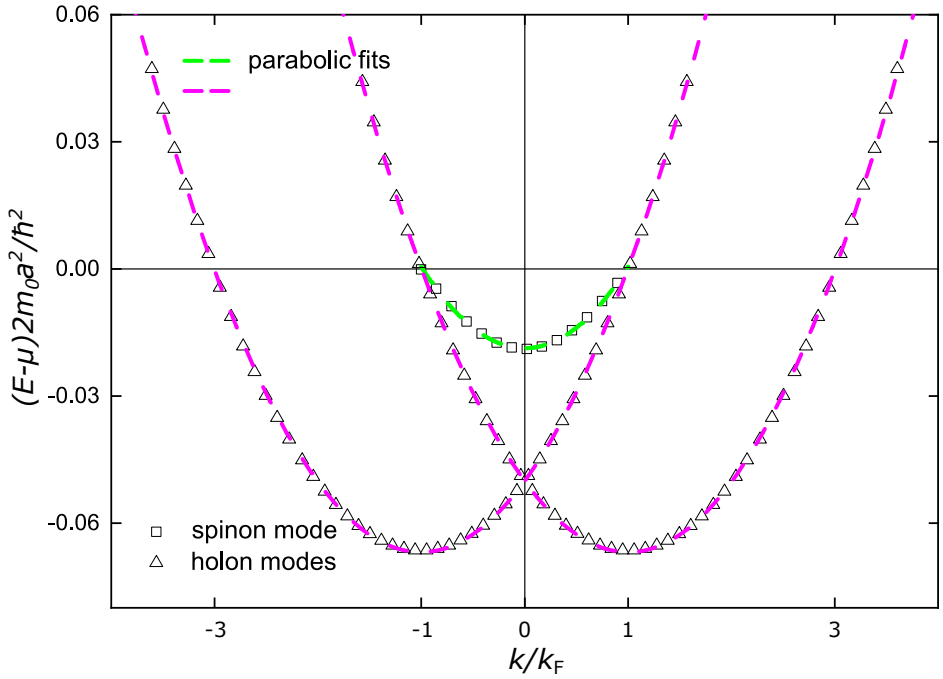

Fig. 6.8 Theoretically obtained spinon (□) and holon (△) spectra as given by the Lieb-Wu equations for unpolarised electrons (*i.e.*, $M{=}N/2$) for an interaction strength $\gamma = 2$, see section 5.6 for full details. Note that the energy scale is $\propto m_0$.

the second occupied subband. From here, lower and upper bounds on the value of m_0 can be obtained given knowledge of m_c, as shown in Fig. 6.9b, where open symbols mark the average value between these two limits.

Even though our current level of resolution of the spinon mode does not allow us to accurately discern between different mass models, our results are compatible with a scenario where m_0 remains constant in density, as expected since in 1D the many-body effects naturally decouple from the electron mass. Note that, even within the error, m_0 systematically falls below the $m^\star_{3D}$ and $m^\star_{2D}$ values previously shown in Fig. 6.4a and Fig. 6.4b and now reproduced in terms of r_s in Fig. 6.9a. Furthermore, even if such a dependence between m_0 and r_s exists, it can already be seen, within error, to be much weaker than that already observed in both 2D and 3D over a comparable range. Finally, note that the upper bound of m_0 was obtained assuming minimal screening, an unlikely scenario as all data for $r_s \gtrsim 2$ was obtained when two subbands were occupied, making the real error therefore most likely smaller than that shown.

Let us now comment on some other effects that could also affect the value of the measured electron mass m_0. At high densities (*i.e.*, $r_s \lesssim 1$), it is expected that the nonparabolicity of the GaAs band will further enhance the effective electron mass with respect to the band mass. However, following from the calculations performed in [31], at the highest density probed

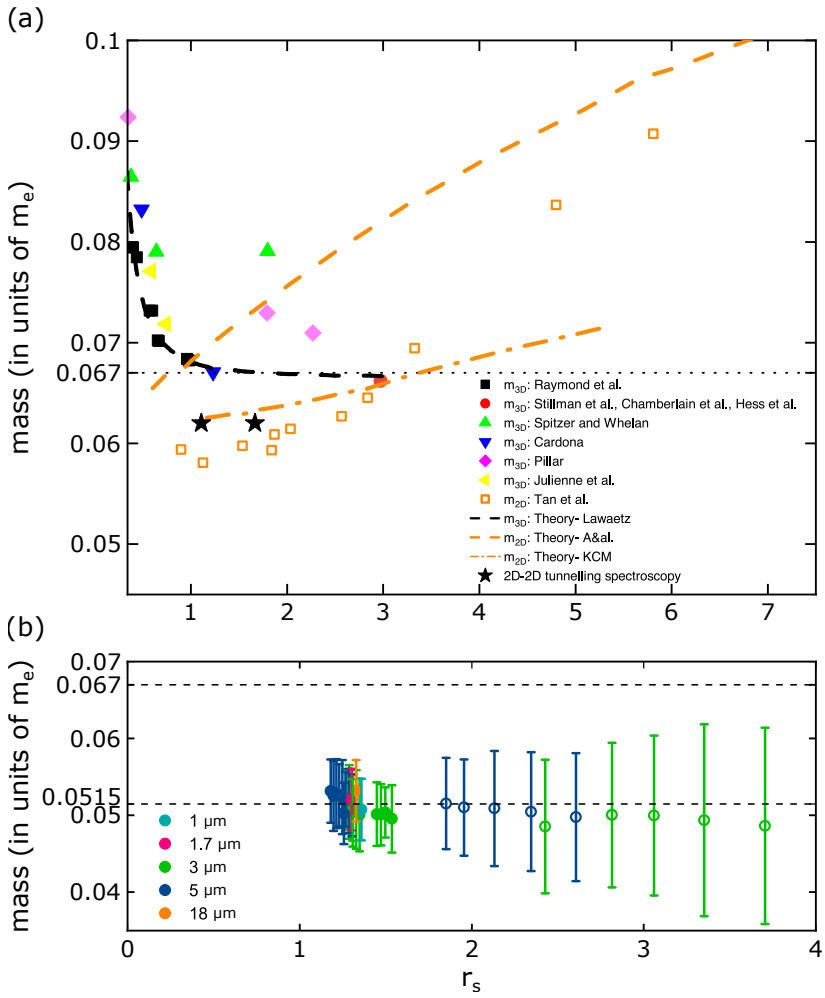

Fig. 6.9 Density dependence of the electron mass in GaAs at different dimensionalities. (a) Three-dimensional (bulk), m^*_{3D}, and two-dimensional, m^*_{2D}, effective mass of electrons in GaAs as a function of interaction parameter r_s (data taken from [103, 114, 24, 50, 113, 21, 101, 63, 115, 84, 9, 75]). (b) Bare electron mass m_0 as extracted using our tunnelling-spectroscopy technique, for a variety of different-length devices. Closed symbols correspond to datasets where both m_s and m_c can be extracted, while for open symbols only m_c is obtained, see text for discussion.

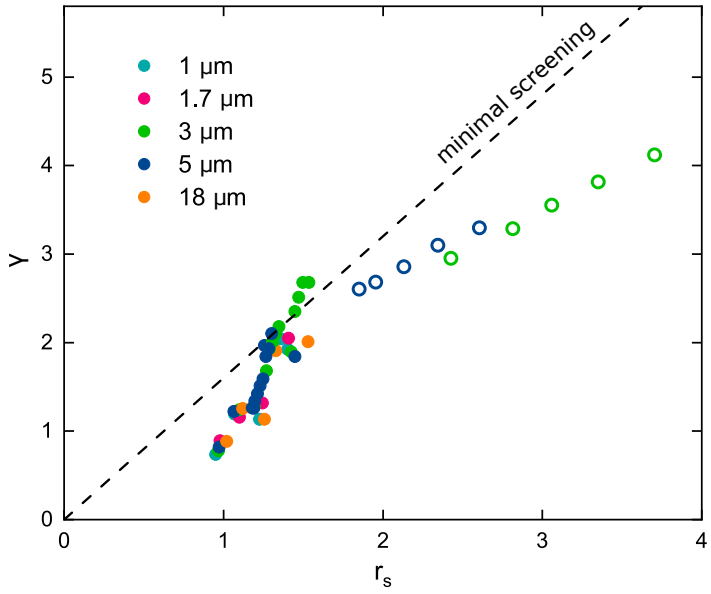

Fig. 6.10 1D-1D inter-subband screening. Same data as that initially shown in Fig. 6.3 but now also including measurements at $r_s > 1.5$. Open symbols have the same interpretation as that in Fig. 6.9b, see text for discussion.

in this experiment, this would correspond to, at most, 5% relative increase, so it cannot by itself explain the observed 22% suppression (seen at both high and low densities). Another effect that is also known to change the mass of carriers in semiconductor structures is lattice strain. This is particularly relevant in our 1D system, as slight crystal distortions could indeed lead to significant deformations in the position and shape of the electrostatically-defined wires. In our samples, it is expected that most of the strain should be caused by the deposited surface gates, as GaAs and $Al_xGa_{1-x}As$ are essentially lattice-matched at $x = 0.3$ (mistmatch $\sim 4.26 \times 10^{-4}$). Independent work carried out by [100, 99] in wafers and using Ti/Au surface gates very similar to ours found a stress-induced tilt of the crystallographic planes of about 0.015°, corresponding to a stress of about 57 MPa and an in-place strain of $\varepsilon_{xx} \sim 4 \times 10^{-5}$. We highlight, however, that according to the authors of that work the measurements were carried out at room temperature, and that it is expected that the strain value may decrease by up to a factor of 2 when cooled down to cryogenic temperatures [80]. Nevertheless, even when taking the worst-case scenario, these figures are still about three orders of magnitude too small to account for any significant change in the curvature of the measured 1D dispersion, and therefore justify the observed mass change.

A systematic interpretation of the emerging picture can be given by Fermi liquid theory which, as discussed in section 2.1, is valid only for $D > 1$. In specific, the bare mass m_0 of electrons is now renormalised due to the many-body effect of the Coulomb interaction,

leading to an effective mass $m^\star$, see section 2.1. In the high-density limit, that is, weak interactions ($r_\mathrm{s} \ll 1$), this can be modelled by the well-understood random-phase approximation [90], which gives

$$\frac{m^\star}{m_0} = 1 + b_1 r_\mathrm{s} \ln r_\mathrm{s} + b_2 r_\mathrm{s} + \mathscr{O}(r_\mathrm{s}^2) < 1, \tag{6.5}$$

where the positive coefficients b_i depend on dimensionality and details of the interaction potential. Note that here the large amount of screening (expected at high densities) will generally speaking contribute to a decrease of the effect of interactions.

For intermediate-to-strong interactions (*i.e.*, $r_\mathrm{s} \gtrsim 1$), the effective mass is expected to get heavier, $m^\star/m_0 > 1$, as a larger degree of dressing of the quasi-particles starts competing with the screening effects. A microscopic calculation of the phenomenological Fermi liquid parameters in this regime, however, is still an open problem, with efforts having been made both on the analytical [134, 9, 104] as well as numerical [110, 34, 26] fronts. Overall, most works tend to converge on the qualitative level, though no exact calculation of how $m^\star$ evolves with r_s as yet been achieved beyond the high-density limit. For completeness, note that at extremely strong interactions (*i.e.*, $r_\mathrm{s} \gtrsim 20-30$), Fermi liquid theory is also expected to break down, as the electrons start forming what is known as a Wigner crystal. This regime is well beyond the limits of our experiment, though recent progress has been claimed in monolayer semiconducting systems [111].

Given the state of the theory, we can conclude from the data that for $r_\mathrm{s} \simeq 1-2$ the Fermi liquid is already in the regime where the quasi-particles consist of a large enough number of electrons to make the effective mass heavier than the single-particle mass. From Fig. 6.9a, we can see that m^* is heaviest for $D = 3$, in which the largest coordination number makes the quasi-particles build out of the largest number of electrons geometrically. Then, m^* decreases for $D = 2$, as expected for a smaller coordination number, and is lightest when $D = 1$, in which the phenomenon of spin-charge separation and the emergence of two separate Fermi seas fully decouples the interaction effects from the mass renormalisation, allowing the observation of the bare band mass m_0 directly. A further argument to support this interpretation is the strong dependence of the observed electron mass on density in $D = 2,3$ but no variation of the mass, within the error, for the density range observed in $D = 1$.

The fact that in GaAs about 22% of the carrier mass may be accounted for by many-body interaction effects is something that was not anticipated by the present understanding of Fermi-liquid theory on the microscopic level, stressing the need for further development on the fundamentals of the many-body theory. In any case, this result alone already provides reliable experimental data on the decoupling of the single- from the many-particle contributions to electronic parameters such as the carrier mass, which could lead to direct improvements in

the modelling of materials. Simultaneously, it also opens a new opportunity for improving the operational efficiency of electronic devices, as additional control of the carrier mass can be achieved via the toolbox of many-body physics. Indeed, lower carrier mass should lead to lower resistivities, resulting in better energy efficiency, as well as faster transistors, e.g. [85].

6.5 Summary

In this chapter we have expanded on the work presented in the chapter 5 by measuring the 1D spectra when multiple 1D subbands are occupied. This allowed the emergence of each Fermi sea to be mapped as the wires were tuned from the weakly to the strongly correlated regime. Furthermore, by decoupling the screening from the density effects, we showed how 1D-1D inter-subband screening could also be observed in our devices. The second half of the chapter used the 1D Fermi-Hubbard model to extract the (bare) mass of electrons free from many-body effects, in GaAs. Here, we showed how by mapping near the bottom of the second occupied subband, interaction parameters as high as $r_s \sim 4$ could be obtained. The extracted mass value was then compared with earlier, independent work in both bulk and 2D GaAs geometries, where it was observed to be about 22% lighter. This suggests an unexpectedly large contribution of the interactions, not anticipated by the current state of Fermi-liquid theory. Given that GaAs is the second most used semiconductor in industry, this result opens up the possibility of engineering new technologies where energy losses may be reduced via optimisation of the carrier mass.

Chapter 7

Further signatures of interaction effects in 1D

In the previous chapters, both when discussing the emergence of two Fermi seas as well as extracting the bare mass of electrons in GaAs, statistics were collected by measuring a total of five devices where the length of the 1D wires was varied from $1-18\,\mu$m. At no point, however, did we justify why length was being varied in the first place. In this chapter we address the original motivation for doing so, by contrasting the observed 1D spectra with one of the main nonlinear Luttinger liquid pictures, the hierarchy-of-modes model. This is a particularly unique theoretical picture as, unlike both the (linear) Luttinger model and the mobile-impurity picture, here physical length is seen a meaningful parameter, rather than simply taken to be infinite. We start by discussing how the hierarchy picture is constructed, putting particular emphasis on how it differs from its closest counterpart, the mobile-impurity model (section 7.1). We then revisit the tunnelling maps, already discussed in chapter 5 and 6, showing how a series of features, not accounted for by the non-interacting model, are seen to emerge as system length is varied (section 7.2).

7.1 A microscopic approach to nonlinear Luttinger liquids

In chapter 2 we saw how early attempts at describing many-body systems of interacting electrons relied on the assumption of a linear relationship between energy and momentum. This led to the well-known Fermi-liquid model at higher dimensions (see section 2.1), valid for both 3D and 2D systems, and the Tomonaga-Luttinger-liquid model in 1D (see section 2.2). As expected, both of these models were, strictly speaking, only valid for low-energy

and low-momentum excitations (*i.e.*, close to the Fermi points where linearity is expected to hold), leaving the problem of high energy largely untreated.

For the specific case of one-dimensional systems, attempts at accounting for the curvature of the dispersion led to what is now commonly known as the mobile-impurity model [53], first discussed in section 2.3.1. Experimentally, evidence in support of this picture, where nonlinearities are expected to manifest as both short-lived plasmonic excitations and momentum-dependent power laws, have so far been reported in both semiconducting quantum wires [59] and carbon nanotubes [129], see also section 2.3.3.

In this chapter we focus on a second approach to dealing with the nonlinear regime in one-dimensional systems, known as the hierarchy-of-modes model [119, 121], see section 2.3.2. Early results in support of this picture, whose key prediction is a length-dependent emergence of higher-order 'replica' modes, have been reported using semiconductor quantum wires similar to our own [94, 119, 121].

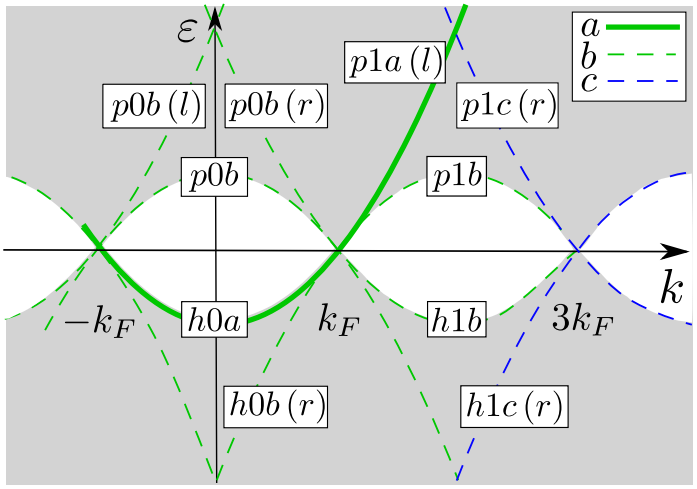

Fig. 7.1 1D spectral function for spinless fermions according to the hierarchy-of-modes picture. First- (0) and second-order (1) modes are shown between $-k_{\rm F} < k < k_{\rm F}$ and $k_{\rm F} < k < 3k_{\rm F}$, respectively, for both particle (p) and hole (h) sectors. Here, white (grey) corresponds to the forbidden region (many-body continuum). Finally, a, b, and c denote the level in hierarchy in powers of 0, 1, or 2 of R^2/L^2, with r/l identifying the origin in the range, right or left. For more details, see [119].

Unlike the mobile-impurity model, the hierarchy-of-modes picture takes a full microscopic approach at solving a system of *spinless* fermions where only short-range interactions are allowed

$$H = \int_{-(L/2)}^{L/2} \mathrm{d}x \Big(-\frac{1}{2m}\psi^\dagger(x)\Delta\psi(x) - UL\rho(x)^2 \Big), \tag{7.1}$$

	$x=0$	$x=1$
pxa		1
hxa	1	
pxb	$16Z^2k_F^2k^2/(k^2-(k_F+\gamma)^2)^2$	$4Z^2\gamma^2(k-k_F+\frac{3}{2}\gamma)^2/(k-k_F+\gamma)^2(k-k_F+2\gamma)^2$
pxb(l)	$4Z^2(k_F+k)^2/k_F^2$	
pxb(r)	$4Z^2(k_F-k)^2/k_F^2$	
hxb		$4Z^2(3k_F-k-\gamma)^2(k_F+k)^2/k_F^2(k-k_F+\gamma)^2$
hxb(l)	$4Z^2\gamma^2/(k+k_F+2\gamma)^2$	$Z^2k_F^2k^2/((k+\gamma)^2-k_F^2)^2$
hxb(r)	$4Z^2\gamma^2/(k-k_F-2\gamma)^2$	

Table 7.1 Spectral weights $A(k,\varepsilon)$ for the modes shown in Fig. 7.1. For details on notation, see caption to Fig. 7.1 and [119]. Here, $\gamma=2\pi/\mathscr{L}$ and $Z=mU/(mU+1)/[\mathscr{L}-NmU/(1+mU)]$, where $\mathscr{L}=L/R$, U is the screening potential, R is the screening radius, L the length of the system, N the particle number, and m the mass.

with the field operators $\psi(x)$ satisfying Fermi relations $\psi(x)\psi^\dagger(x')=\delta(x-x')$, $\rho(x)=\psi^\dagger(x)\psi(x)$ being the density operator, m the bare mass of electrons, U the interaction potential, and L the length of the system.

From the many-body solutions, obtained using Bethe *ansatz* methods, and assuming solely a repulsive regime (*i.e.*, $U>0$), it is found that in addition to the main 1D mode, where the dispersion is expected to remain largely parabolic, with the mass simply renormalised by the Luttinger parameter K (note that in its current form this remains a spinless theory, making K_c and K_s, first introduced in section 2.2.2, degenerate), a hierarchy of extra, higher-order excitations is also expected to emerge. The prediction that multiple, higher-order modes should emerge is, on itself, not unique to the hierarchy-of-modes model, having first been made by Imambekov and Glazmann in [53]. There, however, no statement was made regarding the strength (or, in other words, the spectral weight) of these modes. Here, instead, the spectral weight of each mode is given in powers of R^2/L^2, where R is the screening radius in the system. Note that in every other model concerning 1D electron systems, linear or otherwise, the length of the system is always taken to be essentially infinite, making this therefore currently the only available theoretical picture where L is expected to physically manifest itself in the observed spectrum.

For completeness, Table 7.1 shows the spectral weights along all modes seen in Fig.7.1 (reproduced from [119]). In the next section we show evidence for both *p0b* and *p1b* modes by revisiting the tunnelling spectroscopy maps first discussed in chapter 5.

7.2 A hierarchy of 1D 'replica' modes

In chapter 5 we identified two separate Fermi seas, for spin and charge excitations respectively, by probing an array of 1D wires mapped using tunnelling spectroscopy. Let us now further analyse the measured 1D dispersion.

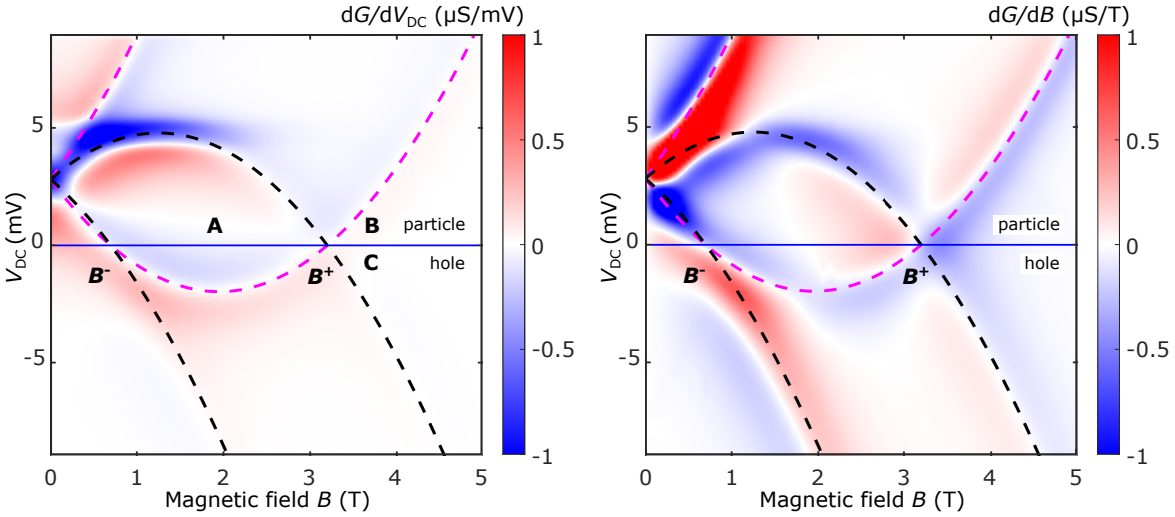

Fig. 7.2 Simulated tunnelling conductance differentials $\mathrm{d}G/\mathrm{d}V_{\mathrm{DC}}$ and $\mathrm{d}G/\mathrm{d}B$ between a 1D non-interacting system (magenta) and a 2DEG (black). The 1D systems was modelled according to equation (3.19). Note that the resulting 1D tunnelling resonance is well captured with a single parabola, as expected since, in the absence of interactions, the spinon and holon dispersions are degenerate with each other.

Fig. 7.2 shows both $\mathrm{d}G/\mathrm{d}V_{\mathrm{DC}}$ and $\mathrm{d}G/\mathrm{d}B$ differentials for a simulated conductance map between a non-interacting 1D system (described by equation (3.19)) and a 2DEG. Note how, unlike what is seen in the experiment, here the observed tunnelling resonances can be fully captured, both in the hole as well as particle sector, using a single parabola (dashed magenta). This is not surprising and follows from Fig. 5.10 where, in the absence of interactions, both Fermi seas are expected to be degenerate with one another.

Let us start by analysing region B in Fig. 7.2 just above the B_+ (*i.e.*, $+k_{\mathrm{F}}$) point. Fig. 7.3 shows region B for a variety of different-length tunnelling devices where a clear feature, not accounted for by the non-interacting picture, can be seen. Looking at both the $\mathrm{d}G/\mathrm{d}V_{\mathrm{DC}}$ and $\mathrm{d}^2G/\mathrm{d}V_{\mathrm{DC}}^2$, as well as G *vs* V_{DC} line-cuts of the raw data, it can be seen that the tunnelling conductance peak broadens and splits, with one boundary following the 1D holon mode (magenta $\times$) while the other branches away from it (blue $+$).

In order to ensure that the enhancement in tunnelling marked by the blue $+$ is not coming from the 2D 'parasitic' region, all data shown in Fig. 7.3 was obtained while applying a positive bias to a gate going this region, $V_{\mathrm{PG}} > 0$ (see section 5.1 for more details). This

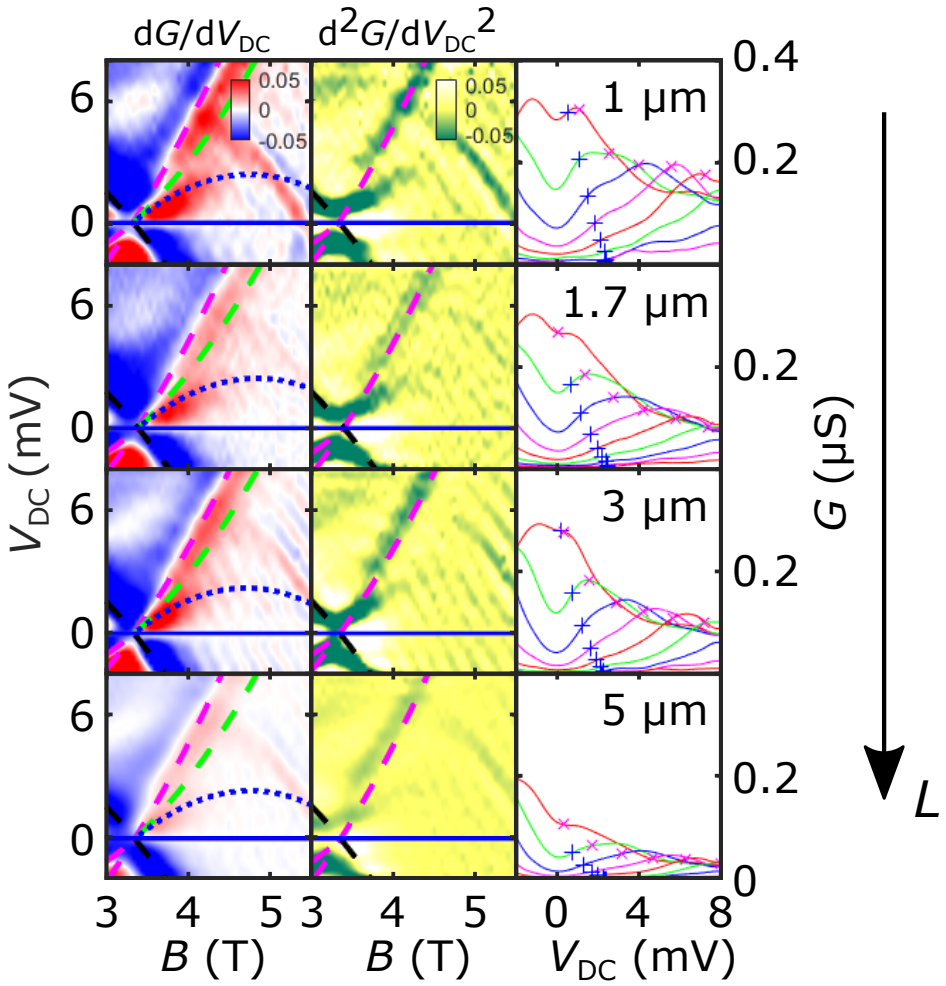

Fig. 7.3 Second-order *p1b* ‘replica’ mode. $\mathrm{d}G/\mathrm{d}V_{\mathrm{DC}}$ (left) and $\mathrm{d}^2G/\mathrm{d}V_{\mathrm{DC}}^2$ (centre) differentials, for devices ranging from $1-5\,\mu$m in length. Right: G *vs* V_{DC} line-cuts at $k > k_{\mathrm{F}}$ (*i.e.*, $B > B^{+}$). ‘x’ and ‘+’ symbols mark, respectively, the position of the fitted dispersions in the particle sector for the holon branch (magenta dashed) and the second-order spinon ‘replica’ mode (blue dotted). Dashed green and black mark, respectively, the extension of the spinon Fermi sea into the particle sector and the dispersion of the bottom 2D spectrometer. Note that conductance has been normalised by device length.

allowed the parasitic 2D features to be moved further to the right, away from B_+. As before (see section 5.4.1), these were then separately mapped before being subtracted from the signal of interest. As an example, Fig. 7.4 shows region B mapped for a 1 μm long device where it can be seen that the observed extra feature in conductance is independent of the 'parasitic' tunnelling signal. Note how use of the 'parasitic' gate is crucial for being able to clearly observe the region around B_+. Furthermore, the extra feature in conductance was also no longer observed once the wires stop conducting, see Fig. 7.5 where the wire-gate voltage V_{WG} was varied just past pinch-off, further suggesting that this feature is 1D in nature and cannot originate from the 'parasitic' 2D region.

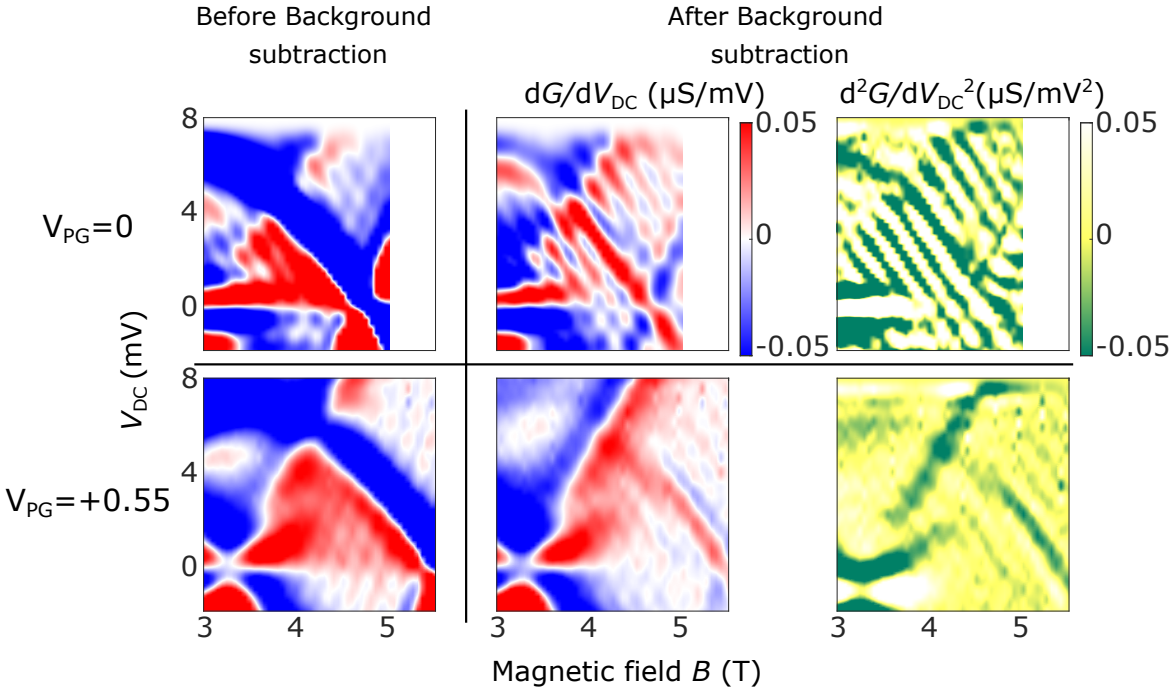

Fig. 7.4 Use of the 'parasitic' PG gate in mapping at high momenta. First and second rows show, respectively, tunnelling spectroscopy performed while V_{PG} is equal to or larger than zero. Note that PG is a gate going over the 'parasitic' 2D injection region, allowing the density is this region to be changed and therefore the position of the 2D-2D background signal, shown here moving further to higher momenta, away from $+k_F$. Left column shows the raw data, while centre and right columns show the tunnelling maps after the 2D-2D background was subtracted.

The feature seen to the right of the B_+ point in Fig. 7.3 is compatible with the second-order replica mode, *p1b*, as predicted by the hierarchy-of-modes picture. Here, it is expected that the strength of the mode marked by the dotted blue curve, which is a 'replica' of the spinon parabola formed between $\pm k_F$, decreases as one moves higher in momentum away from B_+. Note also that in Fig. 7.3, once the background has been subtracted and G normalised by

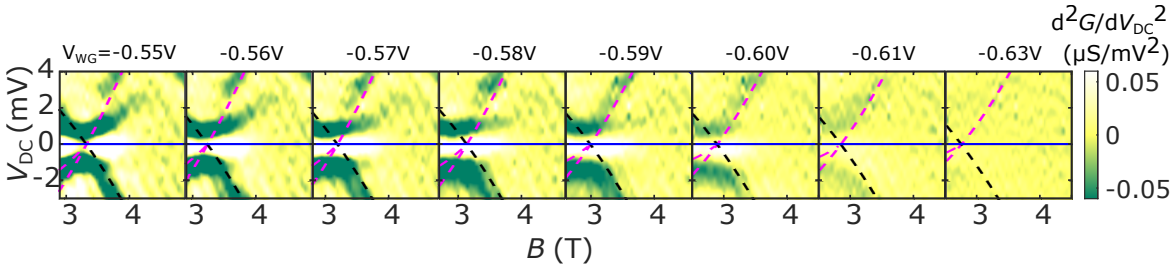

Fig. 7.5 Dependence of the *p1b* 'replica' mode on the wire-gate voltage V_{WG}. As can be observed, the 'replica' responds to changes in V_{WG}, completely disappearing once the wires are pinched-off.

length, one can see qualitatively that the decay away from B_+ is slower the shorter the 1D system, as expected, since the spectral weight of this mode is predicted to be proportional to $1/L^2$.

In order to test the predictions of the hierarchy-of-modes model further, we have looked at another sector of the tunnelling maps, see region A in Fig. 7.2. It was first reported in [94] that, in addition to the 1D spinon mode observed between $\pm k_{\mathrm{F}}$ in the hole sector, a symmetric spinon mode in the particle sector was also observed.

Following from the nonlinear Luttinger-liquid theory, in the main $|k| < k_{\mathrm{F}}$ region of the hole sector, the edge of support, marking the boundary between the forbidden region and the many-body continuum (see white and grey areas in Fig. 7.1 respectively), is expected to coincide with the spinon mass shell, $\varepsilon_{\mathrm{s}}(k)$, which we have already observed to be very close to a parabola, see section 5.5. Furthermore, note that the same result has also been independently verified by several neutron-scattering experiments in antiferromagnetic spin chains [77, 95, 76]. In the same region but now in the particle sector, the edge of support is also expected to be given by $-\varepsilon_{\mathrm{s}}(k)$, in what is commonly referred to as a spinon shadow band. According to the hierarchy-of-modes picture, this would correspond to mode *p0b*.

Fig. 7.6 shows an inverted 'replica' in the particle sector, symmetric to the 1D spinon mode, in all mapped devices up to 5 μm. Note that this feature was already visible in some of the tunnelling maps discussed previously, see for example Fig. 5.10. As before, the hierarchy-of-modes picture also predicts a length-dependent emergence of this mode. Even though such is not particularly clear from $1-5\,\mu$m, the mode can be seen not to be present at all for the 18 μm device.

Both replica features discussed emerge as the effective length of the 1D system is reduced, compatible with the hierarchy-of-modes picture where a level hierarchy emerges as powers of L. We attribute the different lengths at which they become visible in this experiment, with the *p1b* replica only present at $L \lesssim 3\,\mu$m and the *p0b* replica visible to at least $L = 5\,\mu$m, to

different numerical prefactors, which are still unknown theoretically. Therefore, while the spectral weight of each mode does indeed decrease rapidly with distance from k_F, it remains an open question on how to make quantitative estimates of this observation. Note that, in its current form, the hierarchy-of-modes model (see Table 7.1) is valid only for spinless systems, while our system, as expected, has spin.

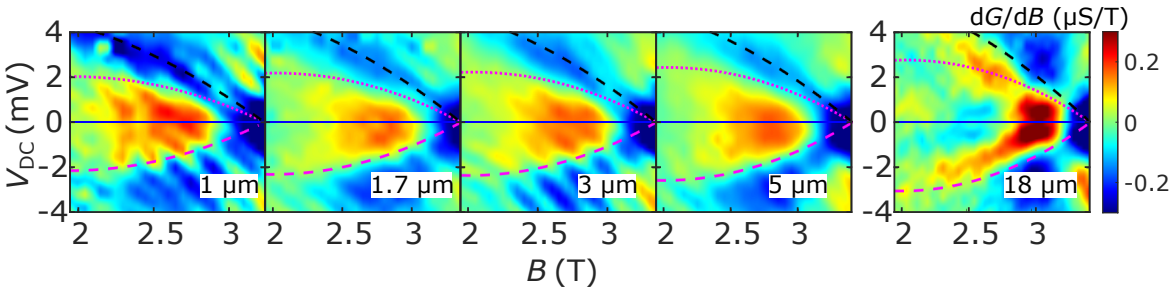

Fig. 7.6 First-order *p0b* 'replica' mode (dotted magenta). $\mathrm{d}G/\mathrm{d}B$ for devices ranging from $1-18\,\mu$m in length mapped around $k < k_F$ (*i.e.* $B < B^+$). The spinon Fermi sea is marked in dashed magenta with the dispersion of the 2D spectrometer in dashed black. As can be observed, *p0b* is visible from $1-5\,\mu$m, but completely absent at $18\,\mu$m. As before, conductance here has also been normalised by device length.

7.3 Summary

In this chapter we concluded the analysis of the measured 1D spectra by comparing it with the hierarchy-of-modes model, one of the leading theories on nonlinear Luttinger liquids. This model is quite unique in the sense that, to our knowledge, is the only one so far that explicitly accounts for the length L of the 1D system as a physical parameter. In specific, it predicts that, in addition to the main 1D mode, higher-order 'replica' modes should also start to emerge, their spectral weight varying in powers $\propto 1/L^2$. Note that, in its current form, this is a spinless model. Experimentally, two features compatible with first- and second-order 'replica' modes were observed in our data, with a full length study being carried out by varying the length of the 1D wires from $1-18\,\mu$m. These results were also compared with simulated tunnelling data for a 1D non-interacting system, further establishing tunnelling spectroscopy as a technique capable of detecting signatures of correlated physics in the many-body spectra.

Chapter 8

Conclusion and outlook

Over the past few chapters we have discussed the many-body problem of electrons inside solids. This is a complex and challenging problem, probably as old as the field of solid-state physics itself, yet it remains far from closed. Theoretically, an analytical approach often proves unfeasible, meaning it is not uncommon for multiple, often contradicting models to exist regarding the same observation. It is then the job of experiment to narrow down the field of available options, and test the validity of each approximation. However, experimentally, the great level of complexity coupled together with defects, disorder, and other known issues most condensed matter systems suffer from often makes it hard to pinpoint an exact source and mechanism.

In this thesis we attempted to tackle the many-body problem by stripping it down to one of its most simple forms, a one-dimensional (1D) wire. This is because, unlike its higher-dimensional counterparts, the dynamics of electrons in 1D can, at least at low energies, be fully captured analytically, in what has come to be known as the Tomonaga-Luttinger liquid (TLL) model. This makes 1D systems the perfect playground in which theory can be put to a test, serving as a starting point for developing new tools capable of tackling non-Fermi-liquid behaviour in higher dimensions. In chapter 2 we reviewed some of the early experimental work done on TLLs, including seminal observations such as power-law behaviour and spin-charge separation. We then discussed some of the more recent developments, both theoretical and experimental, attempting to bring the model to high energies, by dealing with the finite curvature of the dispersion. Work on the so-called nonlinear Luttinger liquids is at the forefront of research in 1D systems, with experimental studies having so far only been carried out using carbon nanotubes and, as in this work, semiconductor quantum wires. Here, early results include the observation of short-lived plasmons, a momentum-dependent power law, and higher-order 'replica' modes, all of which seem to be in agreement with two of the most well-established theories in the field, the mobile-impurity model and the hierarchy-of-modes

model. From the outset, the goal of this thesis was to explore in more detail this high-energy, nonlinear region of the 1D spectrum.

One of the unique aspects of our work was the use of an experimental technique called magnetotunnelling spectroscopy (MTS), discussed in chapter 3. This is an energy- and momentum-resolved tool where quantum mechanical tunnelling between the system of interest and a neighbouring control layer embedded beneath the sample surface (a two-dimensional electron gas) is exploited to determine the energy spectrum of the emergent quasiparticles in a many-body system. Unlike other well-known spectroscopy tools, such as ARPES (angle-resolved photoemission spectroscopy) and STS (scanning tunnelling spectroscopy), MTS is *not* a surface probe, with both system and probe being buried tens of nanometres below the surface. This means the sample is naturally protected from the environment and does not need to be maintained at high vacuum, both which make interacting with it much more straightforward.

In chapter 4 we discussed how to experimentally implement MTS in the study of 1D dynamics, by fabricating a series of semiconductor nanodevices where tunnelling between a 1D array and a control 2DEG could be measured. Here, one of the key improvements over previous work was the development of a novel electron-beam lithography technique for fabricating suspended air-bridge structures. This allowed not only the number of surface gates per device to be increased at no cost of extra contacts but also a higher degree of control over the 'parasitic' 2D region. This was crucial in order to bring the length of the wires down by over an order of magnitude without relying on multiple-column architectures, which had been used previously.

Separate control over the 'parasitic' 2D region also allowed us to subtract, for the first time, the 2D-2D background from the 1D-2D tunnelling signal of interest. This was the key improvement that allowed us to quantitatively investigate, for the first time, the high-energy, nonlinear region of the 1D spectrum, as reported in chapter 5. Specifically, the observation of separate spin and charge modes at low energies, the latter of which we were able to follow into the high-energy regime (up to five times the Fermi energy), led us to conclude the presence of two, rather than the usual one, Fermi seas. This, in turn, is in close agreement with the predictions of the 1D Fermi-Hubbard model.

Most of the work done on 1D systems, both theoretical and experimental, often assumes single-subband occupancy. Even though there have been some experiments where multiple 1D subbands are occupied, conclusions had remained up to now mostly qualitative. In chapter 6 we expanded on the two-Fermi-sea model by bringing it into the multiple-subband regime. This allowed us to observe the emergence of each Fermi sea as the system was tuned from the weakly to the strongly interacting regime. In particular, by decoupling the

effects of the wire's density on the interaction strength from the screening potential, we were able to observe, for the first time, 1D-1D inter-subband screening. The second half of the chapter was then dedicated to the extraction of the bare electron mass of electrons in GaAs, that is, free from many-body effects. While studies in both bulk (*i.e.*, 3D) GaAs and 2D GaAs/AlGaAs heterostructures had already been done, work in 1D had been hindered due to their higher-sensitivity to disorder, a problem which we solved by using an array of wires in order to average out the signal. Comparing the extracted mass to previous results obtained in higher dimensions led to the remarkable observation that over 20 % of the electron mass in GaAs may be due to many-body effects, something that was not anticipated by the current understanding of Fermi-liquid theory.

Finally, in chapter 7 we explored the effect of system length L on the emerging many-body spectrum. While most of the work done in 1D often disregards length as a meaningful physical parameter, one of the key predictions of the hierarchy-of-modes model for nonlinear Luttinger liquids is the emergence of higher-order 'replica' modes, in addition to the main 1D subband itself, as length is reduced. By systematically fabricating and measuring a number of nanodevices $1-18\,\mu$m in length, we observed the emergence of two of the 'replica' modes predicted, $p0b$ and $p1b$. While in its current form the hierarchy model still remains a spinless theory, meaning quantitative tests are hard to perform, our results nevertheless point to its support. This further establishes MTS as a spectroscopy tool on a par with ARPES and STS for detecting signatures of nonlinear behaviour across the whole energy-momentum space.

Overall, the main significance of this thesis is the demonstration of the generic robustness of the spin-charge separation, something first observed over two decades ago at low energies, by mapping its evolution into the nonlinear, high-energy regime. Effectively, our observations invalidate the prediction of the currently available nonlinear-Luttinger-liquid theory about the fate of spinon and holon excitations deep in the many-body continuum, by establishing that the quasiparticle picture does indeed still remain valid even when at energies five times that of the Fermi energy. This sets the question of new conceptual development to the theory of many-body system in lower dimensions, something quite timely as evidenced over the past two years by a new wave of interest in experimentally studying the physics of spin-charge separation and Luttinger liquids in systems like cold atoms, carbon nanotubes and edge states.

The work in 1D systems remains therefore far from finished. For instance, a particularly interesting avenue yet unexplored would be a full temperature study of the emerging dynamics as the interaction strength is varied, with features such as the zero-bias anomaly showing promise for ultra-low temperature thermometry. Furthermore, recent work reported in cleaved-edge-overgrown wires suggests that electron-electron interactions may lead to

spontaneous nuclear spin magnetism forming around the miliKelvin regime, something so far typically only observed at microKelvins. As the lowest temperature accessible in this work was $\sim 300\,\mathrm{mK}$, such study was not possible. Nevertheless, the nanodevices already developed should allow for both tunnelling and transport measurements to be performed in a system where interaction strength can be easily tuned. Finally, an important question left open by the two-Fermi-sea picture is that, at low energies, spinons and holons are expected to follow bosonic statistics, yet the observation of separate Fermi seas seems to suggest that at high enough energies the statistics may switch to fermionic. A full study of the statistical nature of these collective modes is therefore highly needed.

References

[1] https://www.comsol.com.

[2] Abrikosov, A. A., Gorkov, L. P., and Dzyaloshinski, I. E. (1976). *Methods of Quantum Field Theory in Statistical Physics*. Dover Publications Inc., New York.

[3] Abrikosov, A. A. and Khalatnikov, I. M. (1959). The theory of a fermi liquid (the properties of liquid 3He at low temperatures). *Reports on Progress in Physics*, 22(1):329–367. IOP Publishing.

[4] Altland, A., Barnes, C. H. W., Hekking, F. W. J., and Schofield, A. J. (1999). Magnetotunneling as a Probe of Luttinger-Liquid Behavior. *Physical Review Letters*, 83(6):1203–1206.

[5] Altland, A. and Simons, B. D. (2010). *Condensed Matter Field Theory*. Cambridge University Press.

[6] Apostol, M. (1983). Bosonisation of the one-dimensional two-fermion model: boson representation. *Journal of Physics C: Solid State Physics*, 16(31):5937–5957.

[7] Arute, F., Arya, K., Babbush, R., Bacon, D., Bardin, J. C., Barends, R., Bengtsson, A., Boixo, S., Broughton, M., Buckley, B. B., Buell, D. A., Burkett, B., Bushnell, N., Chen, Y., Chen, Z., Chen, Y.-A., Chiaro, B., Collins, R., Cotton, S. J., Courtney, W., Demura, S., Derk, A., Dunsworth, A., Eppens, D., Eckl, T., Erickson, C., Farhi, E., Fowler, A., Foxen, B., Gidney, C., Giustina, M., Graff, R., Gross, J. A., Habegger, S., Harrigan, M. P., Ho, A., Hong, S., Huang, T., Huggins, W., Ioffe, L. B., Isakov, S. V., Jeffrey, E., Jiang, Z., Jones, C., Kafri, D., Kechedzhi, K., Kelly, J., Kim, S., Klimov, P. V., Korotkov, A. N., Kostritsa, F., Landhuis, D., Laptev, P., Lindmark, M., Lucero, E., Marthaler, M., Martin, O., Martinis, J. M., Marusczyk, A., McArdle, S., McClean, J. R., McCourt, T., McEwen, M., Megrant, A., Mejuto-Zaera, C., Mi, X., Mohseni, M., Mruczkiewicz, W., Mutus, J., Naaman, O., Neeley, M., Neill, C., Neven, H., Newman, M., Niu, M. Y., O'Brien, T. E., Ostby, E., Pató, B., Petukhov, A., Putterman, H., Quintana, C., Reiner, J.-M., Roushan, P., Rubin, N. C., Sank, D., Satzinger, K. J., Smelyanskiy, V., Strain, D., Sung, K. J., Schmitteckert, P., Szalay, M., Tubman, N. M., Vainsencher, A., White, T., Vogt, N., Yao, Z. J., Yeh, P., Zalcman, A., and Zanker, S. (2020). Observation of separated dynamics of charge and spin in the Fermi-Hubbard model. *arXiv:2010.07965*.

[8] Aseev, P. P., Klinovaja, J., and Loss, D. (2017). Finite-temperature conductance of strongly interacting quantum wire with a nuclear spin order. *Physical Review B*, 95(12):125440.

[9] Asgari, R., Davoudi, B., Polini, M., Giuliani, G. F., Tosi, M. P., and Vignale, G. (2005). Quasiparticle self-energy and many-body effective mass enhancement in a two-dimensional electron liquid. *Phys. Rev. B*, 71(4):045323.

[10] Auslaender, O. M., Steinberg, H., Yacoby, A., Tserkovnyak, Y., Halperin, B. I., Baldwin, K. W., Pfeiffer, L. N., and West, K. W. (2005). Spin-Charge Separation and Localization in One Dimension. *Science*, 308(5718):88–92.

[11] Auslaender, O. M., Yacoby, A., Picciotto, R. d., Baldwin, K. W., Pfeiffer, L. N., and West, K. W. (2002). Tunneling Spectroscopy of the Elementary Excitations in a One-Dimensional Wire. *Science*, 295(5556):825–828.

[12] Barak, G., Steinberg, H., Pfeiffer, L. N., West, K. W., Glazman, L., von Oppen, F., and Yacoby, A. (2010). Interacting electrons in one dimension beyond the Luttinger-liquid limit. *Nature Physics*, 6(7):489–493.

[13] Bardeen, J. (1961). Tunnelling from a Many-Particle Point of View. *Physical Review Letters*, 6(2):57–59.

[14] Beauchamp, C. (2021). *Superconductivity in AuGeNi Ohmic contacts to a GaAs-based high mobility two-dimensional electron gas*. PhD thesis.

[15] Beauchamp, C. B., Dimitriadis, S., Nicholls, J. T., Levitin, L. V., Casey, A. J., See, P., Creeth, G., Waldie, J., Farrer, I., Beere, H. E., and Ritchie, D. A. (2020). Superconductivity in AuNiGe Ohmic contacts to a GaAs-based high mobility two-dimensional electron gas. *Applied Physics Letters*, 117(16):162104.

[16] Bockrath, M., Cobden, D. H., Lu, J., Rinzler, A. G., Smalley, R. E., Balents, L., and McEuen, P. L. (1999). Luttinger-liquid behaviour in carbon nanotubes. *Nature*, 397(6720):598–601.

[17] Boll, M., Hilker, T. A., Salomon, G., Omran, A., Nespolo, J., Pollet, L., Bloch, I., and Gross, C. (2016). Spin- and density-resolved microscopy of antiferromagnetic correlations in Fermi-Hubbard chains. *Science*, 353(6305):1257–1260.

[18] Braunecker, B., Japaridze, G. I., Klinovaja, J., and Loss, D. (2010). Spin-selective Peierls transition in interacting one-dimensional conductors with spin-orbit interaction. *Physical Review B*, 82(4):045127.

[19] Braunecker, B., Simon, P., and Loss, D. (2009a). Nuclear magnetism and electron order in interacting one-dimensional conductors. *Physical Review B*, 80(16):165119.

[20] Braunecker, B., Simon, P., and Loss, D. (2009b). Nuclear Magnetism and Electronic Order in ^{13}C Nanotubes. *Physical Review Letters*, 102(11):116403.

[21] Cardona, M. (1961). Electron Effective Masses of InAs and GaAs as a Function of Temperature and Doping. *Phys. Rev.*, 121(3):752–758.

[22] Carpentier, D., Peça, C., and Balents, L. (2002). Momentum-resolved tunneling between Luttinger liquids. *Physical Review B*, 66(15):153304.

[23] Caux, J.-S. and Maillet, J. M. (2005). Computation of dynamical correlation functions of Heisenberg chains in a magnetic field. *Phys. Rev. Lett.*, 95:077201.

[24] Chamberlain, J. M., Simmonds, P. E., Stradling, R. A., and Bradley, C. C. (1972). In *Proc. 11th Int. Conf. on Physics of Semiconductors (Warsaw: Polish Scientific publishers)*, pages 1016–1022.

[25] Chang, A. M. (2003). Chiral Luttinger liquids at the fractional quantum Hall edge. *Reviews of Modern Physics*, 75(4):1449–1505.

[26] Chen, K. and Haule, K. (2019). A combined variational and diagrammatic quantum monte carlo approach to the many-electron problem. *Nat. Commun.*, 19:3725.

[27] Cohen-Tannoudji, C., Diu, B., and Laloë, F. (2020). *Quantum Mechanics, Volume 1: Basic Concepts, Tools, and Applications, 2nd Edition*. Wiley.

[28] Coleridge, P. T., Hayne, M., Zawadzki, P., and Sachrajda, A. S. (1996). Effective masses in high-mobility 2D electron gas structures. *Surf. Sci.*, 361-362:560–563.

[29] Creffield, C. E., Häusler, W., and MacDonald, A. H. (2001). Spin and charge Tomonaga-Luttinger parameters in quantum wires. *EPL (Europhysics Letters)*, 53(2):221.

[30] Creffield, C. E., Klepfish, E. G., Pike, E. R., and Sarkar, S. (1995). Spectral Weight Function for the Half-Filled Hubbard Model: A Singular Value Decomposition Approach. *Physical Review Letters*, 75(3):517–520.

[31] Das Sarma, S. and Mason, B. A. (1985). Band nonparabolicity effects on weak-coupling polarons in compound semiconductors. *Phys. Rev. B*, 31(2):1177–1180.

[32] Dash, L. K. and Fisher, A. J. (2001). Does Luttinger liquid behaviour survive in an atomic wire on a surface? *Journal of Physics: Condensed Matter*, 13(22):5035–5046.

[33] Deshpande, V. V., Bockrath, M., Glazman, L. I., and Yacoby, A. (2010). Electron liquids and solids in one dimension. *Nature*, 464(7286):209–216.

[34] Drummond, N. D. and Needs, R. J. (2013). Diffusion quantum monte carlo calculation of the quasiparticle effective mass of the two-dimensional homogeneous electron gas. *Phys. Rev. B*, 87:045131.

[35] Egger, R. and Gogolin, A. O. (1997). Effective Low-Energy Theory for Correlated Carbon Nanotubes. *Physical Review Letters*, 79(25):5082–5085.

[36] Esaki, L. and Tsu, R. (1970). Superlattice and Negative Differential Conductivity in Semiconductors. *IBM J. Res. Devel.*, 14(1):61–65.

[37] Fujisawa, H., Yokoya, T., Takahashi, T., Miyasaka, S., Kibune, M., and Takagi, H. (1998a). Spin-charge separation in single-chain compound Sr2CuO3 studied by angle-resolved photoemission. *Solid State Communications*, 106(8):543–547.

[38] Fujisawa, H., Yokoya, T., Takahashi, T., Tanaka, M., Hasegawa, M., and Takei, H. (1998b). Angle-resolved photoemission spectroscopy of SrCuO2: Spin-charge separation? *Journal of Electron Spectroscopy and Related Phenomena*, 88-91:461–465.

[39] Gaudin, M. (1967). Un systeme a une dimension de fermions en interaction. *Phys. Lett. A*, 24:55–56.

[40] Giamarchi, T. (2003). *Quantum Physics in One Dimension*. International Series of Monographs on Physics. Oxford University Press, Oxford, New York.

[41] Giuliani, G. and Vignale, G. (2005). *Quantum Theory of the Electron Liquid*. Cambridge University Press, Cambridge.

[42] Glazman, L. I., Ruzin, I. M., and Shklovskii, B. I. (1992). Quantum transport and pinning of a one-dimensional Wigner crystal. *Phys. Rev. B*, 45:8454–8463.

[43] Göhmann, F., Klümper, A., and Seel, A. (2004). Integral representations for correlation functions of the XXZ chain at finite temperature. *J. Phys. A*, 37:7625–7651.

[44] Grayson, M., Tsui, D. C., Pfeiffer, L. N., West, K. W., and Chang, A. M. (1998). Continuum of Chiral Luttinger Liquids at the Fractional Quantum Hall Edge. *Physical Review Letters*, 80(5):1062–1065.

[45] Grigera, S. A., Schofield, A. J., Rabello, S., and Si, Q. (2004). Momentum-resolved tunneling between a Luttinger liquid and a two-dimensional electron gas. *Physical Review B*, 69(24):245109.

[46] Gweon, G.-H., Allen, J. W., and Denlinger, J. D. (2003). Generalized spectral signatures of electron fractionalization in quasi-one- and two-dimensional molybdenum bronzes and superconducting cuprates. *Physical Review B*, 68(19):195117.

[47] Haldane, F. D. M. (1981). Luttinger liquid theory of one-dimensional quantum fluids. I. Properties of the Luttinger model and their extension to the general 1D interacting spinless Fermi gas. *Journal of Physics C: Solid State Physics*, 14(19):2585–2609.

[48] Hatke, A. T., Zudov, M. A., Watson, J. D., Manfra, M. J., Pfeiffer, L. N., and West, K. W. (2013). Evidence for effective mass reduction in GaAs/AlGaAs quantum wells. *Phys. Rev. B*, 87(16):161307.

[49] Hayne, M., Usher, A., Harris, J. J., and Foxon, C. T. (1992). Exchange enhancement of the Landau-level separation for two-dimensional electrons in GaAs/$Ga_{1-x}Al_xAs$ heterojunctions. *Phys. Rev. B*, 46(15):9515–9519.

[50] Hess, K., Bimberg, D., Lipari, N. O., Fischbach, J. U., and Altarelli, M. (1976). In *Proc. 13th Int. Conf. on Physics of Semiconductors ed. F. G. Fumi (Rome)*, pages 142–145.

[51] Hilker, T. A., Salomon, G., Grusdt, F., Omran, A., Boll, M., Demler, E., Bloch, I., and Gross, C. (2017). Revealing hidden antiferromagnetic correlations in doped Hubbard chains via string correlators. *Science*, 357(6350):484–487.

[52] Häusler, W., Kecke, L., and MacDonald, A. H. (2002). Tomonaga-Luttinger parameters for quantum wires. *Physical Review B*, 65(8):085104.

[53] Imambekov, A. and Glazman, L. I. (2009). Universal Theory of Nonlinear Luttinger Liquids. *Science*, 323(5911):228–231.

[54] Imambekov, A., Schmidt, T. L., and Glazman, L. I. (2012). One-dimensional quantum liquids: Beyond the Luttinger liquid paradigm. *Reviews of Modern Physics*, 84(3):1253–1306.

[55] Ishii, H., Kataura, H., Shiozawa, H., Yoshioka, H., Otsubo, H., Takayama, Y., Miyahara, T., Suzuki, S., Achiba, Y., Nakatake, M., Narimura, T., Higashiguchi, M., Shimada, K., Namatame, H., and Taniguchi, M. (2003). Direct observation of Tomonaga–Luttinger-liquid state in carbon nanotubes at low temperatures. *Nature*, 426(6966):540–544.

[56] Jackson, J. D. (1998). *Classical Electrodynamics, 3rd Edition*. Wiley.

[57] Jin, Y. (2020). *Measurement of electron-electron interactions in one dimension with tunnelling spectroscopy*. PhD thesis.

[58] Jin, Y., Moreno, M., T. Vianez, P. M., Tan, W. K., Griffiths, J. P., Farrer, I., Ritchie, D. A., and Ford, C. J. B. (2021). Microscopic metallic air-bridge arrays for connecting quantum devices. *Applied Physics Letters*, 118(16):162108.

[59] Jin, Y., Tsyplyatyev, O., Moreno, M., Anthore, A., Tan, W. K., Griffiths, J. P., Farrer, I., Ritchie, D. A., Glazman, L. I., Schofield, A. J., and Ford, C. J. B. (2019). Momentum-dependent power law measured in an interacting quantum wire beyond the Luttinger limit. *Nature Communications*, 10(1):2821.

[60] Jompol, Y. (2008). *Probing Tomonaga-Luttinger Liquid behaviour and spin-charge separation in GaAs quantum wires*. PhD thesis.

[61] Jompol, Y., Ford, C. J. B., Farrer, I., Jones, G. A. C., Anderson, D., Ritchie, D. A., Silk, T. W., and Schofield, A. J. (2008). Probing e–e interactions in a periodic array of GaAs quantum wires. *Physica E: Low-dimensional Systems and Nanostructures*, 40(5):1220–1222.

[62] Jompol, Y., Ford, C. J. B., Griffiths, J. P., Farrer, I., Jones, G. a. C., Anderson, D., Ritchie, D. A., Silk, T. W., and Schofield, A. J. (2009). Probing Spin-Charge Separation in a Tomonaga-Luttinger Liquid. *Science*, 325(5940):597–601.

[63] Julienne, D., Le Saos, F., Fortini, A., and Bauduin, P. (1976). Free carriers's effective mass and relaxation-time analysis by high-pulsed-field Faraday oscillations in III-V compounds. *Phys. Rev. B*, 13(6):2576–2582.

[64] Kane, C., Balents, L., and Fisher, M. P. A. (1997). Coulomb Interactions and Mesoscopic Effects in Carbon Nanotubes. *Physical Review Letters*, 79(25):5086–5089.

[65] Kane, C. L. and Fisher, M. P. A. (1992a). Transmission through barriers and resonant tunneling in an interacting one-dimensional electron gas. *Physical Review B*, 46(23):15233–15262.

[66] Kane, C. L. and Fisher, M. P. A. (1992b). Transport in a one-channel Luttinger liquid. *Physical Review Letters*, 68(8):1220–1223.

[67] Kardynał, B., Barnes, C. H. W., Linfield, E. H., Ritchie, D. A., Brown, K. M., Jones, G. A. C., and Pepper, M. (1996). Direct Measurement of the Band Structure of a One-Dimensional Surface Superlattice. *Physical Review Letters*, 76(20):3802–3805.

[68] Kim, B. J., Koh, H., Rotenberg, E., Oh, S.-J., Eisaki, H., Motoyama, N., Uchida, S., Tohyama, T., Maekawa, S., Shen, Z.-X., and Kim, C. (2006). Distinct spinon and holon dispersions in photoemission spectral functions from one-dimensional $SrCuO_2$. *Nature Physics*, 2(6):397–401.

[69] Kim, C. (2001). Spin–charge separation in 1D Mott-insulators and related systems. *Journal of Electron Spectroscopy and Related Phenomena*, 117-118:503–515.

[70] Kim, C., Matsuura, A. Y., Shen, Z.-X., Motoyama, N., Eisaki, H., Uchida, S., Tohyama, T., and Maekawa, S. (1996). Observation of Spin-Charge Separation in One-Dimensional $SrCuO_2$. *Physical Review Letters*, 77(19):4054–4057.

[71] Kim, M., Xu, S. G., Berdyugin, A. I., Principi, A., Slizovskiy, S., Xin, N., Kumaravadivel, P., Kuang, W., Hamer, M., Kumar, R. K., Gorbachev, R. V., Watanabe, K., Taniguchi, T., Grigorieva, I. V., Fal'ko, V. I., Polini, M., and Geim, A. K. (2020). Control of electron-electron interaction in graphene by proximity screening. *Nat. Commun.*, 11:2339.

[72] Kim, N. Y., Recher, P., Oliver, W. D., Yamamoto, Y., Kong, J., and Dai, H. (2007). Tomonaga-Luttinger Liquid Features in Ballistic Single-Walled Carbon Nanotubes: Conductance and Shot Noise. *Physical Review Letters*, 99(3):036802.

[73] Klitzing, K. v., Dorda, G., and Pepper, M. (1980). New Method for High-Accuracy Determination of the Fine-Structure Constant Based on Quantized Hall Resistance. *Phys. Rev. Lett.*, 45:494–497.

[74] Kukushkin, I. V. and Schmult, S. (2015). Fermi liquid effects and quasiparticle mass renormalization in a system of two-dimensional electrons with strong interaction. *JETP Lett.*, 101(10):693–698.

[75] Kwon, Y., Ceperley, D. M., and Martin, R. M. (1994). Quantum Monte Carlo calculation of the Fermi-liquid parameters in the two-dimensional electron gas. *Phys. Rev. B*, 50(3):1684–1694.

[76] Lake, B., Tennant, D. A., Caux, J.-S., Barthel, T., Schollwöck, U., Nagler, S. E., and Frost, C. D. (2013). Multispinon continua at zero and finite temperature in a near-ideal Heisenberg chain. *Phys. Rev. Lett.*, 111:137205.

[77] Lake, B., Tennant, D. A., Frost, C. D., and Nagler, S. E. (2005). Quantum criticality and universal scaling of a quantum antiferromagnet. *Nat. Mater.*, 4:329–334.

[78] Landau, L. D. (1965). *On the theory of the Fermi Liquid In: Collected Papers of L.D. Landau*. D. Ter Haar (Ed.), Pergamon.

[79] Landauer, R. (1957). Spatial Variation of Currents and Fields Due to Localized Scatterers in Metallic Conduction. *IBM Journal of Research and Development*, 1(3):223–231. Conference Name: IBM Journal of Research and Development.

[80] Larkin, I. A., Davies, J. H., Long, A. R., and Cuscó, R. (1997). Theory of potential modulation in lateral surface superlattices. ii. piezoelectric effect. *Phys. Rev. B*, 56:15242–15251.

[81] Laroche, D., Bielejec, E. S., Reno, J. L., Gervais, G., and Lilly, M. P. (2008). Towards Coulomb drag in vertically coupled quantum wires with independent contacts. *Physica E: Low-dimensional Systems and Nanostructures*, 40(5):1569–1572.

[82] Laroche, D., Gervais, G., Lilly, M. P., and Reno, J. L. (2011). Positive and negative Coulomb drag in vertically integrated one-dimensional quantum wires. *Nature Nanotechnology*, 6(12):793–797.

[83] Laroche, D., Gervais, G., Lilly, M. P., and Reno, J. L. (2014). 1D-1D Coulomb Drag Signature of a Luttinger Liquid. *Science*, 343:631–634.

[84] Lawaetz, P. (1971). Valence-Band Parameters in Cubic Semiconductors. *Phys. Rev. B*, 4(10):3460–3467.

[85] Li, L., Richter, C., Paetel, S., Kopp, T., Mannhart, J., and Ashoori, R. C. (2011). Very Large Capacitance Enhancement in a Two-Dimensional Electron System. *Science*, 332(6031):825–828.

[86] Luryi, S. (1988). Quantum capacitance devices. *Appl. Phys. Lett.*, 52(6):501–503.

[87] Luther, A. and Emery, V. J. (1974). Backward Scattering in the One-Dimensional Electron Gas. *Physical Review Letters*, 33(10):589–592.

[88] Luther, A. and Peschel, I. (1974). Single-particle states, Kohn anomaly, and pairing fluctuations in one dimension. *Physical Review B*, 9(7):2911–2919.

[89] Luttinger, J. M. (1963). An Exactly Soluble Model of a Many-Fermion System. *Journal of Mathematical Physics*, 4(9):1154–1162.

[90] Mahan, G. D. (2000). *Many-Particle Physics*. Springer.

[91] Mattis, D. C. and Lieb, E. H. (1965). Exact Solution of a Many-Fermion System and Its Associated Boson Field. *Journal of Mathematical Physics*, 6(2):304–312.

[92] Matveev, K. A. (2004). Conductance of a quantum wire at low electron density. *Physical Review B*, 70(24):245319.

[93] Meden, V. and Schönhammer, K. (1992). Spectral functions for the Tomonaga-Luttinger model. *Phys. Rev. B*, 46:15753 –15760.

[94] Moreno, M., Ford, C. J. B., Jin, Y., Griffiths, J. P., Farrer, I., Jones, G. a. C., Ritchie, D. A., Tsyplyatyev, O., and Schofield, A. J. (2016). Nonlinear spectra of spinons and holons in short GaAs quantum wires. *Nature Communications*, 7(1):12784.

[95] Mourigal, M., Enderle, M., Klöpperpieper, A., Caux, J.-S., Stunault, A., and Rønnow, H. M. (2013). Fractional spinon excitations in the quantum Heisenberg antiferromagnetic chain. *Nat. Phys.*, 9:435–441.

[96] Nozières, P. and De Dominicis, C. T. (1969). Singularities in the X-Ray Absorption and Emission of Metals. III. One-Body Theory Exact Solution. *Physical Review*, 178(3):1097–1107.

[97] Orbach, R. (1958). Linear antiferromagnetic chain with anisotropic coupling. *Phys. Rev.*, 112:309–316.

[98] Pagano, G., Mancini, M., Cappellini, G., Lombardi, P., Schäfer, F., Hu, H., Liu, X.-J., Catani, J., Sias, C., Inguscio, M., and Fallani, L. (2014). A one-dimensional liquid of fermions with tunable spin. *Nature Physics*, 10(3):198–201.

[99] Pateras, A., Carnis, J., Mukhopadhyay, U., Richard, M.-I., Leake, S. J., Schülli, T. U., Reichl, C., Wegscheider, W., Dehollain, J. P., Vandersypen, L. M. K., and Evans, P. G. (2019). Electrode-induced lattice distortions in GaAs multi-quantum-dot arrays. *J. Mat. Res.*, 34(8):1291–1301.

[100] Pateras, A., Park, J., Ahn, Y., Tilka, J. A., Holt, M. V., Reichl, C., Wegscheider, W., Baart, T. A., Dehollain, J. P., Mukhopadhyay, U., Vandersypen, L. M. K., and Evans, P. G. (2018). Mesoscopic Elastic Distortions in GaAs Quantum Dot Heterostructures. *Nano Lett.*, 18(5):2780–2786.

[101] Piller, H. (1966). In *Proc. 8th Int. Conf. on Physics of Semiconductors (Kyoto), J. Phys. Soc. Japan **21***, pages 206–209.

[102] Pouget, J. P., Khanna, S. K., Denoyer, F., Comès, R., Garito, A. F., and Heeger, A. J. (1976). X Ray Observation of $2k_F$ and $4k_F$ Scatterings in Tetrathiafulvalene-Tetracyanoquinodimethane (TTF-TCNQ). *Physical Review Letters*, 37(7):437–440.

[103] Raymond, A., Robert, J. L., and Bernard, C. (1979). The electron effective mass in heavily doped GaAs. *J. Phys. C: Sol. St. Phys.*, 12(12):2289–2293.

[104] Romaniello, P., Bechstedt, F., and Reining, L. (2012). Beyond the *gw* approximation: Combining correlation channels. *Phys. Rev. B*, 85:155131.

[105] Salomon, G., Koepsell, J., Vijayan, J., Hilker, T. A., Nespolo, J., Pollet, L., Bloch, I., and Gross, C. (2019). Direct observation of incommensurate magnetism in Hubbard chains. *Nature*, 565(7737):56–60.

[106] Scheller, C. P., Liu, T.-M., Barak, G., Yacoby, A., Pfeiffer, L. N., West, K. W., and Zumbühl, D. M. (2014). Possible Evidence for Helical Nuclear Spin Order in GaAs Quantum Wires. *Physical Review Letters*, 112(6):066801.

[107] Schofield, A. J. (1999). Non-Fermi liquids. *Contemporary Physics*, 40(2):95–115.

[108] Schrieffer, J. R., Scalapino, D. J., and Wilkins, J. W. (1963). Effective Tunneling Density of States in Superconductors. *Physical Review Letters*, 10(8):336–339.

[109] Shen, Z. X. and Dessau, D. S. (1995). Electronic structure and photoemission studies of late transition-metal oxides — Mott insulators and high-temperature superconductors. *Physics Reports*, 253(1):1–162.

[110] Simion, G. E. and Giuliani, G. F. (2008). Many-body local fields theory of quasiparticle properties in a three-dimensional electron liquid. *Phys. Rev. B*, 77:035131.

[111] Smoleński, T., Dolgirev, P. E., Kuhlenkamp, C., Popert, A., Shimazaki, Y., Back, P., Lu, X., Kroner, M., Watanabe, K., Taniguchi, T., Esterlis, I., Demler, E., and Imamoğlu, A. (2021). Signatures of Wigner crystal of electrons in a monolayer semiconductor. *Nature*, 595(7865):53–57.

[112] Smoliner, J. (1996). Tunnelling spectroscopy of low-dimensional states. *Semiconductor Science and Technology*, 11(1):1–16.

[113] Spitzer, W. G. and Whelan, J. M. (1959). Infrared Absorption and Electron Effective Mass in *n*-Type Gallium Arsenide. *Phys. Rev.*, 114(1):59–63.

[114] Stillman, G. E., Wolfe, C. M., and Dimmock, J. O. (1969). Magnetospectroscopy of shallow donors in GaAs. *Sol. State Commun.*, 7(13):921–925.

[115] Tan, Y.-W., Zhu, J., Stormer, H. L., Pfeiffer, L. N., Baldwin, K. W., and West, K. W. (2005). Measurements of the Density-Dependent Many-Body Electron Mass in Two Dimensional GaAs/AlGaAs Heterostructures. *Phys. Rev. Lett.*, 94(1):016405.

[116] Tomonaga, S.-i. (1950). Remarks on Bloch's Method of Sound Waves applied to Many-Fermion Problems. *Progress of Theoretical Physics*, 5(4):544–569.

[117] Tserkovnyak, Y., Halperin, B. I., Auslaender, O. M., and Yacoby, A. (2002). Finite-Size Effects in Tunneling between Parallel Quantum Wires. *Physical Review Letters*, 89(13):136805.

[118] Tserkovnyak, Y., Halperin, B. I., Auslaender, O. M., and Yacoby, A. (2003). Interference and zero-bias anomaly in tunneling between Luttinger-liquid wires. *Physical Review B*, 68(12):125312.

[119] Tsyplyatyev, O., Schofield, A., Jin, Y., Moreno, M., Tan, W. K., Ford, C. J. B., Griffiths, J. P., Farrer, I., Jones, G. A. C., and Ritchie, D. A. (2015). Hierarchy of Modes in an Interacting One-Dimensional System. *Physical Review Letters*, 114(19):196401.

[120] Tsyplyatyev, O. and Schofield, A. J. (2014). Spectral-edge mode in interacting one-dimensional systems. *Physical Review B*, 90(1):014309.

[121] Tsyplyatyev, O., Schofield, A. J., Jin, Y., Moreno, M., Tan, W. K., Anirban, A. S., Ford, C. J. B., Griffiths, J. P., Farrer, I., Jones, G. A. C., and Ritchie, D. A. (2016). Nature of the many-body excitations in a quantum wire: Theory and experiment. *Physical Review B*, 93(7):075147.

[122] van Wees, B. J., van Houten, H., Beenakker, C. W. J., Williamson, J. G., Kouwenhoven, L. P., van der Marel, D., and Foxon, C. T. (1988). Quantized conductance of point contacts in a two-dimensional electron gas. *Physical Review Letters*, 60(9):848–850. Publisher: American Physical Society.

[123] Vianez, P., Tsyplyatyev, O., and Ford, C. (2021a). *Semiconductor nanodevices as a probe of strong electron correlations In: Semiconductor Nanodevices: Physics, Technology and Applications*. David Ritchie (Ed.), Elsevier.

[124] Vianez, P. M. T., Jin, Y., Moreno, M., Anirban, A. S., Anthore, A., Tan, W. K., Griffiths, J. P., Farrer, I., Ritchie, D. A., Schofield, A. J., Tsyplyatyev, O., and Ford, C. J. B. (2021b). Observing separate spin and charge Fermi seas in a strongly correlated one-dimensional conductor. *arXiv:2102.05584*.

[125] Vianez, P. M. T., Jin, Y., Tan, W. K., Griffiths, J. P., Farrer, I., Ritchie, D. A., Tsyplyatyev, O., and Ford, C. J. B. (2021c). Decoupling of the many-body effects from the electron mass in GaAs by means of reduced dimensionality. *arXiv:2110.14539*.

[126] Vijayan, J., Sompet, P., Salomon, G., Koepsell, J., Hirthe, S., Bohrdt, A., Grusdt, F., Bloch, I., and Gross, C. (2020). Time-resolved observation of spin-charge deconfinement in fermionic Hubbard chains. *Science*, 367(6474):186–189.

[127] Voit, J. (1993). Charge-spin separation and the spectral properties of Luttinger liquids. *Journal of Physics: Condensed Matter*, 5(44):8305–8336.

[128] Von Delft, J. and Schoeller, H. (1998). Bosonization for beginners—refermionization for experts. *Annalen der Physik*, 7(4):225–305.

[129] Wang, S., Zhao, S., Shi, Z., Wu, F., Zhao, Z., Jiang, L., Watanabe, K., Taniguchi, T., Zettl, A., Zhou, C., and Wang, F. (2020). Nonlinear Luttinger liquid plasmons in semiconducting single-walled carbon nanotubes. *Nature Materials*, 19:986–991.

[130] Wharam, D. A., Thornton, T. J., Newbury, R., Pepper, M., Ahmed, H., Frost, J. E. F., Hasko, D. G., Peacock, D. C., Ritchie, D. A., and Jones, G. A. C. (1988). One-dimensional transport and the quantisation of the ballistic resistance. *Journal of Physics C: Solid State Physics*, 21(8):L209–L214. Publisher: IOP Publishing.

[131] Yang, C. N. (1967). Some exact results for the many-body problem in one dimension with repulsive delta-function interaction. *Phys. Rev. Lett.*, 19:1312–1315.

[132] Yang, T., Grišins, P., Chang, Y., Zhao, Z., Shih, C., Giamarchi, T., and Hulet, R. (2018). Measurement of the Dynamical Structure Factor of a 1D Interacting Fermi Gas. *Physical Review Letters*, 121(10):103001.

[133] Yao, Z., Postma, H. W. C., Balents, L., and Dekker, C. (1999). Carbon nanotube intramolecular junctions. *Nature*, 402(6759):273–276.

[134] Zhang, Y. and Sarma, S. D. (2005). Quasiparticle effective-mass divergence in two-dimensional electron systems. *Phys. Rev. B*, 71:045322.

[135] Zwick, F., Jérome, D., Margaritondo, G., Onellion, M., Voit, J., and Grioni, M. (1998). Band Mapping and Quasiparticle Suppression in the One-Dimensional Organic Conductor TTF-TCNQ. *Physical Review Letters*, 81(14):2974–2977.

Appendix A

Wafer characterisation

All devices measured in this thesis were fabricated out of two wafers, W939 and C2617. For details on wafer structure, see Table A.1. A calculation of the resulting conduction band profile can be found in Fig. 4.3. Results on wafer assessment can be found in [57] for wafer W939 and [60] for wafer C2617. Fig. A.1 reproduces the results for wafer W939. In summary, electron concentrations of 3 (2.2)$\times 10^{15}$ m^{-}2 with mobilities of 120 (165) m^{2}V^{-1}s^{-1} were obtained for the top (bottom) well of wafer W939, while 2.85 (1.54)$\times 10^{15}$ m^{-2} and 191 (55) m^{2}V^{-1}s^{-1} for wafer C2617, as measured at 1.4 K. For completeness, below we outline the assessment protocol.

Low-dimensional quantum systems at low temperatures exhibit quantum behaviour which can be used to characterise and quantify certain structural properties. In order to assess the overall quality of the wafer material, we use a Hall bar geometry in order to measure both the longitudinal, $R_{\mathrm{xx}} = V_{\mathrm{xx}}/I$, as well as transverse resistance, $R_{\mathrm{xy}} = V_{\mathrm{xy}}/I$, of the sample. This allows us to extract both the carrier density, n, as well as the mobility, μ, for each quantum well. Specifically, we do so by measuring both the quantum Hall effect (QHE) as well as Shubnikov-de Haas (SdH) oscillations.

According to the semiclassical Boltzmann formalism, the resistance of system, for instance across a Hall bar, should rise linearly with magnetic field. As observed in the seminal paper by Klitzing *et al.* [73], however, when a high-quality 2DEG is subject to a perpendicular field at low enough temperatures, then after an initial linear rise, R_{xy} becomes quantised instead, in multiples of h/e^2. This is the (integer) QHE and can be explained in terms of the Landau levels rising above the Fermi level: when E_{F} is in between two Landau levels there is no backscattering between states on opposite edges, and so the resistance remains constant; when a new level crosses it, however, there is backscattering, with conductance increase to e^2N/h, where N is the number of edge channels (and equal to the number of populated Landau levels).

A related phenomenon, SdH oscillations, refers to the simultaneous oscillation of R_{xx} between zero and some finite value as the Landau levels cross the Fermi level, see Fig. A.1a for a series of sweeps of R_{xx} *vs* B as V_{gate} (*i.e.*, the density) is varied. It can be shown that the period of these oscillations (in inverse magnetic field) is related to the electron density of the system as

$$n = \frac{2e}{h}\frac{1}{\Delta(\frac{1}{B})} \tag{A.1}$$

Fig. A.1b shows the Fourier transform of R_{xx} as a function of both electron density n and V_{gate}. Notice how a total of two frequencies of oscillations are detected, each arising from one of the quantum wells. From $+0.4\,\mathrm{V}$ to $-0.35\,\mathrm{V}$ one frequency decreases linearly while the other remains essentially constant. The former corresponds to the electron density in the upper well, n_{upper}. On the other hand, the lower well is screened by the upper one and does not start getting depleted until $-0.35\,\mathrm{V}$ (with n_{lower} remaining constant while the upper well is present), before starting to also decrease linearly until depletion around $-0.6\,\mathrm{V}$. The extracted densities are both observed to depend linearly on gate voltage, see Fig. A.1c. Here, n_{Hall} was obtained from the Hall resistivity as $n_{Hall} = (e\mathrm{d}\rho_{xy}/\mathrm{d}B)^{-1}$, which is observed to closely match $n_{upper} + n_{lower}$.

In order to extract the electron mobility, μ, we use the longitudinal conductivity, σ_{xx}, where

$$\sigma_{xx} = ne\mu \tag{A.2}$$

from which we get μ_{eff}, the effective total mobility of the sample as

$$\mu_{eff} = \frac{\sigma_{xx}}{e(n_{upper} + n_{lower})}. \tag{A.3}$$

Note that this combines both 2DEGs.

In order to obtain μ individually for each system, we assume that each layer can be treated as an independent conductor, with the conductivity σ_{xx} being then given by

$$\sigma_{xx} = \sigma_{upper} + \sigma_{lower}. \tag{A.4}$$

This approximation should remain valid as so long as the properties of the lower 2DEG remain unchanged while the upper 2DEG is filled. This gives us

$$\mu_{eff} = \frac{n_{upper}\mu_{upper} + n_{lower}\mu_{lower}}{e(n_{upper} + n_{lower})}, \tag{A.5}$$

see Fig. A.1e.

In order to extract the mobility of the lower layer, note that, after the upper layer is fully depleted (*i.e.*, when $n_{\text{upper}} = 0$), $\mu_{\text{eff}} \equiv \mu_{\text{lower}}$. This is valid as long as $V_{\text{gate}} < -0.35\,\text{V}$. For $V_{\text{gate}} > -0.35\,\text{V}$, μ_{upper} can be extracted given knowledge of n_{upper} and n_{lower}, determined before, as well as μ_{lower}. The results are shown in Fig. A.1f.

Material	**Thickness (nm)**	**Ratio**	**Repeat**	**Purpose**
GaAs	10			Protective cap (avoids oxidisation)
AlGaAs	40	0.33		Doping layer with $1\times10^{18}\,\text{cm}^{-2}$ of Si
AlGaAs	20	0.33		Modulation doping spacer
GaAs	18			Upper quantum well
GaAs/AlGaAs	0.556/0.833		10	Superlattice tunnel barrier
GaAs	18			Lower quantum well
AlGaAs	25	0.33		Modulation doping spacer
GaAs	0.56			Spacer
AlGaAs	15	0.33		Spacer
AlGaAs	40	0.33		Doping layer with $1\times10^{18}\,\text{cm}^{-2}$ of Si
GaAs	0.56			Spacer
AlGaAs	350	0.33		Transition to bulk
GaAs/AlGaAs	2.5/2.5		100	Superlattice (only present in wafer C2617)
GaAs	1000			Substrate

Table A.1 Growth specifications for the wafers used in this work. From surface to substrate.

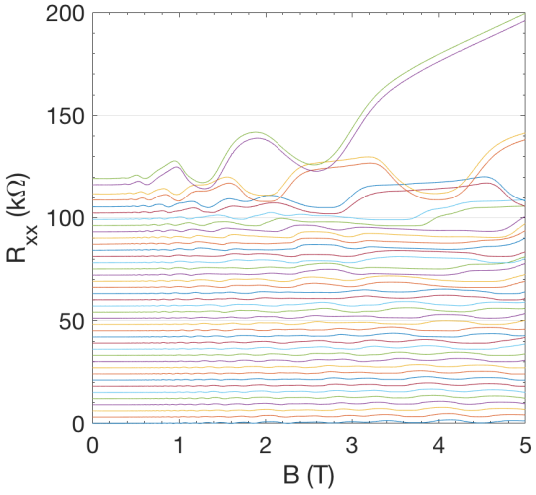

(a) Longitudinal resistance vs B

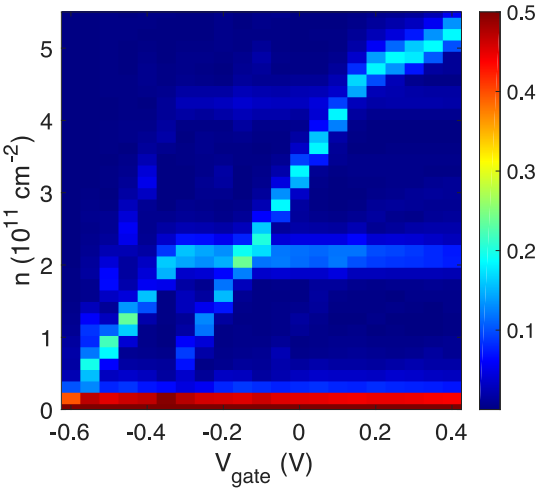

(b) Fourier transform of R_{xx} in B^{-1}

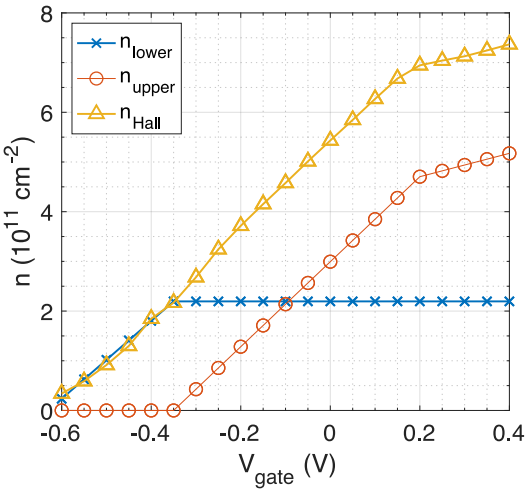

(c) Carrier densities vs gate voltage

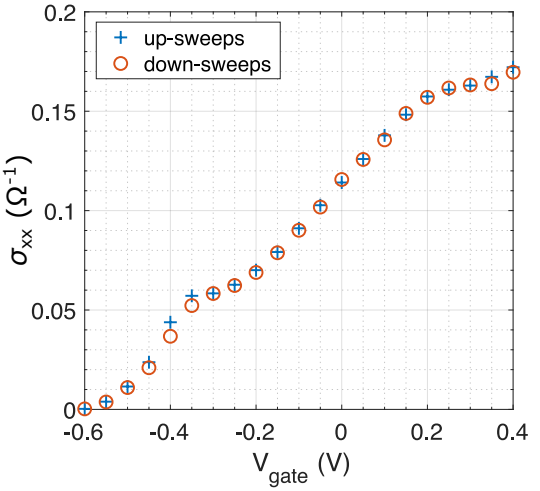

(d) Longitudinal conductivity ($B = 0$) vs V_{gate}

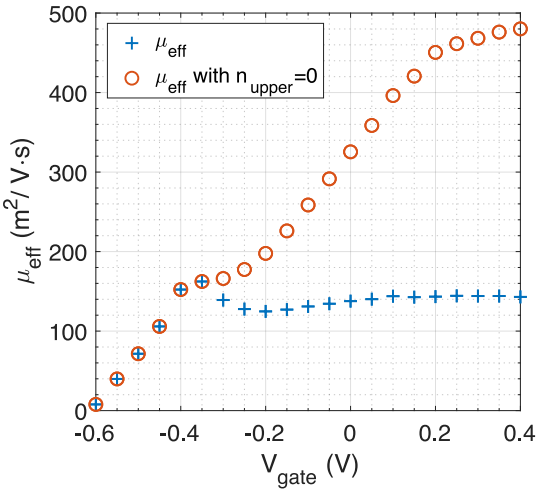

(e) Effective mobility vs V_{gate}

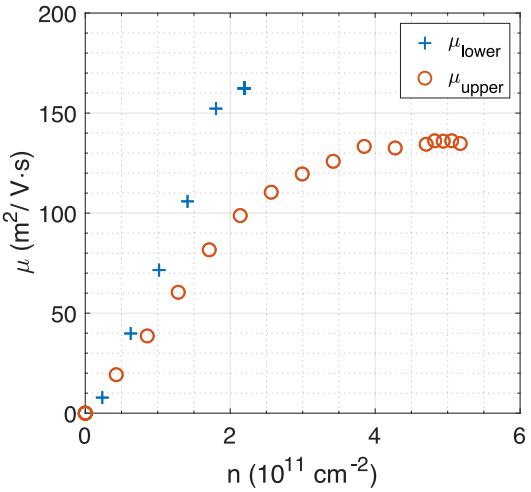

(f) Mobilities of individual layers vs V_{gate}

Fig. A.1 Assessment results for wafer W939. From [57].

Appendix B

Cleanroom fabrication protocol

Photomask for Mesa, Ohmics, and Optical gates: CAV-SP-TLL.

Mesa

1. Prepare etching solution for overcut profile:
   (a) H_2SO_4:H_2O_2:H_2O (1:8:1000);
2. Clean the wafer: acetone (1 min. ultrasound) + IPA (1 min. ultrasound) + N_2 + bake (5 min. @115°C)
3. Check the orientation of the major flat. The mesa should be aligned along it. This can be done under the optical microscope by looking for the direction along which surface defects distort.
4. Apply photoresist:
   (a) test spinner: 5500rpm for 60s
   (b) place sample on the spinning stage and spin for $10-15$s while applying N_2;
   (c) apply Shipley Microposit S1813 positive photoresist;
   (d) spin @5500rpm for 60s;
   (e) remove sample and clean back with acetone;
   (f) bake for 1 min. @115°C to harden the resist;
   (g) let the sample cool down for about 1 min.;
5. Photolithography:

(a) clean photomask: acetone+IPA+N_2;

(b) align mesa pattern to sample (ensuring that pattern is aligned along the major axis);

(c) check for good contact to the sample;

(d) expose for 6.5s (if using SP orange mask aligner) or equivalent dose/time to ensure that the exposed regions can be developed away. Note that for the resist and spin settings used one should expect about 150 nm of S1813.

6. Development:

(a) after exposure, develop the sample in Microposit MF-319 developer for $30-40$s;

(b) clean the sample in Weir DI water until R>10 MΩ +N_2 (note: do not use acetone and/or IPA as this will also remove the resist in the unexposed regions);

(c) check pattern under the optical microscope to ensure correct alignment and/or development; if necessary, increase the development time iteratively until satisfactory profiles are obtained;

(d) if sample is grossly misaligned and/or other severe problems are detected, clean sample with acetone and IPA, ensuring all resist is removed, before starting over;

7. Dektak:

(a) find one or more features and mark their position; these will be used as reference points to determine the etch rate as well as actual depth etched;

(b) Dektak the selected features and obtain a reference level;

8. Etching:

(a) target etch: $\sim 150-170$ nm to ensure it goes through both quantum wells;

(b) 1^{st} dip: $\sim$3 min.;

(c) Dektak same feature as before in order to obtain etch rate;

(d) 2^{nd} dip: dip for the required time, based on the calculated etch rate, until target etch is achieved;

(e) Dektak again to confirm actual depth etched; if necessary, dip again to ensure target etch is reached;

9. Clean the wafer: acetone (1 min. ultrasound) + IPA (1 min. ultrasound) + N_2

Ohmics

1. Apply photoresists:
   (a) pre-bake @115°C for 5 min.;
   (b) set hotplate @180°C
   (c) test spinner: 6000rpm for 60s
   (d) place sample on the spinning stage and spin for $10-15$s while applying N_2;
   (e) apply MicroChem LOR5B; if using LOR5B directly from the fridge, wait until it warms up to room temperature
   (f) spin @6000rpm for 60s;
   (g) remove sample and clean back with MF-319;
   (h) bake for 10 min. @180°C to harden the resist;
   (i) let the sample cool down for about 1 min.;
   (j) test spinner: 5500rpm for 60s
   (k) place sample on the spinning stage and spin for $10-15$s while applying N_2;
   (l) apply Shipley Microposit S1805 positive photoresist;
   (m) spin @5500rpm for 60s;
   (n) remove sample and clean back with acetone;
   (o) bake for 1 min. @115°C to harden the resist;
   (p) let the sample cool down for about 1 min.;
2. Photolithography:
   (a) clean photomask: acetone+IPA+N_2;
   (b) align ohmic pattern to sample (ensuring that pattern is aligned to the mesa pattern already patterned);
   (c) check for good contact to the sample;
   (d) expose for 3.5s (if using SP orange mask aligner) or equivalent dose/time to ensure that the exposed regions can be developed away.
3. Development:
   (a) after exposure, develop the sample in Microposit MF-319 developer for $30-40$s;

(b) clean the sample in Weir DI water until R>10 MΩ +N_2 (note: do not use acetone and/or IPA as this will also remove the resist in the unexposed regions);

(c) check pattern under the optical microscope to ensure correct alignment and/or development; if necessary, increase the development time iteratively until satisfactory profiles are obtained;

(d) if sample is grossly misaligned and/or other severe problems are detected, clean sample with acetone and IPA, ensuring all resist is removed, before starting over;

4. Prepare Ohmics evaporator

   (a) $350-400$ mg AuGeNi alloy;

5. Descum:

   (a) prepare HCl:H_2O solution (1:9);

   (b) RF Plasma ash for 1 min.;

   (c) dip sample in HCl for 15s;

   (d) clean the sample in Weir DI water until R>10 MΩ +N_2;

6. Evaporation:

   (a) load the sample onto the thermal evaporator;

   (b) leave it pumping until a base pressure of $\sim 10^{-7}$ mbar is reached;

   (c) start evaporation at a rate of ~ 0.1 nm/s for the first 3 nm before increasing it to ~ 0.3 nm/s;

   (d) evaporate about $\sim 150-200$ nm of metal;

7. Lift-off:

   (a) after evaporation, place the sample in acetone for 10min, followed by 30min in SVC14 @70°C;

   (b) flush the sample in acetone so that the excess metal is removed; ultrasound if necessary;

   (c) place the sample into a petri dish with IPA and check under the optical microscope to ensure satisfactory lift-off; if not, repeat the previous step iteratively until so;

   (d) dry the sample in N_2;

8. Annealing (RTP600s Rapid Annealer):

(a) anneal at 430°C for 80s;

(b) for details on the recipe used, see SP FS01.rpd;

9. Testing the ohmics:

(a) test the ohmics using a probe station at both room and nitrogen temperatures; the resistance values should be $\sim 6\,\mathrm{k}\Omega$ and $< 1\,\mathrm{k}\Omega$, respectively;

Optical gates

1. Apply photoresists:

(a) pre-bake @115°C for 5 min.;

(b) set hotplate @180°C

(c) test spinner: 6000rpm for 60s

(d) place sample on the spinning stage and spin for $10-15$s while applying N_2;

(e) apply MicroChem LOR5B; if using LOR5B directly from the fridge, wait until it warms up to room temperature

(f) spin @6000rpm for 60s;

(g) remove sample and clean back with MF-319;

(h) bake for 10 min. @180°C to harden the resist;

(i) let the sample cool down for about 1 min.;

(j) test spinner: 5500rpm for 60s

(k) place sample on the spinning stage and spin for $10-15$s while applying N_2;

(l) apply Shipley Microposit S1805 positive photoresist;

(m) spin @5500rpm for 60s;

(n) remove sample and clean back with acetone;

(o) bake for 1 min. @115°C to harden the resist;

(p) let the sample cool down for about 1 min.;

2. Photolithography:

(a) clean photomask: acetone+IPA+N_2;

(b) align optical gates pattern to sample (ensuring that pattern is aligned to patterns already in place);

(c) check for good contact to the sample;

(d) expose for 3.5s (if using SP orange mask aligner) or equivalent dose/time to ensure that the exposed regions can be developed away.

3. Development:

(a) after exposure, develop the sample in Microposit MF-319 developer for $30-40$s;

(b) clean the sample in Weir DI water until R>10 MΩ +N_2 (note: do not use acetone and/or IPA as this will also remove the resist in the unexposed regions);

(c) check pattern under the optical microscope to ensure correct alignment and/or development; if necessary, increase the development time iteratively until satisfactory profiles are obtained;

(d) if sample is grossly misaligned and/or other severe problems are detected, clean sample with acetone and IPA, ensuring all resist is removed, before starting over;

4. Prepare thermal evaporator

(a) Ti+Au;

5. Descum:

(a) prepare HCl:H_2O solution (1:9);

(b) RF Plasma ash for 1 min.;

(c) dip sample in HCl for 15s;

(d) clean the sample in Weir DI water until R>10 MΩ +N_2;

6. Evaporation:

(a) load the sample onto the thermal evaporator;

(b) leave it pumping until a base pressure of $\sim 10^{-7}$ mbar is reached;

(c) evaporate about $\sim$25 nm of Ti, followed by $\sim 120-150$ nm of Au, at a rate of $\sim 0.3-0.4$ nm/s

7. Lift-off:

(a) after evaporation, place the sample in acetone for 10 min., followed by 30 min. in SVC14 @70°C;

(b) flush the sample in acetone so that any excess metal is removed; ultrasound if necessary;

(c) place the sample into a petri dish with IPA and check under the optical microscope to ensure satisfactory lift-off; if not, repeat the previous step iteratively until so;

(d) dry the sample in N_2;

E-beam gates

1. Apply photoresists:

   (a) pre-bake @125°C for 3 min.;

   (b) set hotplate @180°C

   (c) test spinner: 3500rpm for 60s

   (d) place sample on the spinning stage and spin for $10-15$s while applying N_2;

   (e) apply MMA(8.5)MAA copolymer (9%, 1:1 ratio in ethyl lactate)

   (f) spin @3500rpm for 60s;

   (g) remove sample and clean back with MF-319;

   (h) bake for 5 min. @115°C to harden the resist;

   (i) let the sample cool down for about 1 min.;

   (j) test spinner: 8000rpm for 60s

   (k) place sample on the spinning stage and spin for $10-15$s while applying N_2;

   (l) apply PMMA with a molecular weight of 950k (4% solid content in anisole diluted to a 2:1 ratio in MIBK);

   (m) spin @8000rpm for 60s;

   (n) remove sample and clean back with acetone;

   (o) bake for 3 min. @180°C to harden the resist;

   (p) let the sample cool down for about 1 min.;

2. Submit samples to the e-beam suite. Base dose (accounting for proximity correction): $D = 550\,\mu\text{C/cm}^2$, see section 4.3.4 for details.

3. Development:

(a) prepare the H_2O:IPA (3:7) developer;

(b) use a water bath to cool down the developer to $\sim 5^{\circ}$C;

(c) wait at least an hour to ensure the temperature has stabilised;

(d) develop the sample for 60s;

4. Descum:

(a) prepare HCl:H_2O solution (1:4);

(b) RF Plasma ash for 20s;

(c) dip sample in HCl for 10s;

(d) clean the sample in Weir DI water until R>10 MΩ +N_2;

5. Evaporation:

(a) load the sample onto the thermal evaporator;

(b) leave it pumping until a base pressure of $\sim 10^{-7}$ mbar is reached;

(c) evaporate about $\sim$5 nm of Ti, followed by $\sim$20 nm of Au, at a rate of $\sim 0.3 - 0.4$ nm/s;

6. Lift-off:

(a) after evaporation, leave the sample in acetone overnight;

(b) the next day, place the sample (still in acetone) in a hot water bath @45°C, 50rpm for $30 - 45$ min.;

(c) flush the sample in acetone so that the excess metal is removed; do not ultrasound as this will most likely damage the gates;

(d) place the sample in a petri dish with IPA and check under the optical microscope to ensure satisfactory lift-off; if not, repeat the previous step iteratively until so;

(e) dry the sample in N_2;

Air-bridges

For calibration data see [58]. * values were calibrated for target ticknesses of 130, 300, and 130 nm, respectively.

1. Apply photoresists:

(a) pre-bake @150°C for 10 min.;

(b) test spinner: 5700rpm for 60s

(c) place sample on the spinning stage and spin for $10-15$s while applying N_2;

(d) apply PMMA with a molecular weight of 950k (4% solid content in anisole diluted to a 2:1 ratio in MIBK);

(e) spin @5700rpm* for 60s;

(f) remove sample and clean back with MF-319;

(g) bake for 10 min. @110°C to harden the resist;

(h) let the sample cool down for about 1 min.;

(i) test spinner: 4500rpm for 60s

(j) place sample on the spinning stage and spin for $10-15$s while applying N_2;

(k) apply MMA(8.5)MAA copolymer (9%, 1:1 ratio in ethyl lactate);

(l) spin @4500rpm* for 60s;

(m) remove sample and clean back with MF-319;

(n) bake for 10 min. @110°C to harden the resist;

(o) let the sample cool down for about 1 min.;

(p) test spinner: 6000rpm for 60s

(q) place sample on the spinning stage and spin for $10-15$s while applying N_2;

(r) apply 100k PMMA (undiluted);

(s) spin @6000rpm* for 60s;

(t) remove sample and clean back with MF-319;

(u) bake for 10 min. @110°C to harden the resist;

(v) let the sample cool down for about 1 min.;

2. Submit samples to the e-beam suite. Base doses (accounting for proximity correction): $D_p = 880\,\mu$C/cm^2 and $D_b = 600\,\mu$C/cm^2, see section 4.3.4 for details.

3. Development:

(a) prepare H_2O:IPA (3:7) developer;

(b) use a water bath to cool down the developer to $\sim$5°C;

(c) wait at least an hour to ensure the temperature has stabilised;

(d) develop the sample for 60s;

(e) check pattern under the optical microscope; if necessary, increase the development time iteratively until satisfactory profiles are obtained;

4. Descum:

(a) prepare HCl:H_2O solution (1:4);

(b) RF Plasma ash for 25s;

(c) dip sample in HCl for 10s;

(d) clean the sample in Weir DI water until R>10 MΩ +N_2;

5. Evaporation:

(a) load the sample onto the thermal evaporator;

(b) leave it pumping until a base pressure of $\sim 10^{-7}$ mbar is reached;

(c) evaporate about ∼5 nm of Ti, followed by ∼20 nm of Au, at a rate of $\sim 0.3 - 0.4$ nm/s;

6. Evaporation:

(a) load the sample onto the thermal evaporator;

(b) leave it pumping until a base pressure of $\sim 10^{-7}$ mbar is reached;

(c) evaporate $\sim 110 - 130$ nm of Au, at a rate of $\sim 0.2 - 0.3$ nm/s;

7. Lift-off:

(a) after evaporation, leave the sample in acetone overnight;

(b) the next day, place the sample (still in acetone) in a hot water bath @45°C, 50rpm for 90 min.;

(c) flush the sample in acetone so that any excess metal is removed; do not ultrasound as this will most likely damage the air-bridges;

(d) place the sample in a petri dish with IPA and check under the optical microscope to ensure satisfactory lift-off; if not, repeat the previous step iteratively until so; the air-bridges should be visible as black, iridescent stripes;

(e) dry the sample in N_2;

Packaging and bonding

1. Cleave the sample in individual chips;
2. Use GE varnish to fix the sample onto a LCC ceramic package (20 connections), or equivalent;
3. Use a wedge wire-bonding machine to make the bonds (note: ball bonding should be avoided as it was found to significantly damage most electron-beam defined gates, mostly likely caused by the spark used to form the ball); care should be taken to ensure that appropriate grounding is in place; if possible, have an air ioniser in the vicinity whilst bonding.